Power Electronics Integrated Heat Transfer Frequency Response Characterization and Degradation Sensing

By

Timothy A. Polom

A dissertation submitted in partial fulfillment of
the requirements for the degree of

Doctor of Philosophy
(Mechanical Engineering)

at the
UNIVERSITY OF WISCONSIN-MADISON
2019

Date of final oral examination: 08/20/2019

The dissertation is approved by the following members of the Final Oral Committee:

Daniel C. Ludois, Associate Professor, Mechanical and Electrical & Computer Engineering
Matthew S. Allen, Associate Professor, Engineering Physics
Melih Eriten, Associate Professor, Mechanical Engineering
Gregory F. Nellis, Professor, Mechanical Engineering
Bulent Sarlioglu, Associate Professor, Engineering Professional Development

Abstract

Power semiconductor components and modules, universal in converter applications, are comprised of dissimilar, interconnected components. Since the interfaces are prone to thermal-mechanical fatigue, their electrical power conversion capability has limits that worsen over time; costs associated with fatigue and unscheduled maintenance are high. This dissertation develops a methodology for designing power semiconductor products and converter systems to actively sense their own lifetime-varying properties, e.g. degradation, in situ.

It begins by addressing limitations in transient heat transfer characterization of power electronic systems. State-of-the-art modeling methods are studied in the frequency domain, in part to identify asymptotic limits they implicitly impose. This modeling groundwork connects naturally to physical system study. Methods of system identification are developed for characterizing heat transfer frequency response forced by natural semiconductor device loss dissipation. Developed methods express captured dynamics with frequency response function, or Bode plot, magnitude and phase delay.

Experimental applications characterize several frequency decades of transient heat transfer, and multi-variable metrics reveal response sensitivities. Together with modeling investigations, they show which specific dynamic ranges are sensitive to different sources of degradation. For perspective on the several frequency response characterizations of different test setups contributed by the dissertation, sensitivity analysis, leveraged throughout the research, quantifies measurement errors, due to imperfect parameters, and limits of system identification experiments.

Results suggest the achievability of implementing system identification for specifiable-resolution, state-of-health monitoring in actively switching converter systems serving mission

profiles. Furthermore, spatially-varying frequency response functions reveal design opportunity in degradation sensitivity relationships. Using these principles as foundation, methods to integrate system identification are developed. Challenges associated with real-time degradation sensing in a converter embedding multi-chip power modules, a constrained environment, are identified.

This thesis proposes concurrent analysis of circuit topology and modulation, spatially-varying properties of heat transfer, and temperature sensing constraints during design phases to specify performance of an integrated degradation sensing system. The methodology overall empowers early converter conceptualization phases and enables precise, internet-based system health monitoring to, e.g., trigger maintenance. It projects to also add value at additional life cycle phases, such as manufacturing quality assurance and post-mortem failure analysis.

Acknowledgments

This section highlights groups and individuals that played positive roles in the outcome of this dissertation. This section is not all-encompassing; I cannot possibly name them all here.

I first acknowledge the late Prof. Lorenz who orchestrated and stimulated the professional evolution I experienced over the past several years. He contributed many ideas to this dissertation and beyond; his valuable lessons will propagate. I also thank Prof. Ludois who, as promised, got me out the door, and, before that, provided models for great engineering, technology disruption, and balance. Gratitude also goes to my Ph.D. degree committee members, Profs. Allen, Bulent, Eriten, and Nellis. Through course work and directed feedback, Professor Nellis played an especially significant role in helping me find and stay in a technological niche.

It was a privilege to work on a dissertation. Short-term funding for the work came from the German Academic Exchange Service and the mobilEM research training group of RWTH Aachen. Next, I acknowledge WEMPEC for years of constant funding, education, and strong connections to industry experts. Behind the curtain, Ms. Kathy Young and Ms. Helene Demont, with diligence and many dedicated assistants, ensured our privileges were promptly available. Mr. Kyle Hanson established lab infrastructure and workflow with thoughtfulness and focus on safety. Mr. Jim Sember, always available for career advice, took roles of leadership ensuring Prof. Lorenz’s students achieve, with funding, their program milestones. Mechanical and Electrical & Computer Engineering depts. also put forth special efforts to assure these outcomes.

Many thanks to my de facto teammate on this research, Dr. Christoph van der Broeck, who provided technical support with specifying models, used in making arguments in this dissertation,

and a continuous stream of energy for technology. Teammate Dr. Markus Andresen supported experiments establishing research foundations. Mr. Peter Killen kindly shared his knowledge at many timely moments and was a valuable skeptic. Dr. Seth Avery and Mr. Erick Oberstar listened, and supported project ambitions as best they could. Finally, mentoring of and collaboration with Mr. Jacob Free was a valuable, energizing, and signature aspect of this Ph.D. program.

Another signature aspect of the work effort was interaction with three sets of colleagues. Special thanks goes to current and past residents of 1535 Eng. Hall and the Control and Sensor Technology group at WEMPEC/University of Wisconsin. Special thanks to Delta Electronics in Taoyuan, where Dr. Kai-Wei Hu and colleagues ensured I had a welcoming and transformative taste of industry and Taiwan. Special thanks to the Institute for Power Electronics and Electrical Drives at RWTH Aachen. There, the welcoming leadership of chief engineers, group leaders, and Prof. De Doncker ultimately connected me with all of the research associates. This deepened my understanding of power electronic systems and how to have fun in an institute.

With humility, I finally acknowledge invaluable components of my personal life. I am very grateful that friends and family in Wisconsin, in Michigan, and other places always took time to catch up, even after it seemed like I had disapparated. Lastly, I thank Franziska for insinuating that I should hurry up in finishing my dissertation, my mother, Donna, for basically doing the same, and my brother and father, Jon and Bill, for being real engineers. Most of all, I thank this group for their infinite reserve of love and support.

Madison, WI, U.S.A. T.A.P.
August 2019

Table of Contents

Abstract .... ***i***

Acknowledgments .... ***iii***

Table of Contents .... ***v***

List of Figures .... ***vii***

List of Tables .... ***xvi***

Nomenclature .... ***xviii***

Introduction ***1***

Research Motivation 1
Research Overview 2
Statement of Contributions 4
Summary of Chapters 5

Chapter 1 State-of-the-Art Review ***6***

1.1 Power Semiconductor Assemblies and their Reliability 6
1.2 Acquisition of Dynamic Temperature Information 25
1.3 Power Electronics-oriented Heat Transfer Modeling 32
1.4 State Observers 62
1.5 Summary of Identified Research Opportunities 81

Chapter 2 Frequency Domain Heat Transfer Modeling ***84***

2.1 Operational Definitions 84
2.2 Identification of Method-Specific Limits 88
2.3 Finite Element, Computational Platform 101
2.4 Chapter Summary 106

Chapter 3 Spatiotemporal Heat Transfer Experimental Characterization ***107***

3.1 Converter-Integrated System Identification 107
3.2 Component-Level System Identification 138
3.3 Chapter Summary 152

Chapter 4 Sensitivity of Heat Transfer Frequency Response to Degradation ***154***

4.1 Operational Definitions 154
4.2 Model Predictions 156
4.3 Experimental Characterizations 172
4.4 Chapter Summary 186

Chapter 5 In-Situ Degradation Sensing based on Thermal Response Variation ***188***

5.1 Modeling Natural Loss Excitation Harmonics 188
5.2 Extraction of Degradation Information 193
5.3 Evaluation of Methods 198
5.4 Chapter Summary 209

Chapter 6 Integrating Degradation Sensing into Multi-Chip Power Modules 211

6.1 Tracking Chip Temperature Response Variation 211
6.2 Locating Substrate Temperature Detectors 220
6.3 Design Methodology 232
6.4 Chapter Summary 234

Chapter 7 Conclusions, Contributions, and Recommended Future Work 236

7.1 Research Conclusions 236
7.2 Research Contributions 240
7.3 Recommended Future Work 241

References 244

List of Figures

Fig. 1.1-1. Classification of nominal and defective components or assemblies in terms of overstress- and wear out-induced failures [15] 8

Fig. 1.1-2. Electro-thermal-mechanically-induced fatigue in power semiconductor assemblies [16] 9

Fig. 1.1-3. Hierarchy of a physics-based, multi-domain modeling effort to ultimately estimate mechanical stress/strain behavior in power semiconductor assemblies 9

Fig. 1.1-4. Investigation of solder layer voiding/delamination on thermal response [20] 11

Fig. 1.1-5. Investigation into total thermal resistance increases during power cycling [21], [22] 12

Fig. 1.1-6. Principles and approaches for reliability engineering 14

Fig. 1.1-7. Definitions of T_j, ΔT_j, and T_m (= T_{jm}) during ideal, periodic power cycles [32] 14

Fig. 1.1-8. N_f as a function of ΔT_j and T_m (= T_{jm}) 14

Fig. 1.1-9. Histogram of analytical techniques used by archived studies for post-mortem inspection of power cycled semiconductor assemblies [14] 15

Fig. 1.1-10. Representative open-loop model-based method to assess fatigue status using total thermal resistance [39] 17

Fig. 1.1-11. Strategy of measuring V_{ce} to assess fatigue status 19

Fig. 1.1-12. Shifts in structure function expression of thermal responses before and after defect manifestations [54] 20

Fig. 1.1-13. Summary of a thermal-mechanical model-based approach to estimating fatigue status [58] 21

Fig. 1.1-14. Overview of the statistical signal processing methodology to estimate device forward voltage drop and thermal resistance [59] 22

Fig. 1.1-15. Illustration of thermal wave principles for applied NDE 24

Fig. 1.2-1. Images of the Infineon FS100R12PT4 EconoPACK 4 IGBT module; please note that the thermistor component is enclosed by a red circle 25

Fig. 1.2-2. Ratings of different TSEPs – (a) voltage under low current, (b) threshold voltage, (c) voltage under high current, (d) gate-emitter voltage, (e) saturation current, (f) switching time [69] 28

Fig. 1.2-3. Generic diagram of an open-loop observer structure to estimate T_j in real-time 30

Fig. 1.2-4. Pictorial illustration of an open-loop IGBT temperature observer [74] 31

Fig. 1.3-1. Heat transfer analysis for the integrated circuit assembly in [85] 34

Fig. 1.3-2. Commercial power semiconductor assembly data sheet examples of junction-to-case transient thermal impedance curves 37

Fig. 1.3-3. Illustration of time constant spectra from [93] 39

Fig. 1.3-4. Illustration of non-ideal step input properties documented in [96] 41

Fig. 1.3-5. Cauer and Foster thermal model structures [94], [95] 44

Fig. 1.3-6. Summary of a method to populate a Cauer model [49], [100] 46

Fig. 1.3-7. Illustration of the 3D TEC derivation method from [103] 49

Fig. 1.3-8. Relatively early FDM of a semiconductor assembly [107] 52

Fig. 1.3-9. Critical outcomes from a model reduction study using FEA [110] 54

Fig. 1.3-10. Critical outcomes from another model reduction study using FEA [111] 54

Fig. 1.3-11. Critical outcomes from a model reduction study using FD techniques [105] 55

Fig. 1.3-12. Sequence of methods proposed and evaluated in [115] 58

Fig. 1.3-13. FRF-based illustration of cross-coupled, spatially-dependent heat transfer dynamic response properties [115] 58

Fig. 1.3-14. System identification methodology and results when applied to very large scale integration (VLSI) semiconductor chips [116]–[119] 59

Fig. 1.4-1. Fundamental block diagrams illustrating observer systems [121], [122] 63

Fig. 1.4-2. State-space model of a physical system, and open- and closed-loop observer systems [124] 63

Fig. 1.4-3. Observer-based control [125] 63

Fig. 1.4-4. Cascaded observer structure including adaptive, real-time estimation of the Young's Modulus mechanical parameter [136] 66

Fig. 1.4-5. Elements of a system to improve the precision of motor drives to utilize them as embedded sensors within an application 67

Fig. 1.4-6. Closed-loop observer to estimate spatial temperature distributions of frozen fish [141] 68

Fig. 1.4-7. Open-loop electrothermal observer system [142] 70

Fig. 1.4-8. Active junction temperature controller using feedback from a Foster model-based open-loop observer [143] 70

Fig. 1.4-9. Elements of a state-space, Luenberger-style observer to monitor spatial temperature distributions [144] 71

Fig. 1.4-10. Closed-loop, Gopinath-style junction temperature observer using measured baseplate temperature [145] 72

Fig. 1.4-11. Elements of a Kalman filtering system to estimate junction temperature signals with maximal signal-to-noise ratio [61] 73

Fig. 1.4-12. Electrothermal observer system including open-loop models obtained using FD modeling and then model-order reduction [146] 75

Fig. 1.4-13. Categorization of observers for DPSs [154] 76

Fig. 1.4-14. Elements of a thermal observer model obtained by formally treating the open-loop system as a DPS [156] 77

Fig. 1.4-15. Illustration of strategies to sense discrete spatial states within a DPS [155] 78

Fig. 2.1-1. Graphical illustrations of a computational domain for heat transfer analysis 86

Fig. 2.1-2. Relationship of a physical MOSFET-sink sub-assembly with an illustrative model explicitly displaying a spatial coordinate 86

Fig. 2.1-3. Example 3D SETIS plots showing electrothermal response as a function of input frequency and space 87

Fig. 2.2-1. Graphical illustrations of candidate heat transfer problems for SETIS analysis 88

Fig. 2.2-2. Vertical illustration of Fig. 2.2-1(b) 89

Fig. 2.2-3. Parametric FRFs of the spatiotemporal delay term, D(s,x) 91

Fig. 2.2-4. Isometric view of a SETIS map produced using the exact solution to the 1D transient model 92

Fig. 2.2-5. 2D views of the SETIS map shown in Fig. 2.2-4 93

Fig. 2.2-6. Two lumped capacitance finite difference thermal model 94

Fig. 2.2-7. 3D finite difference numerical model of a power semiconductor assembly; shown is the steady-state solution to a 1 W step input 97

Fig. 2.2-8. Isometric view of a SETIS map produced using the FD model in Fig. 2.2-7 97

Fig. 2.2-9. 2D views of the SETIS map shown in Fig. 2.2-8 98

Fig. 2.3-1. Discrete SiC power MOSFET 103

Fig. 2.3-2. FE model details 103

Fig. 2.3-3. Spatially-varying FRF of the model shown in Fig. 2.3-2 104

Fig. 2.3-4. Steady-state solution illustration of an analyzed IGBT power module 105

Fig. 2.3-5. Die-to-ambient FRF for loss excitation from the hot chip in Fig. 2.3-4 105

Fig. 3.1-1. Illustration of the thermal system identification method 108

Fig. 3.1-2. Loss modulator state block diagrams 110

Fig. 3.1-3. Parameter sensitivity of conduction and switching loss modulators 111

Fig. 3.1-4. Amplitude spectrum qualitative representation for candidate loss excitation waveforms, showing limited high frequency excitation ideal and non-ideal step inputs provide 114

Fig. 3.1-5. Elements of the experimental evaluation of electrothermal impedance spectroscopy 115

Fig. 3.1-6. Time-domain data used to calibrate the real-time MOSFET die temperature estimator 117

Fig. 3.1-7. Time domain waveforms extracted during a system identification experiment 118

Fig. 3.1-8. Overlay of three system identification test results using different random noise input perturbations, sample rates, and FFT settings 119

Fig. 3.1-9. Extension of the FRF data from Fig. 3.1-8 to include test results at frequency levels near to DC (using sub-mHz loss trajectories) and to 1 kHz (using single-frequency sinusoid injections) 121

Fig. 3.1-10. FRF data extracted using different experimental design specifications, including frequency content of the perturbation signal 124

Fig. 3.1-11. Overlay of a re-aggregated FRF curve, fusing results shown in Fig. 3.1-9, along with a manually fit FRF 125

Fig. 3.1-12. Comparison of ambient-referred and relative spatial FRF properties 127

Fig. 3.1-13. Simplified FE model in which component 1=heat sink, 2=lead frame (LF), and 3=silicon die 130

Fig. 3.1-14. Spatial FRFs comparing the FE-based and experimentally measured responses 131

Fig. 3.1-15. Die sensitivity functions showing how degradation in terms of R_{conv} (50%), $R_{LF\text{-}Sink}$ (200%), $R_{Si\text{-}LF}$ (100%), and the absence of wire bonds affect the die-to-ambient response; experimental traces are solid lines and model-derived traces are dotted lines 133

Fig. 3.1-16. Die-to-ambient FRF for nine nodes on the die surface 136

Fig. 3.1-17. Ratio of FRFs extracted with total losses represented as (1) die surface heat flux and (2) internal, volumetric generation 136

Fig. 3.2-1. Operating principle of an ex situ ETIS method 138

Fig. 3.2-2. Schematic drawings of the passive conduction loss modulation circuit 139

Fig. 3.2-3. Selected properties of a C3M0120100K SiC MOSFET component [170] 140

Fig. 3.2-4. State block diagram of the ex situ system identification experiment using a diode bridge rectifier for passive loss modulation; experimental parameters are blue colored, while constrained variables are red 141

Fig. 3.2-5. Example lumped capacitance block 143

Fig. 3.2-6. Analytically derived limits to cooling for ensuring its impact on ETIS is negligible 144

Fig. 3.2-7. Equipment used during experimental application of the ex situ ETIS method 144

Fig. 3.2-8. Time-domain data from an ex situ ETIS experiment at f_{fund} = 100 Hz 145

Fig. 3.2-9. Output characteristic of the DUT, Fuji 2SK3677 145

Fig. 3.2-10. Measured power loss AC and DC content 146

Fig. 3.2-11. Baseline experimental FRF extracted using ex situ ETIS 147

Fig. 3.2-12. Experimental FRF of component #1 estimated with five different die temperature sensing LUTs 149

Fig. 3.2-13. Phase FRF with degradation to the die-attach interface of the DUT 150

Fig. 4.2-1. Graphical illustration of a 1D transient analytical model with varying contact resistance 157

Fig. 4.2-2. Isometric view of a SETIS map produced using the exact solution to the 1D transient model with contact resistance (Fig. 4.2-1) 159

Fig. 4.2-3. Spatial ETI FRFs from the 1D transient model with variable convection (cooling degradation) 161

Fig. 4.2-4. Die-to-ambient ETI from the 1D transient model with variable Rc'' 161

Fig. 4.2-5. Spatially-varying sensitivity functions extracted from a FD model 162

Fig. 4.2-6. Sensitivity FRFs as a function of degradation, extracted from a FD model 164

Fig. 4.2-7. Electrothermal impedances as a function of degradation, extracted from a FD model 165

Fig. 4.2-8. Sensitivity functions with increasing TIM degradation, extracted from the FD model 166

Fig. 4.2-9. Sensitivity functions with increasing cooling degradation, extracted from the FD model 167

Fig. 4.2-10. Sensitivity functions with increasing die-attach degradation, extracted from the FD model 168

Fig. 4.2-11. Die sensitivity functions showing how degradation in terms of R_{conv} (50%), $R_{LF\text{-}Sink}$ (200%), $R_{Si\text{-}LF}$ (100%), and the absence of wire bonds affect the die-to-ambient response; experimental traces are solid lines and model-derived traces are dotted lines (repeat of Fig. 3.1-15 for convenience to the reader) 171

Fig. 4.2-12. FE model with wire bonds, building upon Fig. 5 172

Fig. 4.3-1. Experimental FRFs as a function of cooling and TIM degradation 173

Fig. 4.3-2. Experimental cooling and TIM degradation sensitivity functions 175

Fig. 4.3-3. Experimental die-to-ambient and thermistor-to-ambient complex ETI as a function of power electronic converter degradation 176

Fig. 4.3-4. Images taken during a process to manually remove solder from an IGBT die-attach interface 177

Fig. 4.3-5. Data used for calibrating an IGBT die temperature estimator 178

Fig. 4.3-6. Impact of different sources of degradation on IGBT device driving point electrothermal impedance 181

Fig. 4.3-7. Sensitivity function for slight die-attach degradation 182

Fig. 4.3-8. Sensitivity of the computed FRF estimate to parameters of the IGBT temperature estimator (3.2-8) 183

Fig. 4.3-9. Comparison of temperature sensitivities for the effective on-state resistance of the IGBT and MOSFET component characterized in Chapter 3 185

Fig. 4.3-10. Phase FRF with degradation to the die-attach interface of the DUT 186

Fig. 4.3-11. DUT MOSFET after fabricated die-attach alteration 186

Fig. 5.1-1. Half-bridge circuit sourcing a load with impedance Z 189

Fig. 5.1-2. Conduction loss amplitude by harmonic 189

Fig. 5.1-3. Time domain data from simulation of an electrically driven trolley bus over a mission profile 192

Fig. 5.1-4. Total loss spectrum of a single IGBT device of an inverter's power module 192

Fig. 5.2-1. Block diagrams illustrating methods based on FRF data to assess state-of-health 193

Fig. 5.2-2. Diagrams representing theoretical and applied adaptive parameter estimation and control techniques 194

Fig. 5.2-3. Discrete-time implementation of the adaptive thermal resistance observer, having a compact pure thermal resistance gain open-loop model, shown adjacent to a closed-loop current regulated electrical system 195

Fig. 5.2-4. State block diagram description of the adaptive thermal capacitance observer implemented in discrete-time 197

Fig. 5.3-1. Driving impedance phase response to 1 Hz fundamental frequency loss injections as a function of normalized contact resistance 199

Fig. 5.3-2. Spatially-varying FRF phase extracted from a developed 1D transient analytical model 199

Fig. 5.3-3. Simulation model of an adaptive thermal resistance observer used with over-temperature system-level control 200

Fig. 5.3-4. Results from Simulink simulation of Fig. 5.3-3 201

Fig. 5.3-5. First-order thermal model with variable thermal resistance used for adaptive observer simulations 202

Fig. 5.3-6. Simulation of the adaptive observer with the Fig. 5.3-5 physical system 203

Fig. 5.3-7. Simulation of the adaptive thermal capacitance observer in Fig. 5.2-4 204

Fig. 5.3-8. Experimental result showing the observer system in Fig. 5.2-3 tracking thermal resistance 205

Fig. 5.3-9. Experimental result showing the observer system without the ambient temperature NZVR tracking an erroneous thermal resistance value 206

Fig. 5.3-10. Experimental result showing the observer system with the ambient temperature NZVR tracking the correct thermal resistance value 207

Fig. 6.1-1. Small signal thermal response of a SiC MOSFET in a module 213

Fig. 6.1-2. Meshed view of the SiC module's center half-bridge sub-assembly, showing four semiconductor devices and how die-attach degradation was simulated 215

Fig. 6.1-3. For all middle-phase devices excited by self-heating, sensitivity to degradation of each device's die-attach interface 216

Fig. 6.1-4. Cross-coupling FRFs where x = heat source, labeled on plot 217

Fig. 6.1-5. Sensitivity to die-attach degradation located directly under each heat source labeled on the plot 218

Fig. 6.1-6. AC ripple of the low-side, middle-phase MOSFET; computed as a product of FRF amplitude and loss harmonic spectra 218

Fig. 6.2-1. Model and test setups for spatially-varying sensitivity analysis 220

Fig. 6.2-2. Spatially-varying sensitivity function extracted from simulation; plot colors correspond to nodes highlighted in Fig. Fig. 6.2-1(a) 222

Fig. 6.2-3. 2D view of Fig. Fig. 6.2-2 results and a TIM degradation sensitivity function measured with a baseplate-mounted thermistor 224

Fig. 6.2-4. Signal flow for characterization using an IR camera 224

Fig. 6.2-5. Spatially-varying amplitude attenuation illustrated using infrared thermography 225

Fig. 6.2-6. Location of 60 sense pixels used for spatially-varying electrothermal impedance and sensitivity analysis 226

Fig. 6.2-7. AC power loss and spatially-varying temperature response, the latter of which was reconstructed from data extracted from an infrared camera; response to 0.05 Hz harmonic loss perturbation is shown 227

Fig. 6.2-8. Spatially-varying electrothermal impedance magnitudes, before and after altering bolt torque, estimated by dividing computed FFT spectra at the displayed fundamental excitation frequency, f_{fund} 227

Fig. 6.2-9. Spatially-varying electrothermal impedance for test 1 computed using transfer function estimation 228

Fig. 6.2-10. Measured spatially-varying sensitivity function shown in 3D and 2D 229

Fig. 6.2-11. Phase-frequency view of a measured spatially-varying electrothermal impedance 231

Fig. 6.3-1. Power module design for degradation sensing method 233

List of Tables

Table 1.1-1. Commonly accepted power semiconductor assembly failure criteria [19] 10

Table 1.2-1. Summary of temperature sensitive properties [70] 28

Table 1.2-2. Summary of temperature sensitive properties that can be used to estimate power semiconductor device temperature in real-time [71] 29

Table 1.3-1. Advantages and disadvantages of TECs and TEC-related modeling methods 50

Table 2.2-1. Parameters used for plotting Fig. 2.2-4 92

Table 2.2-2. Expected high frequency phase response using transfer functions derived for different modes of heat transfer 95

Table 3.1-1. Test signal specifications for the square wave, DC-to-low frequency system identification experiments 120

Table 3.1-2. Data record specifications for the square wave, DC-to-low frequency system identification experiments 120

Table 3.1-3. Test signal specifications for the single frequency sinusoid system identification experiments 123

Table 3.1-4. Data record specifications for the single frequency sinusoid system identification experiments 123

Table 3.1-5. Summary of physical die-to-ambient FRF parameters embedded within the fit model 126

Table 3.1-6. Thermistor-to-ambient FRF model parameters 126

Table 3.1-7. Lumped thermal parameters embedded within the FE model 132

Table 3.2-1. Die TSEP parameters used to study sensitivity of the FRF 147

Table 4.2-1. Numerical model-based degradation simulation method 163

Table 4.3-1. Calibrated parameters of the IGBT die temperature estimator (3.2-8) 178

Table 5.1-1. Parameter used for evaluation of the developed conduction loss harmonic model 190

Table 5.3-1. Road map of signal properties relevant to detection and diagnosis methods 208

Table 5.3-2. Road map of properties related a priori knowledge related to detection and diagnosis methods 208

Table 6.1-1. Power module finite element model details 212

Table 6.1-2. Temperature-dependent material properties 213

Table 6.2-1. Mechanical parameters of the TIM degradation experiment 223

Nomenclature

Symbols	**Description**
α	thermal diffusivity
β	general gain
Δ	change or difference
ε	emissivity
ρ	density
σ	fitting parameter
τ	time constant
A	area
C	capacitance/capacitor component
d	duty ratio
E	energy
f	frequency
G	conductance
h	heat transfer coefficient
i, I	current
k	thermal conductivity
K	gain
L	inductance/inductor component or length
m	mass
n, N	number of
T	temperature
P	power
q, Q	heat rate or power loss
r, R	resistance/resistor component
v, V	voltage
z	discrete-time variable
Z	impedance

Superscripts

$\hat{(\ )}$	estimated quantity
$(\ )^*$	reference/command quantity
$\dot{(\ )}$	time derivative operator d/dt ( )
$\overline{(\ )}$	average quantity
$(\ )''$	flux quantity, i.e. per unit area
$(\ )^s$	spatial domain quantity

Subscripts

$(\ )_a$	active quantity, e.g. a gain
$(\ )_{amb}$ or $(\ )_\infty$	ambient or quantity evaluated at infinite distance or time

$(\ )_b$	base
$(\ )_c$	contact
$(\ )_{cond}$	conduction
$(\ )_{conv}$	convective
$(\ )_{crit}$	critical
$(\ )_d$	disturbance
$(\ )_{diff}$	diffusive
$(\ )_{dist}$	distant quantity, e.g. impedance
$(\ )_{drv}$	driving quantity, e.g. impedance
$(\ )_D$	drain
$(\ )_{dc}$ or $(\ )_{DC}$	direct-current quantity
$(\ )_{ds}$ or $(\ )_{DS}$	drain-to-source
$(\ )_e$	electrical
$(\ )_G$	gate
$(\ )_{GS}$	gate-to-source
$(\ )_{flir}$	infrared thermographic quantity
$(\ )_{fund}$	fundamental quantity
$(\ )_i$	general indexing variable or integral gain
$(\ )_j$	junction
$(\ )_L$	loss
$(\ )_{lead}$	lead frame
$(\ )_{load}$	load quantity
$(\ )_{MRAC}$	model reference adaptive control
$(\ )_{MRAS}$	model reference adaptive system
$(\ )_o$	observer or output quantity
$(\ )_p$	physical quantity or proportional gain
$(\ )_{pw}$	plane wall
$(\ )_{rad}$	radiative
$(\ )_{ref}$	reference quantity
$(\ )_s$	sampling
$(\ )_{sink}$	heat sink
$(\ )_{sp}$	specific
$(\ )_{sw}$	switching
$(\ )_{th}$	thermal
$(\ )_{tot}$	total
$(\ )_{(on)}$	on-state quantity

$(\ )_{(th)}$	threshold quantity

Independent Variables

( )(kT) or ( )(k)	dependent on discrete time instant
( )(s)	dependent on the Laplace-domain variable (frequency)
( )(s, x, y, z)	dependent on frequency and special coordinate dimension
( )(t)	dependent on time

Abbreviations

AC	alternating current
ADC	analog-to-digital
CAD	computer-aided design
COTS	commercially off-the-shelf
CP	current probe
CPMRE	coherent power of the model reference error
DAC	digital-to-analog
DC	direct current
DPS	distributed parameter system
DSP	digital signal processor
DUT	device under test
EA	estimation accuracy
EGSO	enhanced Gopinath-style observer
ELSO	enhanced Luenberger-style observer
ERes	enhanced resolution
ETI	electrothermal impedance
ETIS	electrothermal impedance spectroscopy
EV	eigenvalue
FD	finite difference
FE	finite element
FFT	fast Fourier transform
FRA	frequency response analysis
FRF	frequency response function
GSO	Gopinath-style observer
GUI	graphical user interface
HALT	highly accelerated lifetime testing
HPF	high-pass filter
IGBT	insulated gate bipolar transistor
LF	lead frame component
LPF	low-pass filter
LSO	Luenberger-style observer
LTI	linear time-invariant
LUF	look-up function
LUT	look-up table
MID	manipulated input decoupling

MIMO	multiple-input-multiple-output
MOR	model order reduction
MOS or MOSFET	metal-oxide-semiconductor field-effect transistor
MRAC	model-reference adaptive control or controller
MRAS	model-reference adaptive system
MRE	model reference error
MSEP	multiply sensitive electrical parameter
NZVR	non-zero virtual reference
ODE	ordinary differential equation
PC	personal computer
PCB	printed circuit board
PDE	partial differential equation
PI	proportional-integral
PICC	physical input cross-coupling
PID	proportional-integral-derivative
PPGD	push-pull gate driver
PWM	pulse-width modulated or modulation
ROM	reduced-order model
SD	sensitivity to degradation
SETI	spatially-varying electrothermal impedance
SETIS	spatially-varying electrothermal impedance spectroscopy
SFb	state feedback
Si	silicon
SiC	silicon-carbide
SISO	single-input, single-output
SOH	state of health or degradation
SNR	signal-to-noise ratio
TIM	thermal interface material
TTI	transient thermal impedance
TSEP	temperature sensitive electrical parameter
WEMPEC	Wisconsin Electric Machines & Power Electronics Consortium
ZVR	zero virtual reference
*n*D	*n* dimensional, where $n = 1, 2, \ldots$

Block Diagrams

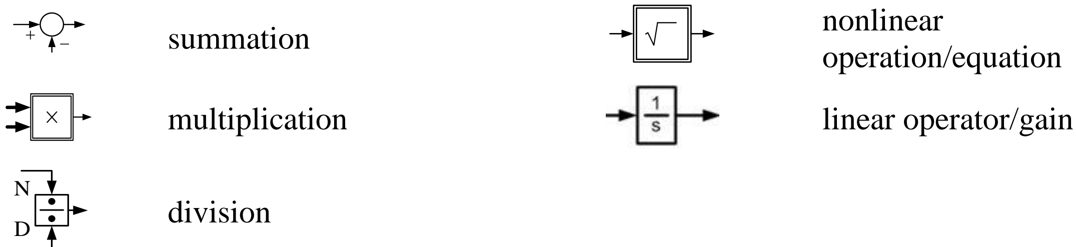

Introduction

This section states this research program's motivation and overview, a summary of research contributions, and a chapter-by-chapter list of the material included in the thesis.

Research Motivation

The motivation of this research is to provide tools enabling in situ monitoring and diagnosis of power semiconductor assemblies during their operation in converter systems. It is desired to develop methods to estimate interacting electrothermal-mechanical properties more accurately and precisely than state-of-the-art methods. This capability supports the clear goal to estimate state-of-health a converter's real-time operation. It also supports the broad goal to fully utilize limited thermal-mechanical capacities of power electronic converters, to maximize their usable lifetime and enable design of converter systems with maximal power density.

This research program addresses limitations in state-of-the-art technology related to reliability of power semiconductor converter systems. Current thermal modeling approaches utilize uncorrelated numerical models or single-trajectory, step response data describing a limited segment of a converter's spatial domain. Metrics currently used to describe dynamic heat transfer are limited, especially in their capability to concurrently display both temporal and spatial domain information. This work develops frequency domain system identification methods and metrics to proceed in this area of study. It proposes related methods to extract response information and directly estimate physical parameters quantifying a system's healthy and degraded spatiotemporal response.

Research Overview

Power semiconductors are ubiquitous in compact electrical power conversion systems enabling innovations in power generation, distribution, and utilization. These systems must perform in electrical and thermal-mechanical domains for decades. Industry acknowledges the high failure-sensitivity of power semiconductors, with thermal-mechanical strain as a driver of power semiconductor assembly failures. This research provides methods for in situ state-of-health estimation and, long-term, full utilization of the materials included in these assemblies.

The research program has several themes, described below.

Spatiotemporal dynamic heat transfer modeling lays the groundwork for the program. Spatiotemporal frequency domain metrics are defined to compare properties encoded by first-principles analytical heat transfer models with those in numerical models. Observations from the study enable eventual reverse engineering of governing model topologies and assumptions based on experimental electrothermal impedance frequency response function data. The study is also used to extract parameters from frequency response data using a reduced-order model.

Techniques for system design, analysis, and commissioning guide the preparation of power electronic systems to serve as the test subjects for frequency response testing. To allow for measurement of driving-point and diffusive impedances, semiconductor device loss models are documented, along with steps to utilize a semiconductor device as its own temperature sensor. A spatially-varying system identification method is defined to guide heat transfer experiments on a converter system.

Data visualization and interpretation is utilized for interpretation and parameterization of space-variant frequency response data. Three-dimensional surface functions are presented as a way

to explicitly retain spatial domain information and assess a converter's electrothermal response. This work shows how experiments can be utilized to quantify pieces of a converter's three-dimensional transient thermal response, while modeling techniques can be leveraged to predict response in between discrete measurements.

Algorithm design leverages identified dynamic ranges of sensitivity specific to a source of degradation, such as solder-layer voiding, thermal interface material pump-out, and cooling system fouling. Complementary methodologies are presented to estimate physical degradation. One approach directly extracts state-of-health from frequency response data. The other utilizes adaptive control techniques to directly estimate parameters which reflect degradation. Both methods are demonstrated as viable in evaluations.

This program leverages transient models of device conduction and switching losses, and temperature sensitive electrical parameter technology, as enabling components, rather than central foci, to develop methods. The methodologies consistently preserve spatial degrees-of-freedom as independent variables, enabling design-for-sensing approaches. In addition to potentially adding precise electrothermal-mechanical monitoring functionality to established converter systems, they add value at additional stages of converter product life cycles.

Statement of Contributions

The following list summarizes key contributions made by this research:

- Developed methods to characterize forced heat transfer frequency response within power semiconductor components and assembled converter systems
- Defined scalar and vector sensitivity functions and analytical methods
- Characterized transient heat transfer sensitivity to cooling and quality of component-to-heat sink and die-attach interfaces
- Utilized models to quantify relationship between source of degradation, temperature sense location, and harmonic frequency range of degradation sensitivity
- Developed a transient, semiconductor device loss modulator having parameter insensitive phase delay accuracy
- Applied spatially-varying sensitivity analysis using infrared thermography
- Analyzed a wide-bandgap multi-chip power module to identify factors which allow for an effective degradation sensing bandwidth to be specified at a design phase
- Developed an adaptive observer method to estimate degradation-sensitive parameters
- Parametrically characterized error of frequency response measurements
- Developed a finite element platform to enable module design-for-sensing studies
- Quantified numerical model uncertainty to unknown model specifications
- Proposed a low-order, dynamic model, combining aspects of analytical and numerical models, to generally describe driving point and diffusive thermal impedances
- Identified implicit, asymptotic limits in thermal models using frequency domain analysis

Summary of Chapters

In Chapter 1, the state-of-the-art of topics relevant to this research program is reviewed. It introduces power semiconductor assembly reliability, semiconductor device temperature sensing, heat transfer modeling, and observers. Identified research opportunities are stated.

In Chapter 2, frequency domain responses of various heat transfer models are surveyed. A methodological limit is addressed, and a finite element modeling platform is presented.

In Chapter 3, system identification methods to extract frequency response functions of heat transfer in power semiconductor systems are developed and applied.

In Chapter 4, models and experiments are used to quantify relationships between source of degradation, temperature sense location, and transient thermal frequency response.

In Chapter 5, methods for estimating active power electronic converter degradation in situ, including usage of naturally modulated losses and adaptive system theory, are presented.

In Chapter 6, limitations toward integrating degradation sensing in multi-chip power module systems are quantified and temperature sensor placement methods are developed.

In Chapter 7, conclusions and contributions of this research program are summarized, and recommended future work is presented.

Chapter 1 State-of-the-Art Review

1.1 Power Semiconductor Assemblies and their Reliability

1.1.1 Importance of the topic for global electrification efforts

Switching power semiconductor assemblies, which include IGBT and MOSFET semiconductor devices, are vital elements of the global movement toward electrification. Power semiconductors are a fundamental circuit element enabling control of all switching power electronic converters. Converter applications are broad, ranging from less complicated voltage bucking DC-DC converters in automotive applications [1] and AC-DC rectifier front ends [2], to multi-level converters acting as DC-AC inverters for grid-connected applications [3] and AC-AC motor driving matrix converters [4].

Even more broadly, power semiconductor technology enables present and future infrastructure supporting terrestrial (and, in the future, extraterrestrial) civilization aspects such as energy efficiency, electromobility, information technology, renewable energy, and smart electricity distribution [5]. As reported in 2011, power electronic applications using IGBT device assemblies have saved $2.7 trillion and $15.8 trillion for United States and worldwide consumers, respectively, and effectively sequestered 35 and 78 trillion pounds of CO_2 emissions [6]. Applications of power semiconductor assemblies are ubiquitous, and downtime in power converter applications due to failures in assemblies is costly [7].

1.1.2 Assembly composition and characterization of failures

The power electronics industry qualifies and quantifies power semiconductors and DC-link capacitors to be the two most failure-sensitive assemblies in converters [7], [8]. Predominant failure modes of power semiconductor assemblies, which manifest during inevitable power cycling of converters, are documented as liftoff of wire bonds and fracturing of solder interfaces, with thermally-induced mechanical strain considered as a principle driving mechanism [9]–[14]. Indeed, these investigations ultimately express lifetime in terms of some representative semiconductor device junction temperature, T_j, and a power cycling-induced excursion of this temperature, ΔT_j. This subsection will further review aspects of the power semiconductor assembly reliability problem.

1.1.3 Failure modes and effects analysis (FMEA)

1.1.3.1 Overview

Failures of components or assemblies can broadly be attributed to overstress or wear out [15]. Overstress failures are the result of a component strained to levels that are greater than its strength. Wear out failures are the result of a component weakening over time due to the accumulation of damage, such that the nominally applied strain is large enough to inflict fatal damage. These definitions are graphically illustrated in Fig. 1.1-1, which also illustrates how overstress and wear out take place in defective components.

This research program focuses on the reliability of power IGBT and MOSFET semiconductor assemblies in terms of electrothermal-mechanically-induced wear out. A typical cross-sectional view of a power semiconductor assembly is shown in Fig. 1.1-2. As shown, the

assembly contains many components, including planar layers and wire bonds, composed of different materials.

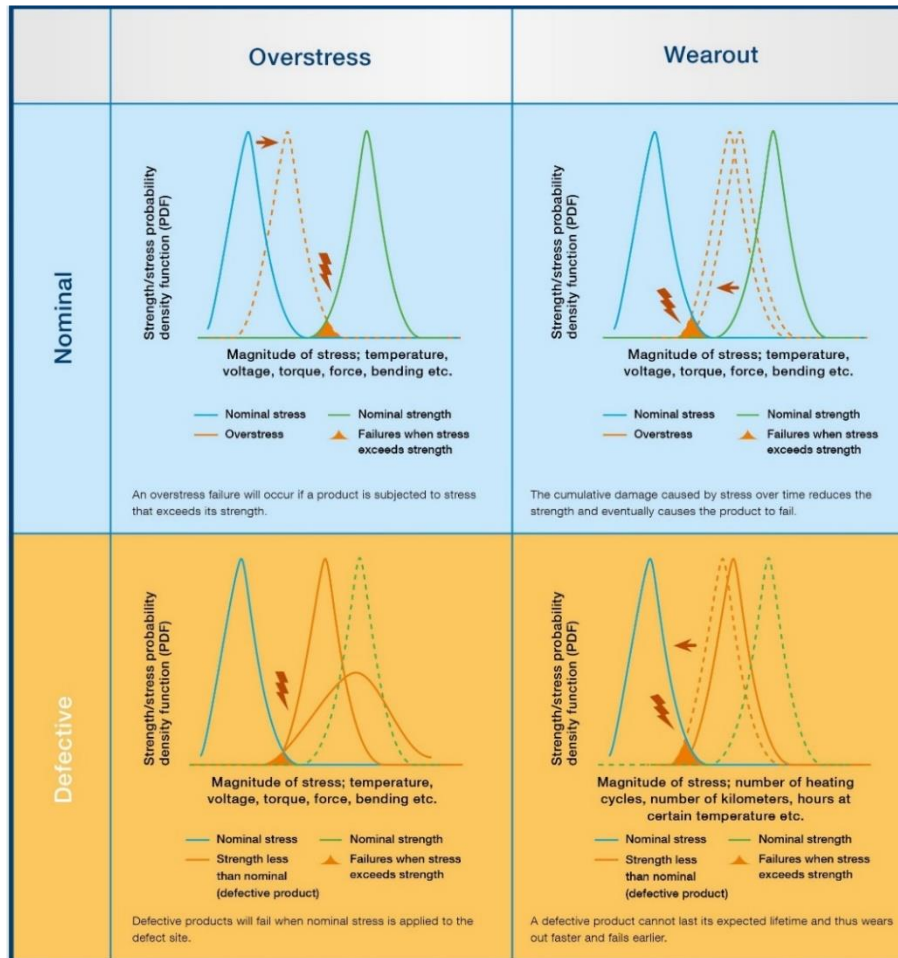

Fig. 1.1-1. Classification of nominal and defective components or assemblies in terms of overstress- and wear out-induced failures [15]

Since different materials are present, the various components within an assembly have differing values for their coefficient of thermal expansion (CTE). This research focuses on defects and failures that are thermally-induced during the electrical operation of the assembly. Thus, when a power electronic system is actively switching, the time-varying conduction and switching losses lead to dynamic heat transfer and spatiotemporal temperature gradients within the assembly. These ultimately lead to mechanical strains, stresses, and degradation until a failure point is reached.

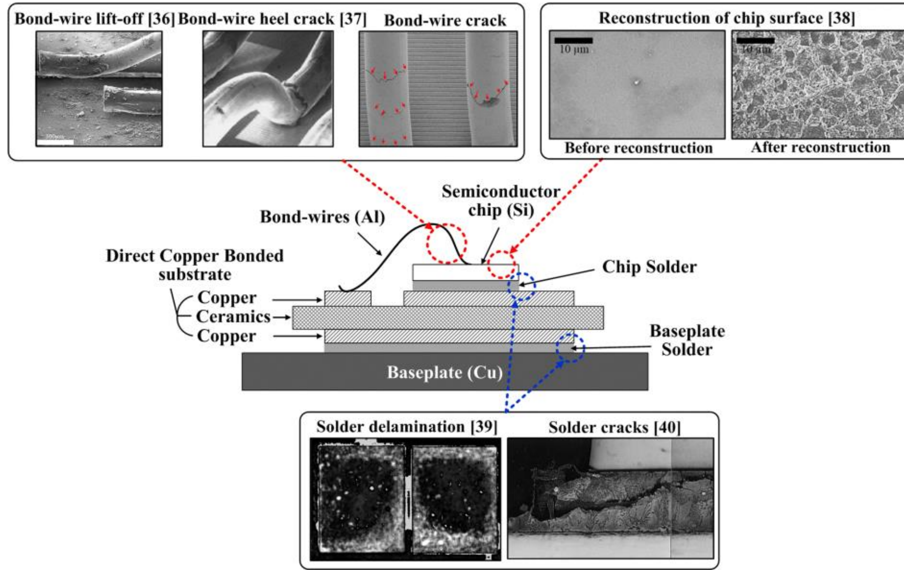

Fig. 1.1-2. Electro-thermal-mechanically-induced fatigue in power semiconductor assemblies [16]

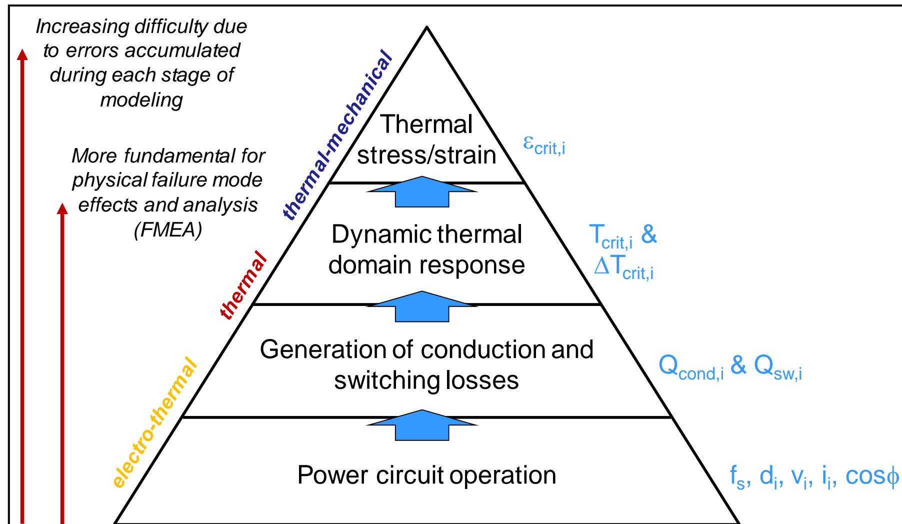

Fig. 1.1-3. Hierarchy of a physics-based, multi-domain modeling effort to ultimately estimate mechanical stress/strain behavior in power semiconductor assemblies

A ground-up, physics-based approach to modeling behavior ultimately leading to power semiconductor assembly failures is shown in Fig. 1.1-3. The lowest level of the pyramid, operation of the power electronic converter, is represented by electrical state variables such as switching voltages, currents, switch duty ratios and frequencies, and power factor. The next level represents

conduction and switching loss generation within the converter. The losses, which dissipate as heat within the semiconductor devices embedded within an assembly, excite dynamic thermal response. Finally, dynamic thermal behavior yields thermally-induced mechanical stresses and strains.

Fig. 1.1-2 illustrates some of the thermal-mechanical failure modes within the scope of this research, i.e. bond wire displacements and solder layer degradation. Failures within power semiconductor assemblies can occur within the semiconductor device, exemplified by the chip reconstruction highlight within Fig. 1.1-2, or within the assembly (also referred to as the "package" or "integration" structure of the device). Select power semiconductor assembly failures are listed below [10], [11], [17], [18].

- Bond wire fatigue, heel fracture, and liftoff
- Solder layer fatigue and voids
- Aluminum metallization reconstruction

Instantaneous fatigue level of semiconductor assemblies is revealed by certain signatures, which can broadly be classified into electrical or thermal property shifts. Table 1.1-1 provides a list of commonly used failure benchmarks identified during a literature review of power cycling experiments to evaluate thermal-mechanical reliability.

Table 1.1-1. Commonly accepted power semiconductor assembly failure criteria [19]

Indicator	Symbol	% deviation for failure
Collector–emitter saturation voltage	$V_{\mathrm{ce(sat)}}$	5%
Gate–emitter threshold voltage	$V_{\mathrm{GE(th)}}$	20%
Collector current	I_{on}	20%
Junction temperature	T_j	20%
Gate saturation current	$I_{G\,\mathrm{(sat)}}$	20%
Thermal impedance	Z_{th}	20%

Mechanical parameters and states are noticeably absent from Table 1.1-1, indicating the power semiconductor assembly failures are perceived in terms of electrical and thermal response,

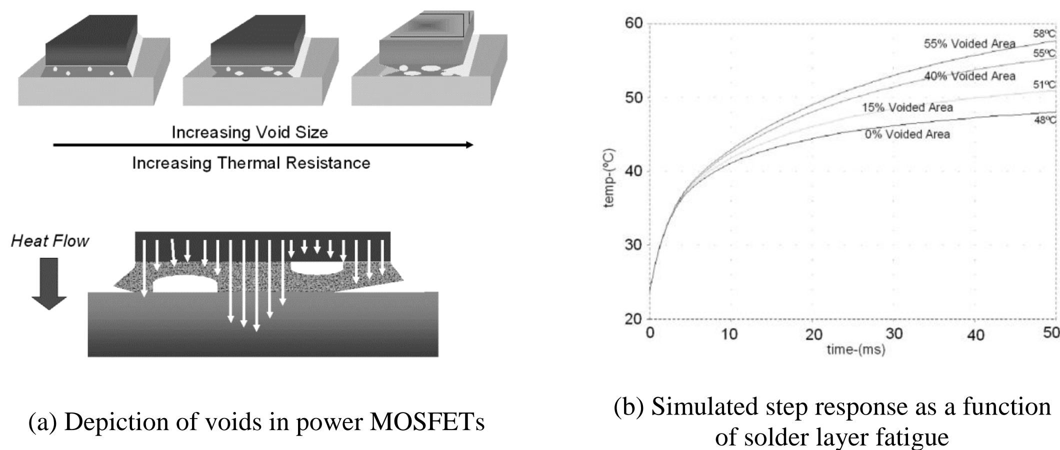

(a) Depiction of voids in power MOSFETs

(b) Simulated step response as a function of solder layer fatigue

Fig. 1.1-4. Investigation of solder layer voiding/delamination on thermal response [20]

not mechanical response, e.g. strain, stress, or a quantified mechanical fatigue variable. Indeed, many studies focus on forward voltage drop or thermal response properties to quantify failure.

Fig. 1.1-4 summarizes a study which links MOSFET assembly solder layer voids to changes in the thermal step response. The study provided many credible experimental results illustrating thermal response property shifts as a function of voided area but did not provide model-based methods to identify the defect in the case it was unable to be imaged with analytical techniques, e.g. scanning acoustic microscopy.

As the next subsection will explain, it is common in the literature to measure or predict the lifetime of power semiconductor assemblies in terms of temporal ΔT temperature excursions at the assumed most critical points within the assembly, especially the point referred to as the "junction." One set of studies, summarized by Fig. 1.1-5, examined how two electrothermal fatigue signatures, the V_{ce} IGBT device forward voltage drop and total thermal resistance, evolve during both small and large ΔT cycles. The study attributed fatigue damage to specific fatigue regimes and milestones, e.g. creep and crack initiation, but still provided models of lifetime in terms of the character of the applied ΔT cycles during experiments. This study is highly representative of the state-of-the-art.

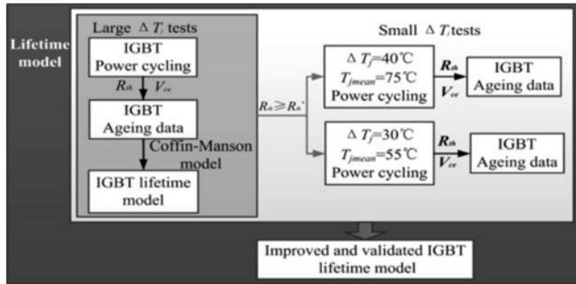

(a) Illustration of a test strategy to evaluate impacts of both large and small ΔT cycling

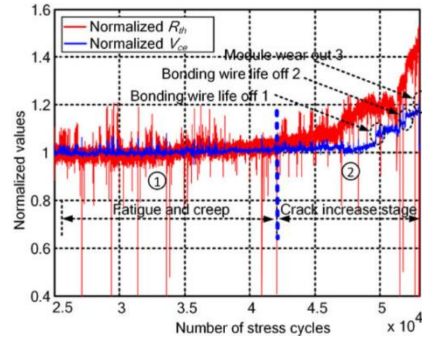

(b) Evolution of total thermal resistance and IGBT forward voltage drop during power cycling tests

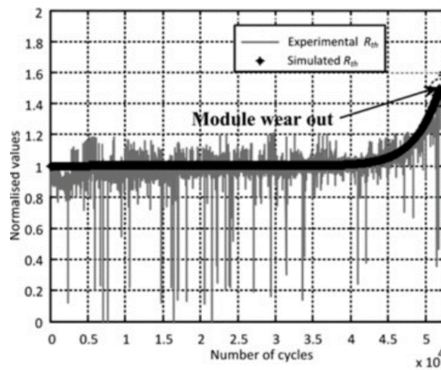

(c) Evolution of total thermal resistance during cycling for ΔT ≈ 90°C

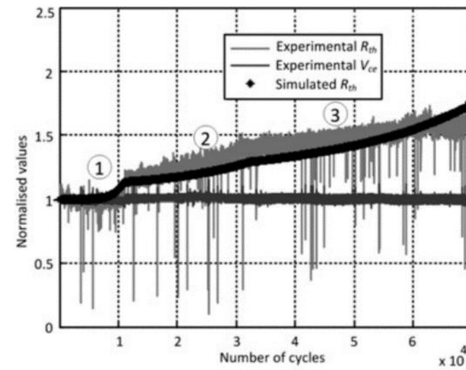

(d) Evolution of total thermal resistance using relatively small ΔT cycles after the assembly was already subjected to large ΔT cycles

Fig. 1.1-5. Investigation into total thermal resistance increases during power cycling [21], [22]

1.1.3.2 Reliability engineering methods

Reliability engineering methods summarize linear and nonlinear fatigue-inducing processes with predominantly empirical models. As a result, statistical methods are often employed to quantify fatigue life in terms of distributions, uncertainties, and confidence.

Several textbooks describe aspects of fatigue engineering science [17], [23]–[28] in ways that are applicable to the power semiconductor assembly reliability problem. Fig. 1.1-6 summarizes some of these ideas. First, the (a) and (b) figures are referred to as bathtub curves, which describe how the probability of a component or assembly failing, i.e. failure rate, changes as a function of the time it is in operation. Please note that this research program focuses on

systematic long-term wear out (and potentially overstress) failures, but not early “infant mortality” failures and random failures.

Finally, Fig. 1.1-6(c) proposes a framework for enhancing physical modeling insight (termed “intermedia”) to supplement empirical reliability engineering methods. Expanding upon the implied vision is an opportunity for research in power electronics.

Reliability in power semiconductor assemblies is most commonly expressed in terms of the $T_j(t)$ temperature history, which is assumed to govern the manifestation of peak thermally-induced mechanical strains and stresses at delicate interfaces. First, as shown in the idealized Fig. 1.1-7, the response history of $T_j(t)$ is recorded and quantified in terms of its minima, maxima, mean, and cycling amplitude $\Delta T_j(t)$. Eventually, life plots like Fig. 1.1-8 are formed which describe how the temperature history, summarized using $\Delta T_j(t)$ and average temperature, influence number of cycles to failure, N_f.

Even though a standard definition for T_j doesn’t exist and its relatively simple summary in terms of average temperature and equivalent $\Delta T_j(t)$ cycles, life plots like shown in Fig. 1.1-8 are pervasive for modeling and predicting the lifetime of power semiconductor assemblies. These plots even serve as models for designing power cycling reliability experiments, procedures for which are outlined in [14], [16], [19], [29].

Reliability engineering often relies on analytical microscopic and spectroscopic techniques to examine components or assemblies after they have failed. Fig. 1.1-9 summarizes techniques that have been used in investigations of power semiconductor assembly reliability. Credible sources of high quality photos of fatigued and/or failed power semiconductor devices, captured using analytical techniques such as scanning electron microscopy (SEM), are [10], [11].

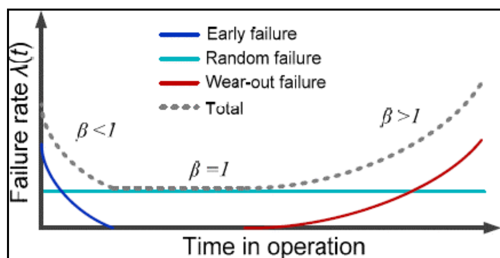

(a) "Bathtub curve" product lifecycle representation [30]

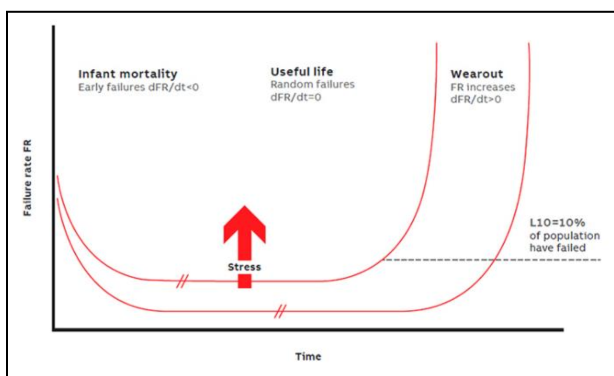

(b) Impact of stress on the bathtub curve [31]

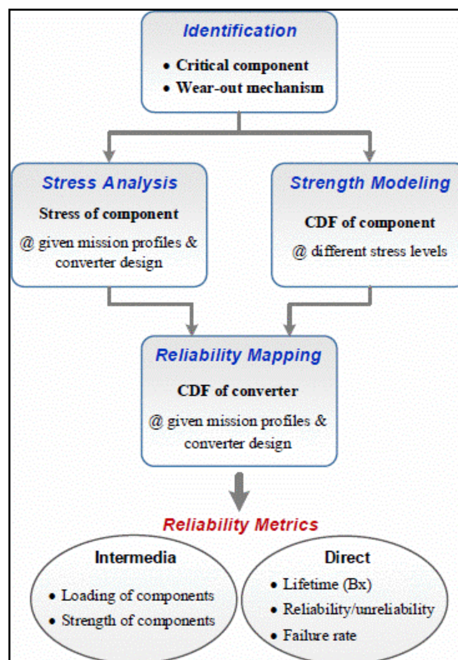

(c) A proposed modeling approach [30]

Fig. 1.1-6. Principles and approaches for reliability engineering

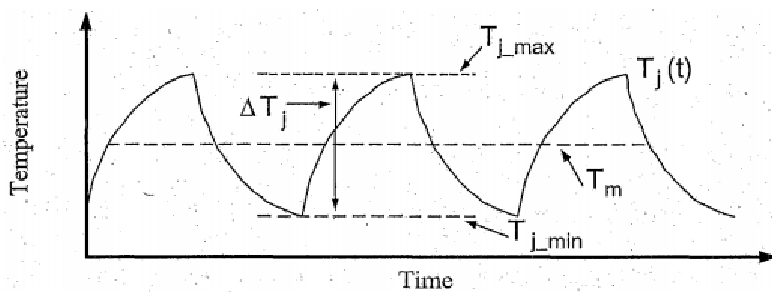

Fig. 1.1-7. Definitions of T_j, ΔT_j, and T_m (= T_{jm}) during ideal, periodic power cycles [32]

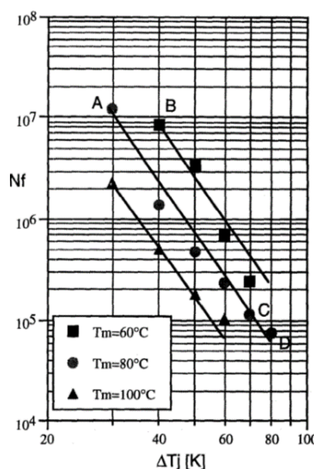

Fig. 1.1-8. N_f as a function of ΔT_j and T_m (= T_{jm})

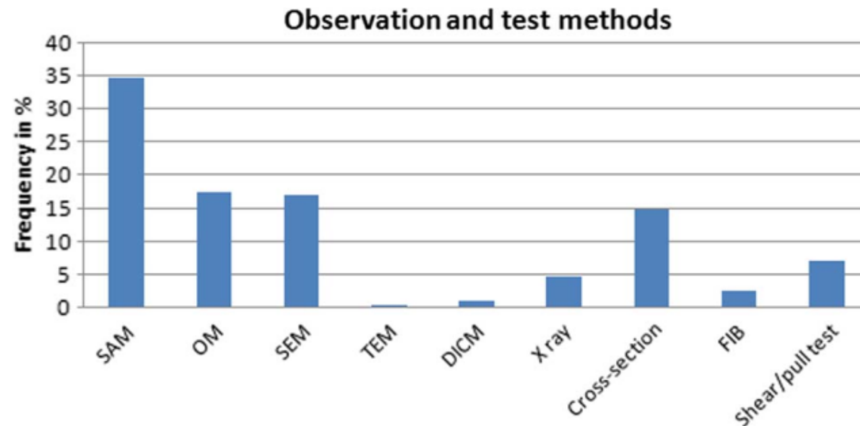

Fig. 1.1-9. Histogram of analytical techniques used by archived studies for post-mortem inspection of power cycled semiconductor assemblies [14]

1.1.3.3 Fatigue modeling

Forming equation models for lifetime metrics, such as N_f, is a common extension of the data-driven life models. Empirical equation life models attempt to fit the graphical life plots using numerical methods such as linear regression. One of the power semiconductor assembly life models maps how equivalent ΔT_j cycles (commonly counted using the rainflow technique [33]) and a supposedly representative mean junction temperature influence N_f. Model (1.1-1), corresponding to Fig. 1.1-8, has A and α fitting parameters, R = 8.314 J/mol·K, and Q = $7.8 \cdot 10^4$ J/mol = 0.8 eV. The model thus has two inputs fitting parameters.

$$N_f = A \, \Delta T_j^{\alpha} \exp\left(\frac{Q}{R \, T_{j\text{-mean}}} \right) \qquad (1.1\text{-}1)$$

More recent papers continue the trend of forming empirical life model equations by adding more parameters to the linear regression fit of higher dimensional experimental data. One highly cited example is referred to as the Bayerer model and is shown in (1.1-2). This single-output model has six inputs and seven fitting parameters.

$$N_f = K\,\Delta T_j^{\beta_1} \exp\left(\frac{\beta_2}{T_j}\right) t_{on}^{\beta_3}\, I^{\beta_4}\, V^{\beta_5}\, D^{\beta_6} \qquad (1.1\text{-}2)$$

Empirical lifetime equation models do not directly provide information about the strain, stress, and fatigue states of the power semiconductor assembly. Furthermore, these models require expensive experimental efforts, and do not directly account for assembly fatigue processes that are often marked with discrete events, such as crack formation, which irreversibly change the thermal-mechanical response of the assembly.

One set of studies from the power electronics field, however, has developed thermal-mechanical models of solder layer stress-strain behavior [17], [34], [35]. The studies identify three major types of thermally-induces mechanical deformations – elastic, plastic, and creep – and maps when these regimes of strain occur with respect to the thermal-mechanical stress. Eventually, the analytical model provides stress-strain hysteresis curves for the solder material. The hysteresis curves are eventually numerically integrated to compute the energy dedicated to mechanical deformation and strain and predict lifetime.

The research of power semiconductor assembly stress and strain models has not been found to be renewed in the literature since [17], [34], [35], important contributions toward building physical models of thermal-mechanical stress and strain, able to predict lifetime. A limitation of the developed models is their one-dimensional nature, only using a single, supposedly representative solder layer temperature. Further research opportunities involve using such a model to evaluate the effectiveness of existing active thermal-mechanical control systems, and design new systems able to more optimally limit creep, elastic, and plastic deformations within the power semiconductor assembly.

Finally, this subsection is concluded by briefly mentioning that fatigue models grounded in thermodynamic sciences have been researched and evaluated [27], [36]–[38]. The thermodynamic models generally focus on entropy as the relevant state-of-health indicator of high-stress points within components or assemblies. The modeling framework is intended to be broadly applicable to multiple physical domains.

1.1.3.4 Fatigue status, state of health (state-of-health) evaluation

The prior subsection documented characteristics of fatigue defects in power semiconductor assemblies. These included electrical and thermal states and parameters that drift during damage accumulation. This subsection will review studies that claim to provide methods capable of evaluating the fatigue status of a power semiconductor assembly when it is installed in the application. Methods capable of this evaluation during real-time converter operation are a special focus of this review.

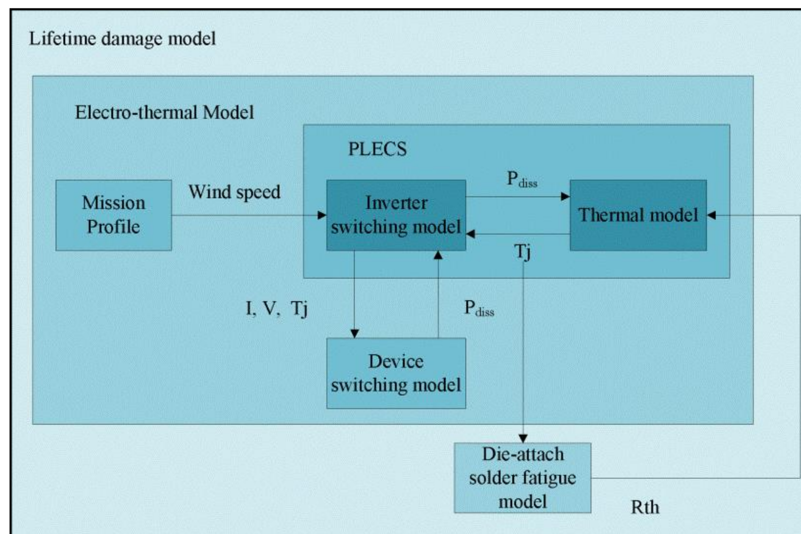

Fig. 1.1-10. Representative open-loop model-based method to assess fatigue status using total thermal resistance [39]

The most widespread method to predicting fatigue status and state-of-health uses a series of open-loop models, spanning multiple domains, following Fig. 1.1-3. Most studies, like that represented by Fig. 1.1-10, directly relate equivalent junction temperature cycles to a failure metric using empirical models like (1.1-1) and (1.1-2). Review publications on this topic exist [40], [41]. The remainder of this subsection will review select categories of these diagnostic methods.

Real-time electrical state and parameter monitoring

Many studies using aspects of electrical states and parameters for indication of fatigue status have been documented. These studies examined states and parameters related to both power circuitry and gate (control) circuitry. For power circuit state examination, one study correlated load current harmonics to changes in assembly case temperature, which changes with the assembly state-of-health [42]. Signal processing techniques were used during implementation of the method to extract fatigue status in real time.

The most widespread technique to assess fatigue status involves monitoring a power semiconductor device's forward voltage drop [43]–[50]. As shown in Fig. 1.1-11(a), this power circuit parameter increases as lifetime is consumed. It also indicates discrete bond wire liftoff events. Fig. 1.1-11(b) shows a circuit schematic used by literature studies to implement real-time V_{ce} sensing in converter systems.

Other studies investigated the usage of gate driver properties for evaluation of fatigue status. Gate currents [51] and impedance spectroscopic [52] techniques were leveraged for this purpose in two studies. Another study, highlighted shifts in the Miller plateau portion of the gate-source waveforms [53].

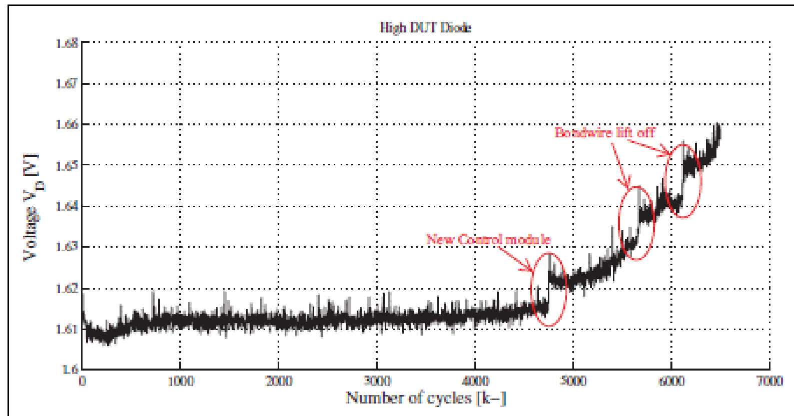

(a) Forward voltage drop as a function of power cycles [44]

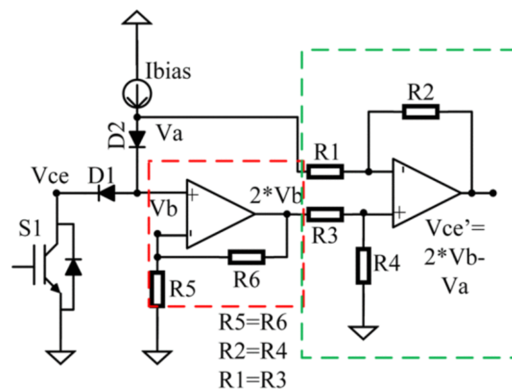

(b) Schematic of a circuit used to measure Vce [44], [54]

Fig. 1.1-11. Strategy of measuring Vce to assess fatigue status

Real-time thermal and/or mechanical response prediction and assessment

As shown in Fig. 1.1-4 and Fig. 1.1-5, thermal resistances are sensitive to the fatigue status of the power semiconductor assembly. Methods have been developed to formally utilize the sensitivity of this steady-state thermal parameter for real-time state-of-health estimation in converters and drives [49], [55]. Most of these publications have not utilized properties of transient heat transfer for this purpose, but one methodology has.

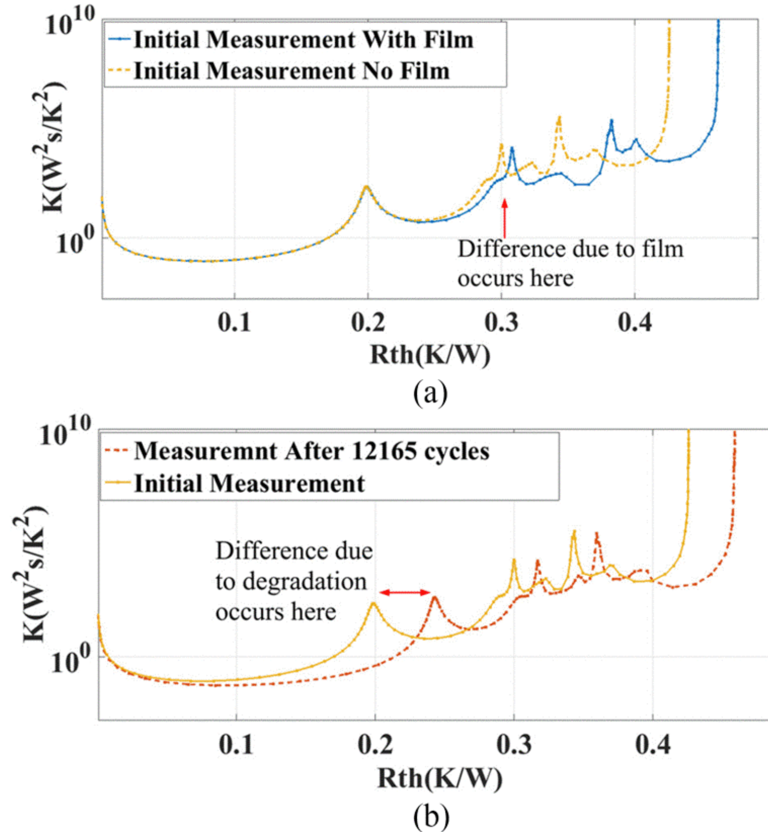

Fig. 1.1-12. Shifts in structure function expression of thermal responses before and after defect manifestations [54]

The transient thermal impedance (TTI) metric has been used to identify and classify changes in the transient thermal performance of power semiconductor assemblies [54], [56], [57]. Some studies are founded upon interpretation of the TTI metric, as it is classically employed by the power electronics industry, but the highest quality study employs structure functions as an additional layer of abstraction that is implied to help more precisely identify fatigue-induced changes in the assembly's thermal response properties. Fig. 1.1-12 illustrates how structure function distributions shift upon consumption of assembly life.

The structure function analysis still uses assumed ideal step response data and does not explicitly quantify phase response, i.e. delay, properties. Also, it is unclear how the shifts shown

in Fig. 1.1-12 should be exploited for a real-time degradation sensing implementation. TTI and the structure function are described further in subsection 1.3.2.

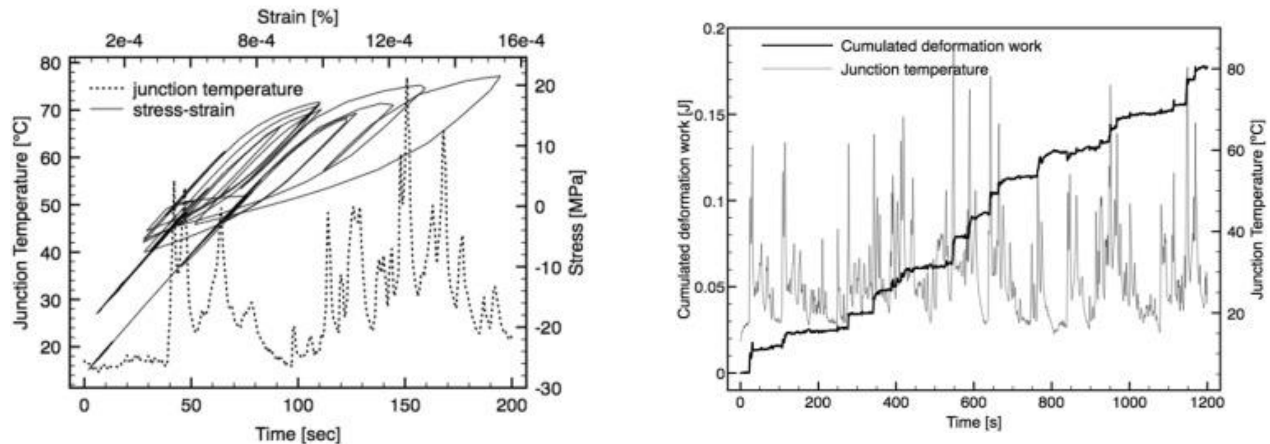

(a) Calculated stress-strain response for the shown experimental temperature profile

(b) Accumulation of die-attach solder deformation work during an urban cycle profile

Fig. 1.1-13. Summary of a thermal-mechanical model-based approach to estimating fatigue status [58]

Modeled mechanical stress/strain response history has been utilized for state-of-health estimation. One high quality study [58] follows a multi-domain modeling methodology, like employed in [39], without relating the temperature response history to a state-of-health metric using empirical relationships. Instead, this study used constitutive models to predict cumulative thermally-induced mechanical strains and stresses, similar to those explored in [17], [34], [35]. Outputs from the so-called reliability odometer are displayed in Fig. 1.1-13, which ultimately shows how mechanical deformation work accumulates during converter operation.

Research opportunities not addressed by these studies are evaluating the accuracy of the proposed constitutive thermal stress and strain model using experiments and numerical analysis. Also, designing and evaluating active thermal-mechanical strain control algorithms based off of identical or similar constitutive mechanical response models is an opportunity.

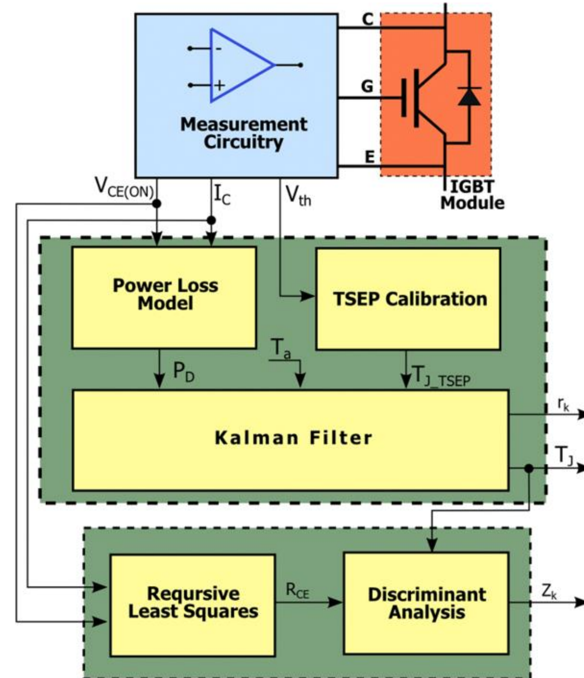

Fig. 1.1-14. Overview of the statistical signal processing methodology to estimate device forward voltage drop and thermal resistance [59]

Real-time statistical signal processing techniques

Statistics and signal processing techniques have been directly used in attempts to more accurately model fatigue status of a power semiconductor assembly. Once study used a so-called auxiliary particle filtering approach to process IGBT on-state V_{ce} and ultimately reduce the variance (increase the precision) of state-of-health projections [60]. A separate study proposed an electrothermal domain methodology utilizing Kalman filtering and recursive least squares algorithms [59]. The proposed system is shown in Fig. 1.1-14. It used measurements of V_{ce} and load current to estimate an equivalent on-state resistance. It also used measurement of the gate voltage threshold as input to a junction temperature estimator. Building upon the work documented in [61], the junction temperature estimate was delivered to a Kalman filter which independently estimates a junction temperature.

Differences between the model-based and estimator-based temperature estimates were attributed to solely to differences in thermal resistance, which was ultimately used as the indicator of power semiconductor assembly solder layer state-of-health. Together with the wire bond state-of-health estimate provided by monitoring the equivalent on-state device electrical resistance, the author claims to have invented a system able to simultaneously evaluate solder layer and wire bond fatigue status. It was not proved that these specific defects independently influence thermal resistance and device on-state electrical resistance, however. Analysis, grounded in physics, oriented toward evaluating the parameter sensitivity of the system, was also not provided.

Since the proposed system contained relatively complicated mathematical and statistical systems not intrinsically related to physics, proposing and evaluating a simpler, model-based approach to accomplish similar state-of-health assessment tasks is a remaining opportunity. An analogous closed-loop observer implementation would allow for simple parameter sensitivity studies could be more simply tuned.

Non-destructive evaluation (NDE) techniques

The multi-disciplinary NDE field contains a wide variety of analytical techniques used to assess the properties of a component or system without causing (more) damage to the system. NDE techniques are commonly used to realize structural health monitoring (SHM) for assessing structural integrity. Studies from the previous subsection which aim to evaluate a power semiconductor assembly's fatigue status using thermal response, especially using transient response properties, has been termed thermal wave NDE.

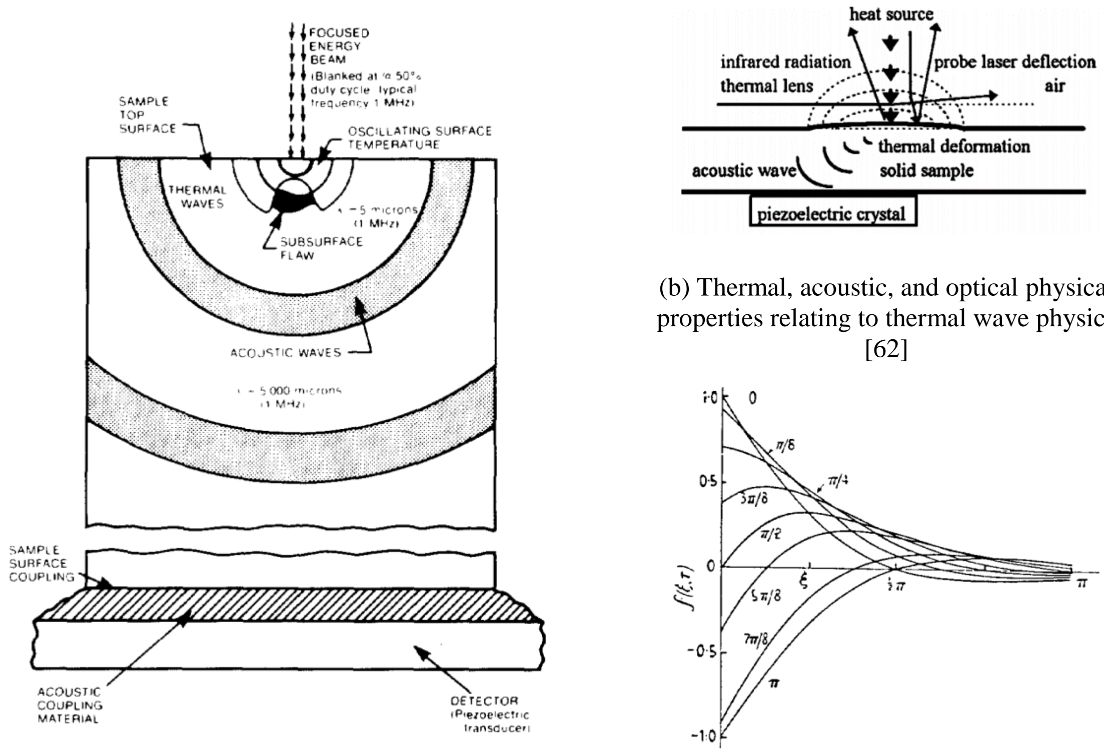

(a) Thermoacoustic detection principle [63], [64]

(b) Thermal, acoustic, and optical physical properties relating to thermal wave physics [62]

(c) Temperature-depth variation as a function of depth for harmonic surface temperature [65]

Fig. 1.1-15. Illustration of thermal wave principles for applied NDE

The above notion aims to quantify thermal diffusion with sensitivity to defects in an assembly. Fig. 1.1-15 presents illustrations from prior art showing how thermal transport has been conceptually used in past research and product development to eventually form images of defects in solid media, especially microelectronic semiconductor device assemblies.

It is unknown of heat-transfer based assessment could potentially replace inspection techniques documented in Fig. 1.1-9 at less cost. More immediately, the paradigm of using a power semiconductor device embedded within an assembled power module and/or converter as a dynamic source of heat for state-of-health assessment has not been documented in the power electronics literature. The opportunity exists develop methods inspired by this thermal wave NDE for effectively imaging power semiconductor assemblies for state-of-health assessment.

1.2 Acquisition of Dynamic Temperature Information

The previous section illustrated that regulation of power semiconductor temperature can extend the lifetime of the assembly. To form a closed-loop control system that actively limits or otherwise manipulates temperature for reliability purposes, one or more measurements or estimates of temperature are required. This section reviews the state-of-the-art methods utilized to measure or estimate temperature within a power semiconductor assembly, especially at an area referred to as the junction of the power device.

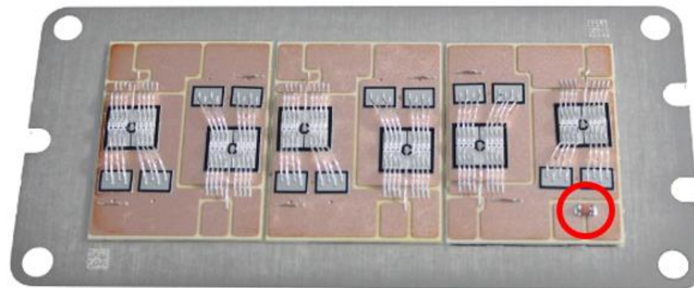

(a) Base plate, DBC, silicon die, and wire bond sub-assembly

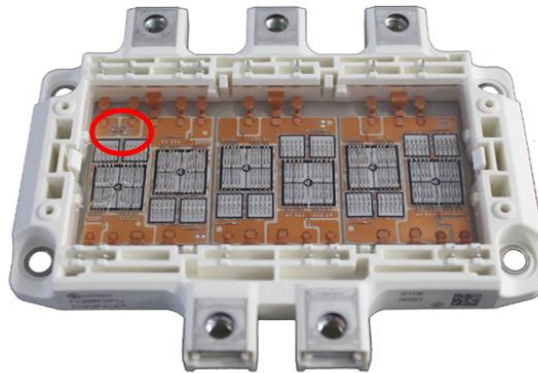

(b) Final IGBT module assembly

Fig. 1.2-1. Images of the Infineon FS100R12PT4 EconoPACK 4 IGBT module; please note that the thermistor component is enclosed by a red circle

This section is separated into several main subsections, which include temperature estimation using dedicated measurement hardware, such as assembly-located thermistor devices, using temperature sensitive electrical parameters (TSEPs), and using open-loop observer

structures. Most of the volume of the text in this section, however, will be spent discussing methods to extract thermal information leveraging transient gate currents, because these signals have potential to be measured non-invasively, i.e. with galvanic isolation.

1.2.1 Temperature estimation using dedicated measurement hardware

It is feasible to estimate the temperature of a surface via an adjacent piece of hardware connected to a signal conditioning and processing unit. In power electronics, it has been common to estimate temperature by use of thermocouples, resistance temperature detectors (RTDs), thermistors, and semiconductor thermometer devices. These technologies will not be reviewed in depth in this document because they are sufficiently summarized in [66] and because of the relative lack of significant innovation regarding their embodiments.

It is noted, however, that some of these devices, specifically thermistors, are very commonly included in current-generation IGBT power module assemblies, such as products from Fuji Electric shown in [67] or that shown in Fig. 1.2-1. However, in the assemblies, they are located a relatively large distance away from the critical semiconductor die area. As a result, the potentially fast thermal response of the die cannot be detected, at least because the mass between the thermistor and die acts as a thermal response filter. Intrinsic lagging properties of the thermistor device itself could further contribute to an attenuated and delayed temperature measurement.

Despite the inclusion of extra components dedicated to temperature estimation in current-generation power semiconductor assemblies, additional temperature sensing better localized to the relatively fast die area is needed to observe and regulate thermal cycles in a way that decelerates fatigue of the assembly at the most sensitive locations.

1.2.2 Temperature sensitive electrical parameter (TSEP) techniques

Low-level semiconductor device parameters, such as the bandgap energy (E_g) or carrier mobility (μ), have clear temperature dependencies [68]. Within the past decade, researchers have, in practice, been investigating how intrinsic temperature dependencies in these parameters, other parameters, and additional low-level parasitic elements can be detected in electrical signals accessible at the application- or integration-level of the power semiconductor assembly. This sub-field in power electronics is referred to as the study of temperature sensitive electrical parameters (TSEPs).

The large number of TSEP studies could be considered overwhelming. Indeed, the three most relevant publications reviewing the studies of TSEPs each have over 60 references [69]–[71]. Because of the eventual focus of this research program on a broader approach to extracting electrical, thermal, and mechanical (multi-domain) information from a very specific signal, the gate current, this section will mostly utilize these three publications to guide a review of this active sub-field. The paramount goal of this sub-section is to identify key considerations and opportunities oriented toward future research developments enhancing power semiconductor assembly reliability via a self-sensing approach [72], [73].

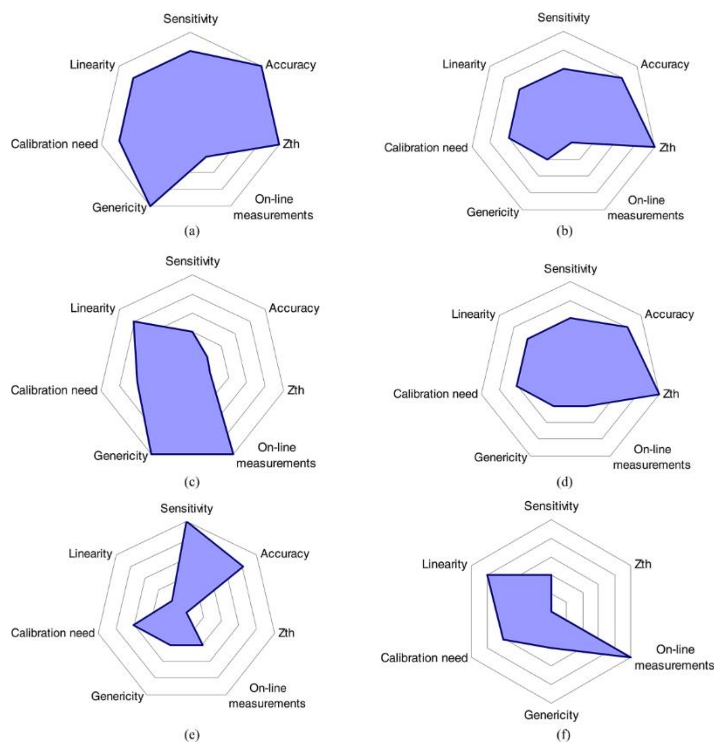

Fig. 1.2-2. Ratings of different TSEPs – (a) voltage under low current, (b) threshold voltage, (c) voltage under high current, (d) gate-emitter voltage, (e) saturation current, (f) switching time [69]

Table 1.2-1. Summary of temperature sensitive properties [70]

		COMMENTS						
	METHOD	DEVICE	DEPENDENTS	ADDITIONAL COMMENTS	POTENTIAL MEASUREMENT FREQUENCY	LINEARITY	REQUIRED SENSING RESOLUTION	REFERENCE
Classical TSEPs	Short-circuit current	IGBT	T	Induces a hard switching fault to create short circuit.	Low/unknown	Good linearity	Around 150 mA/C	[44]
	Saturation current	MOS transistors	T, V	Implementation strategy applies to "choppers." Measurement frequency unknown.	Unknown	Nonlinear (exponential)	Varies depending on temperature range	[43]
Static characteristic	Voltage at low current	Transistors and diodes	T, I	Requires specific current level to maintain linearity.	Low (only when load current comes close to 0 A)	Good linearity	mV/C	[13], [22], [23], [41], [42]
	Voltage at high current	Transistors and diodes	T, I	Requires very accurate current sensors. Measurement influenced greatly by parasitic elements inside modules (bond wires, etc.).	High (each on-state)	Good linearity	mV/C	[45]–[47]
Dynamic characteristics	IGBT turn-off	IGBT	T, I, V, R_g	Changes have also been viewed in harmonics in the output of an IGBT inverter.	High (each switching cycle)	Good linearity	Nanosecond or picoseconds per C	[48], [49], [51], [52]
	Turn-on delay	MOS transistors	T, R_g	Increase in gate resistance when measurement is required is proposed to slow down the process.	High (each switching cycle)	Good linearity	Nanosecond or picoseconds per C	[48]–[50]
	Rise time	MOS transistors	T, I, V, R_g	Increase in gate resistance when measurement is required is proposed to slow down the process.	High (each switching cycle)	Good linearity	Nanosecond or picoseconds per C	[48], [54]

T = temperature, I = current, V = voltage, R_g = gate resistance.

Table 1.2-2. Summary of temperature sensitive properties that can be used to estimate power semiconductor device temperature in real-time [71]

Method	Ref.	Device	Useful Today	Invading	Galv. Conn.	Integration	Signal Proc.	Band-width	Sensitivity
OBSERVER-BASED JUNCTION TEMPERATURE SENSING METHODS									
Open-loop T_j observer	See [71]	All Power Device	Yes	No	No	Not required	Simple	Low	
Closed-loop T_j observer		All Power Device	Yes	Depending on sensor	No	Power module integrated	Simple	Low	
SENSOR-ON-DIE-BASED JUNCTION TEMPERATURE SENSING METHODS									
Diode-on-die tech.	See [71]	All Power Device	Yes	Semicond. invading	Capacitive coupling	Power module integration	Simple	2m-sec response	A few mV/1ºC
R_{gint}		All Power Device	Yes	Semicond. invading	Yes	Power module integrated	Simple	High	0.75mV/1ºC
DEVICE ON-STATE PROPERTIES-BASED JUNCTION TEMPERATURE SENSING METHODS									
BJT V_{BE}	See [71]	BJT	No	No	Yes	Load integrated	Simple	0.2sec response	
MOS. R_{ds}-on		MOS.	Yes	Module invading	Yes	Converter inte.	Simple	Very high	
IGBT V_{CE}		IGBT	Yes	Module invading	Yes	Converter inte.	Simple	Very high	
DEVICE SWITCHING TRANSIENT PROPERTIES-BASED JUNCTION TEMPERATURE SENSING METHODS									
Miller Plateau	See [71]	MOS. IGBT	Yes	No	Yes	Gate drive inte.	Complex	Switching frequency	3n-sec/1ºC
V_{eE} delay		MOS. IGBT	Yes	No	Yes	Power module integrated	Simple	Switching frequency	8n-sec/1ºC
Switching Time		MOS IGBT	Yes	No	Yes	Power module integrated	Simple	Switching frequency	3mC/ºC
Short circuit current		MOS. IGBT	Yes	Converter invading	No	difficult	Simple	High	0.7%/1ºC
V_{eE} peak		MOS. IGBT	Yes	No	Yes	Power module integrated	Simple	Switching frequency	
V_{TH}		MOS. IGBT	Yes	No	Yes	Gate drive inte.	Complex	Switching frequency	3mV/1ºC
IGBT $\int V_{GE}$		IGBT	Yes	No	Yes	Gate drive inte.	Complex	Switching frequency	84mV/1ºC
MOS. i_G peak		MOS.	Yes	No	No	Gate drive inte.	Simple	Switching frequency	2.4mA/1ºC
IGBT $\int i_G$		IGBT	Yes	No	No	Gate drive inte.	Simple	Switching frequency	0.34%/1ºC
Voltage source-$R_{DS\text{-}on}$-L-C		MOS. IGBT	Yes	No	No	Converter inte.	Complex	Depending on signal processing	0.16mA/1ºC
Gate drive-$R_{DS\text{-}on}$-L-C		MOS. IGBT	Yes	No	No	Converter inte.	Complex	Depending on signal processing	0.5n-sec/1ºC

1.2.3 Open-loop thermal estimators or observers

Based on the literature review, a model-based approach to form power semiconductor temperature estimates is perceived as common in both industrial and research environments. The approach relies on models of two main processes: (1) the manifestation of conduction and switching semiconductor device losses, and (2) the thermal transport of the device losses.

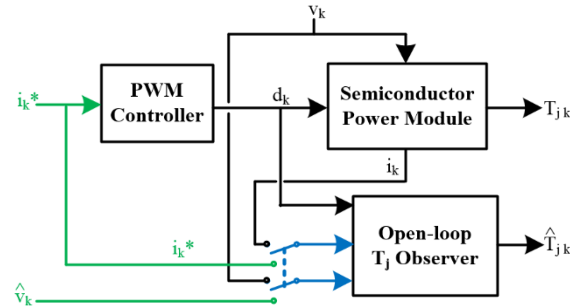

Fig. 1.2-3. Generic diagram of an open-loop observer structure to estimate T_j in real-time

The diagram in Fig. 1.2-3 illustrates this model-based approach. The diagram illustrates the operation of a controlled power semiconductor module. Additionally, an "open-loop T_j observer" block, which contains both halves of the electrothermal process model, is evaluated within controller hardware and software in parallel to operation of the power module. The same inputs and feedback signals interfacing with the physical semiconductor module are inputs to the open-loop model.

The open-loop T_j estimator or observer approach, reviewed further in Section 1.4.3, is common. This is, in part, because of the high number of research publications using this technique. A relatively high quality deployment of this approach is documented in [74].

Although the usage of open-loop T_j estimators or observers is common in the literature, their intrinsic limitations and sensitivities are not well documented. A systematic evaluation of these models, especially their dynamic estimation accuracy, has not been found. Also, parameter sensitivity and trade-offs associated with computational intensity have not been rigorously studied, especially in the context of the intended application of active power semiconductor temperature control.

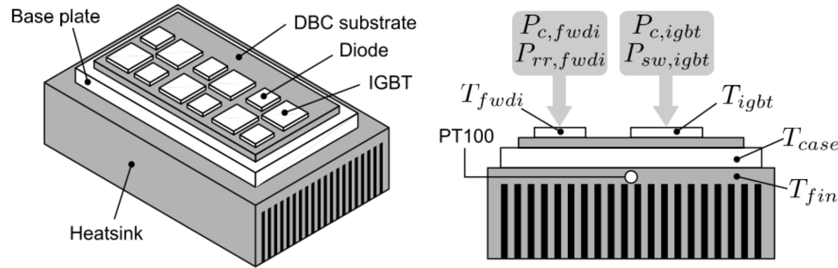

(a) Illustrations of the heat sink-mounted IGBT module, the origins of the IGBT and diode losses, and the thermal model's lumped temperature elements

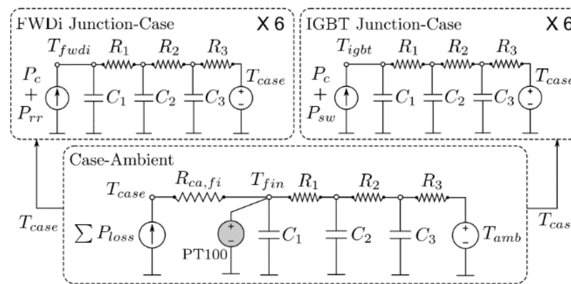

(b) Thermal equivalent circuit model of the IGBT module and heat sink assembly

Fig. 1.2-4. Pictorial illustration of an open-loop IGBT temperature observer [74]

1.2.4 Monitoring gate drive transient output properties

Gate current-related TSEP research was concurrently investigated by three institutions: Center for Energy Technology at University of Bayreuth [75]–[77], COPRE at Aalborg University [78], [79], and WEMPEC at University of Wisconsin-Madison [80]–[82]. The documented methodologies of these groups share common features, e.g. CORPE and WEMPEC both evaluated the natural gate current response during device turn-on, while Bayreuth investigated its response to an AC voltage injection. Additionally, Bayreuth and COPRE's methods are also similarly predicated upon temperature sensitivity of an internal gate resistor component, included in some assemblies.

It is proposed that future research focus on fundamentally expanding the scope of past research, which focused only on extracting temperature information in real time from gate currents.

Although past studies from WEMPEC did experimentally document influences of device bias voltage and load current on the gate current's natural turn-on response [82], a methodology strongly grounded in physical modeling of the power semiconductor assembly and driver circuits, able to capture multi-physical parameter changes, was not employed. A systematic methodology of processing gate currents to extract real-time information from thermal and electrical domains, along with mechanical fatigue information (as shown conceptually in [51]), for usage by higher-level control and/or condition monitoring algorithms, has not been formed.

1.3 Power Electronics-oriented Heat Transfer Modeling

Heat transfer analysis is an established practice, with comprehensive textbooks on the subject emerging as late as the 1940s [83], [84]. However, solutions to governing heat transfer equations are still complicated when analyzing computational domains having geometries more complicated than basic shapes, and when considering temperature (operating point) dependencies in material properties. As a result, the practice of forming accurate transient thermal models which can still practically be evaluated in a converter's processing hardware during real-time converter operation, is a general opportunity.

1.3.1 Analytical methods

1.3.1.1 Introduction

Introductory heat transfer courses often focus on ordinary differential equation (ODE) expression of heat diffusion physics, but the most accurate governing equations of heat transfer are partial differential equations (PDEs), such as Fourier's law of conduction and the Navier-Stokes equations for convection analysis. Of course, it is more difficult to analyze and simulate

PDE models than ODE models. To enable analysis, assumptions, such as the following few listed, are often utilized:

1. 1D or 2D computational domains
2. Component dimensions within the computational domain
3. Nonexistent or linear contact resistances
4. Idealized boundary conditions

Employment of these assumptions limits resulting model accuracy but is done very commonly in the literature. It is thus an opportunity to investigate thermal modeling methods minimally employing these assumptions.

1.3.1.2 Methods employing rigorous mathematical analysis of governing PDEs

A prior work analyzed an assembly resembling a modern IGBT module, shown in Fig. 1.3-1(a). The author began the analysis of the homogenous heat flow equation by stating assumptions that were made during the analysis, which are like the list included in the previous subsection. Assumed boundary conditions are enumerated prior to the author solving the governing heat equation using Laplace and Fourier transform methods.

$$F_T(x,y,s) = \frac{\tau_s(x,y,0,s)}{P(s)} \tag{1.3-1}$$

$$F_T(x,y,s) = F_{T1}(x,y,s) + F_{T2}(x,y,s) \tag{1.3-2}$$

$$F_{T1} = \sum_{n=0}^{\infty}\sum_{m=0}^{\infty} \frac{4U(n,m)\cos(n\pi x/L_x)\cos(m\pi y/L_y)}{(\delta_n+1)(\delta_m+1)L_xL_yk_s\gamma_s}\tanh\gamma_sL_s \tag{1.3-3}$$

$$F_{T2} = \sum_{n=0}^{\infty}\sum_{m=0}^{\infty} \frac{4U(n,m)\cos(n\pi x/L_x)\cos(m\pi y/L_y)}{(\delta_n+1)(\delta_m+1)L_xL_yk_s\gamma_s}\left[\frac{1-\tanh^2\gamma_sL_s}{\tanh\gamma_sL_s + \dfrac{k_c\gamma_c}{k_s\gamma_s}\dfrac{1+(k_c\gamma_c/k_i\gamma_i)\tanh\gamma_cL_c\tanh\gamma_iL_i}{\tanh\gamma_cL_c+(k_c\gamma_c/k_i\gamma_i)\tanh\gamma_iL_i}}\right] \tag{1.3-4}$$

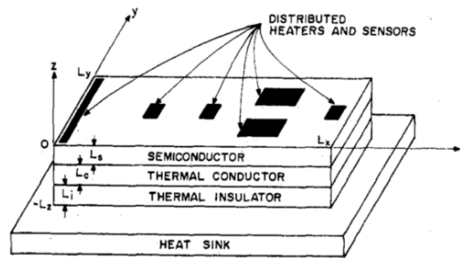

(a) Parametric, three-layer integrated circuit model

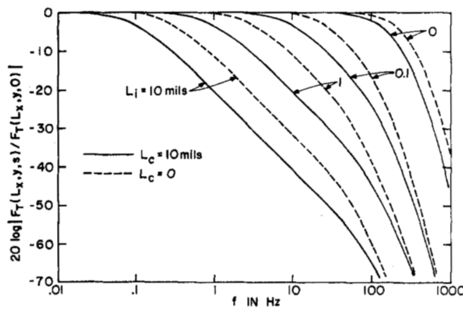

(b) Frequency response amplitude at different locations in the integrated circuit for differing L_c thicknesses

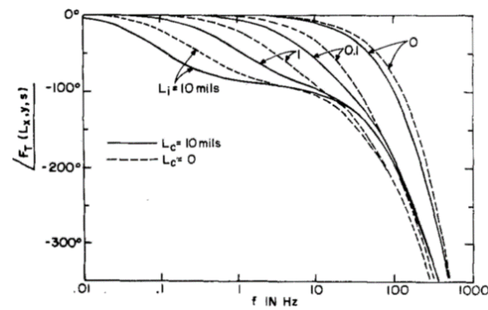

(c) Frequency response phase at different locations in the integrated circuit for differing L_c thicknesses

Fig. 1.3-1. Heat transfer analysis for the integrated circuit assembly in [85]

Solutions are expressed in terms of quantities with summations, which can evaluate to zero in certain limits, and in terms of spatially-dependent thermal transfer functions, i.e. expressions that describe how temperatures at specific locations respond to dynamic injections of heat. Eq. (1.3-1) illustrates the general form of the spatially-dependent transfer function. Eq. (1.3-2)-(1.3-4)

provide the result of the analysis of Fig. 1.3-1(a), which depend on material properties and dimensions. The resulting derivation is used to form frequency response function (FRF) plots documenting the amplitude and phase response of certain temperature states to heat injections at varying frequencies.

Strengths of the study include parameterizing the analysis in terms of material dimensions and properties, such as thermal conductivity, and rigorous utilization of mathematics to derive and plot insightful, spatially-dependent thermal transfer functions. The study did not compare models to experimental data or attempt to interpret the FRF response properties from a device integration design point-of-view, which are remaining research opportunities.

1.3.1.3 Techniques focusing directly on Fourier transform methods

The analytical heat transfer study from the previous subsection did utilize Laplace and Fourier transformations to obtain the final expressions of the analysis. In the past decade, studies have claimed their proposed analytical heat transfer models use Fourier techniques in innovative ways yielding a significant advantage over other methods [86], [87].

One study outlined a Fourier series solution to the governing heat conduction equation which was stated to compare favorably to finite difference and thermal equivalent circuits in terms of required computation for model evaluation [88]. The study included steps to couple the proposed thermal model with IGBT converter simulations, strengthening the breadth of the study. Ultimately, responses from converter experiments with thermocouples, thermal equivalent circuit models, and the proposed Fourier series model are examined during short segments of time. Comparison between model outputs and experiments reveal non-ideal properties in the models, but the honest comparison is a strong contribution.

Overall, the study of [88] provides a broad overview of coupled electrothermal simulations and experimental investigations, including modeling method development, converter hardware simulations, and thermocouple integration. However, the lack of direct comparison of the thermal modeling method with that of, e.g. [85], makes it difficult to ascertain the impact of the contribution.

Another study proposed the direct usage of Fourier techniques to model heat transfer in a power semiconductor assembly. Like [85], this study suggested discretizing the spatial domain of the assembly into cubes with constrained boundary conditions. 3D Fourier series solutions for this sub-problem are combined using closed-loop feedback within the modeling method itself, via the so-called direct Fourier method, as inspired by [89], [90].

The study does include methods to guide implementation of resulting models in Simulink, and steps to couple the thermal model with a power electronic converter simulation model, e.g. an inverter. Comparative results of the transient thermal impedance response metric, to be discussed in the next subsection, are also provided. The comparison includes the author's direct Fourier method model and a 3D finite element simulation using FLOTHERM. The comparative evaluation does not include experimental results.

This lack of comparison is a systematic limitation observed when reviewing state-of-the-art thermal modeling literature: studies often compare the supposedly new method with a numerical model, e.g. finite element model, that has not been calibrated against experimental characterization data.

1.3.2 Transient thermal impedance curves

1.3.2.1 Introduction

Experimental methods to evaluate an assembled power semiconductor's dynamic thermal response have been documented in the research literature. Indeed, the usage of TTI step response has been utilized for over five decades [91], [92]. TTI plots have logarithmically scaled time on the abscissa and power-normalized temperature on the ordinate. TTI curve examples for modern, commercial IGBT and MOSFET power semiconductor assemblies are shown in Fig. 1.3-2.

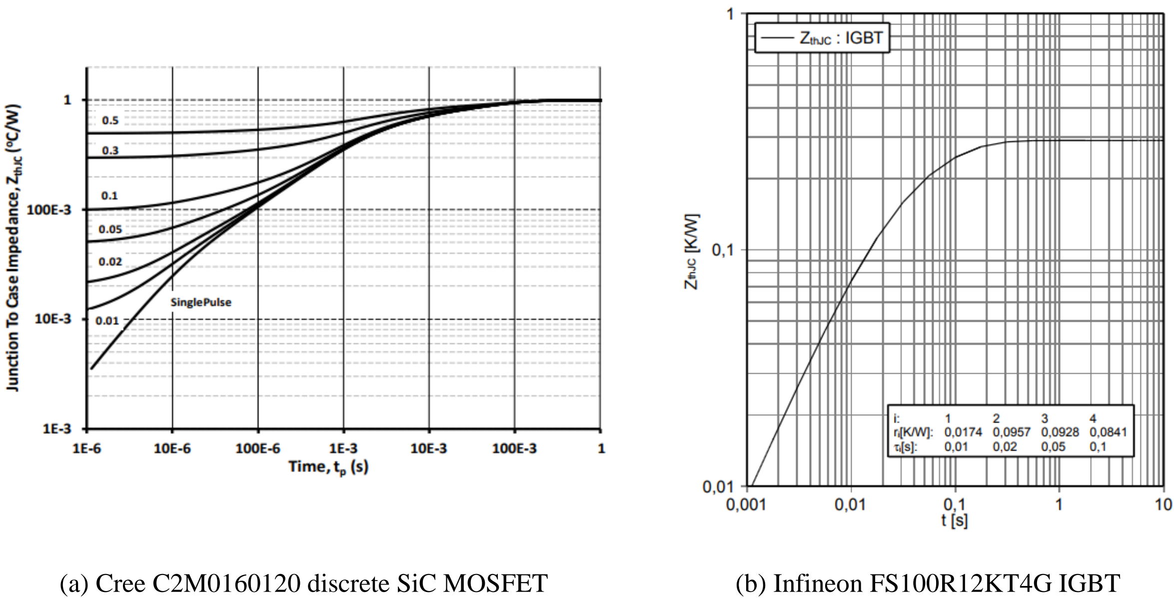

(a) Cree C2M0160120 discrete SiC MOSFET (b) Infineon FS100R12KT4G IGBT

Fig. 1.3-2. Commercial power semiconductor assembly data sheet examples of junction-to-case transient thermal impedance curves

Fig. 1.3-2(a) shows an example of how the TTI metric is occasionally reported in data sheets – as a series of curves. Each curve in the series, besides the "single pulse" curve, corresponds to a particular duty cycle of a power pulse input. For example, the upper-most curve in Fig. 1.3-2(a) provides the temperature response, normalized by the amplitude of the power loss (heat) input, for a 50% duty cycle power loss input as a function of the pulse width duration, t_p. It is assumed that

response information for power pulses of varying duty cycles is primarily provided to facilitate evaluation of a thermal response to extreme power pulses, e.g. short circuit events.

Fig. 1.3-2(b) shows an example of how the TTI metric is most frequently reported in data sheets – as a single normalized step response curve capturing the response of the temperature differential between the power semiconductor device junction and the case of its assembly. The notation $Z_{th,JC}$ is thus adopted to represent this junction-to-case spatial temperature response.

1.3.2.2 Parametric TTI curve analysis

A key publication in the literature archives uses TTI curves in a novel way to provide general insight about the system in question [93]. The study first explicitly introduces logarithmic time as an independent variable in analysis of step response experiments, and a spectrum of time constants, R(z). As shown in (1.3-5), R(z) is formally defined mathematically by a limit, and through experimental data post-processing using convolution and deconvolution operations.

$$R(z) = \lim_{\Delta z \to 0} \frac{\text{magnitude related to the time constants between z and z} + \Delta z}{\Delta z} \qquad (1.3\text{-}5)$$

An example result of the time constant spectrum derivation process is shown in Fig. 1.3-3(a), where an assembly's time constants are plotted on the abscissa and the response amplitude each time constant contributes to the total step response are plotted on the ordinate. Fig. 1.3-3 shows an experimental time constant spectrum for a transistor, along with the derivative of the TTI curve which is used for further post-processing.

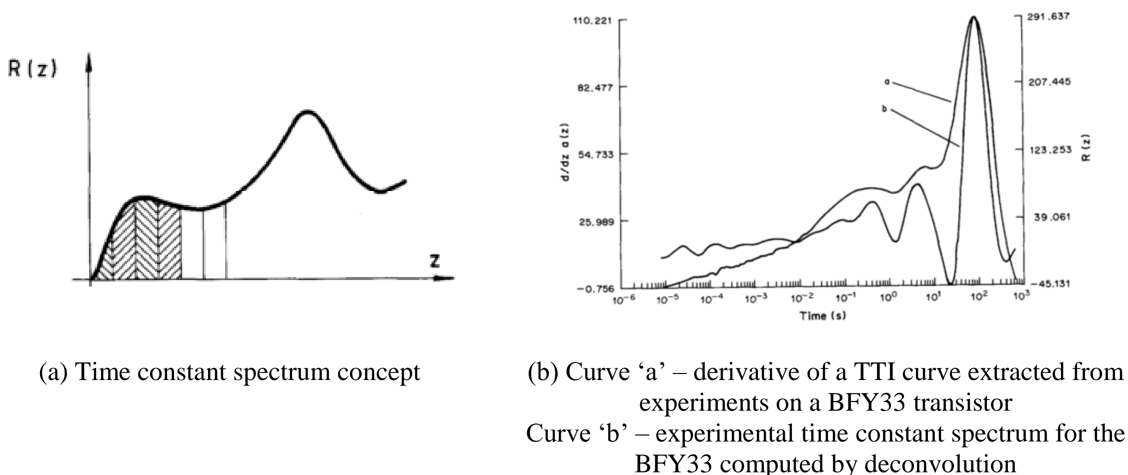

(a) Time constant spectrum concept

(b) Curve ‘a’ – derivative of a TTI curve extracted from experiments on a BFY33 transistor
Curve ‘b’ – experimental time constant spectrum for the BFY33 computed by deconvolution

Fig. 1.3-3. Illustration of time constant spectra from [93]

The study also proposed a mathematical tool called a structure function to accurately represent heat flow captured by a Cauer thermal equivalent circuit model. Ultimately, it plots representative cross-sectional areas for heat conduction against thermal resistances. The author uses the structure function to estimate detailed dimensional information about the test transistors and synthesize equivalent thermal equivalent circuit parameters.

Limits of [93] include using a one-port, i.e. single-input-single-output (SISO) assumption for the modeling procedure without clear indication for extension, assuming 1D heat transfer, and also implying that a Foster thermal equivalent circuit model can uniquely be transformed to a Cauer thermal equivalent, which is not true. However, as mentioned, the study was chronologically the first publication identified during the state-of-the-art review which introduces the concept of a time concept spectrum. Also, the study provides details about instrumentation to extract the TTI step response from a physical specimen, including manipulation of data sampling rate between 300 mHz and 200 kHz to capture die-level temperature information from a calibrated TSEP.

A set of papers [94], [95] from the late 1990s provides further modeling insight regarding the shape of TTI curve responses with a methodology called thermal resistance analysis by induced

transient (TRAIT). These papers attempt to address limits of [93] and other prior studies, namely the utilization of large approximations to form models and identify model parameters, and also treatment of a time constant spectrum as a continuous entity rather than a discrete one. The first paper in the series, [94], presents theory of the TRAIT methodology and perspective, while the second paper [95] presents applications on 3D assemblies.

The TRAIT method attempts to model a representative, total thermal impedance of a physical assembly. The method assumes that changes in power dissipation or heat within an object happen in an ideally stepwise fashion. Eventually, because corresponding amplitude factors (thermal resistances) and time constants become smaller as the model order i increases, it is eventually concluded that the response T(0,t) can be realistically approximated using n terms. It is said that resulting truncation error has a theoretical upper limit that depends on how many terms are included in the model, n. This conclusion is a major theme in and enlightening perspective about the engineering science of forming real-time power electronics-oriented thermal models, and will be revisited later in this state-of-the-art review, especially subsection 1.3.4.

The set of papers documenting and evaluating the TRAIT method are very credible and provide valuable perspective to the thermal modeling problem by providing discussion about model order requirements, truncation, and expected truncation errors. These papers are still very relevant today and should be cited by modern studies of thermal modeling in power electronics. However, despite the high quality of these studies, limitations, which will be summarized in the next sub-section, remain.

1.3.2.3 Advantages and limitations of TTI curves

The method of forming dynamic thermal models by extracting and analyzing TTI curves is advantageous because, in theory, a model can be derived using a single time series of experimental data. Also, it should not be taken for granted that the methodology does have an experimental component, which is not always the case in modern heat transfer modeling for power electronics applications. Finally, the method is generally simple, easy to understand, and relatable due to the common introduction of step response evaluation in introductory control systems courses and textbooks.

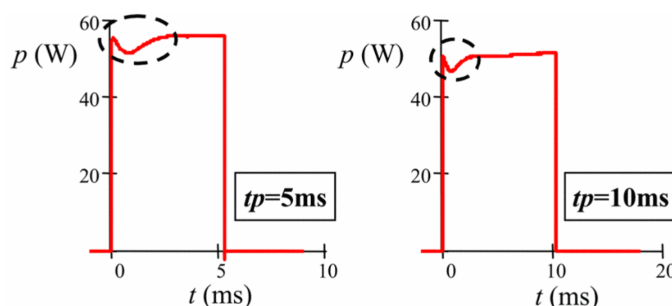

Fig. 1.3-4. Illustration of non-ideal step input properties documented in [96]

The archival literature on TTI-based thermal modeling does not prove beyond a reasonable doubt that step inputs coherently excite relatively fast dynamics in an assembly. The power step increase or decrease (cooling) system perturbations are assumed to be ideal throughout all but one study of thermal modeling in power electronics. Fig. 1.3-4 documents actual step power inputs measured during TTI step response experiments. Please note the circled portion of the waveforms which represent a departure from ideal step behavior.

In TTI-based thermal modeling, phase delay is not characterized. Furthermore, to quantify the quality of the experimental excitation of various dynamic elements within a system, such as mean-squared coherence, have not been documented in any study of experimental thermal system

response modeling. Limitations of step response-based thermal system identification and modeling are summarized as:

1. Ideal step inputs, which are physically impossible to realize, are assumed; for this reason, the step response method intrinsically captures saturation properties of the incipient loss (heat) modulation mechanism
2. Phase response information is usually disregarded or discarded; thermal system phase response interpretation methods are not developed
3. Coherence of presumed dynamic excitations is not provided
4. Step response is not immediately amendable to operating point (nonlinear) thermal modeling of an assembly because step inputs are usually designed to traverse the assembly through a wide range of temperatures

1.3.3 Cauer and Foster lumped parameter thermal equivalent circuits (TECs)

1.3.3.1 Introduction and comparison of model topologies

The previous subsection focused on thermal modeling methods employing TTI curve analysis, but unavoidably mentioned the usage of Cauer and Foster TECs, the formal focus of this subsection. TECs are comprised of lumped thermal resistance and capacitance parameters and are dominant dynamic thermal model expressions in power electronics.

The two prominent TEC models are named after the German mathematician and physicist Wilhelm Cauer (1900-1945) and the United States mathematician Ronald Martin Foster (1896-1998) [97]. The surnames of these mathematicians were attributed to these equivalent circuit forms in the context of network synthesis methods, e.g. for designing filters having specific properties [98]. For usage in problems involving transient heat transfer modeling, these circuits

fundamentally leverage the similarity between governing ODEs and PDEs in electrical in thermal domains [99].

Fig. 1.3-5 illustrates archetypal Cauer and Foster thermal model structures. First, the (a) plot shows a second-order Cauer model having two lumped thermal capacitances, C1 and C2, two lumped thermal resistances, R_{12} and R_{23}, three assumed non-stationary temperature states, and a loss (heat) input that is implied to be controlled by the controlled current source symbol. The units of the loss input are W. The (b) plot presents a higher order Cauer model having six thermal capacitances and resistances, an ideal voltage source representing the final reference (ambient) temperature, and an ideally switched heat input.

Cauer TECs are distinguished by ground-connected thermal capacitances. On the other hand, thermal capacitance elements in Foster TECs are not connected to ground. As shown in Fig. 1.3-5(c), the thermal resistance and capacitances form parallel subsystems which are arranged in series. Again, loss inputs in this diagram are assumed to be ideally switched, an assumption used commonly in modeling approaches utilizing TTI curves.

Cauer models are regarded as faithfully capturing the behavior of internal temperature states in a way that is consistent with the physical response of an assembly. Foster models do not faithfully capture internal temperature state responses. An explanation of the claimed physical consistency of Cauer models and inconsistency of Foster models is provided in [94]. The author's own commentary on the utility of Cauer and Foster models is provided below.

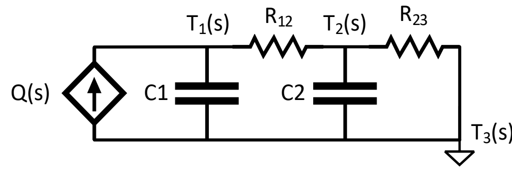

(a) Two-element Cauer model structure labeling the three assumed dynamic temperature states, the assumed controlled loss input, and two lumped thermal resistance and capacitance parameters

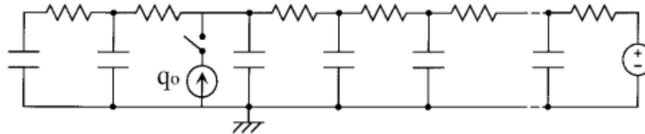

(b) Cauer model illustrating the loss input as an ideally switched element, heat flowing in multiple directions, and an ideal voltage source representing ambient temperature

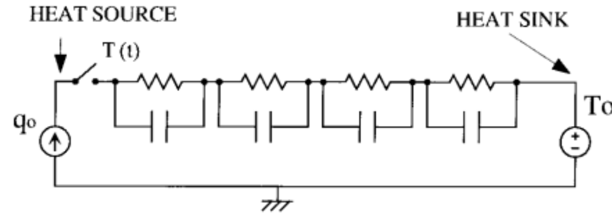

(c) Foster model illustrating the loss input as an ideally switched element and shown to explicitly represent the spatial domain between the heat source and heat sink

Fig. 1.3-5. Cauer and Foster thermal model structures [94], [95]

Cauer models are frequently referred to as physics-based models, while Foster models are frequently regarded as physically inconsistent. However, this does not acknowledge that a Foster model can constitute a physics-based thermal description of an assembly, albeit only of outer, readily measurable temperature states. Correctly formed Cauer and Foster models for an identical assembly will have the exact same pole, zero, and gain properties when viewing the response of the outer temperature state to dynamic heat inputs.

1.3.3.2 Derivation methods

TEC formulation has two main associated tasks: (1) topology selection or selection of the order of the model, and (2) computation of equivalent thermal resistance and capacitance parameters. The first task is often completed implicitly, with the aid intuition about the thermal

domain, and not treated explicitly. No matter the complexity of an assembly's geometry, the second task is often completed using relatively simple expressions from ODE heat transfer analysis, namely (1.3-6) through (1.3-9), introduced in introductory heat transfer textbooks such as [84].

$$R_{pw} = \frac{L_{char}}{k\, A_{char}} \quad (1.3\text{-}6) \qquad R_{conv} = \frac{1}{\bar{h}\, A_{surf}} \quad (1.3\text{-}7)$$

$$C_{tot} = m\, c_p \quad (1.3\text{-}8) \qquad \tau_{lumped} = R_{surf\text{-}surrounds}\, C_{tot} \quad (1.3\text{-}9)$$

$$\tau_{diffusive} = \frac{L_{char}^2}{4\alpha} \quad (1.3\text{-}10) \qquad Bi = \frac{\text{resistance desired to neglect}}{\text{resistance considering}} \quad (1.3\text{-}11)$$

Eq. (1.3-6) estimates a conductive thermal resistance using an ideal plane-wall approximation for a computational domain having characteristic length, L_{char}, characteristic cross-sectional area, A_{char}, and thermal conductivity, k. Eq. (1.3-7) estimates ideal resistance to convection of a surface having an area A_{surf} and an average, linear heat transfer coefficient, $\bar{h}$. Eq. (1.3-8) is a total lumped capacitance of a component or assembly having mass, m, and specific heat capacity c_p. Eq. (1.3-9) estimates a time constant following the lumped capacitance approximation in which $R_{surf\text{-}surrounds}$ is the total resistance between the surface of the assumed lumped capacitance and the temperature of the ambient within which the lumped capacitance is located.

Eq. (1.3-10) and (1.3-11) are also relevant approximations of heat transfer physics included in introductory heat transfer textbooks, but were not utilized in any studies employing a TEC encountered during the state-of-the-art-review. Eq. (1.3-10) approximates a diffusive time constant that quantifies the duration of time required for conduction to occur within a medium. It is expressed as a function of L_{char} and the thermal diffusivity, $\alpha = k/(\rho\, c_p)$ [m^2/s], where ρ is a

material's density. The Biot number, Bi, expressed generally in (1.3-11), quantifies how accurate a lumped capacitance approximation is. If Bi << 1, then the resistance under consideration to be neglected can indeed be neglected with small errors in a resulting lumped capacitance model. In practice, (1.3-9) should only be used if the implications of usage have been evaluated using (1.3-11).

The usage of (1.3-6) through (1.3-9) to estimate lumped parameters within a Cauer TEC without verification is the most common method for dynamic modeling of heat transfer processes in power electronics. It is a widespread practice in power electronics to utilize a lumped capacitance time constant ideology, without verification using a Biot number, to model all modes of heat transfer in an assembly. The physics implied by (1.3-10), which is derived using a semi-infinite body approximation of conduction heat transfer has not been explored in power electronics applications.

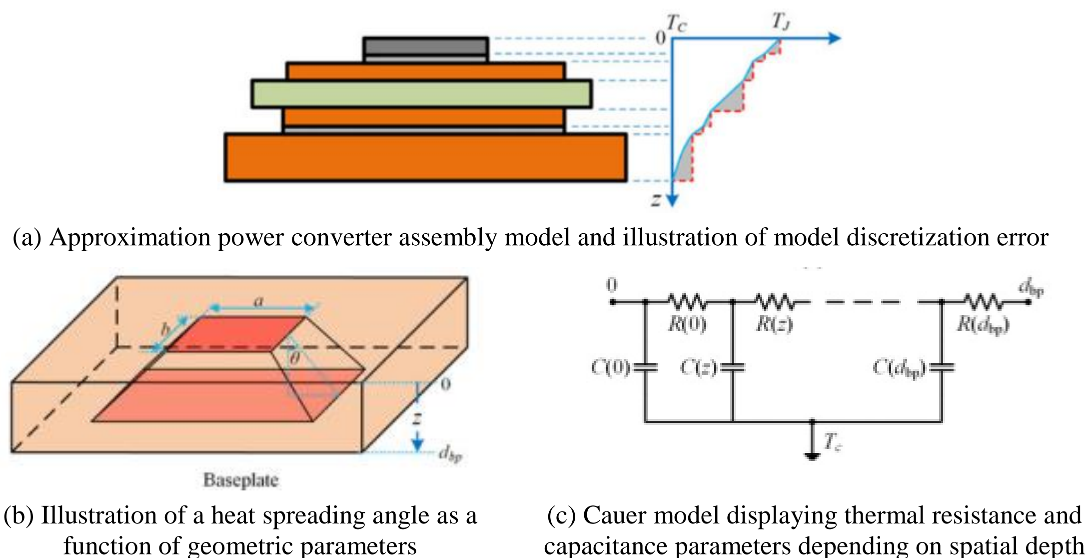

(a) Approximation power converter assembly model and illustration of model discretization error

(b) Illustration of a heat spreading angle as a function of geometric parameters

(c) Cauer model displaying thermal resistance and capacitance parameters depending on spatial depth

Fig. 1.3-6. Summary of a method to populate a Cauer model [49], [100]

An example research program investigating Cauer models is highlighted in Fig. 1.3-6 [49], [100]. In the (a) figure, the study recognized inherent limitations in using the nominal Cauer model

methodology to coarsely discretize a spatial domain. In (b), the authors proposed to use precise geometric assembly data, and a linear model of heat spreading, to more accurately estimate Cauer model parameters. The resulting model is shown in (c), which illustrates the thermal resistance and capacitance parameters as a function of position in the assembly.

Reference [101] proposed a methodology to populate Cauer model parameters utilizing response information from a finite element numerical model of power converter assembly. Following identification of thermal resistances using a steady-state response of the model, the method simulates step responses, and effectively measures how long it takes a heat diffusion wave to reach a nodal location in the model. Per the (d) figure, the method equates diffusion time delays to time constants and then computes thermal capacitance parameters for a Cauer model using (1.3-9).

The method to form Cauer models using an Elmore delay property [101], [102] is advantageous because it does utilize simulation measurements of physical heat wave diffusion from a numerical model. However, the methodology is inconsistent with heat transfer physics, modeling diffusion physics under an unverified lumped capacitance assumption. It also requires a numerical model which, as always, should be calibrated against experimental data. Selection of model order are also not commonly addressed explicitly.

To summarize, the steps commonly taken to form Cauer or Foster TEC models are, in general order of their completion:

1. Topology selection, i.e. order of the TEC
2. Estimation of a total thermal resistance, i.e. the steady-state response between certain spatial locations in components or assemblies

3. Division of total thermal resistance into small resistances between segments of the spatial domain; evaluation of their values using (1.3-6) or steady-state data
4. Estimation of capacitance parameters which correspond to the spatial domain segments established during the previous step using (1.3-8) or step response data

Limitations in common methods to populate TECs have been mentioned throughout this subsection. TEC models are not inherently bad estimators, but lack of a systematic design method, lack of agreement with fundamental heat transfer physics, and other general limitations in derivation methods raise question about their widespread usage.

1.3.3.3 2D and 3D TECs

Instances in the research literature show how traditional TEC models have been extended to capture heat transfer in more than a single coordinate direction. This step can be taken by formally employing numerical modeling techniques, which will be discussed directly in subsection 1.3.4, or by creating a structure linking TEC modules together in a way that captures multi-dimensional heat transfer.

The methodology documented in [103] and represented by Fig. 1.3-7 used step response data at multiple nodal locations within a finite element simulation model to form Foster model responses at each point. This approach to forming a dynamic thermal model attempting to accurately capture 3D heat transfer is essentially a blend of TTI curve analysis and numerical modeling techniques linked together by the author's 3D model template. The resulting model was attractive because it could intrinsically capture so-called thermal cross-coupling, i.e. the impact on having multiple heat sources within an assembly on its spatial temperature response.

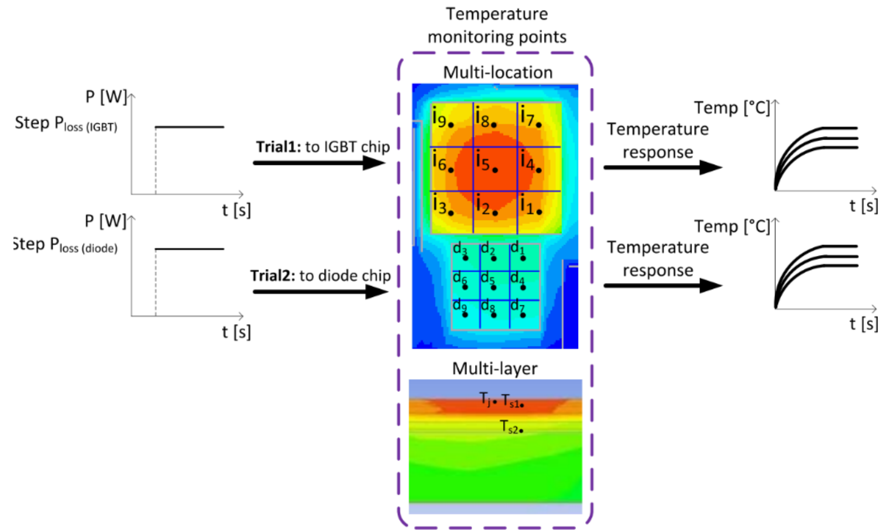

Fig. 1.3-7. Illustration of the 3D TEC derivation method from [103]

Limitations of the method include simulation only evaluation. Also, evaluations of resulting models were completed using step response and suffer from the limitations of this approach already discussed in this review.

The next study reviewed in this subsection also did not compare methods against experimental results , but did use EA FRF metrics for evaluation [104], [105]. Also, a formal, numerical modeling technique, finite differences, was used to form the 3D TEC. It demonstrates how Cauer TECs are, in effect, coarse numerical models.

1.3.3.4 Advantages and limitations of TECs

The usage TECs to predict spatiotemporal thermal response of power semiconductor and converter assemblies for offline and real-time simulations is pervasive in the field of power electronics. As shown in Table 1.3-1, the TEC ideology offers distinct advantages, which can be summarized as simplicity. However, techniques to systematically and comprehensively evaluate resulting TEC models, including their accuracy at different converter operating points, is lacking

in the literature. Because TEC topology selection is often completed non-explicitly, opportunities to further develop formal thermal modeling theory related to topology selection exist. Two related open questions for research related to topology selection are:

1. What is the minimum required model order (number of states in the model) needed to form an accurate thermal model? Why?
2. How is the balance between model complexity and accuracy optimized?

Table 1.3-1. Advantages and disadvantages of TECs and TEC-related modeling methods

TEC advantages	TEC disadvantages
Usually computationally efficient	Derivation methods can be ad hoc, assumption-intensive
Graphical and amenable to intuitive understanding	Generally deployed with a state count that could be too low for broadband accuracy
Can be derived using a single TTI step response curve	Simple appearance can be misleading
Standard; often provided in a data sheet for a segment of the spatial domain	Only provide information about a segment of the spatial domain, e.g. junction-to-case

Table 1.3-1 also displays further disadvantages of TEC modeling expressions and methods. Given the limits, TECs are not inherently bad estimators of dynamic thermal response. However, methods commonly employed to build TEC models are not systematic.

1.3.4 Numerical techniques and model order reduction

1.3.4.1 Introduction

The previously reviewed study from the state-of-the-art [104], [105] builds a 3D Cauer model by the usage of numerical techniques to build a finite difference model (FDM). Another popular numerical model expression is a finite element model (FEM). These techniques are

intended to discretize a physical (spatial) domain that is nominally governed by a PDE. Discretizing a spatial domain using these methods such that it can be modeled by coupled ODEs is established practice. FD methods were documented for usage in heat transfer analysis in 1928, and FE methods were documented for usage in 1965 [106]. This section will provide a brief review of these model discretization methods, and some of the recent trends regarding recent usage of these tools in power electronics.

1.3.4.2 The finite difference (FD) method

FD methods are likely more intuitive for a reader to grasp, so this subsection will review them first. The motivating goal in applying FD methods to a computational thermal domain is to divide the domain into a 1D, 2D, or 3D grid composed of pieces formally called, for the 3D case, control volumes. Fig. 1.3-8(a) shows a 1D discretization of a bar-shaped component into *n* pieces having specified temperature boundary conditions and uniform widths, Δx, and (b) shows a FD mesh of a diode.

When forming a FD mesh, each piece of the discretization is assumed to have uniform temperature, so care should be taken to ensure the mesh is spatially resolved enough to capture the heat transfer of interest. Control volume size also must be considered when selecting a numerical solver, e.g. Euler or Crank-Nicholson, to evaluate transient responses. Literature studies using an FDM or FEM often do not publish fundamental details relating to the mesh selection methodology used, and evaluation of mesh convergence.

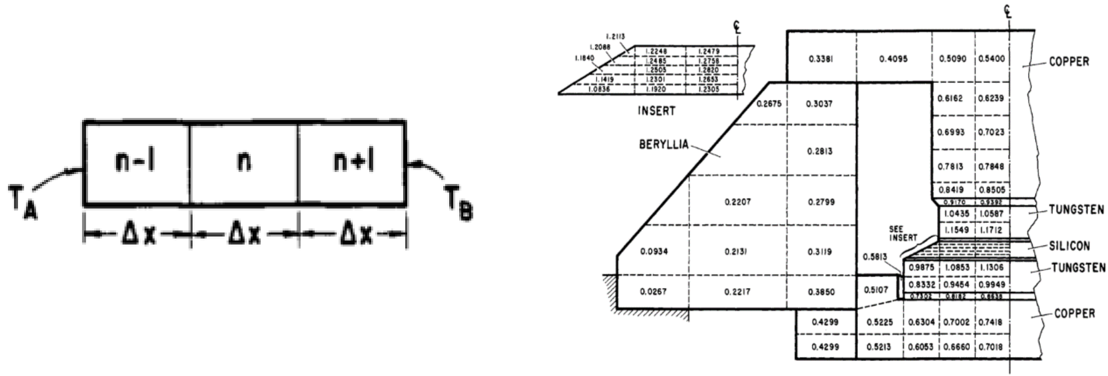

(a) FDM discretization structure

(b) Cross-sectional view of FD discretized p-i-n diode including variable mesh densities

Fig. 1.3-8. Relatively early FDM of a semiconductor assembly [107]

Numerical models, including FDMs and FEMs, are derived following a first-principle conservation law. For application of FDM, conservation of energy is applied, and the sum of heat fluxes entering/exiting a control volume must equal zero. In practice, following FD grid or mesh definition, ODE models relating heat transfer between each control volume are formed using relatively simple equations, such as (1.3-6) through (1.3-8). Note that if materials are assumed to have constant properties and radiation heat transfer is neglected, a resulting FDM resembles a linear time-invariant (LTI) state-space model in the general form of (1.3-12), shown clearly in [27]. Thermal modeling efforts documented in the power electronics literature widely assume LTI system behavior.

$$\bar{C}\frac{d\bar{T}}{dt} + (\bar{K} + \bar{H})\,\bar{T} = \bar{C}\frac{d\bar{T}}{dt} + \bar{S}\,\bar{T} = \bar{g} + \bar{q} + \bar{H}\,\bar{T}_{\infty} = \bar{r} \qquad (1.3\text{-}12)$$

Upon completion of gridding or meshing an assembly model, responses can be computed. For steady-state analysis, the d/dt( ) terms are replaced with zeros, and nodal temperature responses can be computed with the $\bar{S}$ matrix and $\bar{r}$ vectors, shown in (1.3-12). For time domain transient analysis of the FDM, a numerical integrator or solver must be used to discretize time and simulate

how the state space model responds. However, (1.3-12) is intrinsically suitable for response analysis in the frequency domain.

As mentioned in section 1.3.3, Cauer TEC models are commonly formed in the research literature by evaluating simple approximations for thermal parameters, i.e. (1.3-6) through (1.3-8). The beginning of this subsection revealed that FDMs are derived in a similar way, but with more structure following the formal application of a mesh to a component or assembly. This section also revealed considerations that should be taken when building and simulating FDMs, such as spatial resolution of the mesh, inclusion of material property nonlinearity in the model, and selection of the numerical solver. Given the strong trend that Cauer models in the literature frequently have ≤ around 5 states and include linear approximations for material properties, it can be perceived that Cauer models are actually a special case of FDMs, evaluated in real-time with the Euler solution technique. In other words, Cauer models are coarse, unrefined FDMs.

1.3.4.3 The finite element (FE) method

Due to higher mathematical complexity, FE methods will be reviewed now in less detail than FD methods, with references provided for further reading. Application of the FE method in heat transfer essentially represents a different way to formulate (1.3-12), a state-space model for a discretized version of a computational domain. The FE method does formulate energy balance equations to derive state-space matrices, however, unlike FDMs, energy balance equations are not forced to equal zero. Instead, energy balance equations can equal a residual number, which FE methods, such as the Galerkin, minimize. Details of FE methods will not be provided in this document; instead, the reader is referred to high quality references, [84], [108], [109].

In general, the FE method is more general purpose the FD methods, and more suitable to analyzing components or assemblies with relatively complex geometric features. The structure of FE and FD matrices comprising governing state equation models are also different. For example, FD global capacitances matrices are diagonal, while generally non-diagonal in FEMs. The structure of matrices influences if techniques can be used to reduce the time required to complete simulations, and solver selection.

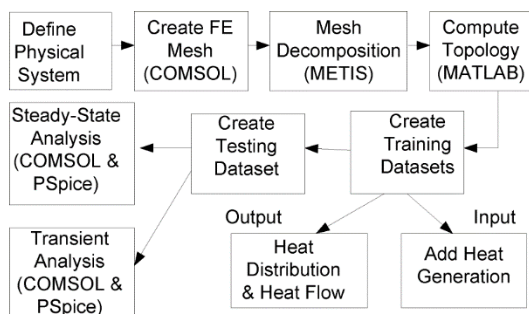

(a) ROM thermal modeling methodology employing FE simulations

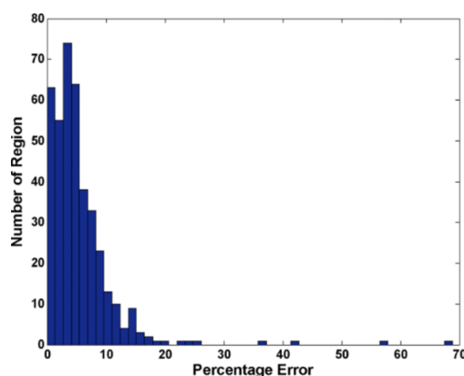

(b) Relationship between model order and resulting error in a selected temperature rise

Fig. 1.3-9. Critical outcomes from a model reduction study using FEA [110]

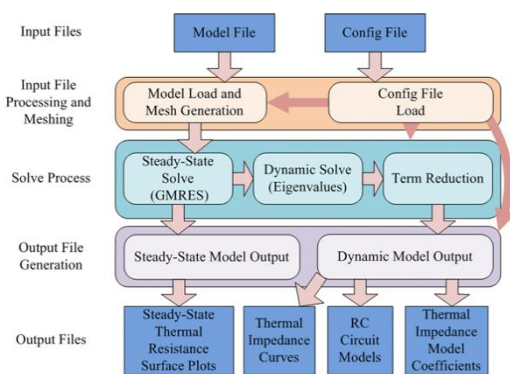

(a) Process for extracting dynamic thermal ROMs

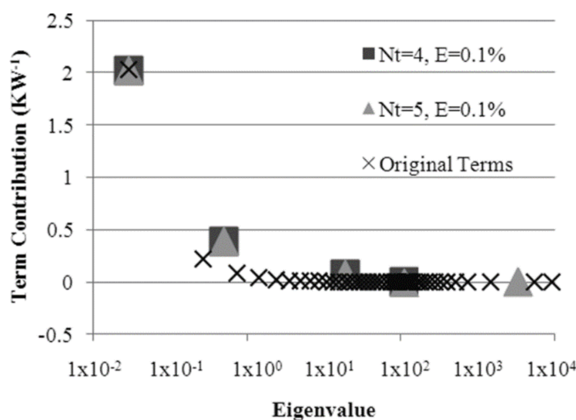

(b) Eigenvalues of a high-fidelity FEM and ROMs with 4 and 5 states

Fig. 1.3-10. Critical outcomes from another model reduction study using FEA [111]

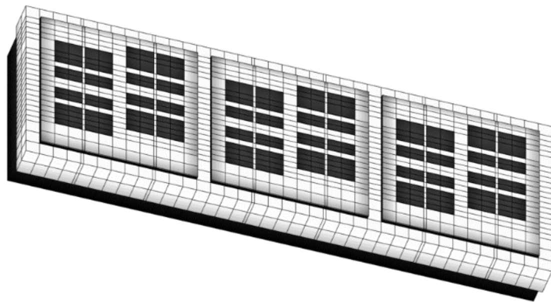

(a) FD mesh of an IGBT module

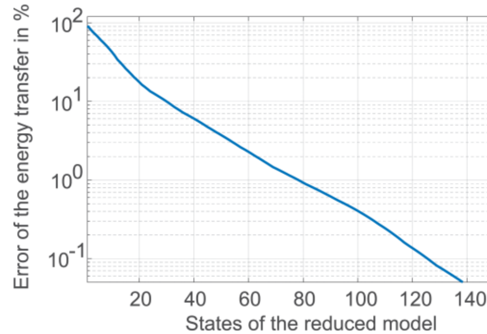

(b) FDM truncation error as a function of states in a resulting ROM

Fig. 1.3-11. Critical outcomes from a model reduction study using FD techniques [105]

1.3.4.4 Truncation to derive a reduced-order model (ROM)

Studies employing numerical techniques are very common in the power electronics literature. Most studies use numerical models for calibration of ad-hoc ROMs, or for general purpose response evaluation. This review of the dynamic thermal modeling state-of-the-art has revealed that TEC models have suboptimal fidelity, but numerical models require too much computation to evaluate during real-time converter operation. Most of the recent innovation regarding the employment of numerical thermal models appropriately relates to systematically reducing the models to have a specified *n* states, and therefore configurable complexity. Fig. 1.3-9 through Fig. 1.3-11 are figures of merit from three separate groups evaluating methodologies to systematically reduce high-fidelity numerical models to optimally trade accuracy for reduced model complexity. Some general methods for model truncation can be classified as follows:

1. (human-managed) When forming an FDM, neglecting elements which capture relatively negligible energy transfer, i.e. have very large thermal resistances; this can be considered manual manipulation of FD meshi

2. (algorithm-managed) Graph partitioning, which can be considered structured PDE mesh manipulation
    a. Feature space analysis (FSA)
    b. Principle components analysis (PCA)
    c. Singular value decomposition (SVD)
    d. k-way partitioning
    e. Sub-space projections

The algorithms listed above largely relate to mathematical and computational subjects and topics, such as eigenvalue analysis, graph theory, and machine learning [112]–[114]. The capability for these techniques to empower engineers in the model reduction process is promising, however, the following areas for necessary further inquiry exist:

1. Reduction methods utilize mathematical projections of numerical models and obscure physical insight. Can insight be recovered in way that allows resulting ROMs to be used for thermal-mechanical assembly and controls design?
2. What are the tradeoffs involving the usage of different algorithms for execution of model reduction?
3. How can methods be utilized optimally given available temperature feedback from TSEPs, thermistors, or other sources?

1.3.4.5 Summary of numerical techniques for thermal modeling

This subsection briefly reviewed two methods for systematically discretizing a computational domain for heat transfer analysis: the FD and FE methods. It was mentioned that usage of these two techniques for steady-state and transient analysis of power electronics thermal

responses is very common in the modern research literature. However, only a single dominant trend of systematic innovation involving the usage of numerical techniques has been identified: reduction or truncation of high fidelity models in a structured way using algorithms. This trend, which appears limited to the last decade of publications, allows for derived model complexity and accuracy properties to be explicitly and intentionally traded. The state-of-the-art of dynamic thermal modeling for real-time power electronics applications is using FD or FE methods and, if necessary, model-order reduction.

1.3.5 Frequency domain analysis

Subsection 1.3.4 concluded that a dominant state-of-the-art thermal modeling methodology is derivation of a high-fidelity numerical model, using finite differences or elements, and then using model reduction algorithms, if necessary. Studies documenting this methodology, however, often do not employ experimental cross-checks of their models. A second relatively recent dominant trend in thermal modeling examines experimental system identification measurements in the frequency domain and has the potential to work cooperatively with the numerical-to-ROM methodology.

A relevant study in the literature documents a methodology to extract experimental frequency response measurements from a multiple-input-multiple-output (MIMO) assembly having multiple sources of heat and temperature detectors [115]. The main focuses of this study are: (a) selection and implementation of pseudo-random binary sequence system perturbations, (b) evaluation of the MIMO, “cross-coupling” thermal dynamics, and (c) prediction of assembly temperatures as a function of known heat inputs using finite impulse response and infinite impulse response (IIR) filters, and by inverting discrete Fourier transform data, shown in Fig. 1.3-12.

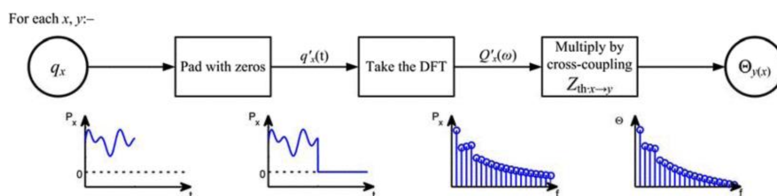

(a) Steps to calculate frequency spectra of input heats and output temperatures

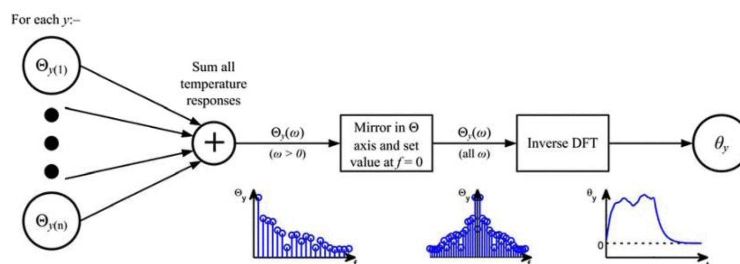

(b) Method to calculate superimposed time-domain thermal responses

Fig. 1.3-12. Sequence of methods proposed and evaluated in [115]

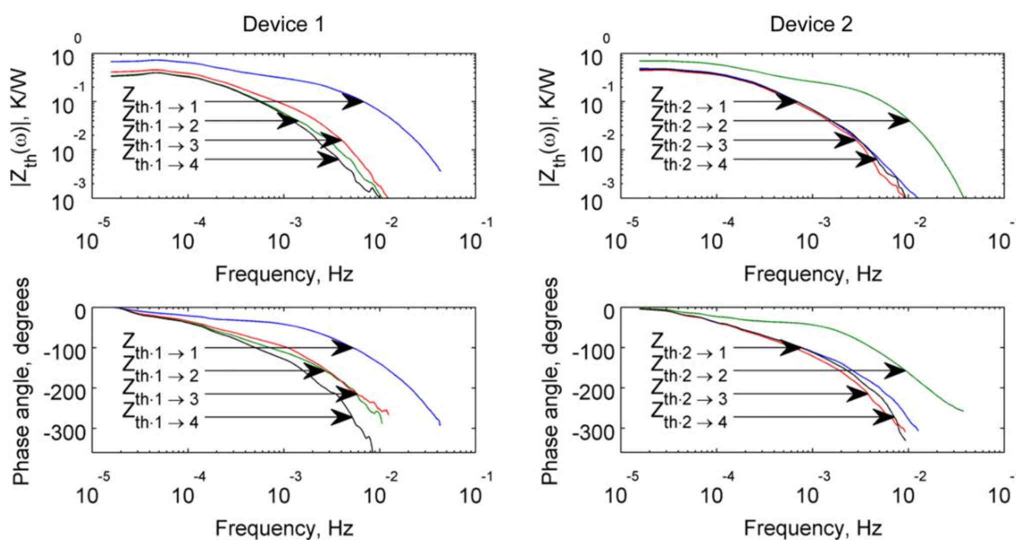

Fig. 1.3-13. FRF-based illustration of cross-coupled, spatially-dependent heat transfer dynamic response properties [115]

The methodology in [115] was applied to an assembly having four heating resistor/thermocouple sub-assemblies mounted to various locations on a 8”x 6” heat sink. Resulting FRFs, shown in Fig. 1.3-13, illustrate how the method can capture spatially-dependent magnitude and phase temperature response properties of the assembly to spatially-dependent heat

inputs. Eventually, the authors attempted to fit the FRFs with FIR and IIR approximations of the behavior. They evaluated how real-time evaluation of the filters can be improved with the additions of temperature feedback, in practice using a reduced-order observer model reduction method.

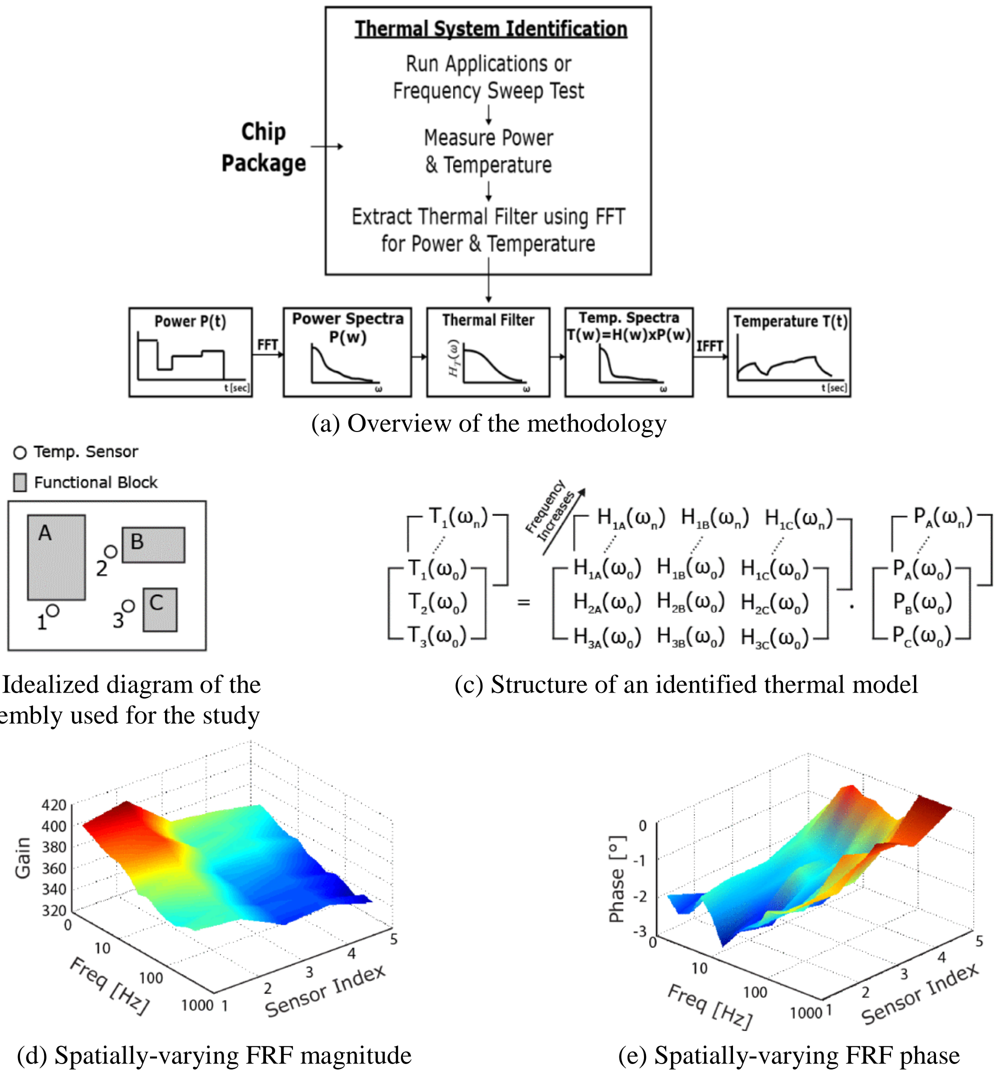

(a) Overview of the methodology

(b) Idealized diagram of the assembly used for the study

(c) Structure of an identified thermal model

(d) Spatially-varying FRF magnitude

(e) Spatially-varying FRF phase

Fig. 1.3-14. System identification methodology and results when applied to very large scale integration (VLSI) semiconductor chips [116]–[119]

Due to the relatively large size of the evaluated thermal assembly and the limited bandwidth of thermocouple temperature detectors, the study only evaluated relatively slow heat transfer dynamics. The study also did not evaluate methods on a power converter having semiconductor devices or mention how the methods would be extended to assembled power

semiconductor converter systems. Also, calibration of thermocouples was not discussed, linearity of resulting models was not assessed, and signal-to-noise ratio limitations were not mentioned. Results were not compared to analytical or numerical thermal models, and, overall, the study lacks heat transfer analysis. Finally, frequency response function (FRF) curves were simply overlaid on 2D plots, as shown in Fig. 1.3-13, which hides influences of the assembly's spatial domain on response dynamics.

A set of studies from the very large scale integration (VLSI) field, specifically 130-nm complementary metal oxide semiconductor (CMOS) technology, builds upon the previous study by explicitly providing spatially-dependent thermal response magnitude and phase response information on multi-dimensional FRF plots [116]–[119]. Key figures of these studies are shown in Fig. 1.3-14.

Fig. 1.3-14(a) diagrams the methodology, like that shown in Fig. 1.3-12, which aims to extract models referred to as thermal filters. The (b) figure shows the MIMO structure of assemblies considered by this study, where the functional blocks are configurable sources of heat. The (c) figure illustrates the structure of resulting thermal models, which resemble a state-space dynamic model. Finally, the (d) and (e) figures plot thermal FRF magnitude and phase which vary with spatial location of sensors on substrate prototypes. The paper describes an interpolation method used to form 3D surfaces from multiple 2D data sets of FRF magnitude and phase response information.

The idea of forming and interpreting spatially-varying thermal FRF plots for use in prognostics and assembly, controls, and observer design has not been documented in the power electronics field, which has different practical issues in VLSI. The presented study from VLSI also

utilizes custom-built hardware for the system identification and does not provide methods for usage with off-the-shelf hardware. Finally, the study does not provide FFT settings, and assumes, without evaluation, that the system in question is ideally linear.

An additional study related to low power integrated circuit (IC) technology is finally highlighted in this subsection [120]. The study uses FE modeling and frequency domain expressions to evaluate how details of custom IC chip assemblies including dimensions, influence thermal response, and claims to provide method to create ROMs. This study reveals the still pervasive practice of discarding or disregarding phase response information from FRF analysis.

1.3.6 Conclusions on thermal modeling in power electronics

As illustrated in this state-of-the-art review, thermal modeling approaches can generally be divided into five categories. Because the fundamental objective of each approach is to approximate the behavior of a domain insufficiently modeled by ODEs, and necessarily modeled by PDEs, the methods are related and can provide similar outputs.

Most power semiconductor assembly data sheets include a single, supposedly representative TTI for limited segments of the spatial domain. TTI curves are thus readily available usable for extraction of model topologies and parameters, especially Cauer and Foster TECs. Experimental TTI step response methods, however, are practically limited by the lack of evaluation of the actual rise time of a step input, and intrinsically limited by the lack of flexibility to assess a model's linearity.

Cauer and Foster TECs are highly intuitive ways to document an assembly's dynamic thermal response and interface well with governing equations and thermal parameter approximations from ODE heat transfer. Unfortunately, methods to populate and objectively

evaluate TEC models are not systematic, and, if they use TTI step response curves, are subject to the same limitations of TTI analysis.

2D and 3D TEC models replicate how formal numerical modeling techniques, such as FD and FE methods, discretize a PDE-governed continuum and allow for its simulation with sets of spatially refined, coupled, ODE equations. Approaches beginning with formal employment of FD and FE methods are therefore much more systematic. Recently, structured model reduction techniques have been interfaced with high fidelity FDMs and FEMs in order to reduce their state count in a way that captures the dominant energy transfer terms of these models. This promising is still often executed without correlation to experiments.

More recent approaches in thermal modeling have leveraged frequency domain techniques to propose experimental approaches to estimate an assembly's dynamic thermal response. These methods show potential to focus their scope on different specification locations within assemblies or evaluate how spatial temperature differences evolve in time. The opportunity exists to evaluate methods in switching power electronic converters.

1.4 State Observers

1.4.1 Conceptual background

Observers can be described as mathematical systems which model the physical behavior and response of a real-world system. They were first documented for use in estimating physical states for control systems in the mid-1960s [121], and they have been investigated both in theory and with respect to applications since then.

(a) Conceptual model of a free system, having no inputs, driving another system

(b) First-order system observer including a free system

Fig. 1.4-1. Fundamental block diagrams illustrating observer systems [121], [122]

Fig. 1.4-1 illustrates concepts of observer systems that were used as the foundation for building initial observer theory [121], [122]. Eventually, the author extends the theory to form what is referred to as Luenberger-style observers. Luenberger-style observers are considered as systems which take measurements of system inputs and "outer" state variables to estimate "inner" state variables, when considering the sequence of energy flow within a system [123]. Fig. 1.4-2 provides an illustration of a resulting closed-loop observer system, which embeds an open-loop model of the physical process of interest.

Fig. 1.4-2. State-space model of a physical system, and open- and closed-loop observer systems [124]

Fig. 1.4-3. Observer-based control [125]

On the other hand, Gopinath-style observers use system inputs and measured inner state variables to measure outer state variables [123], [125]. Fig. 1.4-3 illustrates a cascade of a system controller and observer formed under a Gopinath observer design paradigm. A key result regarding observer concepts is that Gopinath-style observers inherently have parameter sensitivities that Luenberger-style observers do not. This is because Gopinath-style observers require open-loop, dynamic models of behavior between the measured inner system state and the final, outer system state. Luenberger-style observers are considered more desirable because of their decreased parameter sensitivity, but, as the next subsection will show, might be unavailable due to varying access of state measurements.

Luenberger-style and Gopinath-style observers have different estimation accuracy (EA) properties, which are clearly illustrated with EA frequency response function (FRF) plots. Regardless of type, observers require open-loop models of the physical process of interest, and design of a "feedforward" signal, which estimates the excitation given to the physical system. Proper closed-loop observers should exhibit certain properties [123], [124]:

- Nearly zero phase lag of the estimated state of interest, even beyond the bandwidth of the observer controller
- Finite amplitude distortion of the estimated state of interest
- Capability to estimate system disturbances, that are not included in the open-loop system model, limited by the bandwidth of the observer controller

A closed-loop observer effectively functions as a disturbance state filter and sensor replacement technology, mitigating the need to purchase disturbance sensors for applications.

Besides potential zero-lag filtering properties, disturbance estimation is one of the most desirable properties of observer systems.

Observers can be formed using both state-space and state block diagram (SBD) notations. Similar to the general observer design approach documented in [123], [124], Luenberger-style observers formed using methods from traditional linear system theory utilize full-order or reduced-order plant models, and include observer controllers which must be designed. However, the controller design methods differ. Traditional linear system theory provides methods to design a gain matrix to effectively control each state of the plant [126]. The more applied methods for observer design, documented largely by WEMPEC, as shown in the next subsection, designs controllers for the state variables which are measured.

1.4.2 Non-electrothermal observer applications

During the past 50+ years, observer systems have been applied in multiple physical domains. The following mostly chronological list summarizes these applications, which mostly are documented in studies by WEMPEC at University of Wisconsin-Madison:

- Estimation of magnetic states, e.g. flux linkages [127]
- Estimation of electric machine motion states, e.g. position and velocity [128]–[131]
- Estimation of power electronic circuit voltages, currents, and parameters [132]–[134]
- Estimation of mechanical states, such as internal combustion engine torques [135]
- Estimation of mechanical properties, such as rolled paper modulus of elasticity [136]
- Estimation of mechanical defects, such as kinematic error [137]–[140]
- Estimation of temperatures, such as that within frozen fish [141]

The goal of this subsection is to introduce, and review, select observer systems which have features potentially able to track time-varying parameters of a process, like degradation.

Fig. 1.4-4 shows a mechanical domain observer building upon the Luenberger-style motion-type observer. The observer in Fig. 1.4-4 models paper forces and velocities and motor drive motion states within a pressing system. The observer system adaptively manipulates a parameter of the observer itself, the sheet (web) stiffness, K_{sh}, which has mechanical stiffness units of N/m. As shown in the "Adaptive Tension Observer Controller," the system correlates sheet velocity errors to its stiffness in the pressing process, and, following an integration process and multiplication by learning rate (i.e. gain or step size), updates the K_{sh} parameter within the observer. A static model relating stiffness to length, area, and Young's modulus of elasticity is finally used to relate the real-time estimate of K_{sh} to elasticity, a parameter which is valuable for managing paper pressing process machinery.

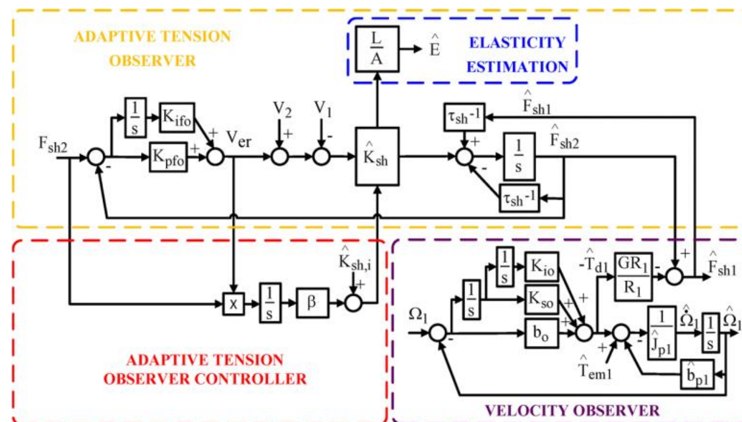

Fig. 1.4-4. Cascaded observer structure including adaptive, real-time estimation of the Young's Modulus mechanical parameter [136]

The study [136] provides many physical models of the mechanical domain processes relevant to the paper pressing machinery, and ultimately synthesizes the documented models into a solution appropriately adapting observer parameters given additional observer-based state

information. The proposal to adapt models or parameters using observer-based disturbance information, is novel, and should be explored in the context of electrothermal observers.

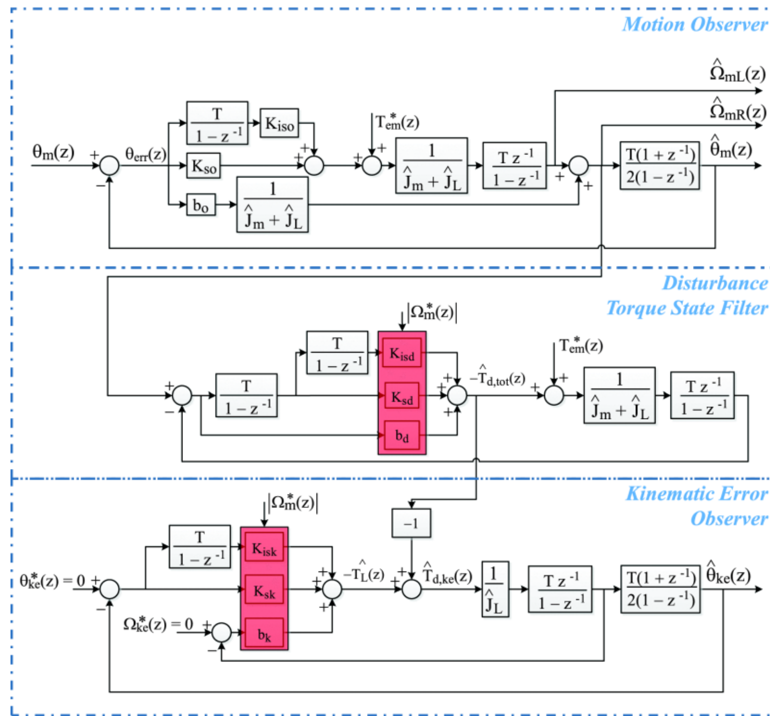

(a) Cascaded observer structure to estimate mechanism kinematic error which would induce disturbance torques [137], [138], [140]

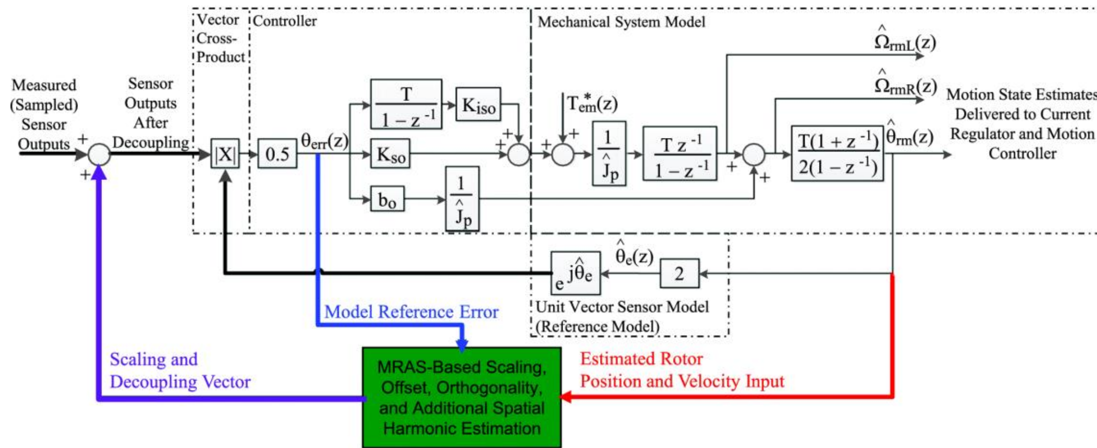

(b) Vector tracking motion observer and MRAS to estimate non-ideal properties of machine rotor position sensors [140]

Fig. 1.4-5. Elements of a system to improve the precision of motor drives to utilize them as embedded sensors within an application

Additional research efforts have worked to use information from observers, namely disturbance torque information, to adapt system parameters to improve the precision of a physical process and/or the motor drive itself. Fig. 1.4-5 illustrates pieces from such studies, which attempt to use the motor drive to extract kinematic error, defined as defects, faults, or deviations from nominal mechanism behavior. In this study, kinematic error estimation methods were evaluated using actuators with intentionally defective gears.

The (a) diagram illustrates a cascade of observers, including a motion ELSO, a disturbance torque state filter, and a kinematic error observer to isolate the contribution of mechanism kinematic error to the bulk disturbance torque estimate. The (b) plot shows a vector tracking motion observer, which embeds a MRAS to identify and decouple non-ideal properties position sensor properties. The compound observer and MRAS system works to correlate position errors to functions which predict spatial harmonic errors induced by position sensors.

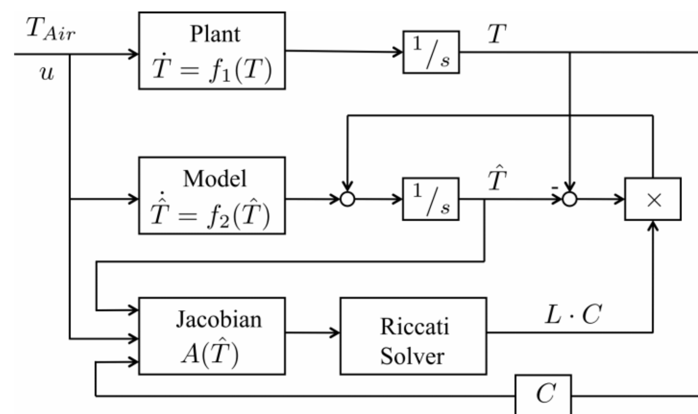

Fig. 1.4-6. Closed-loop observer to estimate spatial temperature distributions of frozen fish [141]

Ultimately, the proposed cascaded system attempts to optimize the accuracy of a motor drive's position estimate. Similar observer structurers were also shown able to detect local defects present on single gear teeth within the geared actuator system. The system leverages observer

technology and models of detailed pieces of the physical system, e.g. the mechanism assembly and position sensor interface, to illustrate how motor drives can serve as embedded application sensors.

The final observer system reviewed that is not related to power semiconductor reliability issues is represented in Fig. 1.4-6. This observer is formed to predict temperature distributions within fish contained in a freezer for storage. The observer embeds a state-space thermal system model and has a gain matrix computed using a Jacobian operation and Riccati solver. The design is claimed to follow an extended Kalman filter ideology and is claimed to be robust to parameter variations and noise, but experimental results directly supporting the claims are not provided.

1.4.3 Electro-thermal domain observers in power electronics

The previous subsection reviewed a broad range of observers from the state-of-the-art and identified their application, and some of their distinguishing features. This subsection will review state-of-the-art electrothermal domain observer systems ultimately designed to support the thermal-mechanical reliability problem in power electronics, which is the focus of this research.

Forming open-loop electrothermal domain observers is a relatively common practice in power electronics. Referring to Fig. 1.4-2, an open-loop observer is a model that attempts to replicate behavior of a physical process. The open-loop observer does not close any control loops on physical system feedback signals; hence, it is open-loop. Open-loop observers are inherently parameter sensitive.

Fig. 1.4-7 illustrates the pieces of an archetypal open-loop electrothermal observer system aiming to estimate temperatures of IGBT and diode devices within a power semiconductor assembly. First, as the (a) figure shows, losses are modeled, in this case, using quasi-analytical expressions. The loss model relates electrical circuit operation to the loss (heat) thermal system

excitation; hence it encompasses electrothermal domain physics. The (b) figure shows the recipient of the loss calculations, a Foster TEC, the second-piece of the open-loop observer's plant model. The open-loop observer in Fig. 1.4-7 represents an observer design that is pervasive in power electronics.

$$P_{T(i)} = P_{con,T(i)} + P_{Switch,T(i)}$$

$$P_{D(i)} = P_{con,D(i)} + P_{Switch,D(i)}$$

$$P_{con,T(i)} = (I_{T(i)} * V_{ce0} + I_{T(i)}^2 * R_s) * a_{T(i)}$$

$$P_{switch,T(i)} = \frac{(E_{on} + E_{off}) * F_{switch} * I_{T(i)} * V_{dc}}{I_{Nom} * V_{Nom}}$$

$$P_{Con,D(i)} = (I_{D(i)} * V_{F0} + I_{D(i)}^2 * R_f) * a_{D(i)}$$

$$P_{switch,D(i)} = \frac{E_{rec} * F_{switch} * \sqrt{I_{D(i)}} * V_{dc}}{\sqrt{I_{Nom}} * V_{Nom}}$$

(a) IGBT and diode conduction and switching loss equations

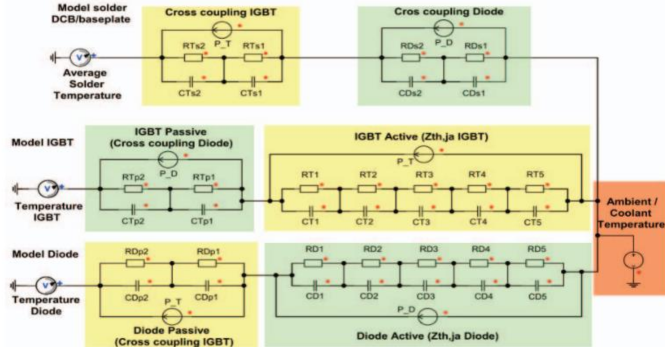

(b) Foster thermal equivalent circuit models

Fig. 1.4-7. Open-loop electrothermal observer system [142]

The research literature has many examples of open-loop observers (or estimators) being used for active thermal-mechanical control. Fig. 1.4-8 documents one instance, where the junction temperature estimator is formed using semiconductor device loss models and Foster TECs.

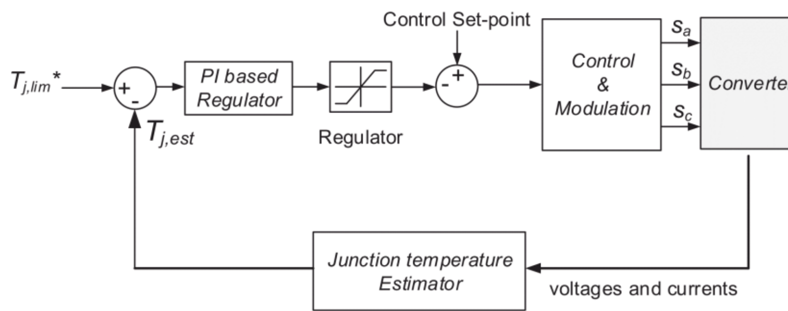

Fig. 1.4-8. Active junction temperature controller using feedback from a Foster model-based open-loop observer [143]

In general, thermal plant models are most commonly formed using already discussed TTI step response curve analysis or ad hoc TEC design. Papers using open-loop observers typically

provide only a few limited series of time domain data in attempts to justify their accuracies. They do not provide its evaluation using comprehensive metrics such as the estimation accuracy FRF.

Relatively few examples of closed-loop electrothermal domain observers are documented in the literature. Three of them will now be reviewed. First, Fig. 1.4-9 shows a traditional linear system theory Luenberger-style observer. The closed-loop observer uses semiconductor device loss calculations and a three-layer Cauer TEC as the bases for the open-loop electrothermal plant model. It closes a control loop on a thermocouple-provided temperature signal.

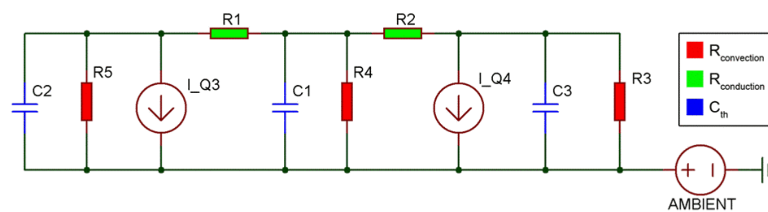

(a) Cauer thermal equivalent circuit model

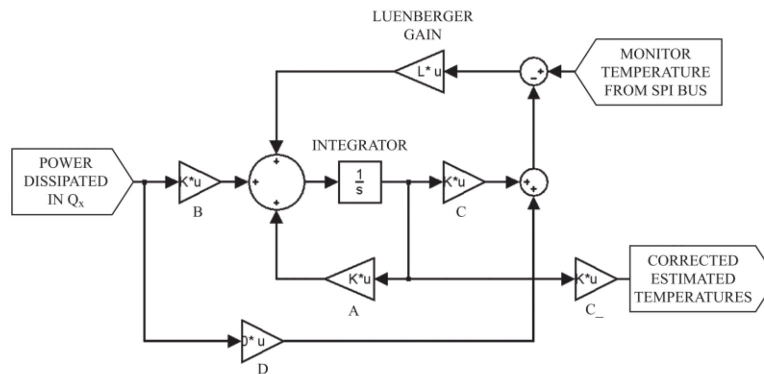

(b) State-space observer model

Fig. 1.4-9. Elements of a state-space, Luenberger-style observer to monitor spatial temperature distributions [144]

The state-space, Luenberger-style observer was evaluated using power step time-domain evaluations with load periods on the order of 10 minutes. Thus, the high-speed dynamic estimation capability of the system was not evaluated. Also, discussion about closed-loop observer controller tuning was not provided, and electrothermal disturbances were not considered during the observer

design. Finally, insightful discussion about the potential applications of the observer system were not provided.

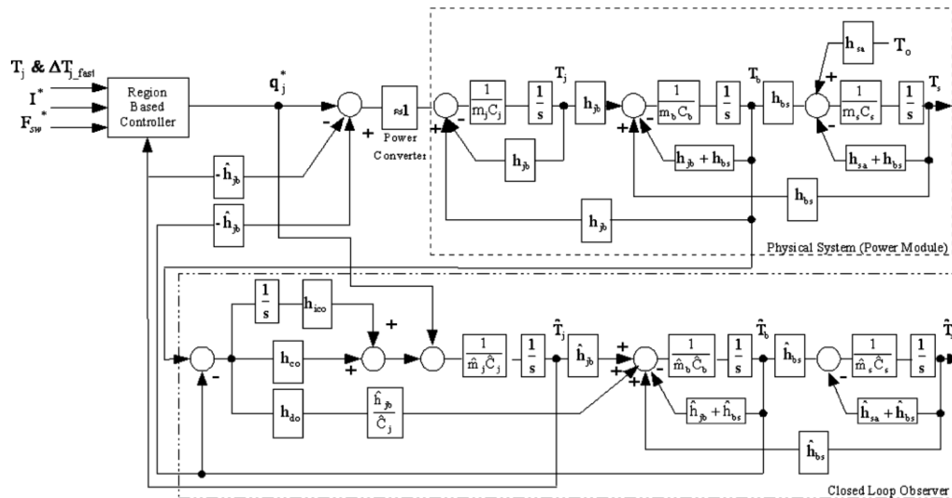

Fig. 1.4-10. Closed-loop, Gopinath-style junction temperature observer using measured baseplate temperature [145]

One of the seminal works regarding active thermal-mechanical control for power semiconductor assembly lifetime management [145] also proposed an Gopinath-style electrothermal domain observer, shown in Fig. 1.4-10. A three-layer Cauer TEC, expressed in SBD format, was the basis for the observer, and ideal loss estimation was assumed.

The physical system considered by the author had access to a single temperature measurement, at the baseplate of the IGBT assembly. The observer was thereby designed to estimate junction temperature, the state which was identified as most critical to the assembly's reliability but was not measured. Because junction temperature is an outer, boundary state estimated using the inner, baseplate temperature state measurement, and no junction temperature measurement, this observer is categorized as Gopinath-style. The junction temperature is effectively open-loop estimated using the segment of the thermal model between the junction and

baseplate. Thus, the observer has intrinsic parameter sensitivities to the parameters of the junction-to-baseplate thermal model segment.

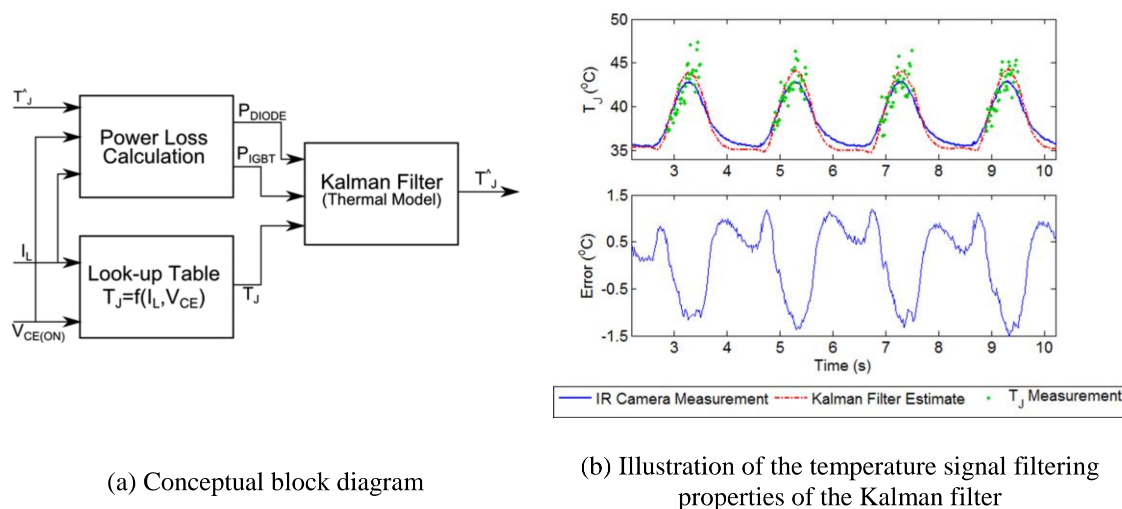

(a) Conceptual block diagram

(b) Illustration of the temperature signal filtering properties of the Kalman filter

Fig. 1.4-11. Elements of a Kalman filtering system to estimate junction temperature signals with maximal signal-to-noise ratio [61]

Unfortunately, the proposed observer in Fig. 1.4-10 was merely proposed in SBD format, without much discussion, at the end of a paper focused on a different dimension of the reliability problem [145]. However, additional studies do provide experimental evaluation of their state estimation methodologies. For instance, the study associated with Fig. 1.4-11 proposes and evaluates a Kalman filter algorithm to provide an estimate of junction temperature which has increased signal-to-noise (SNR) ratio compared with the raw estimate formed using $V_{ce(on)}$.

The (a) figure in Fig. 1.4-11 diagrams the state estimation algorithm, which includes an open-loop estimator of power losses, a look-up table to estimate junction temperature from TSEP signals, and the Kalman filter, which includes Foster TEC model information. This algorithm thus has similarities to closed-loop observer technologies in terms of the signals used and the signals provided. However, the two approaches are different. The Kalman filter approach uses a recursive

predict-correct step, is more statistics-based, and provides less physical insight due to the relatively complicated commissioning steps that must be taken during its design and implementation.

Regardless, the documentation of a Kalman filter as a state estimation technology provided by [61] is valuable and comprehensive, especially because it hints how the system might be used to detect and diagnose assembly degradation. More immediately, Fig. 1.4-11(b) illustrates that the system has at least some capability to filter relatively noisy TSEP measurements during real-time converter operation. The opportunity exists to implement active thermal control using a junction temperature signal from such a system.

The highest quality state-of-the-art investigation of electrothermal domain observers is represented by [146]. The observer design procedure of this publication utilized the state-of-the-art thermal modeling technique of deriving and systematically reducing a high fidelity finite difference model. No other investigation of closed-loop electrothermal domain observers embedding this type of model was found in the literature, so this publication is immediately distinguished in this regard. Furthermore, the embedded thermal ROM was comprehensively derived for an entire IGBT semiconductor assembly.

Fig. 1.4-12 displays the cascaded observer system in relation to an electrothermal-mechanical power converter model. The first Luenberger-style observer attempts to estimate instantaneous spatial temperatures within the IGBT assembly, especially that near the silicon die or junction. The second, cascaded observer attempts to estimate average temperature quantities. The proposed system leverages the customizable tuning capability of closed-loop observers to yield temperature estimates having different properties.

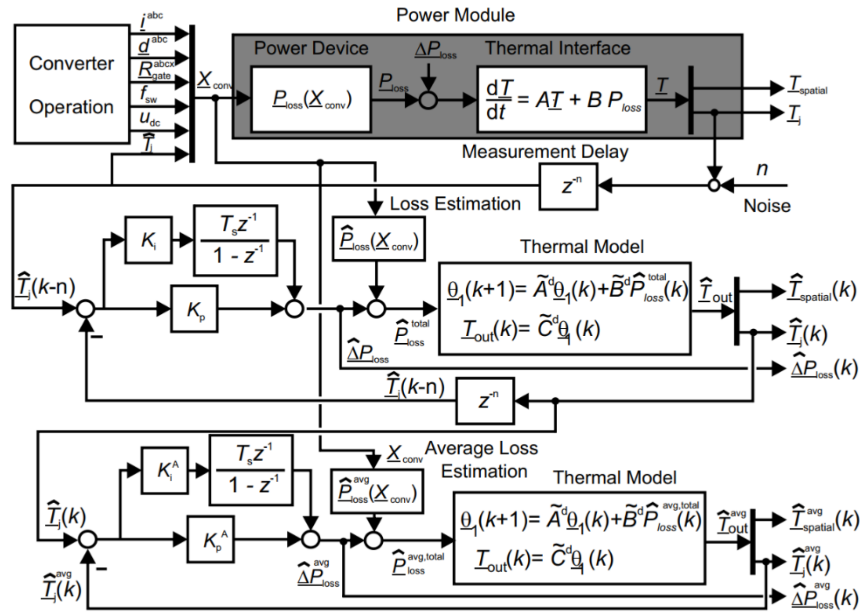

Fig. 1.4-12. Electrothermal observer system including open-loop models obtained using FD modeling and then model-order reduction [146]

The observer systems are shown to estimate loss “disturbances,” the terms following the summing junctions of the observers’ PI controllers. However, these losses are not physically interpreted in terms of their potential sources, e.g. cooling performance decreases, or assembly fatigue. The study represents the state-of-the-art of closed-loop electrothermal observer technology.

1.4.4 Distributed parameter system (DPS)

3D heat transfer modeling results in components and assemblies being most accurately treated as distributed parameter systems (DPSs). DPS systems generally are governed by PDEs, and DPS models theoretically require an infinite number of state variables to represent the dynamics of the computational domain. There is strong synergy between the DPS paradigm and techniques for discrete spatial modeling, e.g. numerical and Fourier series modeling.

The construction of observers in the control systems field predominantly utilizes ODE plant models within observer systems, as shown in the examples from the previous subsection. A recent study [146] is an exception to this trend. The treatment of DPSs as a formal research topic exists in the systems sciences field, and is covered broadly by [147]–[153] in the context of observer design.

This subsection will provide a very brief overview of DPS observer design. First, Fig. 1.4-13 provides a categorization of the types of observers aimed to model DPSs. In this chart, Luenberger-style observers, the most common topology in power electronics, were generalized as a type of finite dimensional observer.

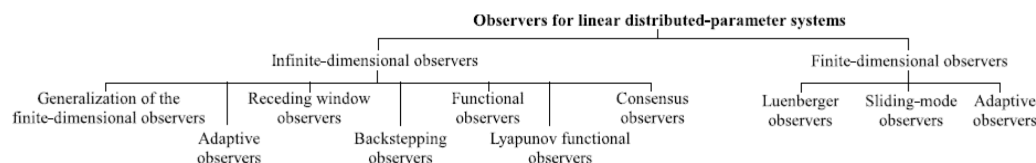

Fig. 1.4-13. Categorization of observers for DPSs [154]

Next, Fig. 1.4-14 documents pieces of an observer design for a power semiconductor manufacturing process, sketched in the (a) figure. The observer design begins with governing heat transfer PDEs under a DPS observer design ideology. The (b) figure diagrams the observer design and evaluation methodology, and the (c) figure shows details of the resulting “neural observer,” which embeds neural network approximation of heat transfer dynamics.

Finally, the mathematically-intense study represented by Fig. 1.4-15 addresses the issue of sensing discrete-spatial states within systems governed by PDEs. The study considers sensing schemes referred to as “pointwise” and “piecewise uniform.” The opportunity to explore potential synergies between [155] and [137]–[140], which also investigate discrete-spatial domain sampling issues, exists.

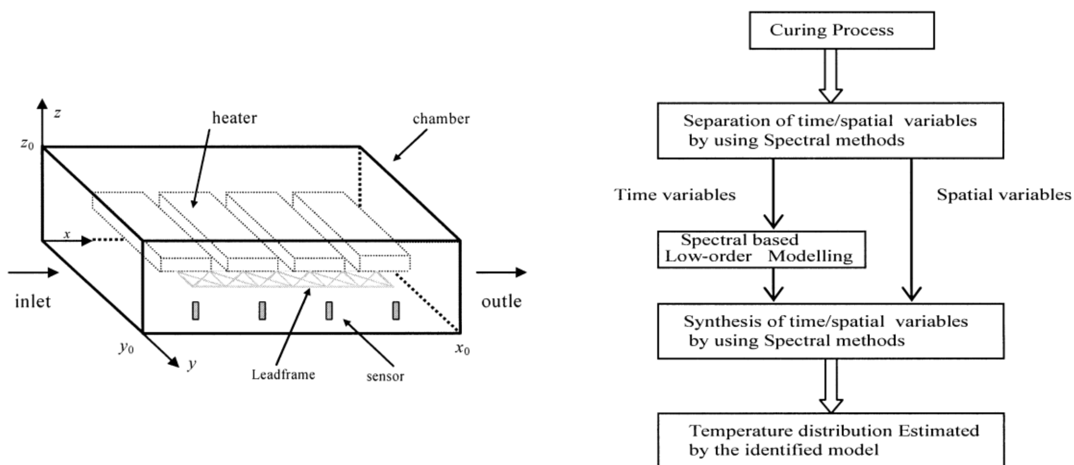

(a) Illustration of the manufacturing process (b) Thermal model and model evaluation processes

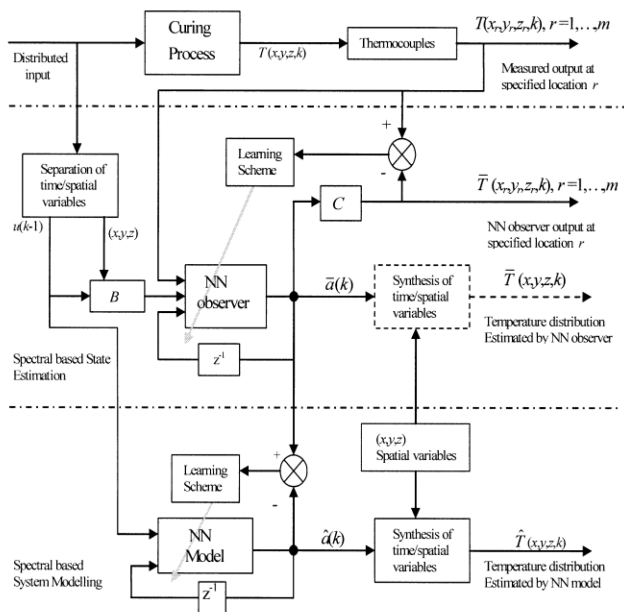

Observer system having neural networks and time/spatial variable separations

Fig. 1.4-14. Elements of a thermal observer model obtained by formally treating the open-loop system as a DPS [156]

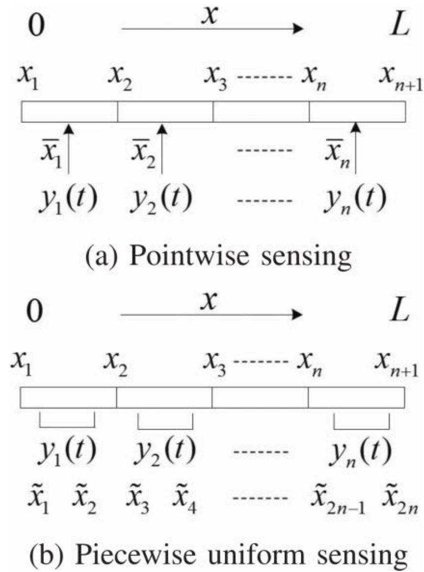

Fig. 1.4-15. Illustration of strategies to sense discrete spatial states within a DPS [155]

1.4.5 Summary of electrothermal observer research opportunities

The state-of-the-art review has identified the following topics as research focus areas relating to the electrothermal observer technology.

1.4.5.1 Topology study and system synthesis

Properties of observers applied to electrical, electromagnetic, and mechanical (motion) domains have been well documented in the power electronics literature. This literature review identified and examined relevant studies of observers modeling electrothermal and thermal domain physics. In general, the electrothermal and thermal domain observer studies are limited and do not document the basic benefits these systems are anticipated to have, and opportunities for innovation. The following subsections will identify limitations in the prior art more specifically, in terms of research opportunities.

Closed-loop observers can be broadly categorized into categories, e.g. Luenberger-style, Gopinath-style, enhanced-Luenberger-style, and enhanced-Gopinath-style. The research literature shows that these observers have different properties in terms of dynamic estimation accuracy, parameter sensitivity, etc. when deployed in electrical, electromagnetic, and motion domains. A topological survey of practical observer options and their tradeoffs has not been documented for electrothermal domain systems.

Prior art documents desirable properties of compound, cascaded observer structures in non-thermal domain applications. One recent study proposed a cascaded thermal domain observer structure. No other studies investigating cascaded thermal domain observer structures have been found in the state-of-the-art.

Observers more complex than standard linear systems can be formed. For example, observers can adaptively update parameters, or have other nonlinear features, such as saturation in the open-loop system model. The state-of-the-art review has documented nonlinear observers designed for non-thermal domain applications. The opportunity exists to investigate electrothermal observers with adaptation mechanisms and nonlinear features.

Finally, most observers documented in the literature have single-domain implementations, e.g. estimate variables confined to electrical, electromagnetic, or the motion domain but no other domain. Hybrid, multi-domain observer concepts have not been documented in the literature. A specific opportunity involves forming an observer normally confined to the electrical domain, e.g. a current observer, and including or estimating parameters sensitive to temperature within the observer system. Thus, a thermally-coupled current observer could be formed. The broad research aspiration is to link the very active TSEP research field with observer technology.

1.4.5.2 Signals and signal processing

Observers can be considered a state estimation and sensor replacement technology. The literature contains examples of how observers can be used to estimate states that are typically difficult to transduce, such as the velocity and acceleration physical motion derivative states. The opportunity exists to evaluate the capability of electrothermal domain observers to estimate temperature derivative and heat (loss) states. Furthermore, the opportunity exists to demonstrate expected impacts of closed-loop observer controller tuning on the intrinsic, nearly-zero-lag noise filtering properties of certain observer types. Systematic tuning methodologies should also be documented.

1.4.5.3 Application-level benefits

The prior three subsections presented opportunities related to the detailed electrothermal observer design and evaluation tasks. Even upon satisfactory address of these items, the highest priority opportunity is connecting technical details to system-level benefits, system value additions, and the overall reliability problem, in clear ways.

The power electronics industry needs reliable methods to identify anomalies (disturbances) related to a component or assembly's fatigue status in real-time. Some methods to detect shifts in degradation have been proposed, but most of them are based on steady-state operating points. The opportunity exists to evaluate the capability of observer technology to detect fatigue- and cooling system-related disturbances. Further, upon the treatment of conduction and switching losses themselves as disturbance elements, and clever design of experiment, observer technology is expected to provide loss characterization techniques to complement costly double-pulse testing methods.

This review concludes that dynamic thermal modeling intrinsically includes both temporal and spatial aspects of computational domains. Open-loop dynamic thermal models, if defined in a way that preserves insight into the physical spatial domain, provide temperature field or gradient information, i.e. dynamic spatial temperature response. These gradients, currently not addressed explicitly by state-of-the-art life plots and thermal control algorithms, can be monitored for real-time lifetime prognosis, or potentially used as control state variables.

1.5 Summary of Identified Research Opportunities

The following research opportunities have been identified in the state-of-the-art review.

- **Identification of limits in how different electrothermal models encode spatiotemporal response; unify best attributes in a general, low-order model**

Efforts to predict electrothermal response typically utilize a single modality, such as a TEC or numerical discretization, as a cookbook solution. Comparative evaluations of fundamentally different model expressions have not been documented. Further, prominent properties of PDE heat transfer models have not been identified and joined with those of lumped, ODE models to create a general, low-order spatiotemporal model more consistent with physics and better suited for correlation with FRFs measured in situ.

- **Development of an experimental method for coherent, in situ measurement of converter spatiotemporal dynamic electrothermal response using FRF metrics**

Methods to form parameterized, compact, real-time thermal models are broad and include step response analysis, coarse TEC population, and numerical techniques with model order reduction. However, no experimental, in situ system identification methodology to extract ground truth frequency domain data from converters has been documented. The opportunity to develop a

method for extracting coherent FRF electrothermal impedance data for multiple segments within a complete spatial domain exists.

- **Application of an experimental, in situ electrothermal response measurement method and interpretation of resulting FRFs using a general, low-order model**

Experimental FRF methods to evaluate a converter's spatiotemporal dynamic electrothermal response have not been documented. Applying such a method and documenting measured FRFs is a research opportunity. Interpreting measured FRFs in terms of a parametric, physics-based, low-order spatiotemporal model is also an opportunity.

- **Identification of relationships between modeled and measured electrothermal response and thermal-mechanical degradations with suitable FRF metrics**

TTI metrics have been used to evaluate the electrothermal response of degraded power semiconductor assemblies. However, shifts in electrothermal impedance FRF properties due to fatigue processes, such as solder layer and thermal interface material voiding, and due to cooling system changes, have not been documented. Predicting degradation-induced FRF property shifts using analytical and numerical models is an opportunity. Measuring the FRF properties on physical specimens is another opportunity.

- **Development of methods to exploit identified degradation-induced electrothermal response shifts for in situ monitoring of its inception, location, and extent**

Techniques exist to interpret shifts in steady-state converter electrothermal response properties, e.g. thermal resistance, in terms of degradation. Documented techniques, however, are not continuous, real-time solutions, and do not directly exploit shifts in FRF properties, and associated thermal parameters, to quantify degradation. Developing techniques to utilize spatiotemporal dynamic properties for localization of bulk degradation, and correspondingly diagnose severity, is also an opportunity.

- **Development of methods to decompose disturbance estimates from closed-loop electrical and electrothermal observers into separate physical root causes**

Closed-loop, Luenberger-style electrical current and electrothermal observers estimate open-loop model inaccuracies as disturbances. Real-time methods to isolate temperature state information from a current observer's bulk disturbance estimate have not been documented, as well as methods to isolate thermal-mechanical degradation state information from an electrothermal observer's bulk disturbance estimate. Capabilities achievable by cascading these observer systems have not been documented.

- **Development of design-for-sensing methods for optimally specifying assembly geometry and temperature detector requirements**

Utilization of spatiotemporal electrothermal FRF metrics for specifying power semiconductor converter system designs has not been documented. Further, methods to enhance degradation monitoring system performance by using an FRF-based design degree-of-freedom (geometry and temperature detector location and quality) optimization procedure have not been investigated. Design methods for shaping electrothermal FRF properties considering active thermal-mechanical control systems is also an opportunity.

Chapter 2 Frequency Domain Heat Transfer Modeling

This chapter investigates state-of-the-art methods for modeling heat transfer and examines how they capture temporal and spatial domain dynamics. Analytical and numerical approaches are utilized. Ultimately, the work in this chapter is aimed toward:

- developing models able to accurately represent multi-scale dynamic electrothermal response properties characteristic to power semiconductor equipment;
- defining new metrics to characterize measure the electrothermal response;
- explicitly displaying spatial domain effects, which are often expressed implicitly;
- identifying asymptotic behavior implicitly enforced by numerical models;
- define compact models, for fitting experimental data, with improved physical basis;
- methodically resolving tradeoffs between model accuracy and compactness;
- and using metrics to guide assembly geometric dimensioning and tolerancing.

Elements of this chapter are also documented in publications [157]–[160].

2.1 Operational Definitions

2.1.1 Mechanical characteristics of power semiconductor sub-assemblies

As described in the state-of-the-art review, power semiconductor materials are embedded within small chips, also known as dies, whose dimensions are generally on the order of 10-100 μm. The semiconductor dies are integrated by large-scale manufacturers (e.g. *Fuji*, *Infineon*,

Semikron, *STMicroelectronics*) or in small-scale laboratories. Once assembled, power semiconductor sub-assemblies have the following characteristics:

1. High local heat fluxes; generation of significant amounts of heat within very small volumes (the dies)
2. Non-monolithic; the assembly interfaces components made of various materials
3. Rectilinear geometric features, e.g. square dies are typically embedded in a rectangular module
4. Relatively small features, e.g. wire bond or ribbon cable interconnects, that may or may not be negligible to temporal heat transfer dynamics
5. Large features, e.g. cold plates, especially compared to the dies and interconnects
6. Exposure to convective boundaries

Eventually, the heat transfer modeling methods documented in this chapter should collectively provide physics-based insight on how each of these characteristics influences the spatiotemporal dynamic thermal response.

2.1.2 Spatiotemporal electrothermal response metrics

Fig. 2.1-1(a) displays a volume whose dynamic thermal behavior can be analyzed. For instance, there may be three critical nodes with temperatures that must be monitored, and there may be dissipation or generation of thermal energy, like shown at the first node in the diagram. Fig. 2.1-1(b) displays the same volume but inhabited by an illustration of a power semiconductor sub-assembly. The point *1* is thus the die of the sub-assembly, a general name for the location where losses are generated. Point *2* can represent a distal temperature detector, like a thermistor, and point *3* is the assumed infinitely stiff ambient.

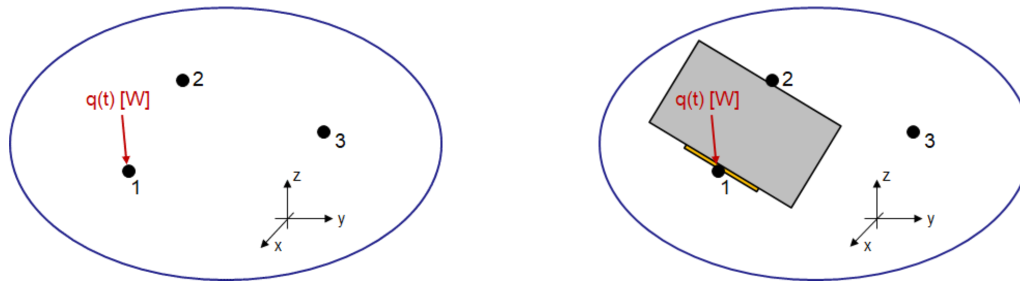

(a) Abstraction showing three temperature nodes in space, one of which has heat input

(b) Population of the abstraction with an illustration of a power semiconductor converter system

Fig. 2.1-1. Graphical illustrations of a computational domain for heat transfer analysis

Like voltage quantities, temperature quantities are only defined relatively, with respect to references; every derived or measured thermal response, even if ambient-referred, is inherently spatial. Using information from two discrete temperature detectors, this research program will extract and analyze both ambient-referred and relative spatial FRF properties, using a hardware setup like shown in Fig. 2.1-2. As a result, a notation defining a relative spatial electrothermal FRF between detectors *1* and *2* (e.g. die and thermistor) under a single Q(s*)* loss excitation, originating at the die, is defined in (2.1-1).

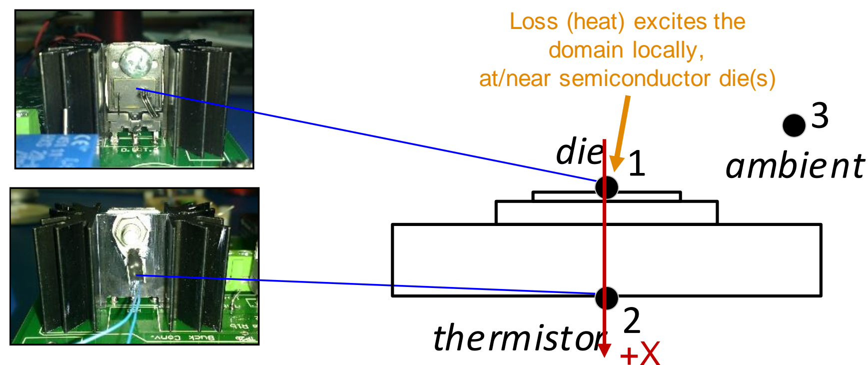

Fig. 2.1-2. Relationship of a physical MOSFET-sink sub-assembly with an illustrative model explicitly displaying a spatial coordinate

This chapter will develop spatially-varying electrothermal impedance (SETI) FRFs following the definition provided by (2.1-1). SETI FRFs are, by definition, presented in a general

format, in which spatial coordinate information, typically implicitly included in state-of-the-art models, is retained and displayed explicitly.

$$\frac{T_1(s) - T_2(s)}{Q(s)} = \frac{\Delta T_{12}^{S}(s)}{Q(s)} \tag{2.1-1}$$

The SETI FRF is defined as the dynamic impedance quantifying how a line of temperature nodes responds to a single heat input. For example, in Fig. 2.1-2 there is a single, local generation of heat via semiconductor device conduction and switching losses. Upon the dynamic generation of losses, the temperature of the assembly will vary as a function of space and time. To explicitly include spatial domain effects, line connecting points *1* and *2* can be defined, and the thermal response of all points along this line can be quantified with the SETI FRF metric.

Examples of SETI FRF magnitude and phase plots are shown in Fig. 2.1-3. Following traditional Bode plot theory, the plots show traditional electrothermal impedance (ETI) as a function of frequency. However, SETI FRF plots show impedance of each spatial location along a line, e.g. a coordinate dimension with respect to a datum.

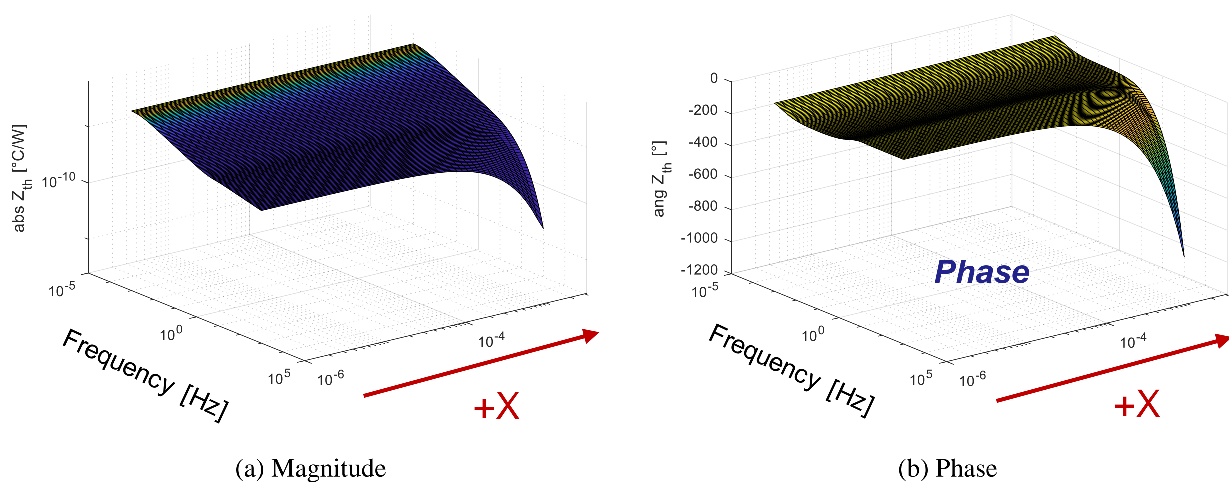

(a) Magnitude (b) Phase

Fig. 2.1-3. Example 3D SETIS plots showing electrothermal response as a function of input frequency and space

2.2 Identification of Method-Specific Limits

2.2.1 Analytical method

Connected systems of lumped capacitance ordinary differential equation (ODE) models (0D transient models) are frequently used in power electronics. However, response attributes can be more accurately modeled by partial differential equation (PDE) models, which generally include temperature response as a function of up to three coordinate dimensions. This subsection will investigate the utility of a spatiotemporal model.

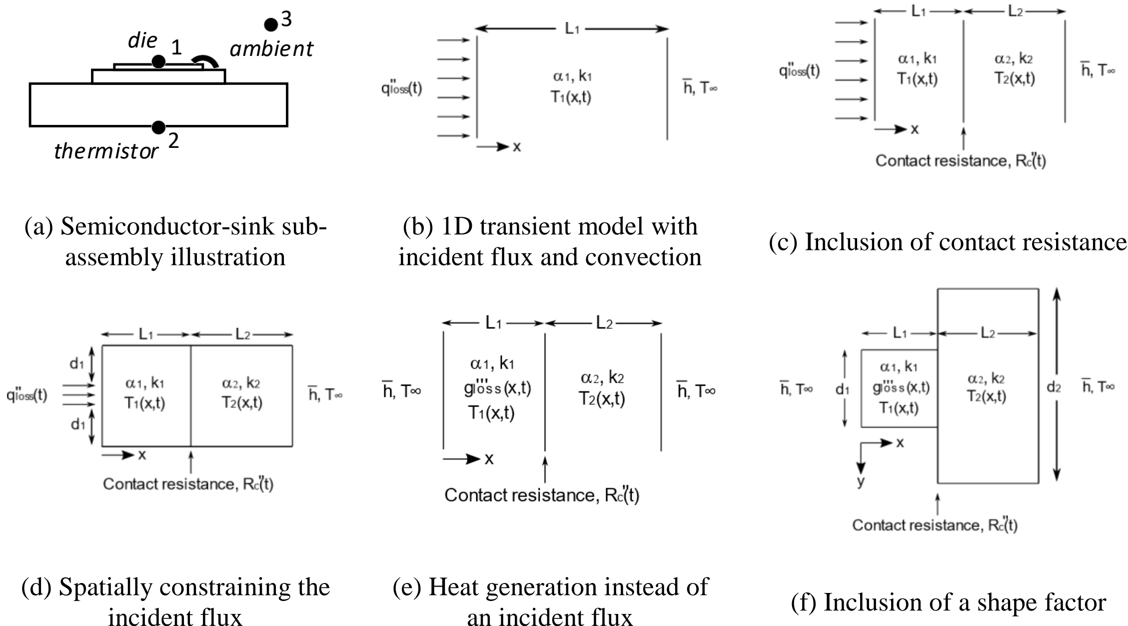

(a) Semiconductor-sink sub-assembly illustration

(b) 1D transient model with incident flux and convection

(c) Inclusion of contact resistance

(d) Spatially constraining the incident flux

(e) Heat generation instead of an incident flux

(f) Inclusion of a shape factor

Fig. 2.2-1. Graphical illustrations of candidate heat transfer problems for SETIS analysis

2.2.1.1 Identification of candidate analytical heat transfer models

Fig. 2.2-1(a) illustrates a power semiconductor sub-assembly. Next, Fig. 2.2-1(b-f) diagrams analytical models which attempt to capture some of the properties mentioned in section 2.1.1. The remainder of this subsection will focus on one of the diagrammed models.

2.2.1.2 1D, transient analytical model

Because of its simplicity, Fig. 2.2-1(b), redrawn in Fig. 2.2-2, is selected for further development. This 1D transient analytical model is described by (2.2-1), and is combined with the displayed boundary conditions (2.2-2) and (2.2-3) to represent the response of a power semiconductor converter with cooling on the bottom (x = L) side.

$$\frac{\partial^2 T(t)}{\partial x^2} = \frac{1}{\alpha}\frac{\partial T(t)}{\partial t} \tag{2.2-1}$$

$$-k\left.\frac{\partial T(s)}{\partial x}\right|_{x=0} = Q''_{loss}(s) \tag{2.2-2}$$

$$-k\left.\frac{\partial T(s)}{\partial x}\right|_{x=L} = h\left[\left.T(s)\right|_{x=L} - T_{\infty}\right] \tag{2.2-3}$$

As shown in Fig. 2.2-2, the top of the computational domain has an incident heat flux boundary condition, which represents the conduction and switching losses dissipated within power semiconductor dies. The bottom of the domain is exposed to a stationary ambient governed by a heat transfer coefficient, h.

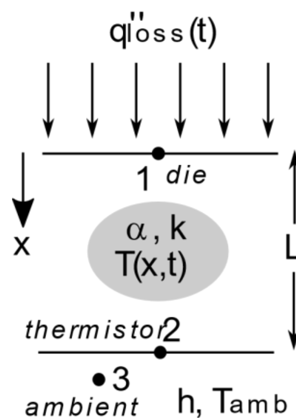

Fig. 2.2-2. Vertical illustration of Fig. 2.2-1(b)

2.2.1.3 Laplace transformation solutions

Convective distal boundary solution

The transfer function solution to the model of (2.2-1) and of Fig. 2.2-2 can be derived with Laplace transforms [84]. The exact solution was derived with assistance of the *Maple* software package and is given by (2.2-4) in which *h_bar* denotes the variable h. However, since the resulting expression is long, it is challenging to gain physical insight from its inspection. Therefore, an approximate solution, documented in the next subsection, was also derived.

$$\frac{T(s,x)}{Q''_{loss}(s)} = \Big(\Big(-\sinh\Big(\sqrt{\frac{s}{\alpha}}\,x\Big)\,\alpha\, h_bar\sqrt{\frac{s}{\alpha}} + \cosh\Big(\sqrt{\frac{s}{\alpha}}\,x\Big)\,k s\Big)\cosh\Big(\sqrt{\frac{s}{\alpha}}\,L\Big) + \sinh\Big(\sqrt{\frac{s}{\alpha}}\,L\Big)\Big(\cosh\Big(\sqrt{\frac{s}{\alpha}}\,x\Big)\,\alpha\, h_bar\sqrt{\frac{s}{\alpha}} - \sinh\Big(\sqrt{\frac{s}{\alpha}}\,x\Big)\,k s\Big)\Big) \Big/ \Big(k s\Big(\sqrt{\frac{s}{\alpha}}\,\sinh\Big(\sqrt{\frac{s}{\alpha}}\,L\Big)\,k + \cosh\Big(\sqrt{\frac{s}{\alpha}}\,L\Big)\,h_bar\Big)\Big) \tag{2.2-4}$$

Semi-infinite solution

A model more compact yet capturing similar physical properties can be derived by assuming the temperature at x = L never deviates from T_{amb}, implemented as boundary condition (2.2-5). The transfer function solution for this semi-infinite body problem is (2.2-6), which includes the term (2.2-7). Please note that the convective heat transfer coefficient, *h*, does not appear in (2.2-6) due to the elimination of the convective boundary.

$$-k\left.\frac{\partial T(s)}{\partial x}\right|_{x=L} = 0 \tag{2.2-5}$$

$$\frac{T(s,x)}{Q''_{loss}(s)} = \sqrt{\frac{\alpha}{k^2}}\,\frac{1}{\sqrt{s}}\;D(s,x) \tag{2.2-6}$$

$$D(s,x) = \exp\left(-\left(\frac{s \cdot x^2}{\alpha}\right)^{1/2}\right) = \exp\left(-\left(s \cdot \tau_{diff}(x)\right)^{\sigma}\right) \quad (2.2\text{-}7)$$

Thermal filtering is a term attributed to the tendency of solids to attenuate heat fluxes and temperature rise [161]. Examination of (2.2-6) reveals the exponential term, labeled D(s,x) in (2.2-7), that quantifies an aspect of this property.

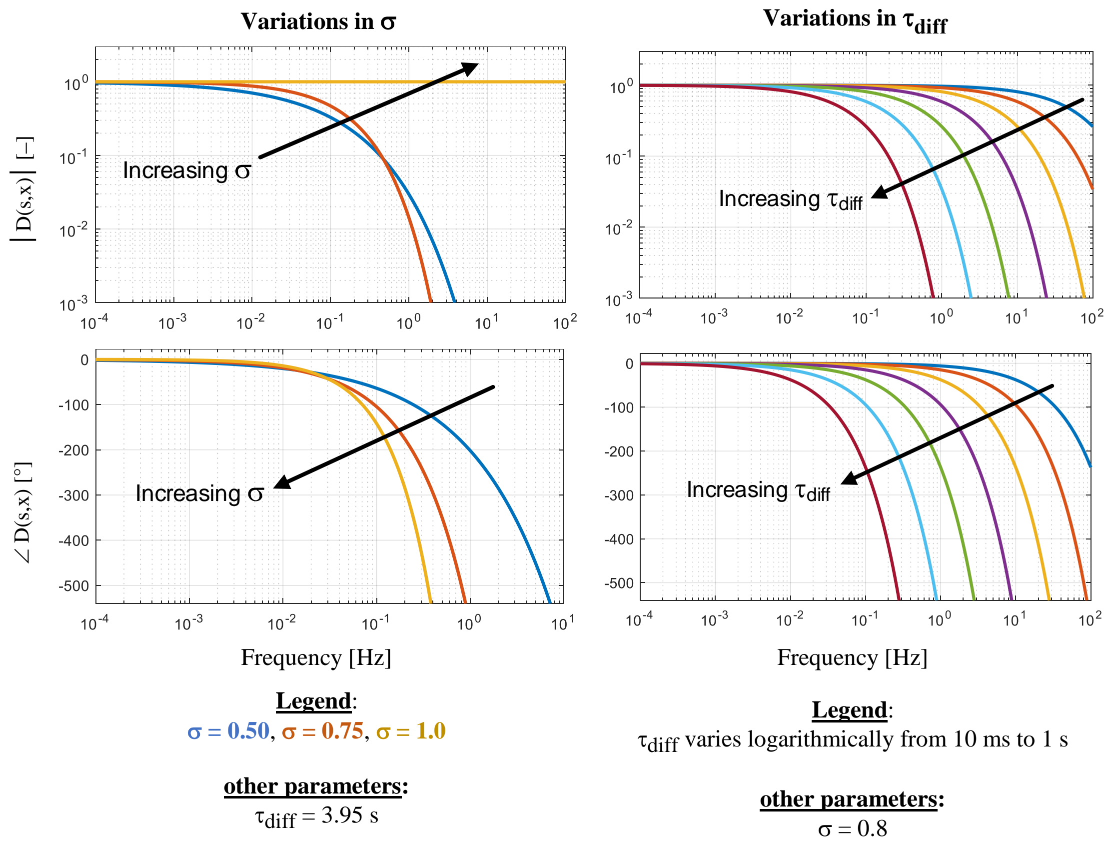

Fig. 2.2-3. Parametric FRFs of the spatiotemporal delay term, D(s,x)

D(s,x) governs amplitude attenuation and phase delay in a solid as a function of the loss injection frequency spatial location. In (2.2-7), it is parameterized to show a diffusive time constant (τ_{diff}), which is a function of position within a component or assembly, and a fitting parameter (σ). Fig. 2.2-3 plots the FRF magnitude and phase of D(s,x).

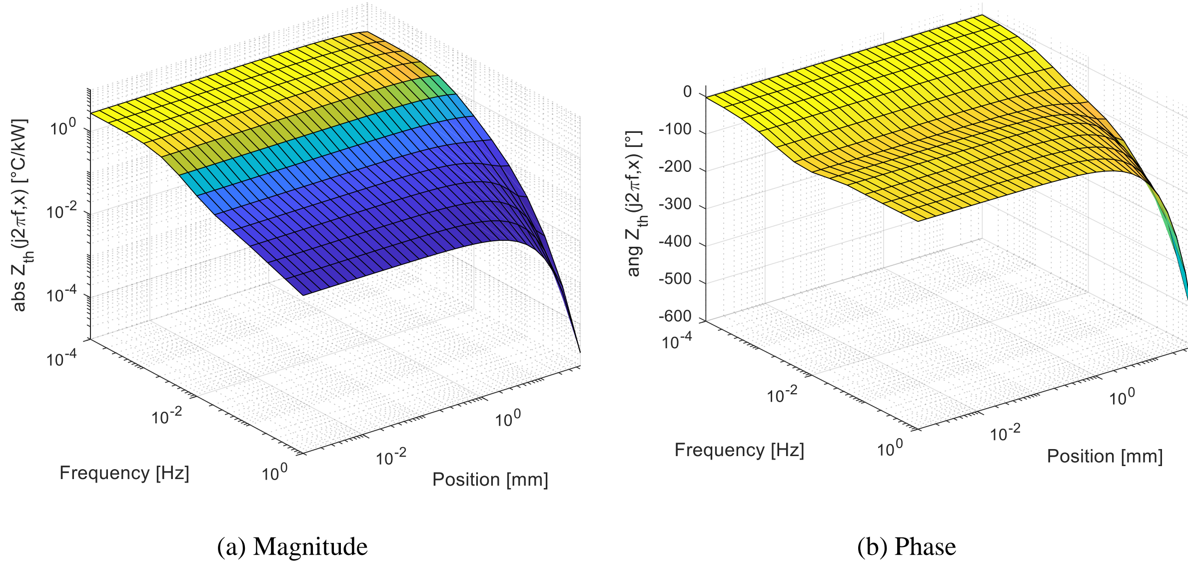

(a) Magnitude (b) Phase

Fig. 2.2-4. Isometric view of a SETIS map produced using the exact solution to the 1D transient model

2.2.1.4 Response evaluation

Model parameters

Eq. (2.2-4) requires thermophysical/fluid and geometric parameters for its evaluation as a function of frequency and space. Table 2.2-1 documents a set of parameters to be used to form baseline SETIS maps, presented in the next subsection.

Table 2.2-1. Parameters used for plotting Fig. 2.2-4

Parameter	Variable	Value	Unit
Thermal diffusivity	α	90	mm^2/s
Thermal conductivity	k	60	W/(m-°C)
Heat transfer coefficient	h	500	W/(m^2-°C)
Domain length	L	46	mm

Spatially-varying electrothermal impedance surfaces

Matlab was used to evaluate (2.2-4) as a function of frequency and spatial location in the solid. Fig. 2.2-4 and Fig. 2.2-5 plot the graphical solution. Some basic observations of the solution

now follow: Fig. 2.2-4 illustrates that there is a DC gain (zero phase lag) property for all locations within the solid. Fig. 2.2-5 more clearly illustrates the amplitude attenuation and phase delay that occur with position and increasing harmonic frequency. Graphical analysis of (2.2-6) indicates these properties, namely the tendency for the solution surface to approach zero amplitude and $-\infty°$ phase, are well captured by D(s,x).

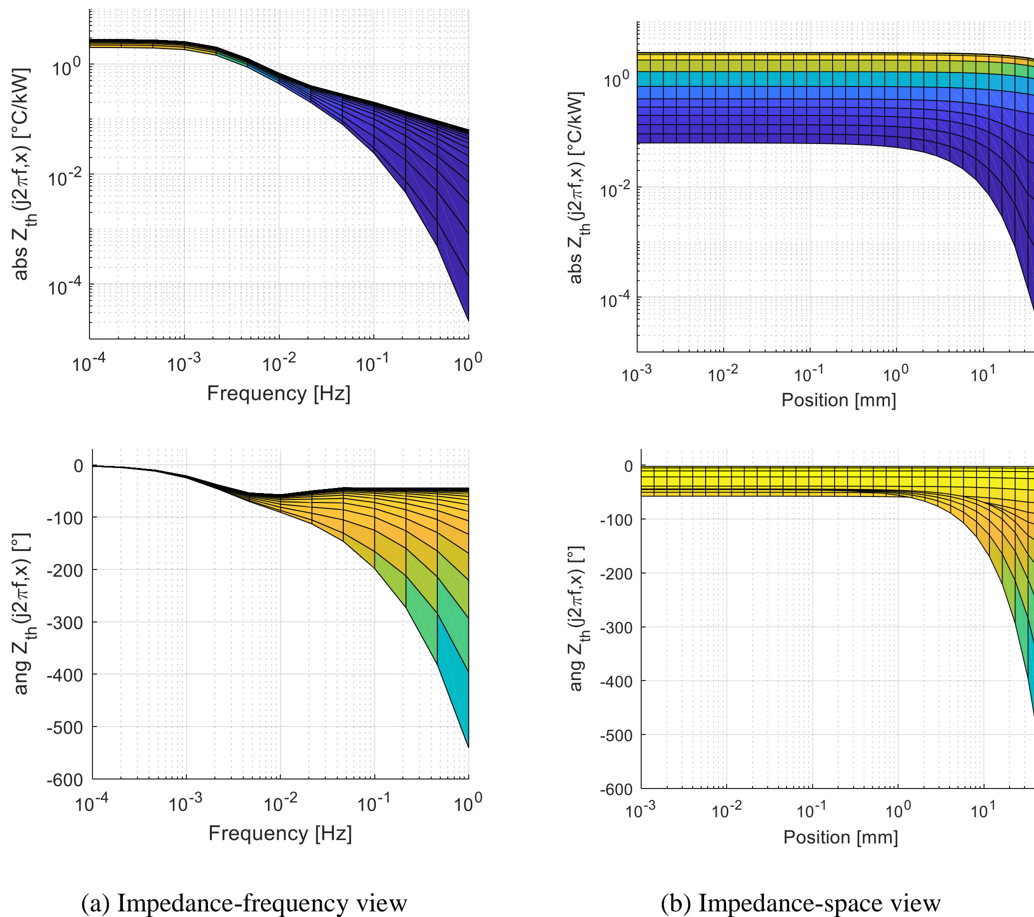

(a) Impedance-frequency view (b) Impedance-space view

Fig. 2.2-5. 2D views of the SETIS map shown in Fig. 2.2-4

2.2.1.5 Identification of asymptotic high frequency response characteristics

The high frequency behavior of the system can be observed in Fig. 2.2-9(a). The magnitude plot illustrates that the driving point impedance (at position $x \rightarrow 0$) has high frequency amplitude attenuation of -0.5 decade/decade and a -45° high frequency phase delay. Relatively far from the

heat generation, the amplitude does not have a stationary attenuation rate and phase delay; instead they rapidly decrease. As will be shown in subsection 2.2.2.1, the high frequency response properties are different than typical, ODE-based lumped parameter models predict in this regime.

2.2.2 Numerical, finite difference method

2.2.2.1 Intentionally low-order FD model

The previous subsection methodically developed parametric spatiotemporal analytical models and identified salient high frequency response properties. This subsection will alternatively develop a numerical model based on the lumped parameter methodology commonly employed in the power electronics literature. Unlike the state-of-the-art literature, however, this investigation will interpret high frequency response properties from these models with the goal of identifying limits intrinsic to the modeling method.

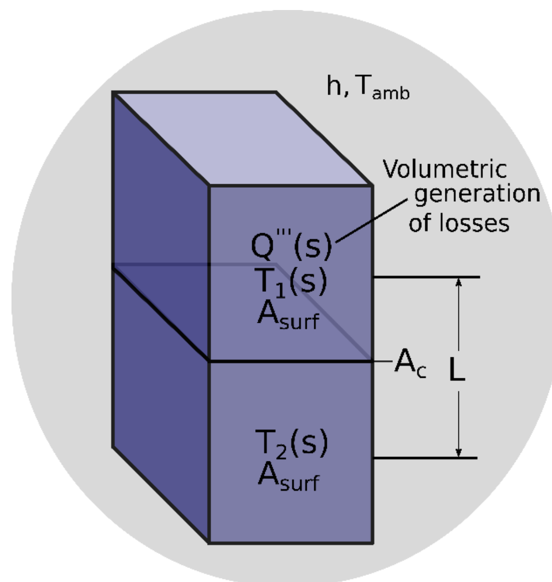

Fig. 2.2-6. Two lumped capacitance finite difference thermal model

Table 2.2-2. Expected high frequency phase response using transfer functions derived for different modes of heat transfer

Mode number	**Mode of heat transfer**	**Transfer function model**	**Phase as $s \rightarrow \infty$**
1	Driving point impedance with heat sinking*:* T_1 response to loss with conduction to T_2 and convection to stationary T_{ref}	$\frac{T_1(s) - T_{ref}}{V \cdot Q'''(s)} = \frac{\frac{1}{C_1 C_2}\left(C_2 s + \frac{1}{R_{par}}\right)}{s^2 + \frac{1}{R_{par} C_{par}} s + \frac{1}{C_1 C_2}\left(\frac{1}{R_{par}^2} - \frac{1}{R_{cond}^2}\right)}$	–90°
2	Distant point impedance*:* T_2 response to conducted loss injections from T_1 with stationary T_{ref}	$\frac{T_2(s) - T_{ref}}{V \cdot Q'''(s)} = \frac{\frac{1}{R_{cond} C_1 C_2}}{s^2 + \frac{1}{R_{par} C_{par}} s + \frac{1}{C_1 C_2}\left(\frac{1}{R_{par}^2} - \frac{1}{R_{cond}^2}\right)}$	–180°
3	Adiabatic driving point impedance*:* T_1 response to loss with no conduction ($R_{12} = \infty$) and no convection ($R_{conv} = \infty$)	$\frac{T_1(s) - T_{ref}}{V \cdot Q'''(s)} = \frac{1}{C_1 s}$	–90°

Graphical description

The model of Fig. 2.2-6 is used to quantify FRF phase response in the high frequency limit. The model has two identical masses, in perfect contact, within an environment having temperature T_{amb} and convective heat transfer coefficient h. The left-hand, $T_1(s)$ mass has uniformly distributed volumetric heat generation (loss), Q'''(s), while the second mass acts only as a heat sink.

Quantitative description

Table 2.2-2 documents modal transfer functions describing heat transfer in Fig. 2.2-6, using (2.2-8)–(2.2-12).

$$R_{cond} = \frac{L}{k\, A_c} \quad (2.2\text{-}8) \qquad R_{conv} = \frac{1}{h\, A_{surf}} \quad (2.2\text{-}9)$$

$$R_{par} = \frac{R_{cond}\, R_{conv}}{R_{cond} + R_{conv}} \quad (2.2\text{-}10)$$

$$C_1 = C_2 = m\, c_p \quad (2.2\text{-}11) \qquad C_{par} = \frac{C_1\, C_2}{C_1 + C_2} \quad (2.2\text{-}12)$$

Identification of asymptotic high frequency response characteristics

Limitations toward modeling non-driving point impedances

Considering mode 2, the model suggests that a low-order lumped parameter modeling approach to capture the response of distant bodies, e.g. substrate/heat sinks or additional semiconductor devices embedded within an assembly, yields a traditional –n decade/decade amplitude attenuation property and a high frequency phase delay at –90n°, where n is $n_{poles} - n_{zeros}$. In general, the high frequency phase response of the bottom volume depends on the number of lumped elements, which is a function of how the spatial domain is divided. These pole and zero constraints apply to all connected systems of lumped capacitances, like Fig. Fig. 2.2-6, which are common in power electronics [162].

Identification of requirements for modeling driving point impedances

Table 2.2-2 shows that the global maximum high frequency phase response is -90°, even for mode number 3, in which the loss injection is so fast that conduction and convection can't occur, and the $T_1(s)$ mass can only integrate the loss. If this model is to be used to represent high frequency, die-level heat transfer, i.e. a driving point impedance, it enforces $n_{zeros} = n_{poles} - 1$. More broadly, inspecting all the heat transfer modes in Table 2.2-2, this model enforces $n_{zeros} \leq n_{poles} - 1$. Both identified pole-zero relationships are relevant for fitting experimental FRF data, a step that will be completed in a future chapter.

2.2.2.2 Computer-aided, model order reduction-based FD model

The MOR-based FD model documented in this subsection, shown in Fig. 2.2-7, was co-specified by the author and collaborator Christoph H. van der Broeck using the method documented in [105]. The author is responsible for motivating, forming, and interpreting the plots shown in Fig. 2.2-8 and Fig. 2.2-9.

Graphical description

Fig. 2.2-7 graphically illustrates a FD meshed PDE model attempting to replicate the MOSFET-sink sub-assembly outlined in the previous chapter. Efforts were made to specify the model consistently with the fabricated experimental test system, including TIM and forced air convection.

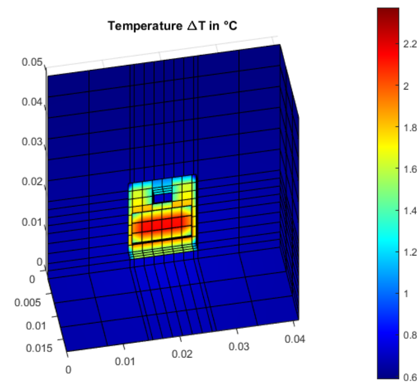

Fig. 2.2-7. 3D finite difference numerical model of a power semiconductor assembly; shown is the steady-state solution to a 1 W step input

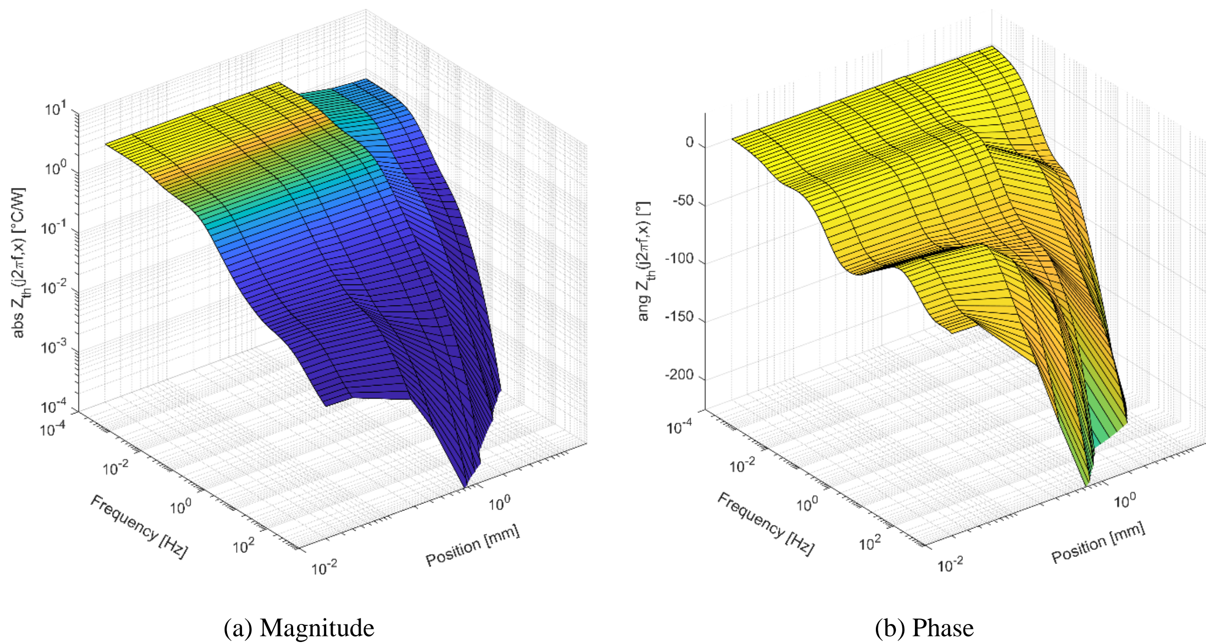

(a) Magnitude (b) Phase

Fig. 2.2-8. Isometric view of a SETIS map produced using the FD model in Fig. 2.2-7

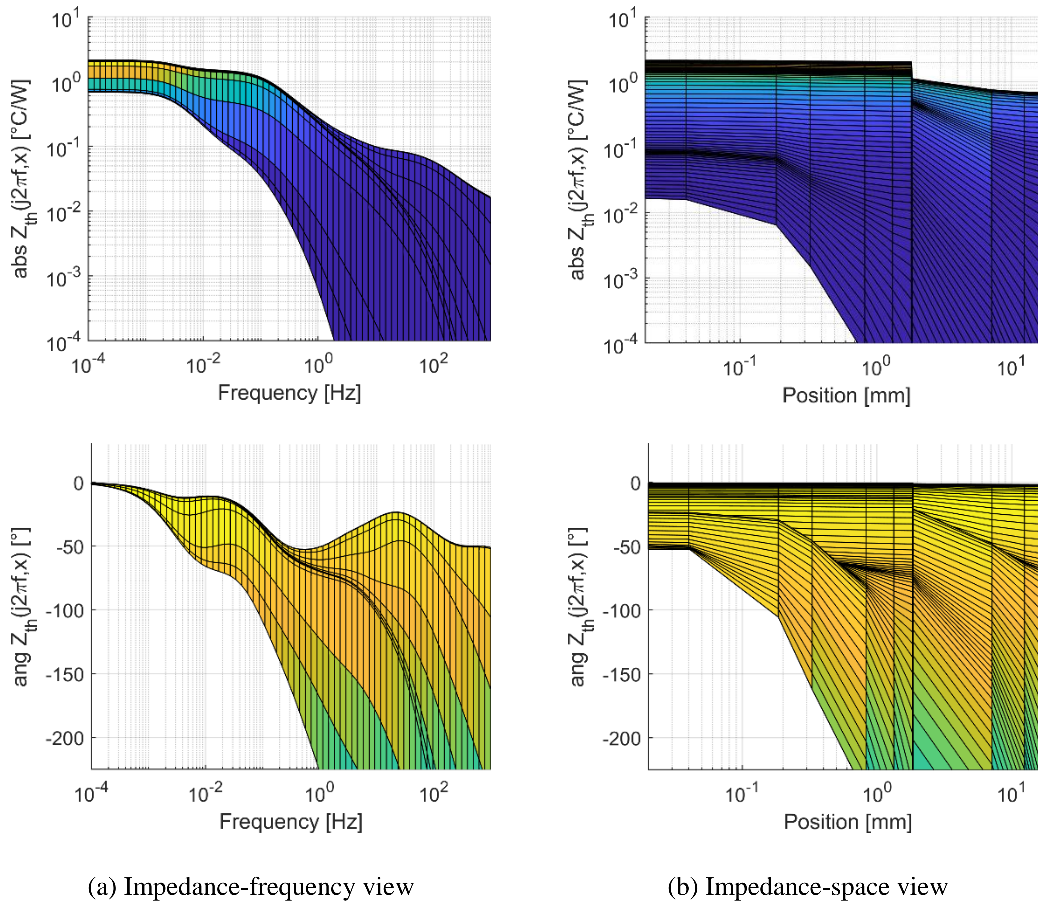

(a) Impedance-frequency view (b) Impedance-space view

Fig. 2.2-9. 2D views of the SETIS map shown in Fig. 2.2-8

Spatiotemporal transient response evaluation

The MOR process took the relatively high order FD numerical model displayed in Fig. 2.2-7 and systematically reduced it to 20 states. Then, the output matrix (the C matrix in classical state-space notation) was arranged so that 12 temperature nodes equally spaced between points 1 and 2 in Fig. 2.1-2 were the output states. This enabled the creation of spatially-varying FRF plots, shown in Fig. 2.2-8 and Fig. 2.2-9.

It can be seen from inspection that the surfaces in Fig. 2.2-8 and Fig. 2.2-9 have more complex character than the surfaces encoded by the 1D transient analytical model, shown in Fig. 2.2-4 and Fig. 2.2-5. These differences originate from the assembly details included in the MOR-

based FD model, which looks more like Fig. 2.2-1(a), compared to the highly defeatured which has a graphical interpretation like Fig. 2.2-1(b).

Inspecting Fig. 2.2-8 and Fig. 2.2-9, it can be seen that the driving point ($x = 0$ p.u. position) impedance has several inflections and curved features, while the distant ($x > 0.8$ p.u. position) impedance has relatively few, like the distant impedance shown in Fig. 2.2-4 and Fig. 2.2-5. Based on this observation, and the comments in the previous paragraph, it is thus concluded that the 1D transient model appears suitable for the description of distant (non-driving point) impedance. A corollary is that driving point impedance quantities in power semiconductors are not accurately described by the defeatured, 1D transient model illustrated in Fig. 2.2-1(b) and Fig. 2.2-2.

Identification of asymptotic high frequency response characteristics

Interpreting the driving point impedance to identify embedded assumptions

The driving point impedance, as displayed in Fig. 2.2-8 and Fig. 2.2-9, has a -1 decade/decade amplitude attenuation rate and a -90° phase response in the high frequency limit. This suggests that the driving point model implicitly encodes $n_{zeros} = n_{poles} - 1$ and a behavior represented by mode 1 of Table 2.2-2.

Limitations in the physical consistency of distance point impedance models

The distant impedance, as displayed in Fig. 2.2-8 and Fig. 2.2-9, appears to capture the increasing amplitude attenuation and phase delay properties apparent in the analytical model SETI FRF in Fig. 2.2-4 and Fig. 2.2-5, and captured by the exponential term in (2.2-6). However, inspection of the distant impedance FRF equations reveals that these models encode the $n_{zeros} = n_{poles} - 1$ property. Per prior conclusions, this is appropriate for modeling driving point

impedance models, but it is more computationally efficient and consistent with first-principles for distant impedance models to use the D(s,x) term.

2.2.3 Low-order, hybrid model synthesis

Previous subsections derived and investigated analytical and numerical spatiotemporal thermal models. It was observed that these two modeling methodologies differently encode heat transfer physics. This subsection proposes a general, reduced-order spatiotemporal model that blends properties from both PDE and coupled, lumped ODE modeling paradigms.

2.2.3.1 Identification of salient analytical and numerical model properties

The documented analytical solution (2.2-6) contains an exponential, spatiotemporal delay term that quantifies the dominant high frequency SETI response property of a component. However, the analytical model was highly defeatured, and its driving point impedance quantity appears to be insufficiently detailed to capture the driving point impedance within a power semiconductor sub-assembly. More featured numerical models can capture apparently lumped features, but they do not naturally encode diffusion physics well represented by the spatiotemporal delay term. Subsection 2.2.2 provided discussion about this intrinsic numerical modeling issue.

2.2.3.2 Combination of the salient properties to form a single, general model

Properties from the analytical, semi-infinite body transfer function solution can be generalized and combined with the classical lumped parameter modeling paradigm to form a general, reduced-order SETI FRF model template. Eq. (2.2-13) is the proposed FRF model template, which will be populated using data from experiments in the next chapter. First, the proposed n_{pole}-order, parameterized FRF model has lumped thermal resistance (R_i) and time

constant (τ_i) parameters. The exponential term from (2.2-7) is included in (2.2-13). So, in addition to having lumped elements, the model includes the spatiotemporal delay term identified during analysis of first-principles physical heat transfer solutions.

$$\frac{T(s,x)}{Q(s)} = \exp\left(-\left(s\cdot\tau_{diff}(x)\right)^{\sigma}\right)\sum_{i=1}^{n_{poles}}\frac{R_i}{\tau_i\, s+1} \tag{2.2-13}$$

2.3 Finite Element, Computational Platform

This section presents a method to form spatially-varying electrothermal impedance FRFs using FE of transient heat transfer. To illustrate the modeling procedure, spatially-varying FRF surfaces are extracted from a simple model of a discrete wide-bandgap power transistor. The result is a virtual converter prototyping platform for parametrically studying effects of geometry and interfaces, such as wire bonds, on heat transfer dynamics and spatial temperature gradients that accelerate component fatigue.

2.3.1 Modeling Method

2.3.1.1 State-space reconstruction of FE model data

While numerical techniques such as FE modeling can be computationally intense, they can represent complicated geometry and also have attractive capabilities for parametric analysis. This sections develops a method to process transient numerical models, created by commercial FE software, directly using state-space analysis to create FRF figures.

Transient and steady-state FE models have governing equations given by (2.3-1) and (2.3-2), respectively. Global matrices for capacitance *(**C**)* and conductivity (***K***) and vectors of nodal

temperatures (T) and boundary conditions (f_{Load}) are used to describe the system and are dependent upon specifications of the model including geometry, materials, and boundaries.

$$\boldsymbol{C} \cdot \dot{T} + \boldsymbol{K} \cdot T = f_{Load} \quad (2.3\text{-}1)$$

$$\boldsymbol{K} \cdot T = f_{Load} \quad (2.3\text{-}2)$$

Transient thermal FE matrices and vectors are typically structured in state-space form, (2.3-3) and (2.3-4), using (2.3-5)–(2.3-7) where *(I)* is an identity matrix and the disturbance matrix *D* is zeroed. *N* corresponds to the number of nodes in the FE model.

$$s \cdot T(s) = \boldsymbol{A} \cdot T(s) + \boldsymbol{B} \cdot U(s) \quad (2.3\text{-}3)$$

$$T(s) = \boldsymbol{C} \cdot T(s) + D \cdot U(s) \quad (2.3\text{-}4)$$

$$\boldsymbol{A} = -C^{-1}K \quad (2.3\text{-}5)$$

$$\boldsymbol{B} = C^{-1}f_{Load} \quad (2.3\text{-}6)$$

$$\boldsymbol{C} = (I)\ of\ size\ NxN \quad (2.3\text{-}7)$$

Commercial FE software conceals $\boldsymbol{C}$, $\boldsymbol{K}$, and f_{Load} data, corresponding to the specified mesh, boundary conditions, and time step, within low-level data structures, like binary files. This work utilizes *ANSYS Parametric Design Language* (ADPL) command snippets inserted into the user interface to reconstruct these files in state-space form for further processing.

2.3.1.2 Capturing nonlinear heat transfer

The modeling procedure takes raw binary outputs from *ANSYS* and reconstructs (2.3-1), and ultimately (2.3-3) and (2.3-4), for frequency domain analysis in, for example, *Matlab*. It is limited in that the binary file extraction procedure only provides a single state-space model with a single configuration of mesh, boundary conditions, and material properties. In transient thermal numerical analysis, including temperature-dependent material properties can lead to more accurate

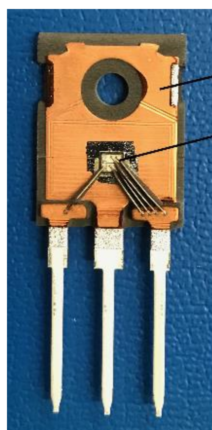

(a) Decapsulated physical specimen, revealing the semiconductor device

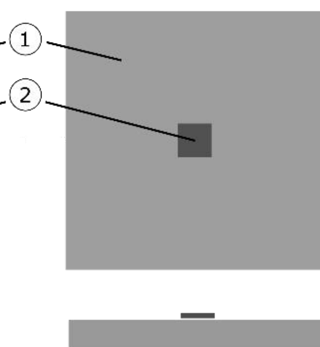

(b) Simplified model including substrate (1) and semiconductor device (2)

Fig. 2.3-1. Discrete SiC power MOSFET

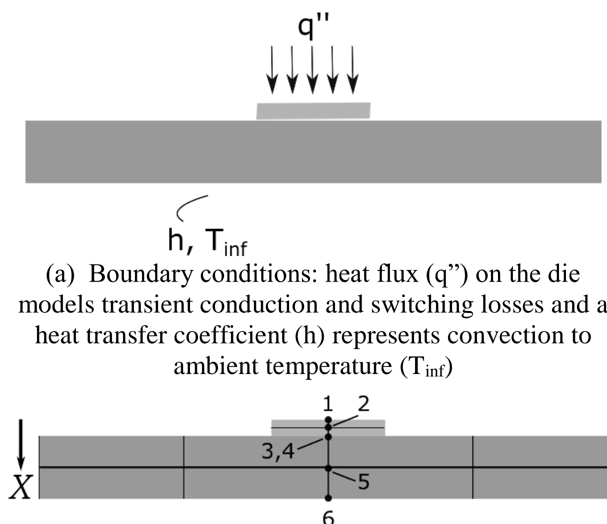

(a) Boundary conditions: heat flux (q") on the die models transient conduction and switching losses and a heat transfer coefficient (h) represents convection to ambient temperature (T_{inf})

(b) Cartesian mesh in which the displayed six nodes align with a single vector (*X*) to form a SETI surface

Fig. 2.3-2. FE model details

solutions, however, the resulting FE matrices then become a function of temperature and the dynamical system is nonlinear. To address this, the method forms FRFs for material properties at a single temperature and therefore is best described as small-signal analysis. It enables identification of heat transfer nonlinearities by, for example overlaying FRFs extracted from models with different material properties, as done in another section.

2.3.1.3 Example Application

Defeatured WBG component model

Fig. 2.3-1 and Fig. 2.3-2 show a decapsulated silicon carbide (SiC) power MOSFET and an associated solid model, which has been simplified by removing wire bonds, die-attach, the mounting hole, and drain, gate, and source terminals. After defeaturing, the model's geometry was imported to the *ANSYS Mechanical* software in which mesh and boundary conditions like those illustrated in Fig. 2.3-2 were applied.

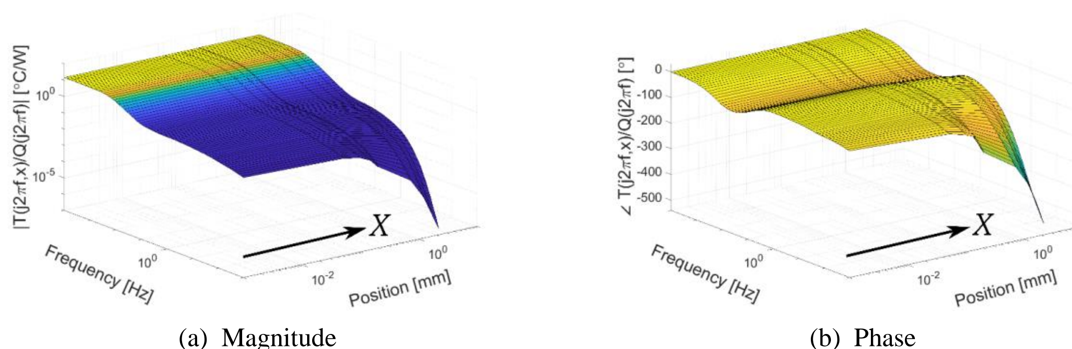

(a) Magnitude (b) Phase

Fig. 2.3-3. Spatially-varying FRF of the model shown in Fig. 2.3-2

Forming spatially-varying electrothermal impedance plots

FRF quantities can be generalized in space to identify how spatial domain properties influence a response continuum. The usage of commercial FE software allows for specification of a mesh which enables spatially-varying FRFs to be extracted. The gathered FRFs along a coordinate vector can then be graphically assembled to build spatially-varying FRF surfaces.

Fig. 2.3-2(b) shows how the mesh aligns nodes 1-6 with a vector entering the assembly center through the semiconductor die. Using a state-space form of the FE model, a spatially-varying FRF surface was generated for the nodes aligned with the coordinate vector and is illustrated in Fig. 2.3-3. These response plots reveal how the thermal response varies as a function of harmonic frequency of semiconductor device heat dissipation and spatial location within the assembly. They are relevant toward reliability of assemblies.

To create spatially-varying FRFs, an FE model that has been transformed into a state-space representation is used to map the frequency domain thermal response of each node along a coordinate vector. These FRF quantities are calculated, then the magnitude and phase terms of the FRFs are plotted as a function of harmonic frequency of the loss injection and the spatial location of the node. Interpolation ultimately provides 3D surface plots that lend themselves to graphical analysis for identifying effects of geometric features on response and degradation.

Multi-chip IGBT power module

The FE modeling method extracts a single LTI state-space model for a single setup in an *ANSYS Mechanical* GUI. The method outputs an LTI model for a single loading (loss distribution) configuration. Fig. 2.3-4 shows an example IGBT power module. Fig. 2.3-5 shows the computed die-to-ambient FRF from a state-space model for the case of device losses distributed within the hot chip in Fig. 2.3-4. To compute response to a different chip's losses, a new model is needed.

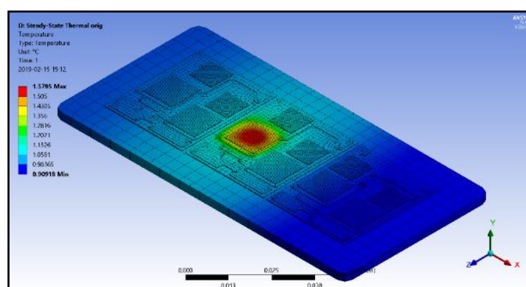

Fig. 2.3-4. Steady-state solution illustration of an analyzed IGBT power module

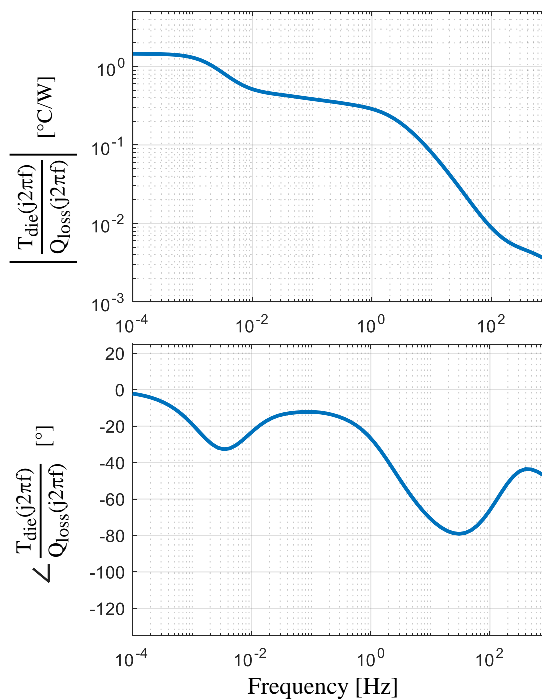

Fig. 2.3-5. Die-to-ambient FRF for loss excitation from the hot chip in Fig. 2.3-4

2.4 Chapter Summary

This chapter compared first-principles, analytical and numerical models. Of interest in the investigation was how these modalities encode spatial domain information, and how this information can be retrieved. It was observed that numerical models dedicate many dynamic states (mesh nodes) which, in the aggregate capture diffusion dynamics. On the other hand, an analytical model was observed to capture diffusion in a single term depending on temporal and spatial domain variables. A general, yet compact lumped and diffusive model was therefore derived. Finally, a finite element utility was presented. It allows for direct frequency domain analysis, an uncommon practice in power electronics, and retains potential accuracy that can be achieved with modern computer-aided design and mesh tools.

Chapter 3 Spatiotemporal Heat Transfer Experimental Characterization

This chapter presents systems identification methods for extracting frequency domain electrothermal impedance properties, examined in Chapter 2, from power semiconductor and converter hardware. Methods utilize power electronic hardware as actuator and sensor for heat transfer experiments to be used for sensitivity analysis and forming compact models. Elements of this chapter are also documented in publications [157]–[159].

3.1 Converter-Integrated System Identification

3.1.1 Method Development

This subsection describes the experimental methodology to extract parameterized, compact, spatiotemporal thermal models characterizing both fast (die-level) and slow (sink-level) heat transfer in an assembled converter system.

3.1.1.1 Overview

Excitation, measurement, and identification of electrothermal response

The proposed thermal modeling method intentionally utilizes a power semiconductor device, embedded within a converter system, as a source of losses (heat). The method is realized by using controlled device conduction and switching losses to dynamically generate heat constrained by converter limitations, such as the maximum achievable loss amplitudes and its switching frequency. The steps of the method are shown in Fig. 3.1-1.

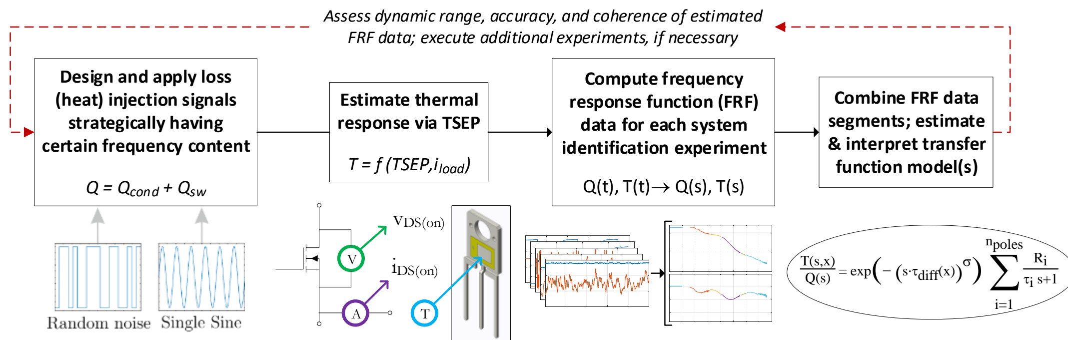

Fig. 3.1-1. Illustration of the thermal system identification method

The method illustrated in Fig. 3.1-1's chart is now summarized. Conduction and switching loss models allow an injection of known heat (in units of W) to be made. The injection encompasses a spectrum of frequency content, or a single frequency, and the history of its value must be stored. During this intentional operation of the converter as a loss modulator, critical temperature response variables must be measured with instruments, or with a TSEP, such as MOSFET $R_{DS(on)}$. After the experiment, FRF data relating the response of temperature to the power loss injection is computed using Fourier transform methods.

For context, please note that the FRFs derived following the electrothermal impedance spectroscopy method are discretely-positioned lines of the FRF surface plots examined in Chapter 2. Although spatially-varying FRF plots are a more general expression of a power semiconductor assembly’s electrothermal response, scalar FRF traces are extracted in this chapter since the temperature of power electronic systems can only be monitored with sensors at discrete locations.

FRF fitting and interpretation

The computed FRF data quantify a dynamic thermal impedance, with units of °C/W, between the spatial location of the temperature measurement and a reference temperature. They

also quantify response phase delay. Upon their extraction, they should be fit with a transfer function model following (2.2-13).

A unique challenge of power electronics thermal system identification and modeling is the high potential for widely diverse (multiple time-scaled) dynamic content to exist within the physical system. Partial fraction decomposition is an optional step to estimate of time constant and resistance parameters and thereby mathematically parses multiple time scale dynamics captured by wide-band FRF data.

The curve fitting step also allows an engineer to eventually address the trade-off between thermal model accuracy and the computational intensity involved its real-time evaluation, i.e. the number of states (or poles/eigenvalues) it contains. Within the maximum allowable state count, a constraint related to converter DSP hardware, the accuracy of the FRF fit model should be maximized.

Interpretation of results with heat transfer theory

Once FRF data is obtained and it is fit with parameters following (2.2-13), the resulting thermal parameters can then be interpreted using heat transfer theory. Eq. (1.3-6)–(1.3-10) can be used for this purpose. These low-level interpretations can perhaps, ultimately, be used to propose geometric design modifications to improve the degradation sensing capability of a converter, for example.

3.1.1.2 Loss modulator design

Because the experimental component of the method relies on dynamic thermal excitations to the power semiconductor assembly (via device losses), total conduction and switching loss must

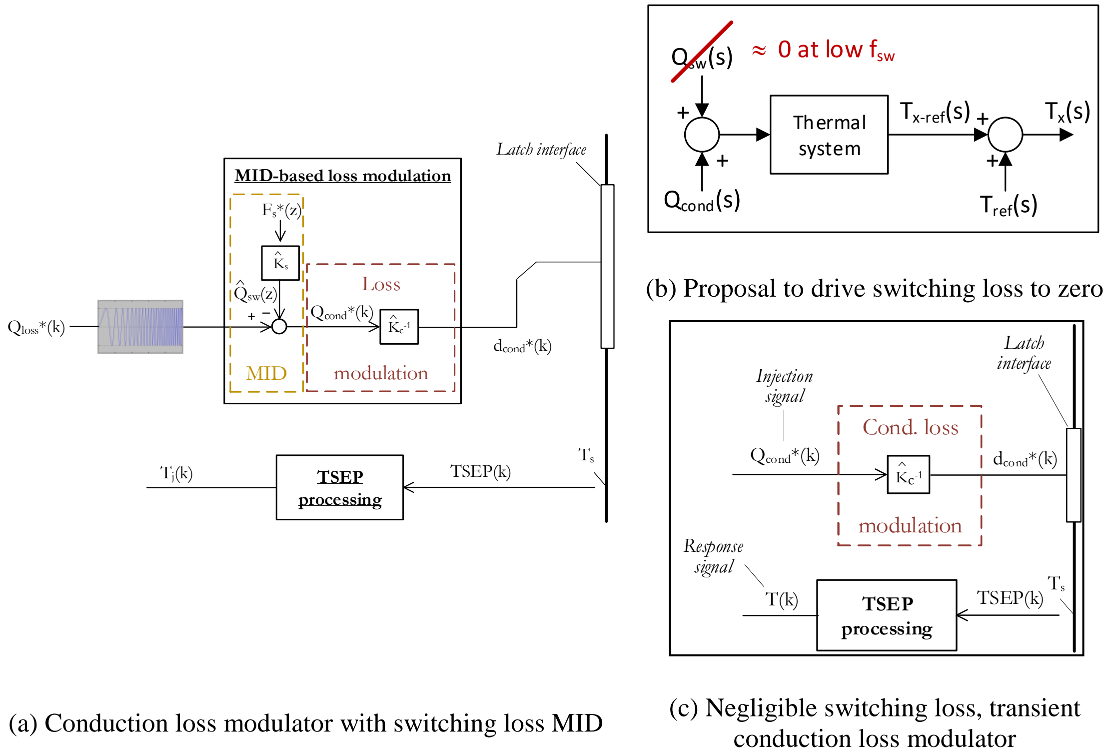

Fig. 3.1-2. Loss modulator state block diagrams

be precisely manipulated during experiments. This subsection will document the design of a loss modulation system to be experimentally deployed.

State block diagrams

Prior work documented that generation of conduction and switching losses are not SISO in power electronic converters, even for relatively simple converter configurations [163]. Fig. 1 from [164] presents a state block diagram which illustrates PICC for a buck converter. In this embodiment, PICC exists because both the conduction and switching loss gain parameters depend on the amount of switched load current.

Cross-coupled loss elements can be decoupled with manipulated input decoupling (MID) to achieve accurate loss manipulation. MID-based loss modulation has been documented in prior work [163]. Both MID-based conduction loss and MID-based switching loss modulators are

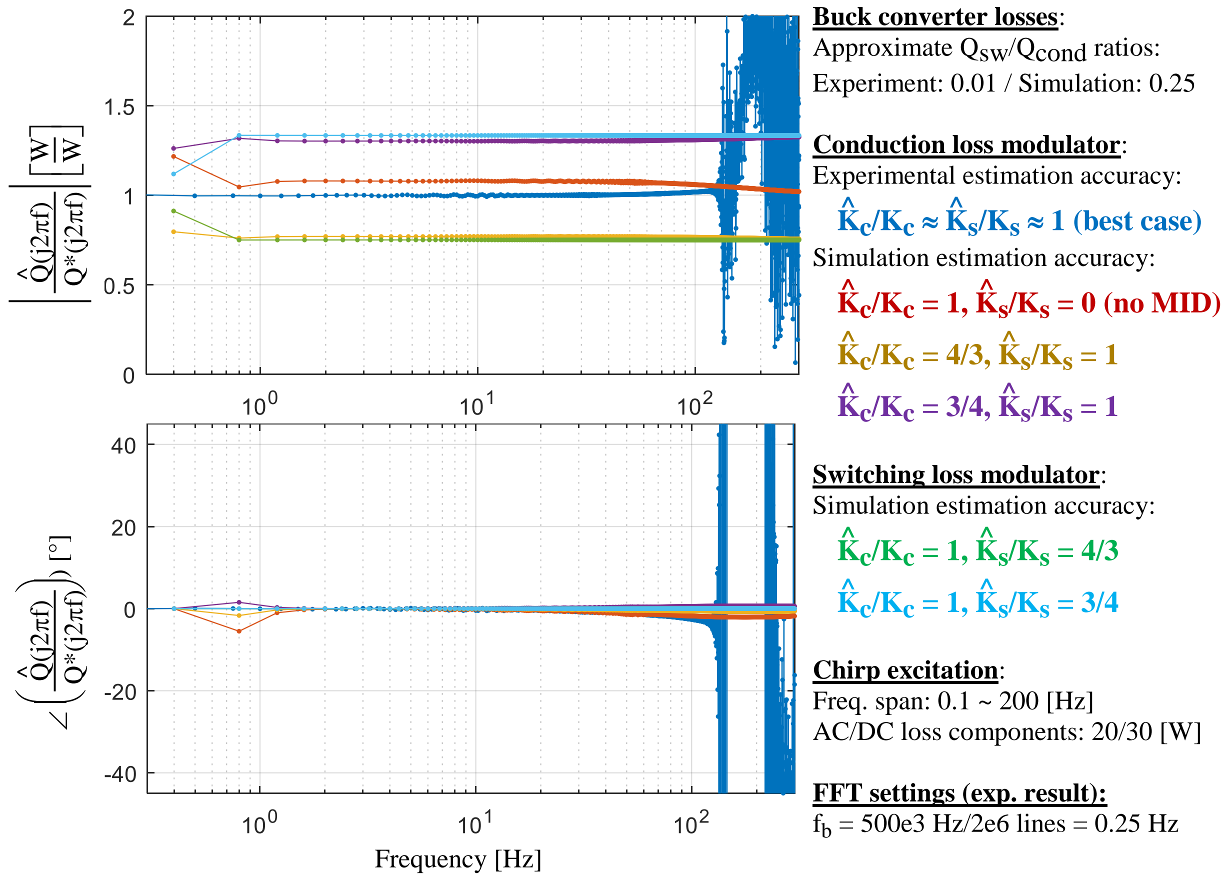

Fig. 3.1-3. Parameter sensitivity of conduction and switching loss modulators

theoretically suitable for the SETIS methodology. However, experiments should modulate the converter's dominant loss element to maximize signal-to-noise ratio.

When intentionally modulating conduction losses for active thermal-mechanical control or system identification, switching losses must nominally be decoupled. Fig. 3.1-2(a) presents a state block diagram for a conduction loss modulator in which switching losses are estimated and decoupled. It is possible, however, that a converter can be configured such that one loss component is negligible. Fig. 3.1-2(b) illustrates negation of switching loss by manipulation of converter switching frequency. If switching loss can be decoupled, a physics-based conduction loss modulator can be utilized without switching loss MID.

Parameter sensitivity

The proposed physics-based conduction and switching loss modulators have been parameterized with a conduction loss gain, K_c, and a switching loss gain, K_s [163]. Fig. 3.1-3 presents an experimental and simulation parameter sensitivity study using the estimation accuracy (EA) FRF metric. The results suggest that conduction and switching loss modulators have linear magnitude parameter sensitivities, but no phase parameter sensitivity.

$$\frac{\hat{Q}_{cond}(s)}{Q_{cond}(s)} = \frac{\hat{D}(s)\,\hat{I}^2_{DS(on)}(s)\,\hat{R}_{DS(on)}(s)}{D(s)\,I^2_{DS(on)}(s)\,R_{DS(on)}(s)} \quad (3.1\text{-}1) \qquad \frac{\hat{I}_{DS(on)}(s)}{I_{DS(on)}(s)} = \frac{K}{\tau_{sensor}s+1} \quad (3.1\text{-}2)$$

$$\frac{\hat{Q}_{cond}(s)}{Q_{cond}(s)} = \left(\frac{K}{\tau_{sensor}s+1}\right)^2 \quad (3.1\text{-}3) \qquad \hat{R}_{DS(on)}(t) = R_o \quad (3.1\text{-}4)$$

$$R_{DS(on)}(t) = R_o + \beta\left[T_{die}(t) - T_{amb}\right]^2 = R_o + \beta\Delta T^{s}_{die\text{-}amb}(t)^2 \quad (3.1\text{-}5)$$

$$\Delta T^{s}_{die\text{-}amb}(t) = A \Rightarrow [\Delta T^{s}_{die\text{-}amb}(s)]^2 = A^2 \quad (3.1\text{-}6)$$

$$\frac{\hat{R}_{DS(on)}(s)}{R_{DS(on)}(s)} = \frac{1}{\mu+1} = \left.\frac{\hat{Q}_{cond}(s)}{Q_{cond}(s)}\right|_{const\text{-}temp} \quad (3.1\text{-}7) \qquad \mu = \frac{\beta}{R_o}A^2 \quad (3.1\text{-}8)$$

$$\Delta T^{s}_{die\text{-}amb}(t) = A\sin(\omega t) \Rightarrow [\Delta T^{s}_{die\text{-}amb}(s)]^2 = \frac{2A^2\omega^2}{s(s^2+4\omega^2)} \quad (3.1\text{-}9)$$

$$\frac{\hat{R}_{DS(on)}(s)}{R_{DS(on)}(s)} = \frac{s^2+4\omega^2}{(s^2+4\omega^2)+2\mu\omega^2} = \left.\frac{\hat{Q}_{cond}(s)}{Q_{cond}(s)}\right|_{harmonic\text{-}temp} \quad (3.1\text{-}10)$$

Eq. (3.1-1) through (3.1-10) comprise a general, analytical parameter sensitivity analysis of the loss modulator. These parameter sensitivity properties will be leveraged later in this research program for designing parameter-insensitive degradation monitoring systems.

3.1.1.3 System identification experiment design

Loss/heat perturbation signal design

Multiple signal types can be used to excite thermal response. However, there are best practices for designing the perturbation that can increase the likelihood of systematically extracting coherent FRF data. Perturbation signal design methods attempt to balance tradeoffs between experiment length (and data record size) and the size of the frequency range that can be characterized in a single experiment.

Compact, multi-band experiments to capture dynamic ranges

Ideally, the entire frequency range of interest would be characterized using time series data from a single, short system identification experiment. To meet this objective, the input signal can be designed to have a wide dynamic range. Random noise input or swept frequency (chirp) input signals have a range of harmonic content that can be specified. If coherent FRF data for the entire frequency range of interest is unable to be extracted using a single experiment, the frequency range can be partitioned into bands, and the dynamic range of the input signal can be bounded by the limits of the bands. Then, during post-processing, the FRF data can be combined on a single plot.

In FFT analysis, the frequency resolution (base frequency, f_b) is inversely proportional to the data record length (T_b) [165]. Therefore, if it is desired to resolve relatively small values of frequency, e.g. mHz, a long record of data must be captured. A system identification experiment is governed by the slowest dynamic desired for characterization.

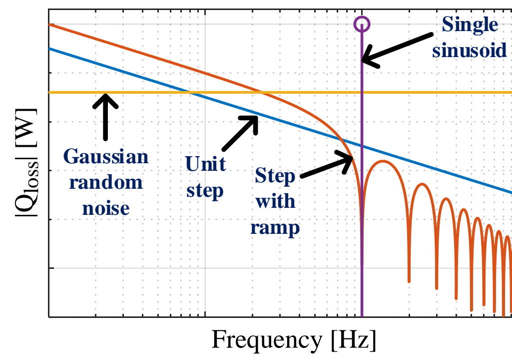

Fig. 3.1-4. Amplitude spectrum qualitative representation for candidate loss excitation waveforms, showing limited high frequency excitation ideal and non-ideal step inputs provide

Point methods to maximize SNR and extract high frequency content

Electrothermal impedance FRF magnitude is decreases with increasing excitation frequency. Therefore, more loss is required to perceive high frequency AC response; in other words, SNR decreases at higher frequencies. The harmonic content of an input perturbation can be consolidated to occupy a single harmonic, as shown in Fig. Fig. 3.1-4.

3.1.1.4 Fourier transform post-processing

Loss and temperature data are then transferred to a PC for Fourier transform-based post-processing with *Matlab*. Magnitude (in units of thermal impedance, °C/W) and phase (in delay units of °) FRF data is extracted using Welch's modified periodogram method [166]. For all sets of data subjected to the frequency-domain analysis, the magnitude-squared coherence is also computed to provide an objective assessment of FRF measurement quality.

Resulting complex FRF data can be graphically displayed using separate magnitude and phase plots, which explicitly show frequency on the abscissa. Data can also be displayed on a single complex plot in which frequency is implicit. These plots are commonly referred to as Bode and Nyquist plots in the control systems literature.

3.1.2 Application of the Method

3.1.2.1 DC-DC converter with integrated temperature sensing

Components and signal flow

The spectroscopy method was applied to a DC-DC converter illustrated in Fig. 3.1-5. The converter is controlled by an *AixControl* digital controller and switches between 5-10 kHz. *LEM HXS 20-NP* and *AD8422* integrated circuit components sense $i_{\mathrm{DS(on)}}$ and $v_{\mathrm{DS(on)}}$.

After calibration experiments, $R_{\mathrm{DS(on)}} = v_{\mathrm{DS(on)}} / i_{\mathrm{DS(on)}}$ estimates temperature of the decapsulated power MOSFET's die during real-time operation. A thermistor was included to sense heat sink temperature. In this setup, loss and temperature signals from the digital control system were delivered to a *Teledyne LeCroy HDO 6054-MS* for data recording.

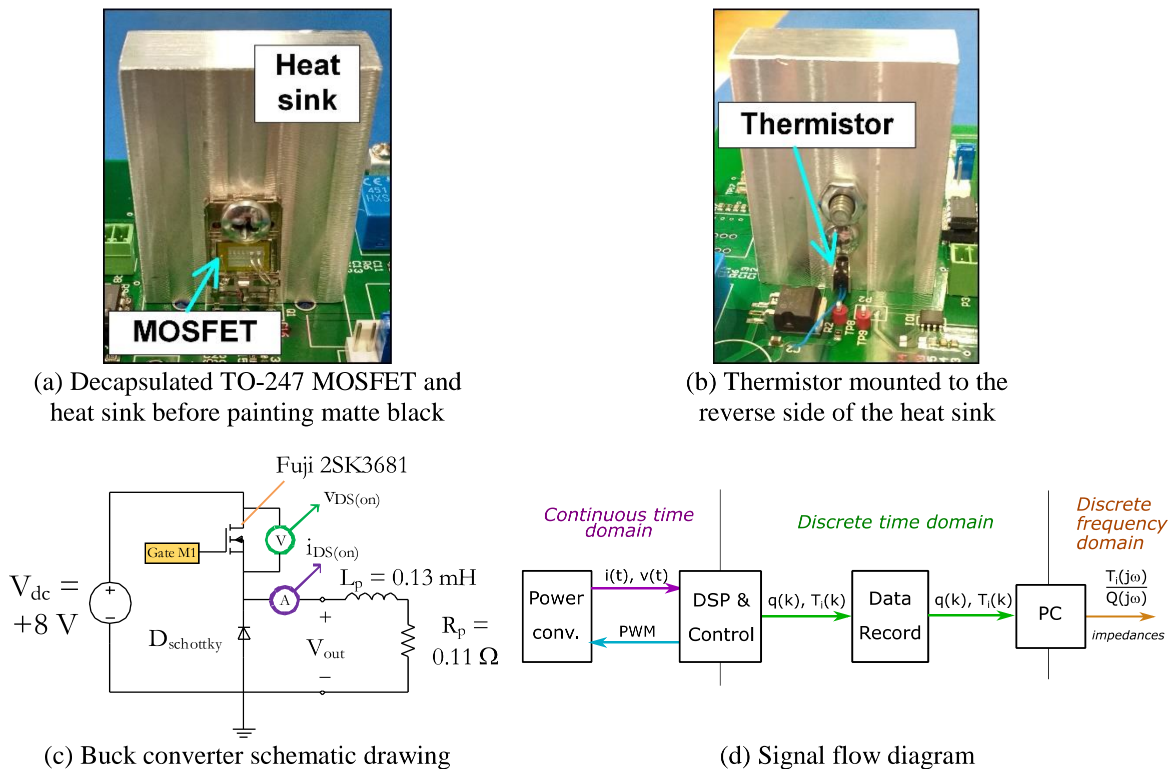

(a) Decapsulated TO-247 MOSFET and heat sink before painting matte black

(b) Thermistor mounted to the reverse side of the heat sink

(c) Buck converter schematic drawing

(d) Signal flow diagram

Fig. 3.1-5. Elements of the experimental evaluation of electrothermal impedance spectroscopy

The system was integrated on a single PCB, which eventually contains the buck converter, the sensing circuitry, and the power semiconductor and cooling assembly, painted matte black for infrared camera compatibility. A blower forced air to cool the MOSFET and heat sink subassembly.

Heat injection and characterization via loss modeling

The buck converter operates with a single active power MOSFET, *Fuji* 2SK3681, which heats the semiconductor device and cooling assembly dynamically. Eq. (3.1-11) and (3.1-12) form a switching period-averaged loss model for the MOSFET device.

$$Q_{cond} = d\, R_{DS(on)}\, i^2_{DS(on)} = d\, K_c \tag{3.1-11}$$

$$Q_{sw} = f_s\, (E_{on} + E_{off}) = f_s\, E_{sw} = f_s\, K_s \tag{3.1-12}$$

$$R_{DS(on)} = \frac{V_{DS(on)}}{I_{DS(on)}} = f(temperature,\ load\ current) \tag{3.1-13}$$

$$T_{die}(kT) = b_1 + b_2\, i(kT) + b_3\, i(kT)^2 + b_4\, r(kT) + b_5\, r(kT)^2 + b_6\, i(kT)\, r(kT) \tag{3.1-14}$$

Die temperature linear regression estimator

The $R_{DS(on)}$ TSEP relationship (3.1-14) is used to estimate die temperature in real-time for its simple signal processing requirement and potential to provide high bandwidth estimation [167], [168]. Sensed $R_{DS(on)}$ and $i_{DS(on)}$ information (*r(kT)* and *i(kT)* discrete-time signals) are empirically correlated to a single pixel of an infrared camera (*FLIR* E50) measurement with it aimed at the semiconductor die.

It was desired to perform transient thermal characterization in situ, so a calibration procedure usable under switching operation was developed. Building upon the steady-state approach in [164], a linear regression estimator was formed using calibration data obtained during

dynamic switching operation of the converter, while the infrared camera monitored the die temperature at a 30 Hz rate. Such data is shown in Fig. 3.1-6, which is 100 s of data obtained during converter operation with MOSFET duty ratio randomly manipulated at a 0.2 Hz rate. Fig. 6 shows $i_{DS(on)}$, $v_{DS(on)}$, and $R_{DS(on)}$. Also shown is die temperature as measured by the camera, T_{flir}, and T_{fit}, the output of a linear regression estimator.

A multiple linear regression model was fit to the calibration data in *Matlab*. A generic second-order linear regression model, (3.1-14), was eventually implemented to estimate T_{die} at each discrete sample time instant kT. Upon its calibration, accuracy assessments quantify the estimation system to have normally distributed errors at ~10% standard deviation. The error was characterized experimentally by computing the difference between time domain outputs of the infrared camera and a previously implemented estimator, such as T_{prior} shown in Fig. 3.1-6, given unseen data from a random converter trajectory.

The system was fabricated with heat sink temperature sensing via a thermistor detector (type B57703M from *TDK Group Company*). Using the infrared camera, its temperature was correlated to its sense voltage for real-time heat sink temperature sensing during experiments.

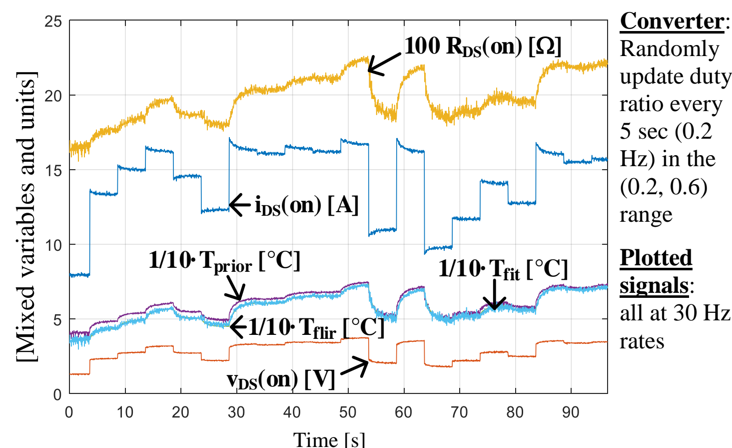

Fig. 3.1-6. Time-domain data used to calibrate the real-time MOSFET die temperature estimator

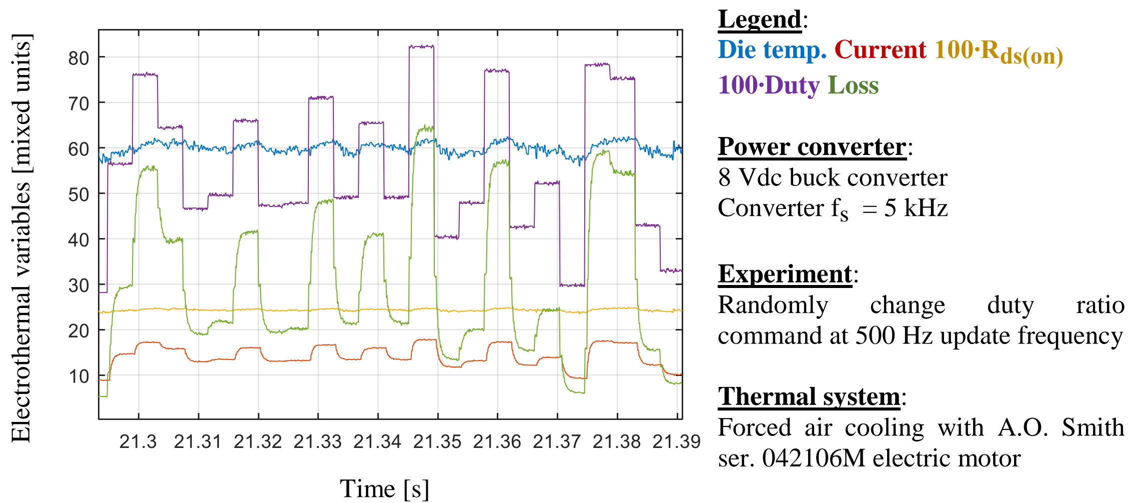

Fig. 3.1-7. Time domain waveforms extracted during a system identification experiment

3.1.2.2 Conduction loss modulator design

The buck converter operates with a single active, decapsulated power MOSFET, *Fuji* 2SK3681, which dynamically heats the semiconductor device and cooling system assembly. For further simplicity in executing the thermal system identification methodology, the converter is configured with low DC bus voltage, such that switching loss is negligible. Thus, the system requires only an inverse model of the conduction loss equation to form a duty ratio-controlled conduction loss modulator following Fig. 3.1-2(b) and Fig. 3.1-2(c). Since both $i_{DS(on)}$ and $v_{DS(on)}$ are sensed with calibrated transducers, loss modulator accuracy is confidently assumed to be high.

3.1.2.3 Characterization of multiple time-scale dynamics

Multi-band experiments to capture mid-range dynamics

From approximate heat transfer calculations, it was anticipated that the slowest and fastest thermal dynamics in the experimental test bed differ by 5-7 orders of magnitude. Due to the very high time scale separation of the dynamics, they were unable to be concurrently excited, with

coherence, by a single loss injection signal. As a result, multiple experiments were executed using different injections, data recording frequencies, and FFT settings.

An example of the time domain data extracted during a system identification experiment is shown in Fig. 3.1-7. A preliminary FRF, displaying results and specifications from tests for three separate frequency bands, is shown in Fig. 3.1-8.

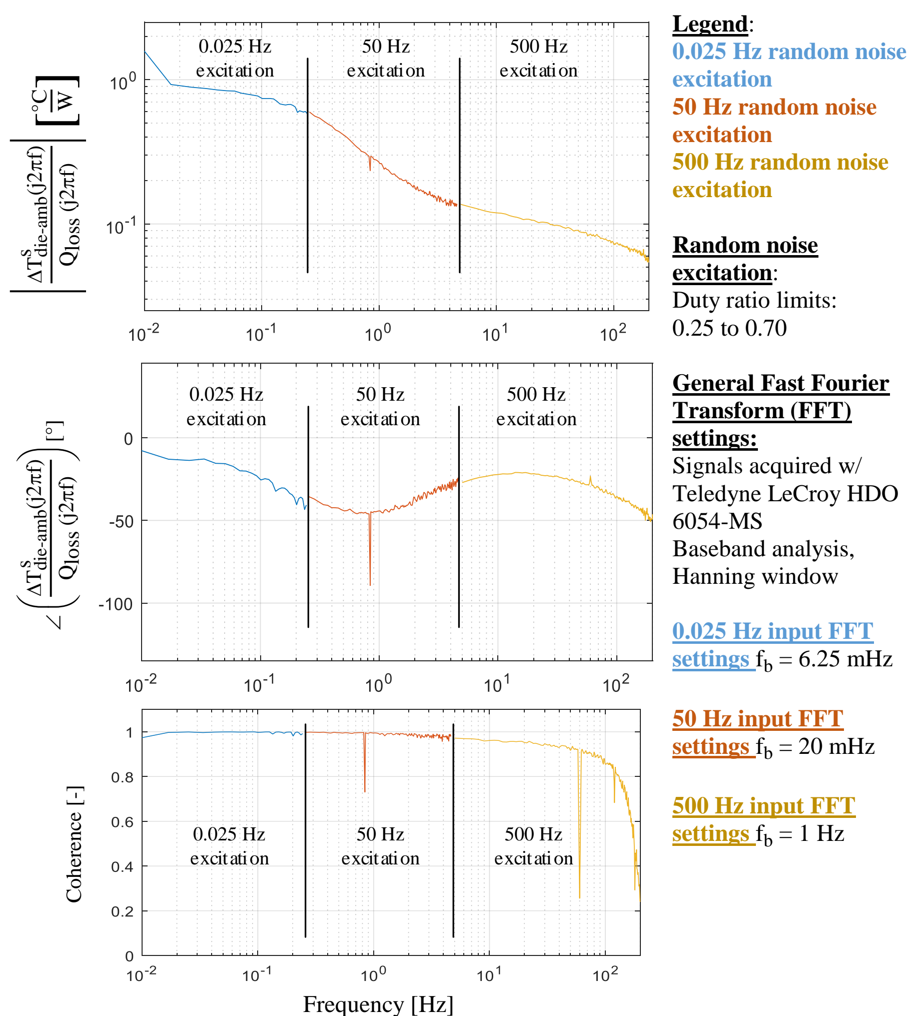

Fig. 3.1-8. Overlay of three system identification test results using different random noise input perturbations, sample rates, and FFT settings

Experiments to separately capture DC-to-low and high frequency dynamics

Prior steady-state tests on the converter indicated the assembly's total thermal resistance $R_{dc} \approx 2$ °C/W. As a result, long duration experiments with even lower (sub-mHz) frequency, square wave loss injections were completed, and, as shown in Fig. 3.1-9, the FRF was extended to capture the DC response property of both $\Delta T^{s}_{die\text{-}amb}(j2\pi f) / Q_{loss}(j2\pi f)$ and $\Delta T^{s}_{thermistor\text{-}amb}(j2\pi f) / Q_{loss}(j2\pi f)$. Table 3.1-1 and Table 3.1-2 document the signal and data acquisition specifications for these long, square wave experiments. As the tables show, high degrees of data decimation were utilized to extract coherent, low frequency FRF data.

Table 3.1-1. Test signal specifications for the square wave, DC-to-low frequency system identification experiments

Test signal				Power electronics
Frequency [mHz]		Loss injection [W]		
Floating	Rounded	Lower bound	Upper bound	Switching [Hz]
0.125	0.125	6.5	30	5000

Table 3.1-2. Data record specifications for the square wave, DC-to-low frequency system identification experiments

Oscilloscope							
DAQ					ERes filtering max.		Time-domain averaging [-]
Sampling [Hz]	Sparsing [-]	Sparsed [Hz]	ks/div	Length [ks]	Bits [-]	Freq [Hz]	
1000	10000	0.1	2	20	3	8	none

Next, the diminishing FRF coherence of the driving point impedance, $\Delta T^{s}_{die\text{-}amb}(j2\pi f) / Q_{loss}(j2\pi f)$, at higher frequencies, visible in Fig. 3.1-8, was addressed. To concentrate the SNR of very small amplitude temperature response signals with high frequency loss injections, test trajectories were consolidated to have single-frequency content. Then, the now DC-descriptive FRF was supplemented with data points from single-frequency loss injections experiments, as shown in Fig. 3.1-9.

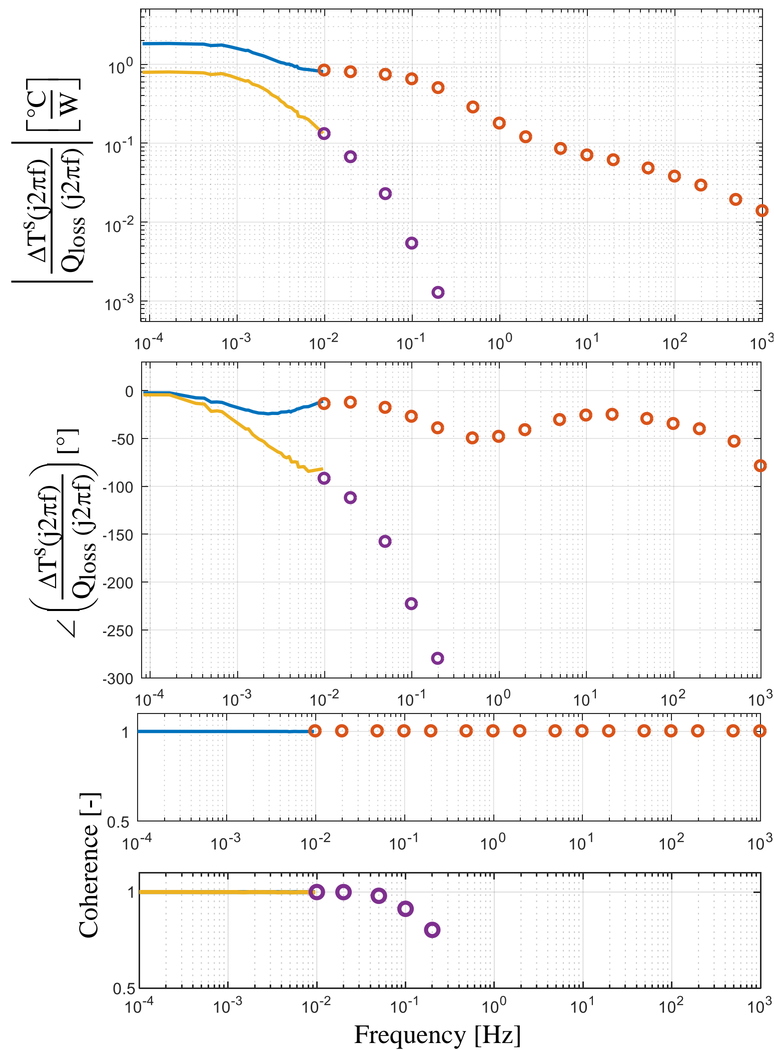

Die-to-ambient FRF: Slow square wave | Single-sinusoids
Thermistor-to-ambient FRF: Slow square wave | Single-sinusoids

Fig. 3.1-9. Extension of the FRF data from Fig. 3.1-8 to include test results at frequency levels near to DC (using sub-mHz loss trajectories) and to 1 kHz (using single-frequency sinusoid injections)

Single frequency tests are conveniently suitable for parametric design based off the frequency range and resolution desired for characterization with the SETIS method. Eq. (3.1-15)–(3.1-19) document the single frequency sinusoid system identification experiment design rules that were utilized in this work.

It can be observed that the signal oversampling ratio, $f_{sampling}$ / f_{fund} was safely selected to be 100. Next, the data record length, T_{record}, was selected to capture ten oscillations of the sinusoidal waveforms. The break frequency of the digital ERes filter included in the oscilloscope was selected to be at least 100 times larger than the fundamental frequency of the injection signal. Finally, the number of time domain averages was selected based on a desired total experimental length, $T_{experiment\text{-}total}$.

$$T_{fund} = 1 / f_{fund} \quad (3.1\text{-}15)$$

$$f_{sampling} = 100 \cdot f_{fund} \quad (3.1\text{-}16)$$

$$T_{record} = 10 \cdot T_{fund} \quad (3.1\text{-}17)$$

$$f_{ERes} \geq 100 \cdot f_{fund} \quad (3.1\text{-}18)$$

$$n_{averages} = T_{experiment\text{-}total} / T_{record} \quad (3.1\text{-}19)$$

Eq. (3.1-15)–(3.1-19) illustrate how the single frequency sinusoid system identification experiments can be methodically designed as a function of the fundamental frequencies of the loss injections, which depends on the frequency range and resolution desired for characterization. Table 3.1-3 and

Table 3.1-4 are the test matrices for the executed single sine experiments with entries that generally reflect Eq. (3.1-15)–(3.1-19).

Comparison of FFT data extracted from multi-band and point experiments

To demonstrate the capability of multiple perturbation signal designs to ultimately provide coherent FRF data, data obtained using band-limited random noise and pure tone sinusoids were compared. The comparison is shown in Fig. 3.1-10. The FRF data points from the single-sine tests

in agree well with the multi-band results, consolidated from multiple data sets, including those in Fig. 3.1-8.

Table 3.1-3. Test signal specifications for the single frequency sinusoid system identification experiments

Test No.	Test signal				Power electronics
	Frequency [Hz]		Loss injection [W]		
	Floating	Rounded	Lower bound	Upper bound	Switching [Hz]
0	0.01	0.01	20	40	5000
1	0.021544347	0.02	20	40	5000
2	0.046415888	0.05	20	40	5000
3	0.1	0.1	20	40	5000
4	0.215443469	0.2	20	40	5000
5	0.464158883	0.5	20	40	5000
6	1	1	20	40	5000
7	2.15443469	2	20	40	5000
8	4.641588834	5	20	40	5000
9	10	10	20	40	5000
10	21.5443469	20	20	40	5000
11	46.41588834	50	20	40	5000
12	100	100	20	40	5000
13	215.443469	200	20	40	5000
14	464.1588834	500	20	40	5000
15	1000	1000	20	40	10000

Table 3.1-4. Data record specifications for the single frequency sinusoid system identification experiments

Test No.	Oscilloscope							
	DAQ					ERes filtering max.		Time-domain averaging [-]
	Sampling [Hz]	Sparsing [-]	Sparsed [Hz]	s/div	Length [s]	Bits [-]	Freq [Hz]	
0	1000	1000	1	50	500	3	8	1
1	1000	500	2	50	500	3	8	1
2	1000	200	5	20	200	3	8	1
3	1000	100	10	10	100	2.5	14.5	1
4	1000	50	20	10	100	2	29	1
5	1000	20	50	2	20	1.5	60.5	4
6	1000	10	100	1	10	1	120.5	10
7	1000	5	200	0.5	5	0.5	250	20
8	1000	2	500	0.2	2	0	500	40
9	5000	5	1000	0.1	1	0	1000	100
10	5000	2	2000	0.05	0.5	0	2000	200
11	10000	2	5000	0.02	0.2	0	5000	400
12	50000	5	10000	0.01	0.1	0	10000	1000
13	50000	2	20000	0.005	0.05	0	20000	998
14	100000	2	50000	0.002	0.02	0	50000	1506
15	500000	5	100000	0.001	0.01	0	100000	4986

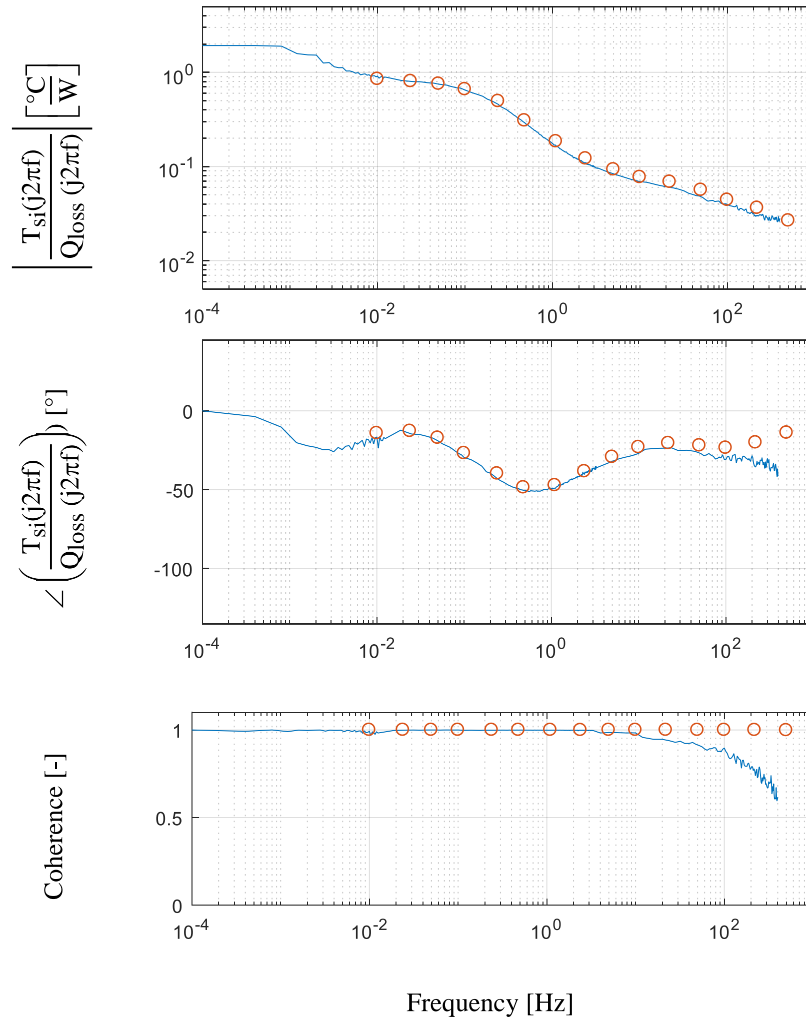

Legend: **Band-limited random noise tests** | **Single-sine tests**

Fig. 3.1-10. FRF data extracted using different experimental design specifications, including frequency content of the perturbation signal

The capability to extract coherent FRF data using multiple injection signal types has been demonstrated. Please note that single-sine results are truncated at 1 kHz because the $v_{DS(on)}$ sensing circuit limits converter switching frequency to ~10 kHz. FRF measurements of the $\Delta T^{s}_{thermistor\text{-}amb}(j2\pi f)$ / $Q_{loss}(j2\pi f)$ are truncated at 0.2 Hz due to thermistor SNR limits.

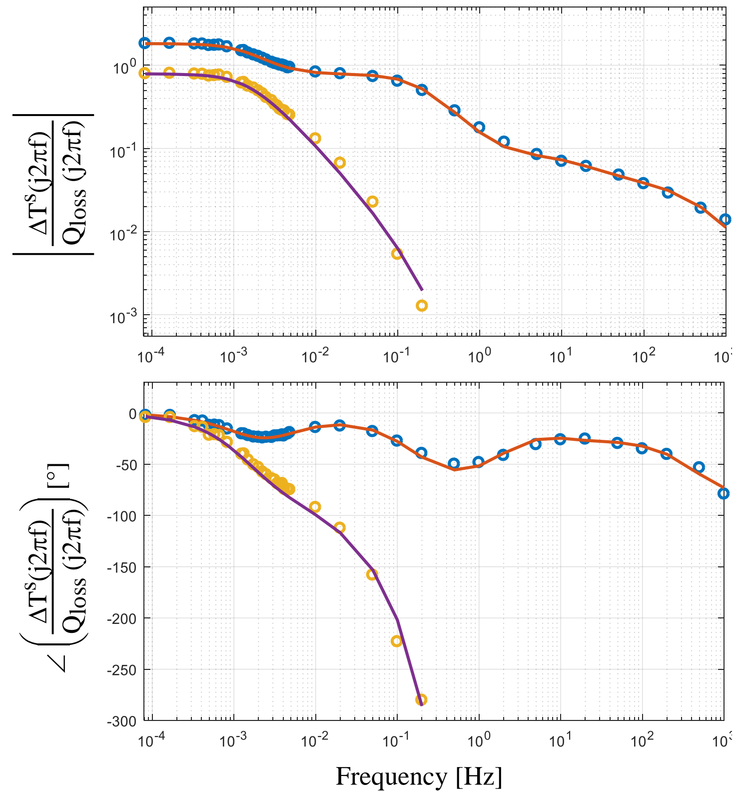

Die-to-ambient FRF: Experimental data | Curve fit
Thermistor-to-ambient FRF: Experimental data | Curve fit

Fig. 3.1-11. Overlay of a re-aggregated FRF curve, fusing results shown in Fig. 3.1-9, along with a manually fit FRF

3.1.2.4 FRF fitting and interpretation of results

To begin the theoretical component of the SETIS methodology, a manual FRF fitting procedure, following (2.2-13), was completed to parameterize the two extracted FRFs, $\Delta T^s_{die\text{-}amb}(j2\pi f)$ / $Q_{loss}(j2\pi f)$ and $\Delta T^s_{thermistor\text{-}amb}(j2\pi f)$ / $Q_{loss}(j2\pi f)$.

Die-to-ambient, driving point FRF

For the die-to-ambient FRF, it was assumed that the temperature measurement and loss injection are co-located, and the quantity is a driving point impedance. This assumption zeros the

representative diffusive time constant from (2.2-13), Additionally, $n_{zeros} = n_{poles} - 1$ in the FRF fitting procedure, following the conclusions from subsection 2.2.2.1.

During the fitting procedure, it was found that a 5-pole/4-zero network provides the best compromise between compactness and accuracy of fit to experimental data. Fig. 3.1-11 presents the die-to-ambient FRF fit model and Table 3.1-5 documents its parameters. The final column provides physical descriptions of the heat transfer process each element of the model is estimated to represent, formulated with (1.3-6)–(1.3-10).

Table 3.1-5. Summary of physical die-to-ambient FRF parameters embedded within the fit model

	Time constant [ms]	**Equivalent response freq. [Hz]**	**Associated resistance [°C/W]**	**Estimate of the associated heat transfer physics**
Slow	106 000	0.0015	1.05	bulk convection to ambient
	910	0.175	0.70	rel. distal conduction through heat sink
↓	11	15	0.033	conduction at assembly-sink TIM
	2.3	70	0.014	conduction through assembly lead frame
Fast	0.45	350	0.030	device/die-level conduction

Table 3.1-6. Thermistor-to-ambient FRF model parameters

Parameter	**Variable**	**Value**	**Unit**
Thermal resistance	R	0.79	°C/W
Lumped time constant	τ	110 000	s
Representative diffusive time constant	τ_{diff}	3.9	s
Fitting parameter	σ	0.80	–

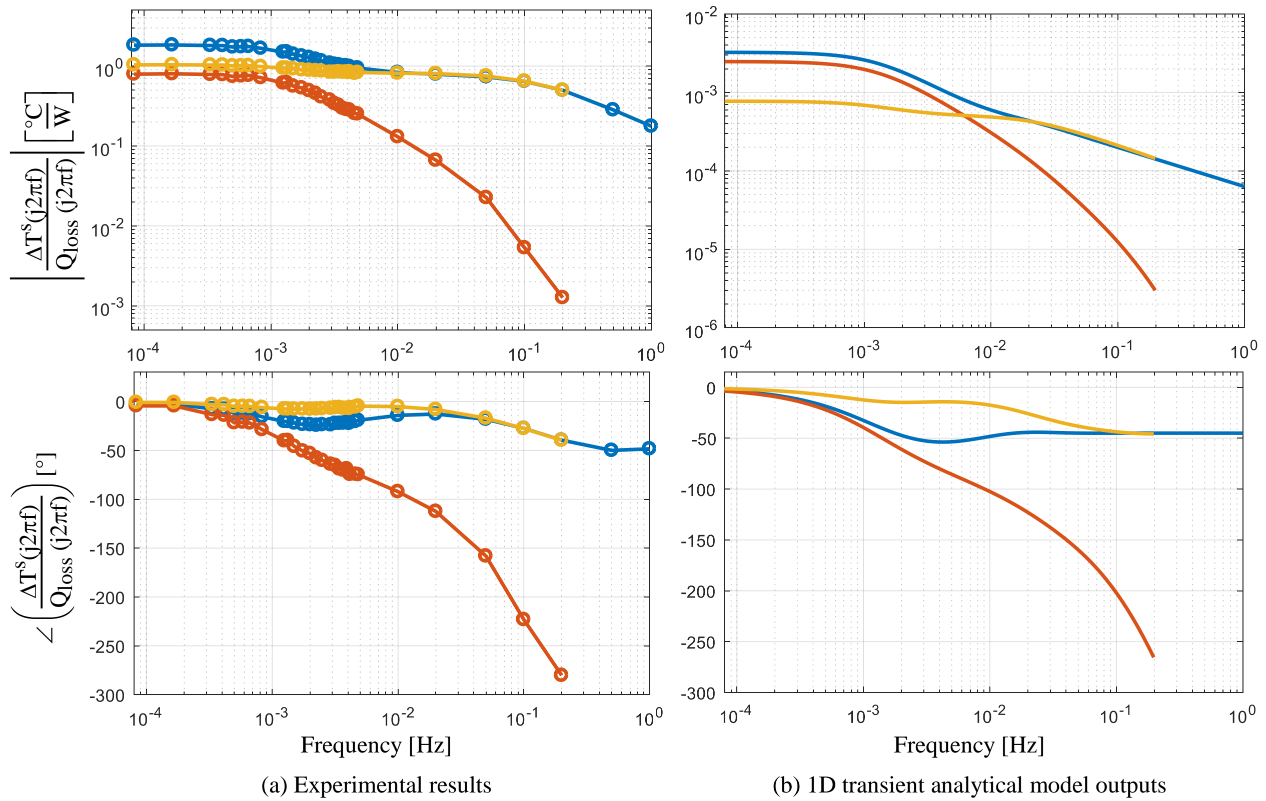

(a) Experimental results

(b) 1D transient analytical model outputs

Legend: $\frac{\Delta T^S_{die\text{-}amb}(j2\pi f)}{Q_{loss}(j2\pi f)}$ | $\frac{\Delta T^S_{thermistor\text{-}amb}(j2\pi f)}{Q_{loss}(j2\pi f)}$ | $\frac{\Delta T^S_{die\text{-}thermistor}(j2\pi f)}{Q_{loss}(j2\pi f)}$

Fig. 3.1-12. Comparison of ambient-referred and relative spatial FRF properties

Thermistor-to-ambient, distant FRF

Consistent with findings from 0, the thermistor-to-ambient (distant response impedance) in Fig. 3.1-11 has fewer pole/inflections than the driving point impedance. Therefore, during the process to fit the general model (2.2-13) with parameters to describe heat transfer in this spatial domain segment, a lower-order model was suitable. First, a total thermal resistance, R, was first estimated. Then, a lumped capacitance time constant, τ, representing bulk convection dynamics, was estimated.

Unlike for the die-to-ambient fit model, the spatiotemporal delay term was needed to achieve a high accuracy curve fit. So, during this step, continuously increasing rates of amplitude

attenuation and phase delay in the thermistor-to-ambient FRF data were quantified. The delay term D(s,x) was included and its parameters τ_d and σ were specified to maximize the accuracy of the curve fit, observable in Fig. 3.1-11. The parameters for the die-to-ambient model, following (2.2-13), are shown in Table 3.1-6.

Die-to-thermistor, relative FRF

To eliminate a dynamic element in the open-loop model, models of heat transfer for the limited die-to-sink/substrate spatial domain segment can be implemented in a DSP. By subtracting the ambient-referred FRF data from the prior two subsections, the $\Delta T^{s}_{die\text{-}thermistor}$ $(j2\pi f)$ / $Q_{loss}(j2\pi f)$ relative spatial FRF can be directly computed. The result using extracted experimental FRF data is shown in Fig. 3.1-12.(a).

In the resulting FRF, the scaling parameter associated with convection (R) is indeed reduced. However, the slow pole is not exactly zeroed, and the result is slight magnitude attenuation and phase delay around 0.002 Hz, the break frequency of the slowest (convection) pole in the system. This result has theoretical basis represented by Fig. 3.1-12.(b), which plots responses from the previously derived 1D transient model. This result shows that terms corresponding to convection dynamics must still be included to maximize accuracy of reduced-order thermal models.

3.1.3 Discussion

3.1.3.1 Identification of limits in analytical model accuracy

Comparing Fig. 3.1-12.(a) to Fig. 3.1-12.(b), it can be observed that properties of the measured $\Delta T^{s}_{thermistor\text{-}amb}(j2\pi f) / Q_{loss}(j2\pi f)$ are well captured by this highly defeatured spatiotemporal model. However, the physics of $\Delta T^{s}_{die\text{-}amb}(j2\pi f) / Q_{loss}(j2\pi f)$, a driving point impedance, and, subsequently, $\Delta T^{s}_{die\text{-}thermistor}(j2\pi f) / Q_{loss}(j2\pi f)$, are not well captured by this model. The fit is unsatisfactory, especially beyond ~0.1 Hz, where the analytical model's behavior already is asymptotic. This poor fit is attributed to the analytical model's lack of detail, e.g. geometric discontinuities, boundary conditions, and interface definitions.

However, the 1D transient analytical model, especially the spatiotemporal delay term, appears to capture diffusion physics well. It provides a more compact alternative to purely lumped models which intrinsically assume traditional (non-exponential) asymptotic FRF behavior no matter the spatial domain location of interest.

3.1.3.2 Applications for the method

Due to the 10 kHz switching frequency limit of the experimental test bed, it is acknowledged that future work is required to completely characterize the driving point impedance high frequency response property and, hopefully, identify the asymptotic behavior. On the other hand, the high frequency behavior for devices relatively distant from heat sources has been established. This result is generally relevant for accurate integration of thermistor device feedback into observers, or modeling responses of devices located in multi-chip modules, referred to as thermal cross-talk.

The collective methodology and analysis documented in Chapter 2 and now provides the spatiotemporal thermal response modeling groundwork needed to make necessary improvements in state-of-the-art active thermal-mechanical control systems, and fatigue modeling, which can

examine temperature and strain gradients, rather than lumped quantities. More immediately, upon loss characterization and temperature detector commissioning, the methodology can potentially be used for comprehensive, assembly end-of-line evaluation of assembled converters.

3.1.4 Model-Experiment Correlation

3.1.4.1 Model definition

Die-to-ambient and heat sink-to-ambient FRFs have been extracted from a prototype DC-DC converter, Fig. 3.1-5, using system identification. Response parameters, i.e. thermal resistances and time constants, were extracted during post-processing steps in this study. This section compares outputs of an FE model to those from system identification to evaluate accuracy of the modeling approach.

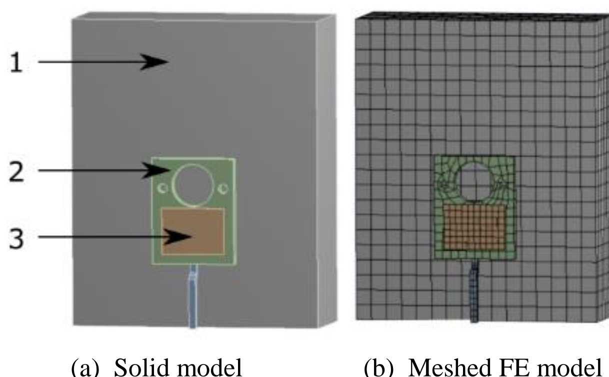

(a) Solid model (b) Meshed FE model

Fig. 3.1-13. Simplified FE model in which component 1=heat sink, 2=lead frame (LF), and 3=silicon die

The geometry of a developed FE model, shown in Fig. 3.1-13, was simplified to reduce mesh requirements and computation. It had 3410 nodes and 2447 linear elements throughout the three solids in the assembly model: a heat sink, lead frame with drain terminal, and a silicon semiconductor device. Heat losses were modeled as a surface heat flux aimed at the front of the semiconductor device, like Fig. 2.3-2(a). All exposed surfaces were convective boundaries.

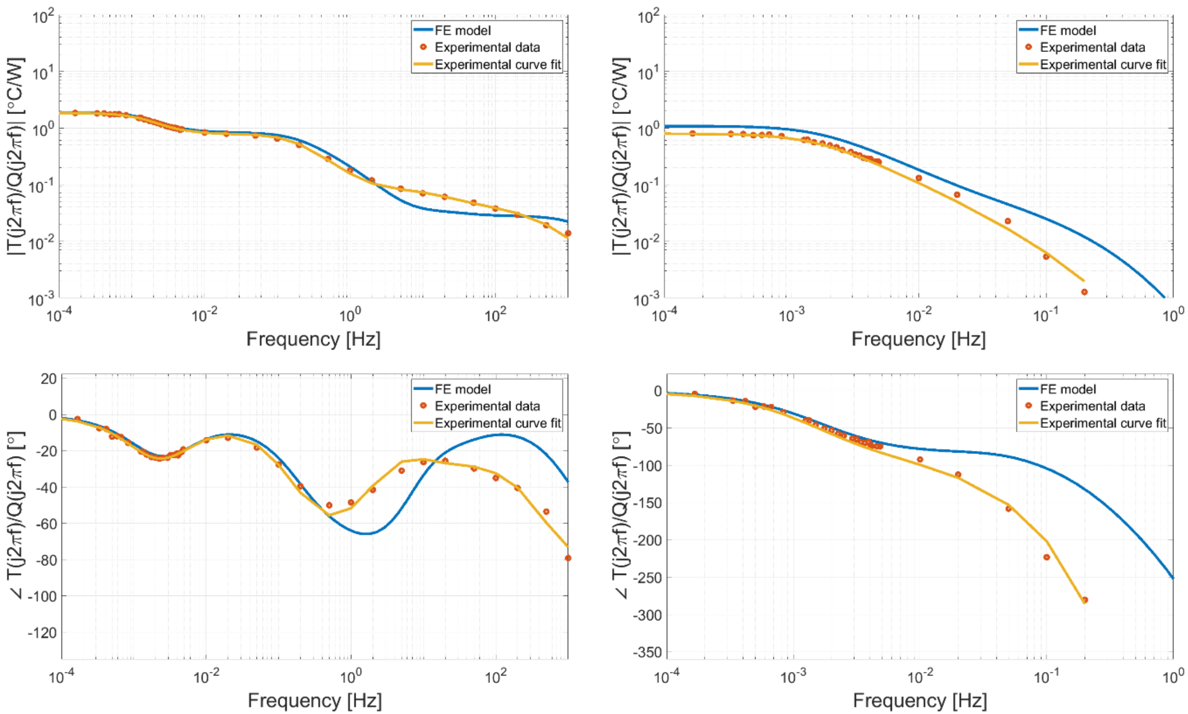

(a) Magnitude and phase, die-to-ambient (b) Magnitude and phase, thermistor-to-ambient

Fig. 3.1-14. Spatial FRFs comparing the FE-based and experimentally measured responses

3.1.4.2 Overlay of results

Fig. 3.1-14 shows die-to-ambient and sink-to-ambient FRFs from model and experiment and Table 3.1-7 presents three lumped resistances of the model. The FRFs in Fig. 3.1-14 quantify the dynamic thermal response of two points in the assembly: (1) the MOSFET device and (2) the outer surface of the heat sink, measured with a thermistor.

Model FRFs were obtained with silicon, copper, and aluminum material properties specified at 22°C. Since materials can be specified by in the *ANSYS* interface, the method is effectively applying a thermal small signal analysis when working with materials having non-negligible temperature dependency. As highlighted before, FRFs obtained with models having different material properties can be directly compared to quantify nonlinearity.

Table 3.1-7. Lumped thermal parameters embedded within the FE model

Variable	Description	Value [°C/W]
① R_{conv}	Convection resistance – external surfaces to ambient	1.1
② $R_{LF\text{-}Sink}$	Contact resistance between the lead frame (2) and heat sink (1)	0.65
③ $R_{Si\text{-}LF}$	Contact resistance between the die (3) and lead frame (2)	0.025

3.1.4.3 Sensitivity function correlation method

Efforts to correlate model and experiment initially utilized lumped thermal resistance and time constant parameters obtained from post-processing to specify boundary conditions and contacts. The subsequent fitting process then manipulated the parameters listed in Table 3.1-7, two thermal contacts and a convective resistance, using detailed parameters embedded within the *ANSYS* model.

Normalized sensitivity functions were utilized to identify frequency bands influenced by specific model parameters and ultimately tune the model. For example, the dashed red trace in Fig. 3.1-15 shows the result of the normalized die-to-ambient FRF response in which R_{conv} is increased 50% from its original value of 1.1 °C/W, while the other two parameters were kept constant. Similarly, the dashed orange trace quantifies variation if $R_{LF\text{-}Sink}$ increases by 200%.

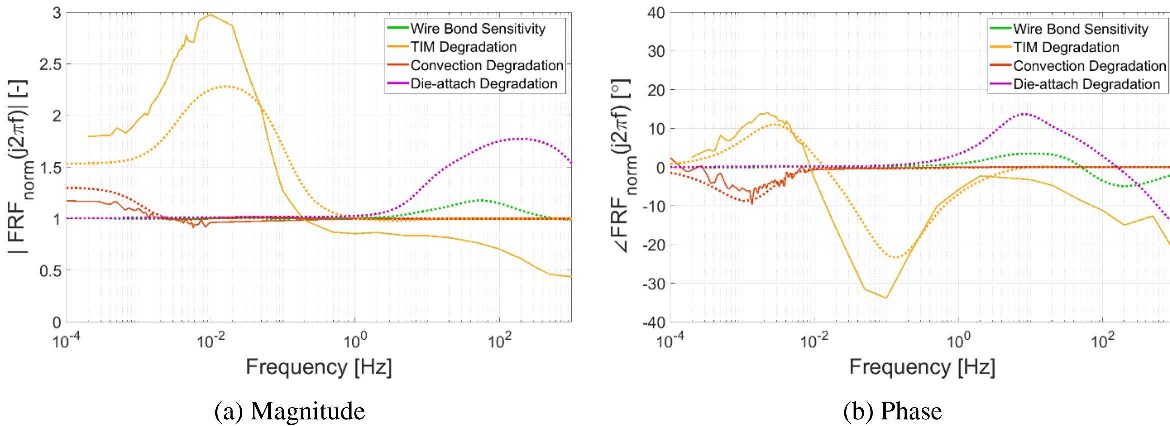

(a) Magnitude (b) Phase

Fig. 3.1-15. Die sensitivity functions showing how degradation in terms of R_{conv} (50%), $R_{LF\text{-}Sink}$ (200%), $R_{Si\text{-}LF}$ (100%), and the absence of wire bonds affect the die-to-ambient response; experimental traces are solid lines and model-derived traces are dotted lines

3.1.4.4 Regime-specific agreement

Die and heat sink response in the low frequency regime

Fig. 3.1-14(a-b) show that the die response model and experimental result match below ~1 Hz. At these relatively low frequencies, details near the die negligibly impact the response; in this regime, the die-to-ambient response can be treated as a low-order lumped capacitance without incurring substantial errors.

The large amount of solid material between heat dissipation in the device and the outer surface of the heat sink attenuates the outer surface's AC response, so the heat sink-to-ambient FRF shown in Fig. 3.1-14(c-d) is truncated at 1 Hz. R_{conv} and $R_{LF\text{-}Sink}$ have the most dominant effect on the heat sink-to-ambient response, with R_{conv} impacting frequencies from DC to 10 mHz and $R_{LF\text{-}Sink}$ impacting frequencies from 10 mHz to 1 Hz. Attempts to further reduce the difference between model and experimental measurement of the heat sink's response in Fig. 3.1-14(c-d) were limited. Differences in heat sink-to-ambient FRF are expected to be a result of the FE model not including the thermistor.

Die response in the high frequency regime

Above 10 mHz, the model and experimental curves in Fig. 3.1-14(a-b) have similar wavy shapes. However, the accuracy is limited. Variations in geometry or boundary conditions close to the die were observed to cause the response of the model to change in this high frequency regime. Specifically, this response is highly sensitive to the $R_{Si\text{-}LF}$ contact resistance parameter, representing the die-attach interface, whose effect is shown in Fig. 3.1-15 for 100% degradation for illustration. As shown by the difference between the curves in Fig. 3.1-14(a-b), efforts to close the gap between model and experiment by manipulating this parameter were limited at the time of this publication.

Please recall that TSEPs were used during application of system identification in the lab. More specifically, $R_{DS(on)}$ was correlated to a single pixel of an IR measurement of the die during a pre-calibration. A corresponding curve fit was ultimately implemented in control software to estimate die temperature in real-time.

3.1.4.5 Uncertainty quantification

Die temperature sensing location uncertainty

Simulated die temperature response depends on the FE node(s) selected to represent the die temperature state. Indeed, the die-to-ambient FRF in Fig. 3.1-14 is spatially-averaged response of nine nodes in the model. Fig. 3.1-16 displays the isolated responses of the nine averaged nodes. The envelopes of the traces in this figure quantify the uncertainty of the model response in Fig. 3.1-14(a-b).

Even after the IR-based calibration procedure executed in the lab focused on a single pixel, it cannot yet be said with exactness the die location's temperature that the $R_{DS(on)}$ TSEP captured.

However, the results in Fig. 3.1-16 quantify the importance of correctly specifying the physical location of the die temperature sense point in terms of resulting model accuracy.

Spatial distribution of losses

Simulated FRFs also depend on how conduction and switching semiconductor device losses are distributed in the spatial domain. Prior results modeled these losses as a surface heat flux, having units of W/m^2. To properly dimension FRFs with losses modeled as a surface flux, 1 W was divided by chip surface are within the *ANSYS* environment. A more physical option would be to distribute the losses within the spatial domain, such that the implemented units would be W/m^3.

To identify how spatial distribution of losses impact FRF outputs, a simulation case was executed in which the FE model setup was identical except for the spatial model of losses. For the comparison case, losses were distributed uniformly within the volume of the semiconductor chip. Fig. 3.1-17 plots the response sensitivity. It shows that the sink-to-ambient FRF is not sensitive to the spatial modeling of the loss excitation. On the other hand, the die-to-ambient FRF exhibits sensitivity to this modeling detail beginning at approximately 10 Hz.

The result suggests that caution must be practiced when modeling high frequency thermal impedance response spectra, especially degradation sensitivities therein. To close the gap between modeled and experimental FRFs, detailed insight regarding the spatial distribution of losses must be obtained. For a model-based approach, technology computer-aided design (TCAD) packages, for example, *Sentaurus Device*, a *Synopsys* software product, are capable of executing such device-level FE simulations [169].

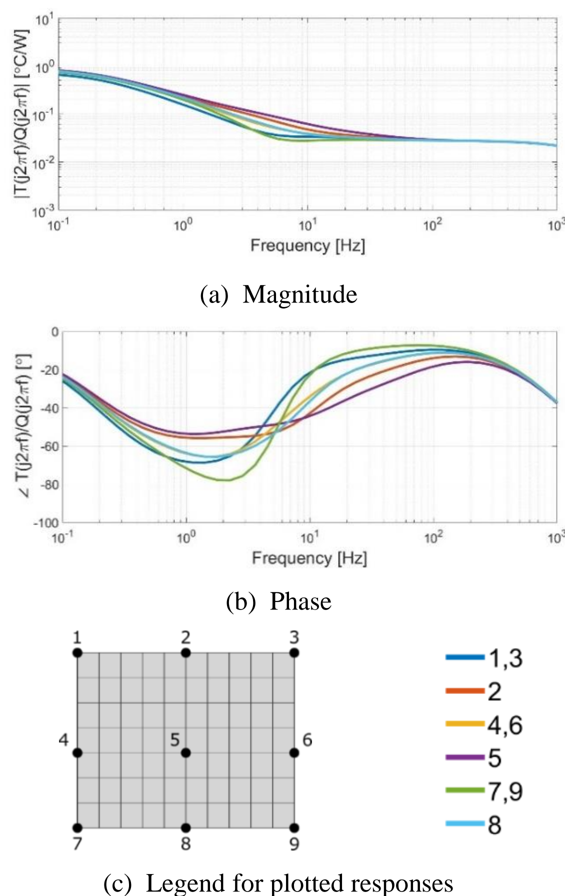

(a) Magnitude

(b) Phase

(c) Legend for plotted responses

Fig. 3.1-16. Die-to-ambient FRF for nine nodes on the die surface

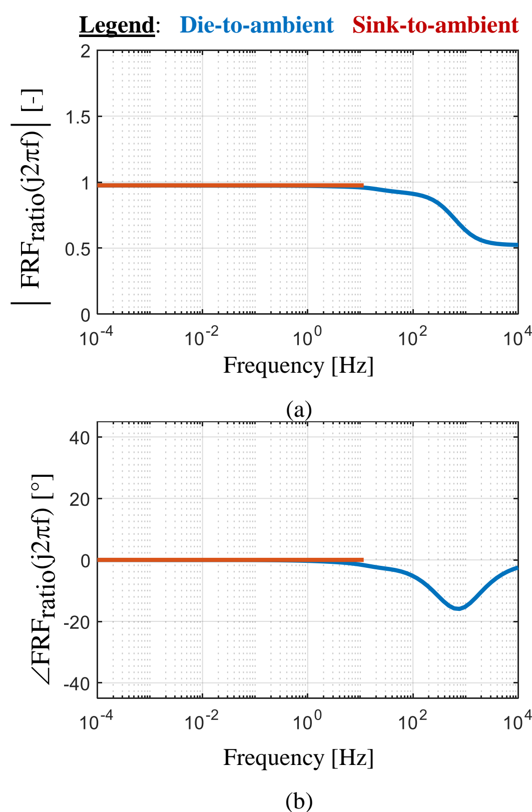

(a)

(b)

Fig. 3.1-17. Ratio of FRFs extracted with total losses represented as (1) die surface heat flux and (2) internal, volumetric generation

3.1.4.6 Discussion

In the overall body of simulation work completed, detailed features not in the main vertical path of heat conduction (die to substrate to sink) have less impact on transient heat transfer than those within it. It is therefore concluded that inexact model specifications near the semiconductor die, such as spatial distribution of the losses and the topography of the die-attach interface, are sources of error that limit accuracy of the medium-to-high frequency die response accuracy in Fig. 3.1-14. However, any desires to enhance the fit must be balanced by limits identified via uncertainty analysis and quantification.

3.1.5 Section Summary

This section predominantly presented the experimental component of a converter-integrated systems identification method. First, steps for treating an active power electronic converter as a heat transfer experiment were outlined. Included in the documentation is a loss modulator design method and a parameter sensitivity study, detailed best-practice instructions for designing system identification experiments with a balance between experimentation time and the extent to which the dynamic range of the power converter system is characterized in terms of coherent FRF data.

Next, this subsection documented the application of the method on a power electronic system. Documented are discussion of the experimental setup, presentation of intermediate results, parameterized physics-based models following the proposed reduced-order model template from subsection 2.2.3, interpretation of the experimental results obtained, and a comparison of experimentally results with those obtained from models. The section concluded with comments about the limits and utility of systems identification.

3.2 Component-Level System Identification

ETIS system identification can be deployed while a converter is actively switching. As this section will show, it can also be deployed while embedded semiconductor devices are at least temporarily in the on-state. This ex situ version of the method can characterize individual semiconductor components and modules before they are installed in a converter, as well.

It is desired for an ex situ characterization technique to be simpler and faster to execute than the converter-integrated variant. Fig. 3.2-1 illustrates an ex situ method, which is similar to prior developments: harmonic heat excitation, $P_{loss}(t)$, is actuated by semiconductor device conduction and/or switching losses, and die temperature is concurrently estimated using a device TSEP.

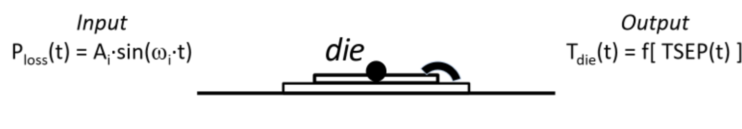

Fig. 3.2-1. Operating principle of an ex situ ETIS method

This section will explore how intrinsic semiconductor device properties can be utilized to simplify the temperature estimation, i.e. relax the need for a detailed, multi-variable look-up table or function to relate die temperature to the TSEPs. It will be shown how FRFs can be estimated using a device's forward conduction property with load current independence. The presented developments in this section aim to identify minimal TSEP calibration requirements for extracting coherent FRF data and enable a less resource-intensive characterization method.

3.2.1 Method Development

3.2.1.1 Passive conduction loss modulation

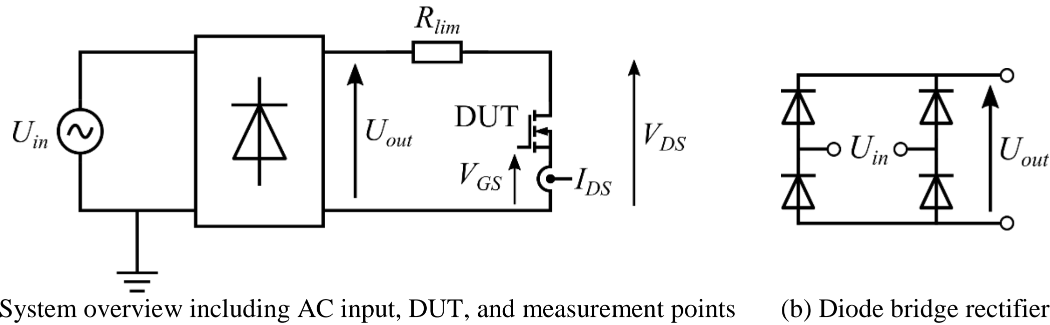

(a) System overview including AC input, DUT, and measurement points (b) Diode bridge rectifier

Fig. 3.2-2. Schematic drawings of the passive conduction loss modulation circuit

Counter to prior characterizations which worked with actively switching devices, current developments examine a DUT while a fixed gate-to-source voltage, V_{GS}, is applied to it. Then, sinusoidal losses are dissipated in the DUT.

Fig. 3.2-2 illustrates a circuit, based on a standard diode bridge rectifier, for implementing the method. An AC source voltage, U_{in}, is first delivered to the diode bridge to produce a rectified AC output voltage, U_{out}, at a frequency twice the fundamental frequency of U_{in}. Circuit analysis results in expressions (3.2-1) and (3.2-2) describing the DUT loss dissipation. Dissipated conduction losses can be observed to have a DC offset and a single harmonic component. The loss amplitude parameter, K, can be adjusted via the amplitude of the AC input voltage, U_o, and the current limiting resistor, R_{lim}.

$$Q_{loss} = {}^{1}\!/_{2}\, K\, (1 - cos(2\omega t)) \quad (3.2\text{-}1)$$

$$K = \frac{U_o^2\, R_{DS,on}}{\left(R_{lim} + R_{DS,on}\right)^2} \quad (3.2\text{-}2)$$

3.2.1.2 Nonlinear chip temperature self-sensing

Experiments documented in prior sections illustrated the multi-variable dependence of a semiconductor device’s forward conduction property on its on-state current and temperature. Fig. 3.2-3 illustrates these properties for a commercial SiC power MOSFET component.

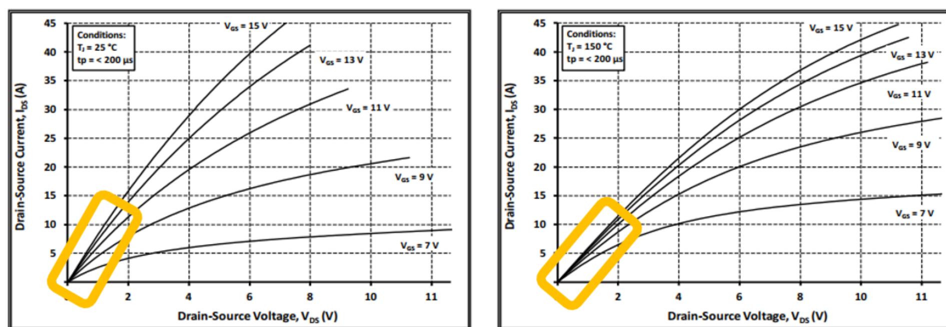

(a) Output characteristics at 25°C and 150°C die temperatures

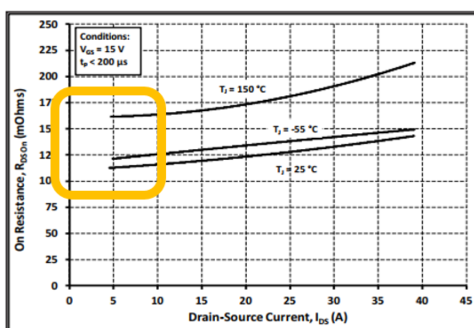

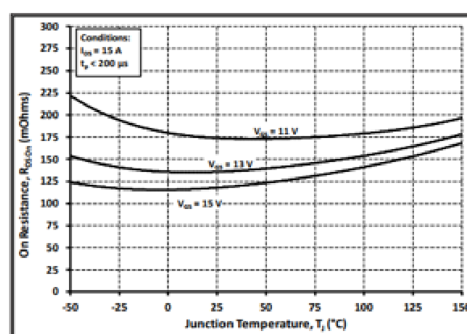

(b) On-state resistance v. drain-source current

(c) On-state resistance v. die temperature

Fig. 3.2-3. Selected properties of a C3M0120100K SiC MOSFET component [170]

Fig. 3.2-3(a) shows the relation between on-state, drain-source current of the MOSFET. It can be observed that this relationship changes between 25°C and 150°C device temperature, providing another perspective to observe that MOSFET on-state resistance, $R_{DS,on}$, is sensitive to device temperature. Fig. 3.2-3(b) displays the data captured by Fig. 3.2-3(a) in a different way to explicitly show the device output property for a fixed V_{GS}. Fig. 3.2-3(c) next illustrates the dependency of on-state resistance on temperature.

The sensitivity illustrated by Fig. 3.2-3(c) has already been and will continue to be exploited to estimate die temperature. However, for this ex situ implementation, experiments will conceptually operate within the boxes included in Fig. 3.2-3 such that the measured value of $R_{DS,on}$ is independent of current. Thus, as shown in Fig. 3.2-1, die temperature is extracted from a single TSEP, $R_{DS,on}$, rather than $R_{DS,on}$ and load current.

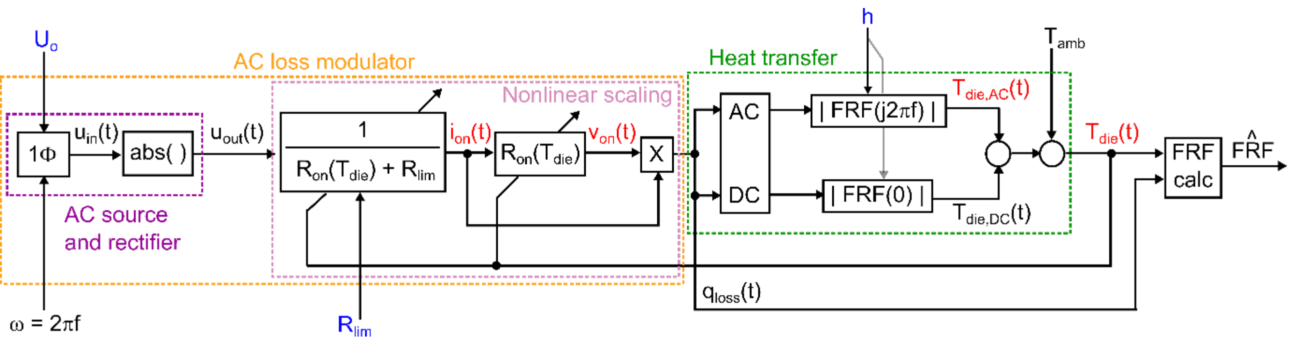

Fig. 3.2-4. State block diagram of the ex situ system identification experiment using a diode bridge rectifier for passive loss modulation; experimental parameters are blue colored, while constrained variables are red

3.2.1.3 Limits of system identification experiments

Parameter sensitivity analysis

A state block diagram of ex situ electrothermal impedance spectroscopy is shown in Fig. 3.2-4. It shows two major subsystems – an AC loss modulator, comprised of nonlinear scaling and an AC source and rectifier, and transient heat transfer. An excitation frequency, ω, of a dynamic range desired for characterization is an input to the method. As shown on the right side of Fig. 3.2-4, acquiring FRF data at these discrete frequencies is the objective.

Fig. 3.2-4 shows, in blue text, independent variables governing a system identification experiment. For example, the amplitude of the input AC voltage, U_o, is a free parameter. R_{lim} and a representative convective heat transfer coefficient, h, are also listed as parameters for manipulation. The figure also shows constrained parameters, in red colored text. For instance, to maximize SNR of probed signals, $i_{on}(t)$ and $v_{on}(t)$ should be large. It is also desired to maximize the AC response component of $T_{die}(t)$, labeled as $T_{die,AC}(t)$, to ensure AC temperature response can be induced and measured, even at high frequency.

On the other hand, $T_{die}(t)$ cannot exceed a component maximum, typically listed around 150°C in data sheets, to prevent its self-destruction. Although not listed, in future developments of optimal electrothermal impedance spectroscopy characterization methods and products, duration of experiment should also be listed as an independent variable or constraint.

Cooling limitation

Each constraint and manipulated input could be analyzed in detail to quantify their overall impact on experiments. As an example, one limit of h is now quantified.

Prior modeling and experimental work illustrated how only low frequency thermal response is sensitive to this parameter. If ex situ system identification were used to characterize status of a semiconductor die-attach, it would be desired to ensure the test was insensitive to cooling. Subsequently ensuring the break frequency corresponding to convection, (3.2-3), is 1-2 orders of magnitude less than the smallest fundamental frequency to be characterized, achieves this insensitivity.

$$f_{conv} = \frac{1}{2\pi \cdot \tau_{conv}} = \frac{1}{2\pi} \cdot \frac{h \cdot A_{surface}}{m \cdot c_p} \qquad (3.2\text{-}3)$$

Eq. (3.2-3) is a function of materials intrinsic to a component: surface area, mass, and specific heat capacity. It can be evaluated using a DUT parameters to ensure h does not cause a constraint violation. To provide a more comprehensive evaluation, a rectangular block with length ratio 1.0 x 0.3 x 0.1 (Fig. 3.2-5) was analyzed using density ρ = 5000 kg/m^3 and c_p = 500 J/kg-K. With a factor of 100 separation between f_{conv} and smallest desired system identification frequency, three potential minima for smallest frequency were analyzed, and the largest width dimension of the rectangular part was swept.

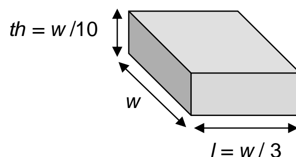

Fig. 3.2-5. Example lumped capacitance block

Fig. 3.2-6 shows that larger thermal convection resistance and, thus, smaller values of h are needed for the purpose of desensitizing an experiment to cooling dynamics. It shows how a requirement to characterize FRF down to 1 Hz imposes a challenging maximum h of around 200 W/m^2-K for a 10 mm DUT. However, the figure also includes an evaluation of the model using dimensions and material properties more resembling the DUT used later during tests. This

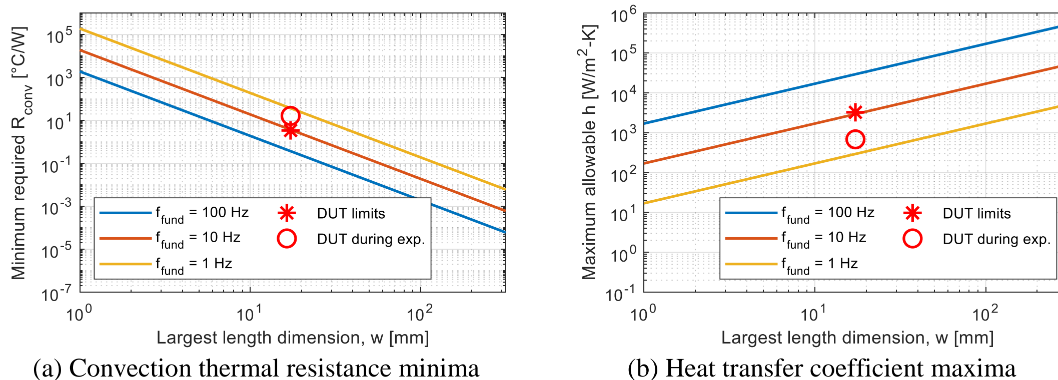

(a) Convection thermal resistance minima (b) Heat transfer coefficient maxima

Fig. 3.2-6. Analytically derived limits to cooling for ensuring its impact on ETIS is negligible

evaluation shows these estimates satisfy the constraint, and that an estimate of the convection resistance and heat transfer coefficient of executed experiments also satisfy limits.

3.2.2 Application of the Method

3.2.2.1 Hardware setup

A test bench to realize Fig. 3.2-2 was built using a *Pacific SmartSource 345-ASX* AC power supply and a *KBPC2504* diode bridge rectifier module. A 10 Ω, 100 W cannister-shaped resistor was utilized as R_{lim}, and measurements were made using *Teledyne LeCroy CP030* current and *HVD3106* differential voltage probes connected to a *HDO6054* oscilloscope.

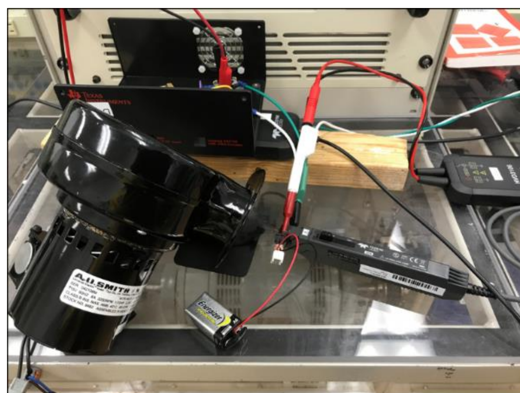

(a) Hardware overview including DUT, blower, and probes

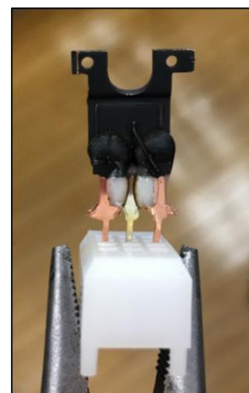

(b) Decapsulated Fuji 2SK3677 silicon power MOSFET with matte black paint

Fig. 3.2-7. Equipment used during experimental application of the ex situ ETIS method

Fig. 3.2-8. Time-domain data from an ex situ ETIS experiment at f_{fund} = 100 Hz

Decapsulated *Fuji 2SK3677* discrete power MOSFETs were utilized as DUT for tests. As Fig. 3.2-7 shows, the DUT was installed in a plastic fixture which had sockets for probes. Throughout all experiments, it was kept in the on-state by applying $V_{GS} \approx 9$ V with a battery. A centrifugal fan was directed aimed at the DUT.

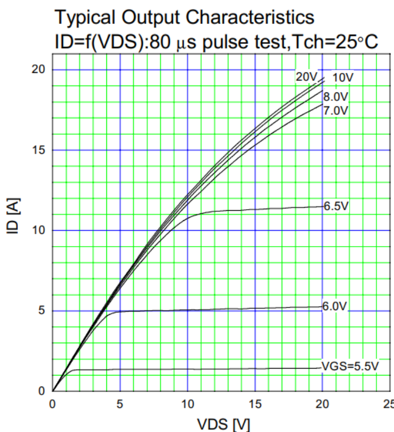

Fig. 3.2-9. Output characteristic of the DUT, Fuji 2SK3677

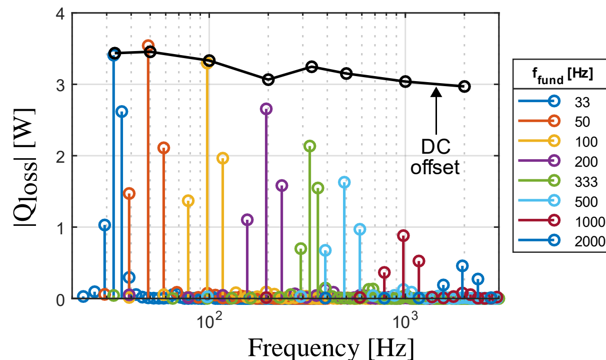

Fig. 3.2-10. Measured power loss AC and DC content

3.2.2.2 Baseline results

Experiments were carried out within the range of the AC source utilized in the lab – approximately 30-2000 Hz conduction loss fundamental frequency. A screenshot of time domain data is shown in Fig. 3.2-8. It shows v_{DS} and i_{DS} in the top-left and -right windows, respectively. The bottom-left window overlays DUT conduction losses (in blue) along with its on-state resistance. The bottom-right window shows an estimate of MOSFET die temperature computing using oscilloscope arithmetic (in red) and an FFT spectrum of the losses.

Conduction loss FFT spectra, computed by the oscilloscope, were consistently recorded during variable frequency experiments. They, along with DC offset of the loss excitations, are collectively shown in Fig. 3.2-10 for each of the test frequencies. Peaks at the loss excitation frequency can be observed, along with the diminishing amplitude of the harmonic peaks. This non-ideal property is attributed to the non-ideal diode bridge rectifier employed during experiments. Despite this attenuation, computed high frequency FRF data had coherence ≈ 1.

An initial FRF is displayed in Fig. 3.2-11. It quantifies transient heat transfer across approximately two decades of response. Please note, although not graphically shown, that coherence greater than 0.99 was measured for each displayed data point.

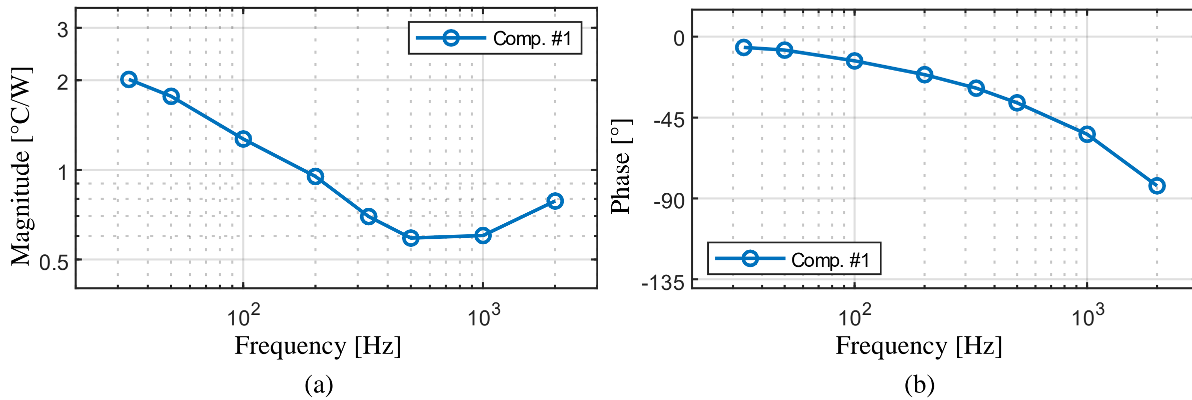

Fig. 3.2-11. Baseline experimental FRF extracted using ex situ ETIS

Table 3.2-1. Die TSEP parameters used to study sensitivity of the FRF

Eq.	A_1	A_2	A_3	B_1	B_2	C_1
(3.2-4)	100	–	–	–	–	-40
(3.2-5)	120	–	–	–	–	–
(3.2-6)	290	-110	20	–	–	–
(3.2-7)	100	–	–	-0.2	–	–
(3.2-8)	1000	-100	–	0.1	0.2	0.1

3.2.2.3 Sensitivity analysis

Die temperature estimation

The FRF shown in Fig. 3.2-11 was estimated using linear TSEP model (2.3-1), populated with parameters shown in Table 3.2-1 which were formed by curve fitting a data sheet plot; separate, dedicated calibration experiments were not executed. The post-processing framework to compute FRF data was utilized to quantify the sensitivity of resulting FRF estimates to the functional relationship between die temperature, on-state resistance, and load current.

$$T_{die} = A_1 R_{DS,on} + C_1 \tag{3.2-4}$$

$$T_{die} = A_1 \log\left(R_{DS,on}\right) + C_1 \tag{3.2-5}$$

$$T_{die} = A_1 R_{DS,on} + A_2 R_{DS,on}^2 + A_3 R_{DS,on}^3 \tag{3.2-6}$$

$$T_{die} = A_1 R_{DS,on} + B_1 I_{DS,on} \tag{3.2-7}$$

$$T_{die} = A_1 R_{DS,on} + A_2 R_{DS,on}^2 + B_1 I_{DS,on} + B_2 I_{DS,on}^2 + C_1 R_{DS,on} I_{DS,on} \tag{3.2-8}$$

Eq. (2.3-2)–(3.2-8) present additional models included in the sensitivity analysis. These models are referred to as logarithmic, cubic, multi-variable-linear, and multi-variable quadratic. Table 3.2-1 documents model parameters.

Eq. (2.3-1), with parameters listed in Table 3.2-1, was utilized as the control for the analysis, which means its corresponding FRF data was utilized as baseline for computing sensitivity functions. For the response plot Fig. 3.2-12, the second, red curve utilized linear model (2.3-1) with A_1 increased by 50%, while all other responses utilized (2.3-2)–(3.2-8) and Table 3.2-1 parameters directly.

Fig. 3.2-12 generally shows that the selected TSEP model influences extracted FRFs. The amplitude of the extracted FRFs are scaled approximately linearly when using different models to estimate die temperature, with amplitude errors between 5 and 50%. Sensitivity of the phase response is not so straightforward. The multi-variable TSEP relationships indicate increasing high frequency sensitivity, while the sensitivity function for FRF data extracted with models excluding $I_{DS,on}$ is negligible.

If sufficiently small currents were utilized, and experiments operated in a space where the current-independence assumption is accurate, then Fig. 3.2-12 indicates the following: phase responses, estimated using a model relating only $R_{DS,on}$ to die temperature, are accurate. For this reason, and since the phase response sensitivity functions for the linear, logarithmic, and cubic models in Fig. 3.2-12(b) are nearly zero, FRF calculations only need loss and raw $R_{DS,on}$ time

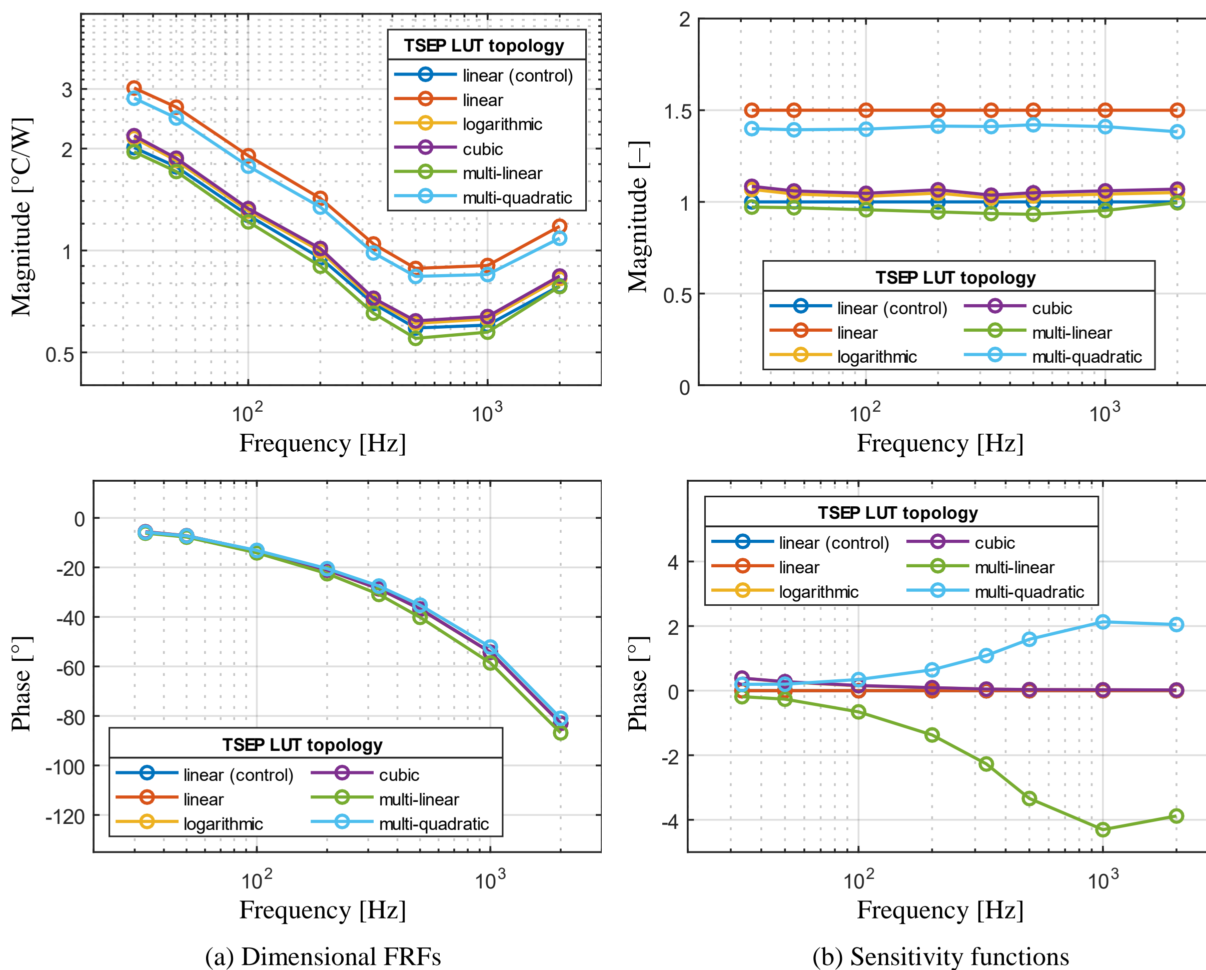

(a) Dimensional FRFs

(b) Sensitivity functions

Fig. 3.2-12. Experimental FRF of component #1 estimated with five different die temperature sensing LUTs

series data; a relationship quantifying how die temperature and $R_{DS,on}$ is not needed to obtain accurate FRFs.

This conclusion implies that compact dynamic thermal models can be constructed based on measurements of encapsulated components, using only measured phase response and an estimate of a component's static DC gain thermal resistance.

Part-to-part variation

To conclude the experimental investigation, three additional *Fuji 2SK3677* MOSFET components not having any die-attach alterations were characterized using ETIS. The phase

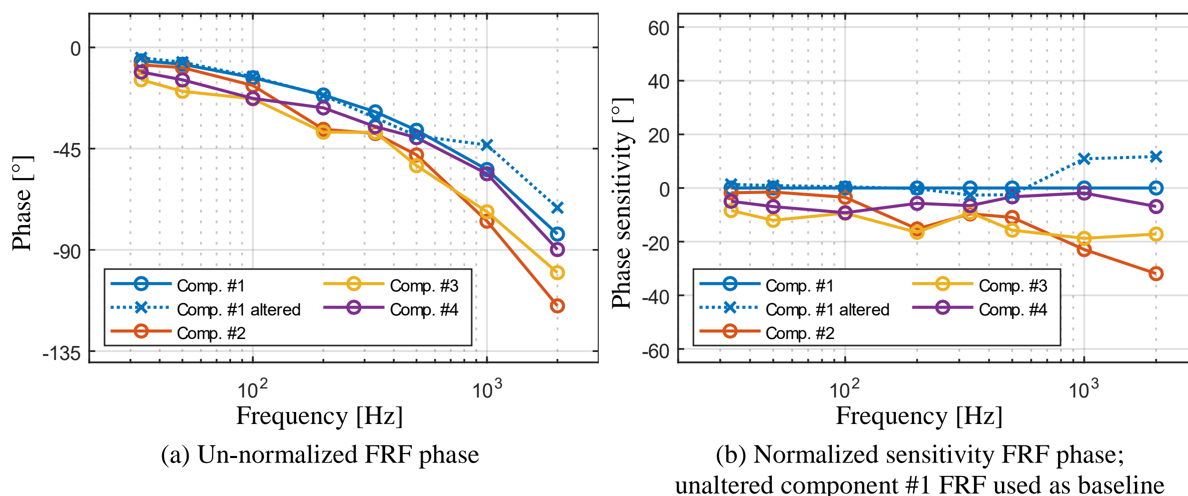

(a) Un-normalized FRF phase

(b) Normalized sensitivity FRF phase; unaltered component #1 FRF used as baseline

Fig. 3.2-13. Phase FRF with degradation to the die-attach interface of the DUT

components of the measured FRF and sensitivity functions are displayed in Fig. 3.2-13. At low frequency, the measured difference in phase response values is about 10°, while around 40° at higher frequency. These differences are significantly larger than the effective tolerance shown in the phase plot of Fig. 3.2-12(b).

3.2.3 Discussion

3.2.3.1 Study limitations

The contents of the executed study represent a significant contribution to the power electronics community. The following limitations are however identified to guide future work. First, as can always be said, it desired to characterize a wider frequency range, with a higher density of tested frequency points. FRFs presented in this section comprise 8 discrete test frequencies for conservative reasons related to quality assurance of data: only FRF data at the fundamental frequency of the loss perturbation, with coherence ≈ 1 were retained. Harmonics of the extracted time-domain data could be analyzed to further resolve FRF plots. Related, harmonics apparent in time domain responses, which are visible in the bottom-right window of Fig. 3.2-8, for example,

should be further characterized. Analysis stemming from Fig. 3.2-4, especially focusing on nonlinear response properties, can support this goal. Finally, Fig. 3.2-7(b) illustrates how the DUT was fixtured in a plastic-encapsulated component. Sensitivity of FRF measurements to the fixturing of the test MOSFETs could be measured.

3.2.3.2 Industrial application

Prior executions of converter-integrated ETIS were relatively time consuming because of the larger thermal capacitance/mass of evaluated converter systems and limits of embedded voltage and current sensors. This section presented a method for a single power semiconductor component or module outside of its converter application, using oscilloscope measurements to achieve higher accuracy and SNR. Especially given the critical assumption about single-variable temperature sensitivity, it simplifies characterization of heat transfer FRF properties.

The most significant result of the section identified the high frequency impact of a die-attach alteration on a measured FRF during a single controlled test. Models developed in this document generally predicted high frequency sensitivity of die-attach degradation. The most significant theoretical outcome of this section is the conclusion that a measured phase response can be used in tandem with a DC gain value to form compact thermal models without access to a semiconductor die. This knowledge can allow for related research to be executed faster.

3.2.4 Section Summary

This section presented a less integrated, but faster and simpler method to characterize transient heat transfer with FRFs. Unlike converter-integrated ETIS, the presented method utilizes direct conduction loss manipulation to operate upon a semiconductor DUT while it is gated on. An

embodiment of the method, utilizing an established power electronic circuit topology, was presented. It allowed for the relatively rapid characterization of discrete semiconductor components. Select results quantified transient thermal response sensitivity to a fabricated alteration of a semiconductor component's die attach, and quantified sensitivity of measurements to parameters governing a nonlinear die temperature estimator.

3.3 Chapter Summary

This chapter developed methods for measuring transient heat transfer FRFs in power electronic equipment using dynamic self-heating of embedded semiconductor devices. The first method can characterize an assembled converter in active, switch-mode operation. Design of an active loss modulation system to implement the method was developed. Following parameter sensitivity analysis revealed its insensitivity in terms of phase. Next, the utilization of TSEPs and other embedded temperature detectors was introduced, and system identification experimental design was discussed. The method was applied to a converter prototype. Spatial FRF data having near-unity coherence, including 7 decades of die-to-ambient response, were extracted. Fitting of data using lumped model illustrated a good fit to a compact model.

A complementary method, using harmonic conduction loss passively modulated via a power electronic circuit, was then investigated. Parameters governing power electronic circuit and DUT cooling were identified and analyzed to identify constraints and tradeoffs which govern system identification experiments. For this second method, the DUT remains in the on-state, allowing for its response to be characterized outside of an assembly with several layers and unknown values of contact resistance. Application of the method to discrete MOSFET components without heat sinking allowed for relatively rapid characterization. Sensitivity of the method to

empirical parameters of a TSEP regression model and part variation were identified, respectively, using numerical and experimental approaches.

Chapter 4 Sensitivity of Heat Transfer Frequency Response to Degradation

A research goal is to integrate systems for thermal-mechanical degradation detection and diagnosis into converter systems. This chapter documents an initial step toward this end: identifying which properties change with degradation and quantifying the form and extent of changes. To start, a scope of degradation sources and sensitivity metrics are defined. Next, analytical and numerical models are used to emulate impacts of degradation on heat transfer. Resulting scalar and vector electrothermal impedance figures are interpreted using FRF and complex impedance plots. Finally, converter- and component-level heat transfer sensitivities to thermal-mechanical defects are experimentally investigated. Elements of this chapter are also documented in publications [159], [160], [171].

4.1 Operational Definitions

4.1.1 Scope of degradation sources

The three sources of thermal-mechanical degradation targeted for eventual real-time, in situ identification are:

1. Cooling system degradation – due to changes in fluid or pump properties
2. Thermal interface material (TIM) degradation – due to material displacements, i.e. creep, and manifests as interface asymmetries or voiding
3. Solder interface degradation, especially at the die-attach – due to material displacements, i.e. creep and delamination, and manifests as voiding

4.1.2 Degradation sensitivity metrics

Previous chapters documented the usage of FRF and complex SETI/ETI as metrics for viewing the open-loop electrothermal response. This chapter will utilize a new metric, the SD FRF, to clearly demonstrate how these properties change upon the inception and accumulation of degradation. The SD FRF, which is generally a function of the Laplace variable *s* and a spatial coordinate dimension, *x*, is displayed in (4.1-1).

$$FRF_{SD}(s,x) = \frac{FRF_{degraded}(s,x)}{FRF_{healthy}(s,x)} \qquad (4.1\text{-}1)$$

The SD FRF is like the estimation accuracy FRF metric. It is a ratio of FRF data extracted from a system with a degradation to that of a baseline case. SD FRF quantities can be plotted on FRF or complex impedance SETI/ETI plots, but this document will emphasize the usage of FRF plots because they retain visibility of small, high frequency impedances.

This chapter documents sensitivity analyses which were completed using models and experiments. To do this, detailed boundary and interface parameters were manipulated. In figures based on outputs from a model, a percent level of degradation is provided based on (4.1-2). For example, if a die-attach contact resistance under degradation is 1.1 °C/W and 1.0 °C/W when healthy, then the percentage degradation, R_{pct}, is 10%.

$$R_{pct} = \left(\frac{R_{degradation\text{-}increase}}{R_{tot\text{-}healthy}} - 1\right) \cdot 100\% \qquad (4.1\text{-}2)$$

Although parameters manipulated in the model-based sensitivity analyses can be interpreted as such DC thermal resistance changes, this chapter will reveal how their impacts on heat transfer amplify in transient cases.

4.2 Model Predictions

4.2.1 1D transient analytical model

4.2.1.1 Specification

Fig. 4.2-1 re-illustrates the PDE model of Fig. 2.2-1(c). It has heat flux at the top of the domain to represent device losses, convection at the bottom of the domain to represent cooling and contact resistance, at x = L_1, which represents a TIM or internal, structural degradation of the assembly. Eq. (4.2-1)−(4.2-5) quantify the system in terms of thermal diffusivity, conductivity, and convection coefficients (α_i, k_i, h_i) and contact resistance, R_c''.

$$\frac{\partial^2 T_i(t)}{\partial x^2} = \frac{1}{\alpha_i}\frac{\partial T_i(t)}{\partial t} \quad \text{where } i = 1, 2 \tag{4.2-1}$$

$$-k_1 \left.\frac{\partial T_1(s)}{\partial x}\right|_{x=0} = Q''_{loss}(s) \tag{4.2-2}$$

$$-k_1 \left.\frac{\partial T_1(s)}{\partial x}\right|_{x=L1} = \frac{1}{R_c''}\left[\left.T_1(s)\right|_{x=L1} - \left.T_2(s)\right|_{x=L1} \right] \tag{4.2-3}$$

$$-k_1 \left.\frac{\partial T_1(s)}{\partial x}\right|_{x=L1} = -k_2 \left.\frac{\partial T_2(s)}{\partial x}\right|_{x=L1} \tag{4.2-4}$$

$$-k_2 \left.\frac{\partial T_2(s)}{\partial x}\right|_{x=L2} = h\left[\left.T_2(s)\right|_{x=L2} - T_\infty \right] \tag{4.2-5}$$

Eq. (4.2-6) and (4.2-7) document the exact analytical solutions to the Fig. 4.2-1 heat transfer problem Once again, *h_bar* in (4.2-6) and (4.2-7) represents the variable h listed in (4.2-1)−(4.2-5). Also, *R_c_flux* represents R_c''. These resulting transfer functions embed h and R_c''. By manipulating these parameters, the model was used to predict how spatially-varying FRF properties change with cooling system and structural degradation.

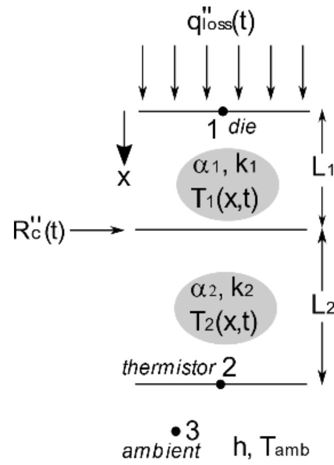

Fig. 4.2-1. Graphical illustration of a 1D transient analytical model with varying contact resistance

$$
\begin{aligned}
\frac{T_1(s,x)}{Q''_{loss}(s)} = \Bigg(& -s\, R_c_flux\, k \bigg(\Big(\Big(\sqrt{\tfrac{s}{\alpha}} \sinh\Big(\sqrt{\tfrac{s}{\alpha}}\, x\Big) k \\
& + \cosh\Big(\sqrt{\tfrac{s}{\alpha}}\, x\Big) h_bar \Big) \cosh\Big(\sqrt{\tfrac{s}{\alpha}}\, L\Big) \\
& + \sinh\Big(\sqrt{\tfrac{s}{\alpha}}\, L\Big) \Big(\sqrt{\tfrac{s}{\alpha}} \cosh\Big(\sqrt{\tfrac{s}{\alpha}}\, x\Big) k \\
& + \sinh\Big(\sqrt{\tfrac{s}{\alpha}}\, x\Big) h_bar \Big) \Big) \cosh\Big(\sqrt{\tfrac{s}{\alpha}}\, x_1\Big)^2 \\
& + s\, R_c_flux \sinh\Big(\sqrt{\tfrac{s}{\alpha}}\, x_1\Big) \Big(\Big(\Big(\sqrt{\tfrac{s}{\alpha}} \cosh\Big(\sqrt{\tfrac{s}{\alpha}}\, x\Big) k \\
& + \sinh\Big(\sqrt{\tfrac{s}{\alpha}}\, x\Big) h_bar \Big) \cosh\Big(\sqrt{\tfrac{s}{\alpha}}\, L\Big) \\
& + \sinh\Big(\sqrt{\tfrac{s}{\alpha}}\, L\Big) \Big(\sqrt{\tfrac{s}{\alpha}} \sinh\Big(\sqrt{\tfrac{s}{\alpha}}\, x\Big) k \\
& + \cosh\Big(\sqrt{\tfrac{s}{\alpha}}\, x\Big) h_bar \Big) \Big) k \cosh\Big(\sqrt{\tfrac{s}{\alpha}}\, x_1\Big) \\
& + \Big(\sqrt{\tfrac{s}{\alpha}} \left(k^2 s\, R_c_flux + \alpha\, h_bar\right) \sinh\Big(\sqrt{\tfrac{s}{\alpha}}\, x\Big) \\
& - \cosh\Big(\sqrt{\tfrac{s}{\alpha}}\, x\Big) k s \Big) \cosh\Big(\sqrt{\tfrac{s}{\alpha}}\, L\Big) - \Big(\\
& - k s \left(h_bar\, R_c_flux + 1\right) \sinh\Big(\sqrt{\tfrac{s}{\alpha}}\, x\Big) \\
& + \sqrt{\tfrac{s}{\alpha}} \cosh\Big(\sqrt{\tfrac{s}{\alpha}}\, x\Big) \alpha\, h_bar \Big) \sinh\Big(\sqrt{\tfrac{s}{\alpha}}\, L\Big) \Big) \bigg) \Bigg) \Bigg/ \\
& \Bigg(\sqrt{\tfrac{s}{\alpha}}\, k \bigg(k s\, R_c_flux \Big(\cosh\Big(\sqrt{\tfrac{s}{\alpha}}\, L\Big) \sqrt{\tfrac{s}{\alpha}}\, k \\
& + \sinh\Big(\sqrt{\tfrac{s}{\alpha}}\, L\Big) h_bar \Big) \cosh\Big(\sqrt{\tfrac{s}{\alpha}}\, x_1\Big)^2 \\
& - \sinh\Big(\sqrt{\tfrac{s}{\alpha}}\, x_1\Big) k s\, R_c_flux \Big(\sinh\Big(\sqrt{\tfrac{s}{\alpha}}\, L\Big) \sqrt{\tfrac{s}{\alpha}}\, k \\
& + \cosh\Big(\sqrt{\tfrac{s}{\alpha}}\, L\Big) h_bar \Big) \cosh\Big(\sqrt{\tfrac{s}{\alpha}}\, x_1\Big) \\
& - \sqrt{\tfrac{s}{\alpha}} \left(k^2 s\, R_c_flux + \alpha\, h_bar\right) \cosh\Big(\sqrt{\tfrac{s}{\alpha}}\, L\Big) \\
& - \sinh\Big(\sqrt{\tfrac{s}{\alpha}}\, L\Big) s\, k \left(h_bar\, R_c_flux + 1\right) \bigg) \Bigg)
\end{aligned}
\tag{4.2-6}
$$

$$\frac{T_2(s,x)}{Q''_{loss}(s)} = \frac{-\left(\left(\left(\sqrt{\frac{s}{\alpha}}\cosh\left(\sqrt{\frac{s}{\alpha}}\,x\right)k - \sinh\left(\sqrt{\frac{s}{\alpha}}\,x\right)h_bar\right)\cosh\left(\sqrt{\frac{s}{\alpha}}\,L\right) - \sinh\left(\sqrt{\frac{s}{\alpha}}\,L\right)\left(\sqrt{\frac{s}{\alpha}}\sinh\left(\sqrt{\frac{s}{\alpha}}\,x\right)k - \cosh\left(\sqrt{\frac{s}{\alpha}}\,x\right)h_bar\right)\right)\alpha\right)}{\left(\left(\left(\left(\sqrt{\frac{s}{\alpha}}\cosh\left(\sqrt{\frac{s}{\alpha}}\,x_1\right)^2 k^2 s R_c_flux - \cosh\left(\sqrt{\frac{s}{\alpha}}\,x_1\right)\sinh\left(\sqrt{\frac{s}{\alpha}}\,x_1\right)k s\, h_bar\, R_c_flux - \sqrt{\frac{s}{\alpha}}\left(k^2 s R_c_flux + \alpha\, h_bar\right)\right)\cosh\left(\sqrt{\frac{s}{\alpha}}\,L\right) - \sinh\left(\sqrt{\frac{s}{\alpha}}\,L\right)s\,k\left(\sqrt{\frac{s}{\alpha}}\cosh\left(\sqrt{\frac{s}{\alpha}}\,x_1\right)\sinh\left(\sqrt{\frac{s}{\alpha}}\,x_1\right)k R_c_flux - \cosh\left(\sqrt{\frac{s}{\alpha}}\,x_1\right)^2 h_bar\, R_c_flux + h_bar\, R_c_flux + 1\right)\right)\right)k\right)} \tag{4.2-7}$$

4.2.1.2 Spatially-varying electrothermal impedance

Fig. 2.2-4 and Fig. 2.2-5 show SETI FRF maps for a baseline version of the 1D transient model with $R''_c = 0$ and h at a nominal value. Fig. 4.2-2 displays SETI FRF maps for the analytical model with non-zero values of contact resistance.

A visible break between the two surfaces at L_1, the specified location of the contact resistances, can be seen in Fig. 4.2-2. The spatially-varying impedance surfaces also reveal that contact resistance causes the solid, which previously acted as a single diffuse body, to have two distinct behaviors within the $T_1(s,x)$ and $T_2(s,x)$ regions. The contact point $x=L_1$ functions like a discontinuity in the computational domain.

Pertinent to sensitivity analysis, the response surfaces reveal that the $T_1(s,x)$ region's impedance magnitude elevates with increasing contact resistance. The phase response also shifts – in particular, the trough in the phase response around 0.1 Hz becomes smaller with increasing contact resistance.

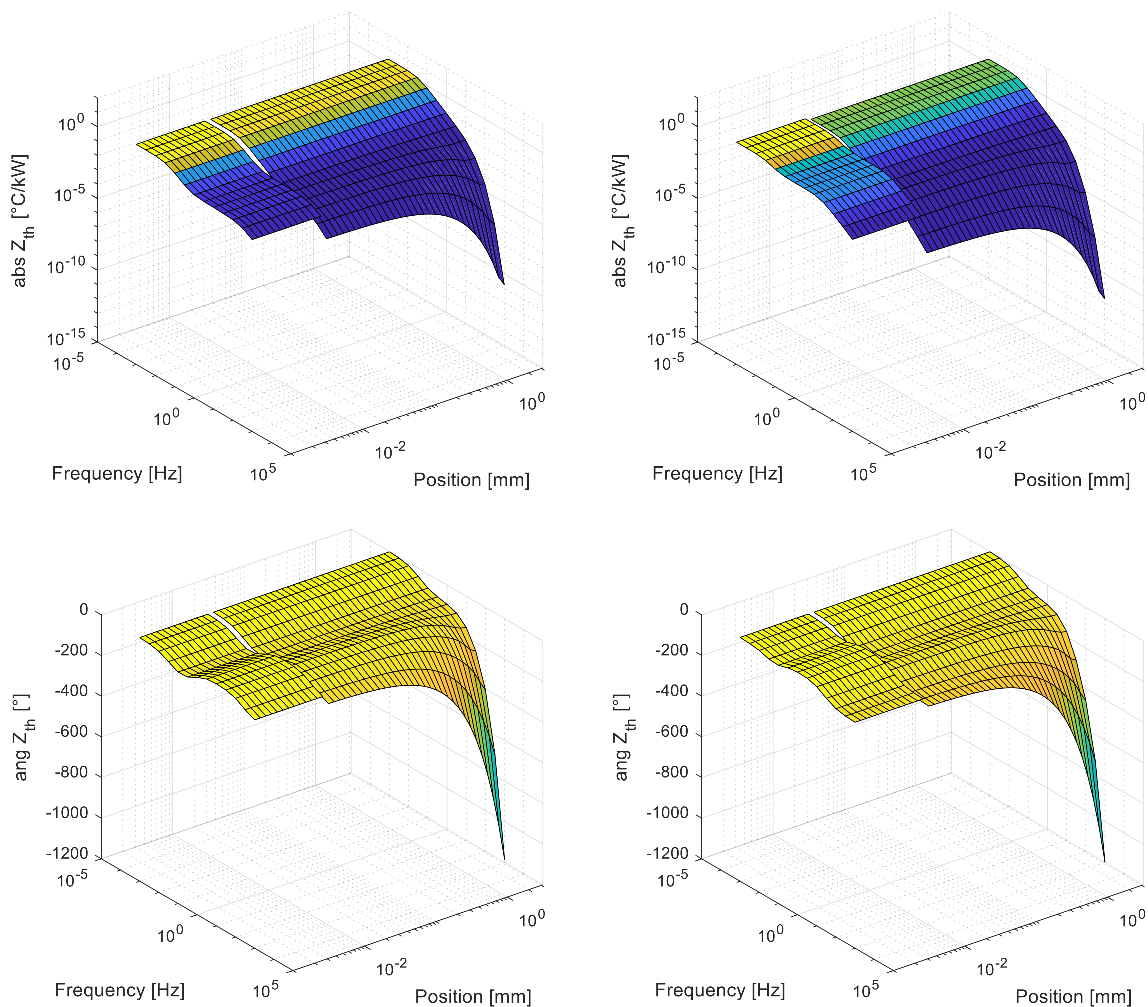

(a) $R_c'' = 100$ mm^{2}K/W (b) $R_c'' = 1000$ mm^{2}K/W

Fig. 4.2-2. Isometric view of a SETIS map produced using the exact solution to the 1D transient model with contact resistance (Fig. 4.2-1)

Please note that the $R_c'' = 100$ mm^{2}K/W corresponds to a 3.3% increase in the total die-to-ambient thermal resistance, and $R_c'' = 1000$ mm^{2}K/W corresponds to a 30.3% increase. From the state-of-the-art review, it was identified that a 30% increase in thermal resistance is often considered the threshold in which a power semiconductor sub-assembly is declared failed. So, $R_c'' = 0 - 1000$ mm^{2}K/W is effectively 0 to 30% additional thermal resistance.

4.2.1.3 Scalar electrothermal impedances

To further quantify property shifts due to degradation, scalar FRFs were utilized. Following Fig. 2.1-2 and Fig. 2.2-1(a), responses at three discrete locations were inspected. Ultimately, the $\Delta T^{s}_{die\text{-}amb}(j2\pi f)\,/\,Q_{loss}(j2\pi f)$ and $\Delta T^{s}_{thermistor\text{-}amb}(j2\pi f)\,/\,Q_{loss}(j2\pi f)$ FRFs were then formed by evaluating (4.2-6) and (4.2-7) at $x=0$ and $x=L_1+L_2$ positions, respectively.

Fig. 4.2-3 illustrates analytical ETI FRF responses for both the die-to-ambient and thermistor-to-ambient spatial domains with varying cooling performance, produced by manipulating h within (4.2-6) and (4.2-7). In the FRF plots, differences in the curves are perceivable below ~5 mHz. Differences in magnitude response are greatest at the DC ($\omega=0$) point, while differences in phase response properties are greatest around 2 mHz. Above ~10 mHz the healthy and degraded FRF curves align, so Fig. 4.2-3 shows that relatively low frequency heat transfer is sensitivity to cooling degradation for both driving point and distant point impedances.

Next, Fig. 4.2-4 reveals the significant sensitivity of the driving point impedance, $\Delta T^{s}_{die\text{-}amb}(j2\pi f)\,/\,Q_{loss}(j2\pi f)$, to R''_c. The FRF magnitude tends to increase, specifically when loss excitations are at low enough frequencies to allow the contact resistance boundary, shown in Fig. 4.2-1, to influence heat conduction. Phase response also exhibits sensitivity to R''_c. Additionally, with a non-zero R''_c, the asymptotic high frequency ($\omega\rightarrow\infty$) limit is $-90°$, compared to the $-45°$ value without degradation, captured by the $1/\sqrt{s}$ term in (2.2-6). The $-90°$ high frequency phase response property is consistent with $-90n°$ high frequency phase response in lumped models, as discussed in section 2.2.

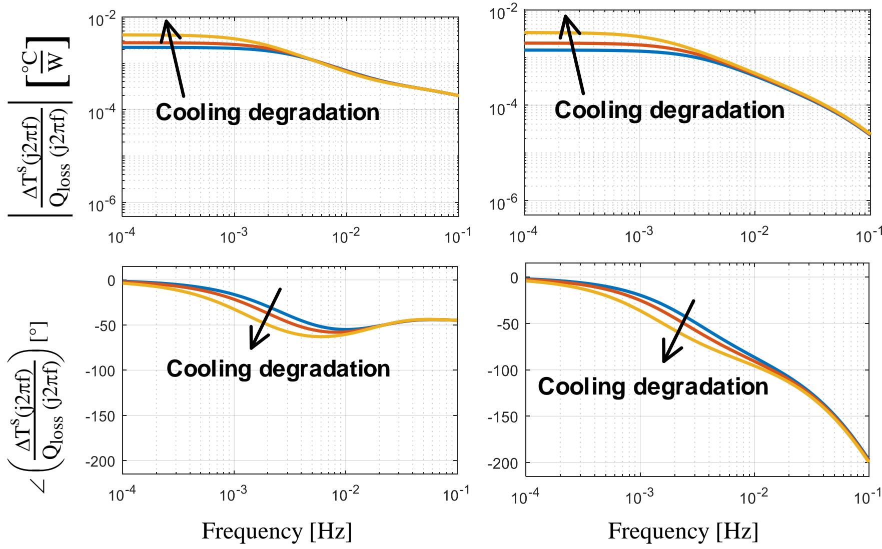

(a) Response at x = 0

(b) Response at x = 1 p.u.

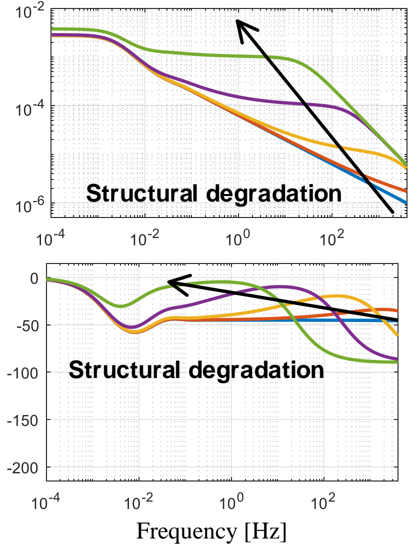

Legend: $R_c'' =$ 0, 1, 10, 100, 1000 (mm²-K)/W
Parameters: $L_1 = 10$ μm, $L_2 = 75$ mm, $\alpha = 90$ mm²/s, k = 60 W/(m-K), h = 500 W/(m²-K)

Legend:
h = 700, 500, 300 W/(m²-K)

Parameters: $L_1 = 10$ μm, $L_2 = 75$ mm, $\alpha = 90$ mm²/s, k = 60 W/(m-K), $R_c'' = 0$

Fig. 4.2-3. Spatial ETI FRFs from the 1D transient model with variable convection (cooling degradation)

Fig. 4.2-4. Die-to-ambient ETI from the 1D transient model with variable Rc''

In general, increasing R_c'' decreases the phase delay at intermediate frequencies which depend on the extend of the degradation. Larger R_c'' decreases the effective amount of capacitance of the T_1 section of the model, resulting in a less attenuated and delayed driving point impedance response. As a final note: the FRF at $x=L_1+L_2$ was not provided for contact resistance increases because it has approximately zero sensitivity to the parameter R_c''.

4.2.1.4 Summary of conclusions

The following statements summarize the degradation sensitivities embedded within the 1D transient analytical model:

- Cooling system degradation is perceivable at the DC-to-low frequency region in both driving point and distance point impedances.
- Distance point impedances have minimal sensitivity to interfacial degradations.

- Interfacial degradations are embedded in the mid-to-high frequency response and changes in the impedance are proportional to the value of R_c''.

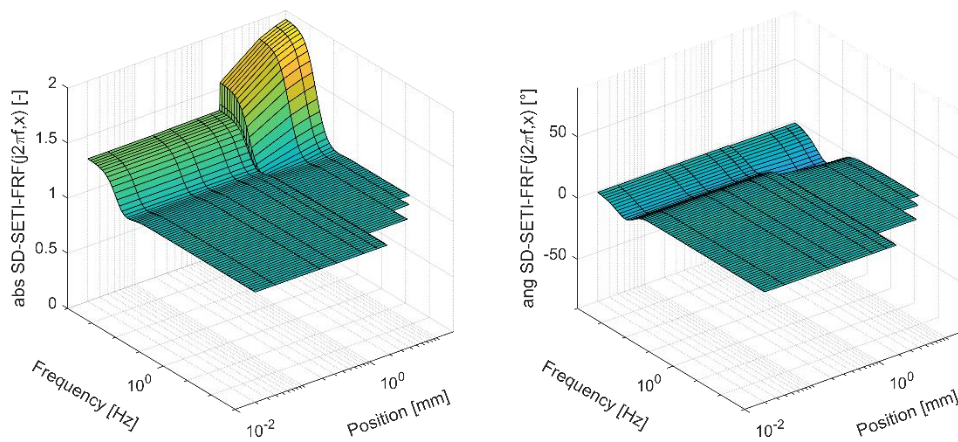

(a) **Degraded cooling system (100%)**

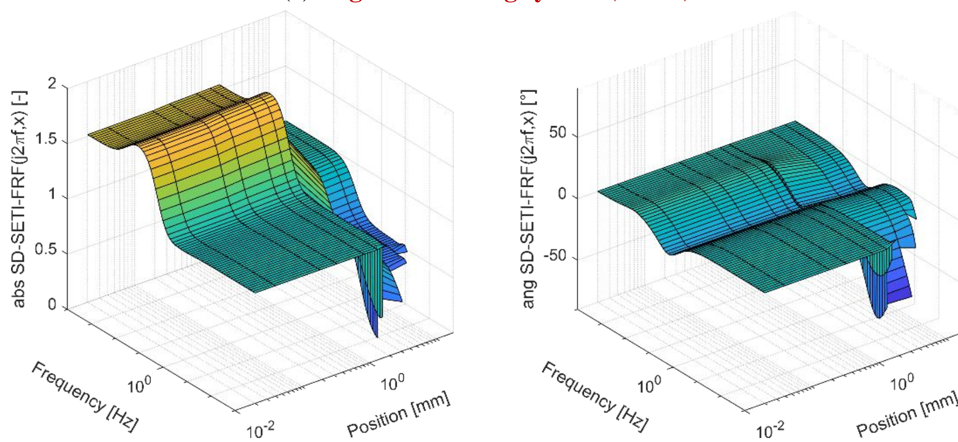

(b) **Degraded TIM (100%)**

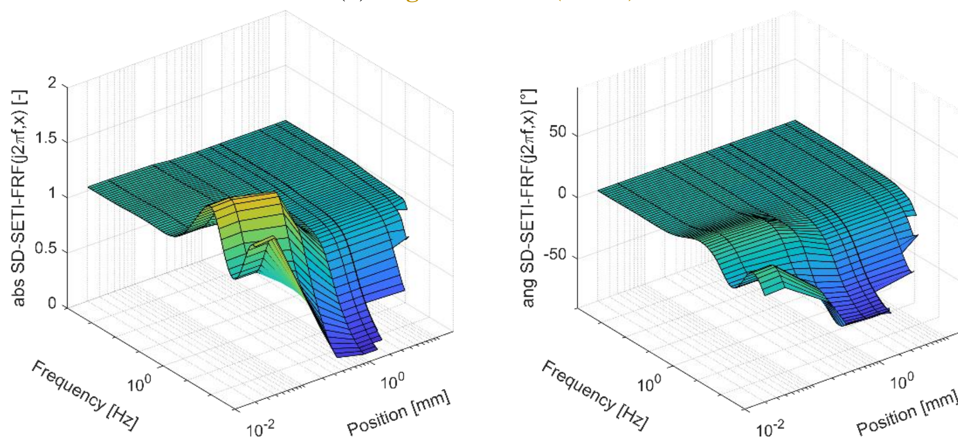

(c) **Degraded die-attach solder (100%)**

Fig. 4.2-5. Spatially-varying sensitivity functions extracted from a FD model

4.2.2 Finite difference numerical model

4.2.2.1 Specification

This subsection utilizes the baseline FD model introduced in subsection 2.2.2.2. To simulate thermal-mechanical degradation, the models were modified by manipulating the properties as shown in Table 4.2-1.

Table 4.2-1. Numerical model-based degradation simulation method

	Classification	***Degradation***	***Simulation method***
1	Boundary, thermofluid	Cooling system	Convective heat transfer coeff., h = ↓ 50%
2	Internal, structural	Therm. interface material (TIM)	Resistivity of TIM, ρ_{tim} = ↑ 50%
3		Solder interfaces	Resistivity of solder, ρ_{solder} = ↑ 50%

Unlike the previous subsection using an analytical model, this subsection will utilize complex impedance plots and, most often, normalized sensitivity functions for identification of spatiotemporal limits in degradation sensitivity.

4.2.2.2 Degradation sensitivity spatial variance

Fig. 4.2-5 provides the results of computing (4.1-1) for each of the three sources of degradation listed in Table 4.2-1. Since regions with non-unity magnitude and non-zero phase are sensitive to a source of degradation, the graphics provide a quick way to visually identify harmonic frequency-location operating points with high sensitivity to degradation. Detailed discussion will be saved until after scalar sensitivity functions are presented in following subsections, but it is remarked now that these surfaces illustrate spatial sensitivity gradients. As this document will eventually show, they can be used along with the loss modulation property of a converter to

identify high sensitivity regions as potential locations of temperature detectors aimed to implement real-time degradation sensing.

4.2.2.3 Unique impacts of different sources of degradation

Fig. 4.2-6 presents scalar sensitivity functions illustrating how the three different degradation sources listed in Table 4.2-1 impact different dynamic ranges in the transient thermal response of the FD model. The conclusions are like those made in subsection 4.2.1. Changes to the convective heat transfer coefficient impact the DC-to-low frequency response, while manipulation of the die-attach interface impacts the high frequency response of the semiconductor device. For the derived model, intermediate frequencies are sensitive to TIM degradation, with peak sensitivity to the approximate 100 mHz harmonic.

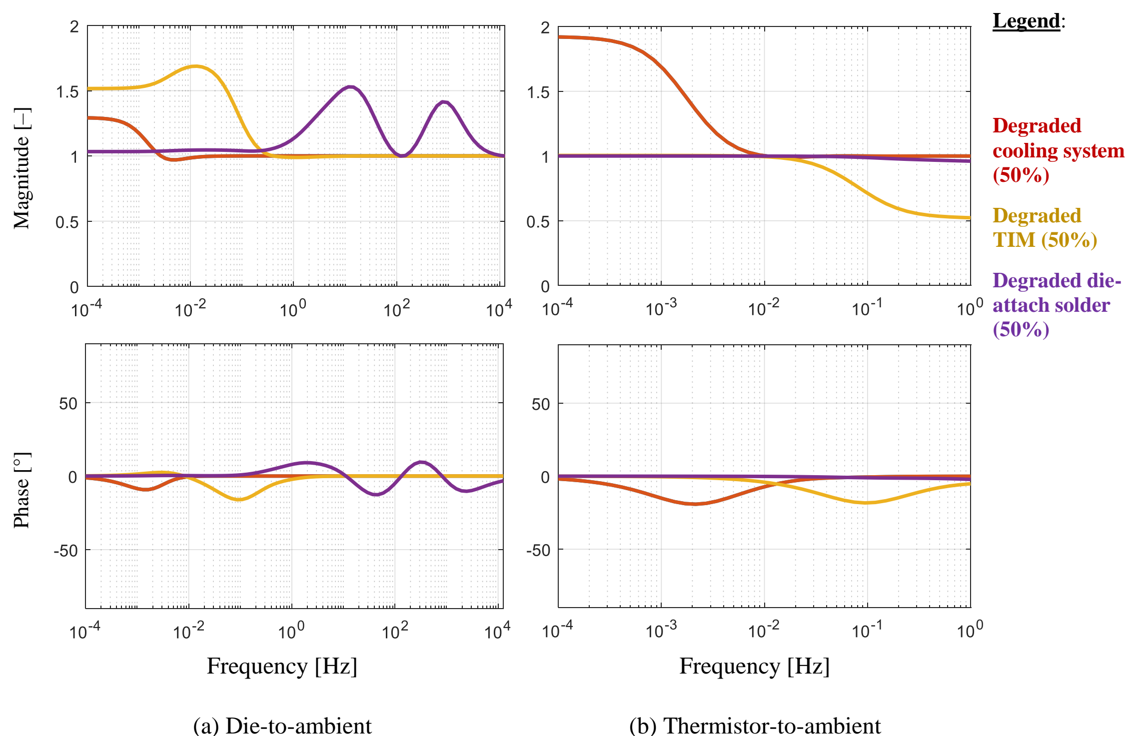

Fig. 4.2-6. Sensitivity FRFs as a function of degradation, extracted from a FD model

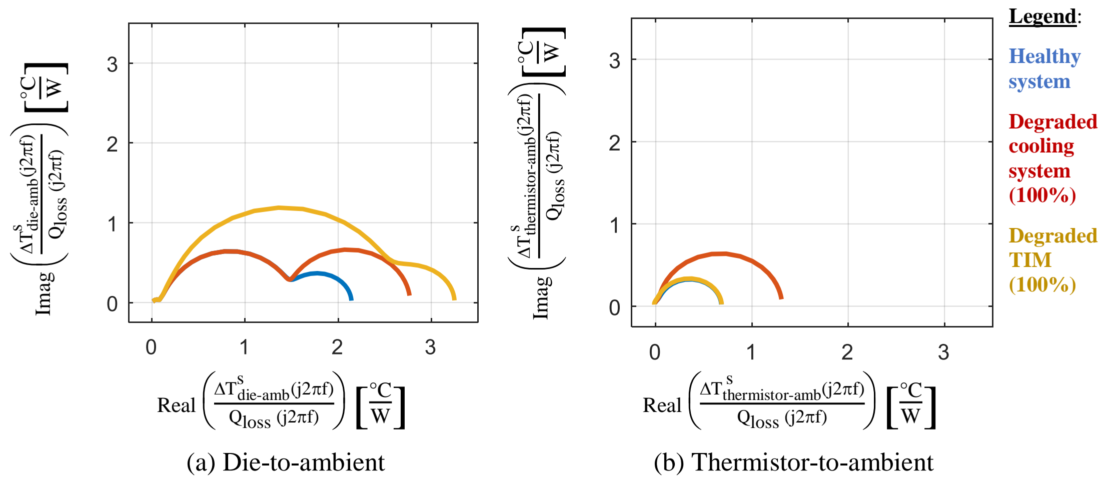

Fig. 4.2-7. Electrothermal impedances as a function of degradation, extracted from a FD model

Complex impedance plots can also be utilized to compare FRF data. Fig. 4.2-7 plots non-normalized electrothermal impedances extracted from the model for simulated degradation to cooling and the TIM, along with a baseline healthy response. Since a TIM-based contact resistance interface was designed into model, two lobes are present in displayed die-to-ambient FRF data. Upon degradation to only the cooling system, the first lobe does not amplify, but the second lobe does amplify proportional to the convective heat transfer coefficient. The thermistor-to-ambient FRF, which has one lobe, also amplifies proportional to h. Additionally, Fig. 4.2-7(a) shows that accumulation of only TIM degradation, the diameter of the second lobe (related to cooling) remains about the same, but the diameter of the first lobe amplifies. This results in a change in the intersection point between the two dominant lobes, implying a change in a governing thermal time constant.

4.2.2.4 Sensitivity growth with extent of degradation

Fig. 4.2-9 illustrates sensitivity to the extent of cooling system degradation. The plots were formed by manipulating the model's heat transfer coefficient, h.

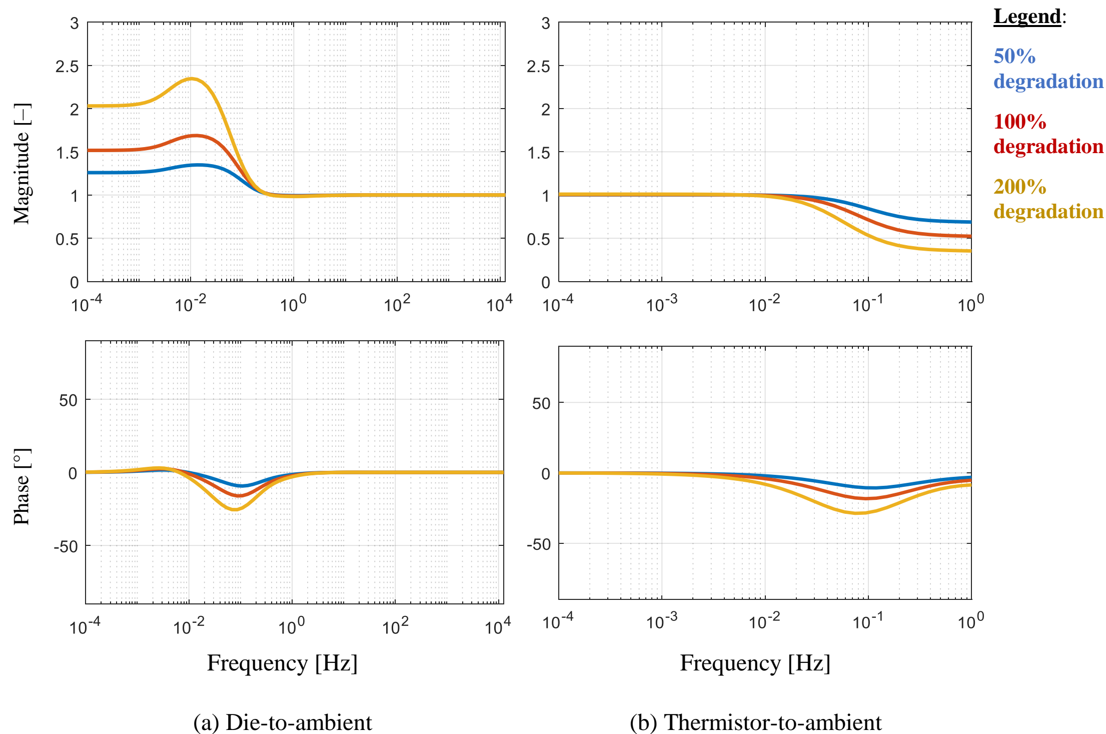

(a) Die-to-ambient

(b) Thermistor-to-ambient

Fig. 4.2-8. Sensitivity functions with increasing TIM degradation, extracted from the FD model

Manipulation of h changes DC-to-low FRF amplitude. Fig. 4.2-8 reveals that the die-to-ambient response also has this sensitivity to TIM degradation. However, the model predicts that the thermistor-to-ambient response has no sensitivity to TIM degradation until around 10 mHz. Fig. 4.2-8 also shows that TIM degradation only induces amplification and phase delay in the die-to-ambient FRF. Further, it shows how the thermistor-to-ambient FRF has a different sensitivity property. The phase delay property, which begins at around 10 mHz, is similar, however, amplitude attenuation is predicted. This suggests a smaller magnitude heat sink response, at certain frequencies, under conditions of degradation.

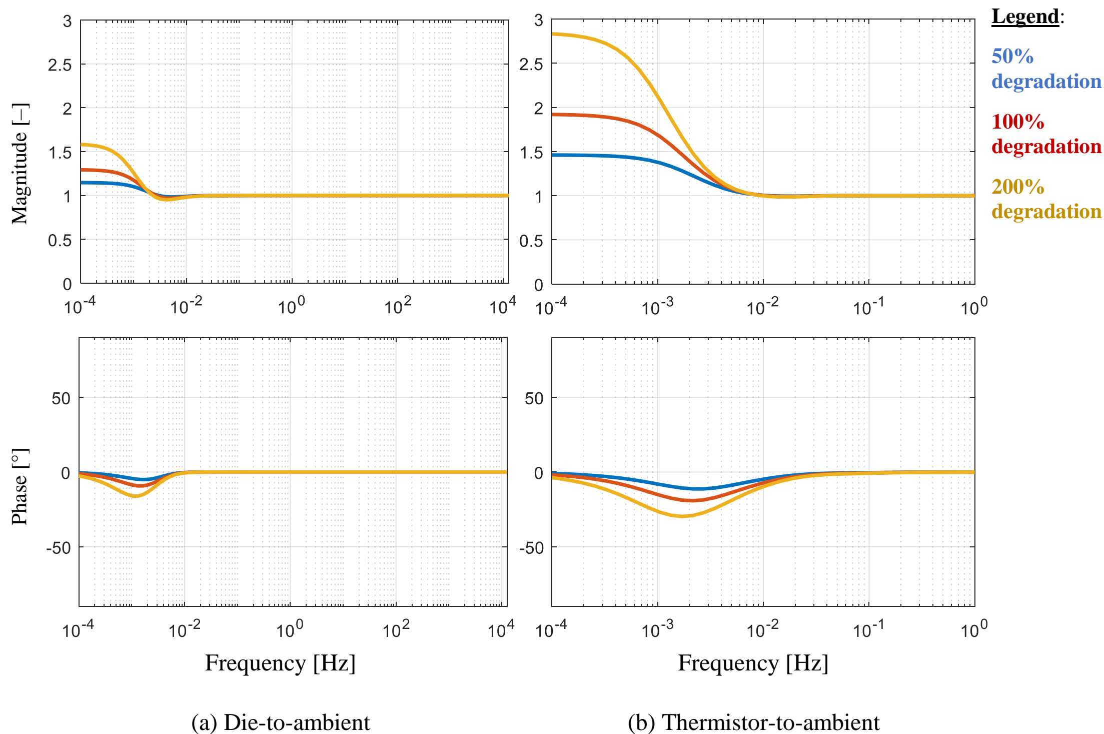

(a) Die-to-ambient (b) Thermistor-to-ambient

Fig. 4.2-9. Sensitivity functions with increasing cooling degradation, extracted from the FD model

Fig. 4.2-9 reinforces that only the low frequency dynamic range is sensitive to cooling system degradations. Both the (a) and (b) plots show that the amplitude sensitivity is approximately proportional to the value of h. Both plots also show that phase delay increases with increasing degradation, and that the excitation frequency which induces phase delay minima decreases with increasing degradation.

The (a) and (b) plots have differences, however. They indicate that the thermistor-to-ambient FRF has higher sensitivity to cooling system degradations that that of the die-to-ambient spatial domain segment. Due to the higher sensitivity, the heat sink response is theoretically better suited for real-time characterization of cooling system performance. The same conclusion can be drawn from Fig. 4.2-5(a).

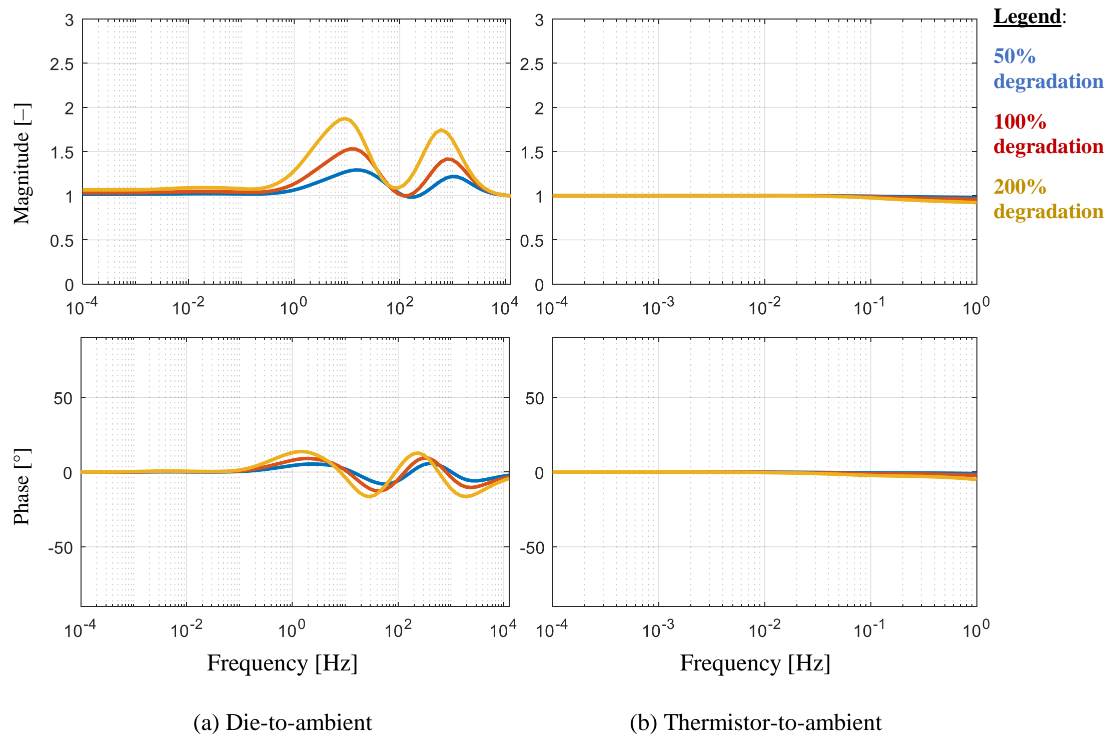

Fig. 4.2-10. Sensitivity functions with increasing die-attach degradation, extracted from the FD model

Finally, Fig. 4.2-10 quantifies how die and heat sink frequency response sensitivity varies with the extent of die-attach degradation. First, it is remarked that, within the frequency range displayed, the thermistor-to-ambient response has little sensitivity to die-attach solder degradation. The remainder of this discussion will therefore focus on the die-to-ambient SD FRF results, which do exhibit sensitivity according to the model.

As in sensitivity functions showing cooling system and TIM degradations, the DC gain property is increased exactly according to (4.1-2). However, despite these relatively small steady-state thermal resistance increases, relatively large sensitivity regions, centered at around 10 Hz and 1 kHz, can be observed in Fig. 4.2-10. The maximum value of amplitude sensitivity is about half that of the degradation percentage implemented in the model.

Fig. 4.2-10 also characterizes phase response sensitivity to the die-attach. There is no low frequency phase response sensitivity in the die-to-ambient response, and phase response sensitivities generally appear in the 100 mHz to 10 kHz frequency range. The model predicts degradation-induced phase response differences on the order of 1-10° for levels of degradation ≤ 50%. Results of this type create a requirement for phase detection resolution. As a final note, the extracted phase response sensitivities have zero crossings. To implement real-time degradation sensing, special attention must be paid to these non-sensitive points since they translate with increasing degradation.

4.2.2.5 Summary of conclusions

The following statements summarize the salient impacts the three degradation modes have on heat transfer FRF properties according to the developed numerical simulation model:

- Sensitivity to different degradation sources manifest at different frequency bands, related to the distance the defect is from the loss excitation.
- More precisely, for the developed model, cooling system degradation appears at DC-to-low frequencies, TIM degradation appears at low-to-medium frequencies and die-attach solder degradation occurs at relatively high frequencies.
- In complex impedance plots, distinct lobes represent dominant lumped thermal resistance properties embedded within a system's response.

4.2.3 Finite element numerical model

4.2.3.1 Interface and boundary

While normalized plots are useful in fitting model response to experimental data, they are doubly useful in that they enable identification of specific impacts of degradation in devices and components. $R_{LF\text{-}Sink}$ represents TIM that is used in the lab to connect the MOSFET to the heat sink. Degradation of the TIM, corresponding to an increase in $R_{LF\text{-}Sink}$, causes an increase in temperature gradients actuated by a converter, which would likely increase thermal-mechanical rate-of-degradation. Variations in R_{conv} represent cooling pump faults or fouling.

TIM and cooling degradation were experimentally emulated and FRFs were extracted for two cases: one in which the speed of the cooling fan being used to cool the system was decreased and the other in which the screw that secured the LF to the sink was loosened to decrease the LF-sink mounting force. These two responses were then normalized by the nominally operating system FRF response to form sensitivity functions. The experimental cooling and TIM degradation sensitivity functions are displayed in Fig. 4.2-11, which is a copy of Fig. 3.1-15 provided for convenience of the reader.

R_{conv} and $R_{LF\text{-}Sink}$ were then manipulated in the model to emulate similar conditions. The model-based cooling and TIM degradation sensitivity functions are the same functions in Fig. 4.2-11 used to assist in tuning the model to match test results. Overall, Fig. 4.2-11 shows that R_{conv} impacts DC to 10 mHz, and $R_{LF\text{-}Sink}$ approximately impacts the 1 mHz to 1 Hz band. R_{conv} and $R_{LF\text{-}Sink}$ impact the die-to-ambient segment's low frequency response due to the long convective time constant that governs the system response and the large distance (~2 mm) between the LF-sink interface and the physical location of the loss dissipation. While the magnitude of the

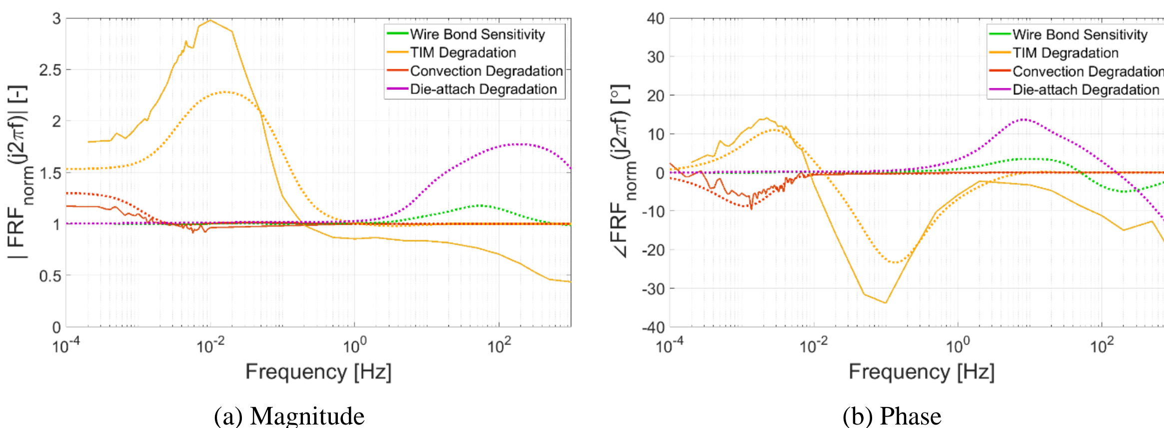

(a) Magnitude (b) Phase

Fig. 4.2-11. Die sensitivity functions showing how degradation in terms of R_{conv} (50%), $R_{LF\text{-}Sink}$ (200%), $R_{Si\text{-}LF}$ (100%), and the absence of wire bonds affect the die-to-ambient response; experimental traces are solid lines and model-derived traces are dotted lines (repeat of Fig. 3.1-15 for convenience to the reader)

responses is slightly dissimilar between models, the shape of the waveforms is very similar below 1 Hz, which is the maximum frequency the model predicts will be sensitive to TIM degradation.

4.2.3.2 Wire bonds

The FE model was further detailed, as shown in Fig. 4.2-12, to include gate and source wire bond connections for identifying their effects on transient conduction. Wire bond position and sizes were obtained from the manufacturer and they interfaced the silicon die and lead frame with ideal contact in the model. This more detailed model increased the number of mesh nodes and elements to 6410 and 4288, respectively.

A wire bond sensitivity function is shown in Fig. 4.2-11. It was computed as the ratio of FRFs with ideally connected wire bonds to that without wire bonds. The traces reveal that the wire bonds have an impact on transient heat transfer within the 1 Hz – 1 kHz frequency band. The magnitude sensitivity is about 20% and the phase sensitivity is about 5° at maximum.

Please note that this is a binary test result – wire bonds were either totally present or not – and wire bond microcracking and partial liftoff was not simulated. However, the obtained results help enable identification of a minimum required resolution for diagnostic systems utilizing sensed

changes in transient heat transfer. The results suggest that it might be possible to detect wire bond fatigue using precise, in situ measurements of high frequency heat transfer.

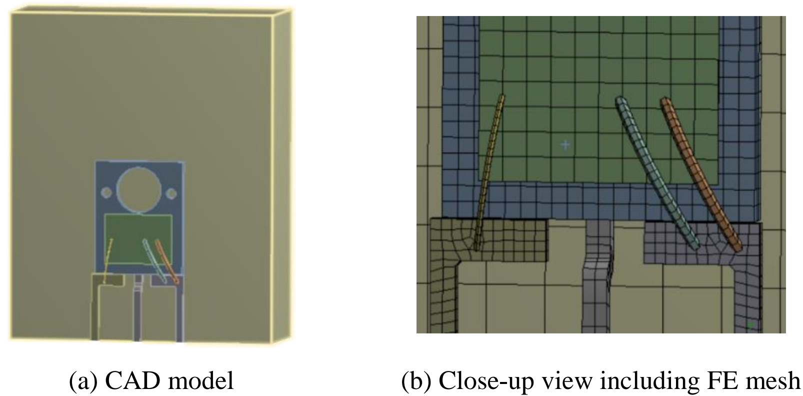

(a) CAD model (b) Close-up view including FE mesh

Fig. 4.2-12. FE model with wire bonds, building upon Fig. 5

4.3 Experimental Characterizations

To experimentally characterize the impacts of degradation sources on transient thermal response, system identification was applied on a power electronic test platform with separate manipulations to cooling, a TIM, between a power semiconductor component and heat sink, and die-attachment. Cooling was manipulated with a Variac transformer to reduce the amplitude of a blower fan's input AC voltage, reducing the rate of air flow past a heat sink. The TIM was degraded by manipulating the bolted joint that nominally pressed a power MOSFET tightly against a heat sink. Die-attach manipulation will be described later in this section. The system identification experiments executed had very similar parameters to those documented in Table 3.1-1 through Table 3.1-4.

4.3.1 MOSFET converter characterization of cooling and TIM sensitivity

4.3.1.1 Scalar electrothermal impedances

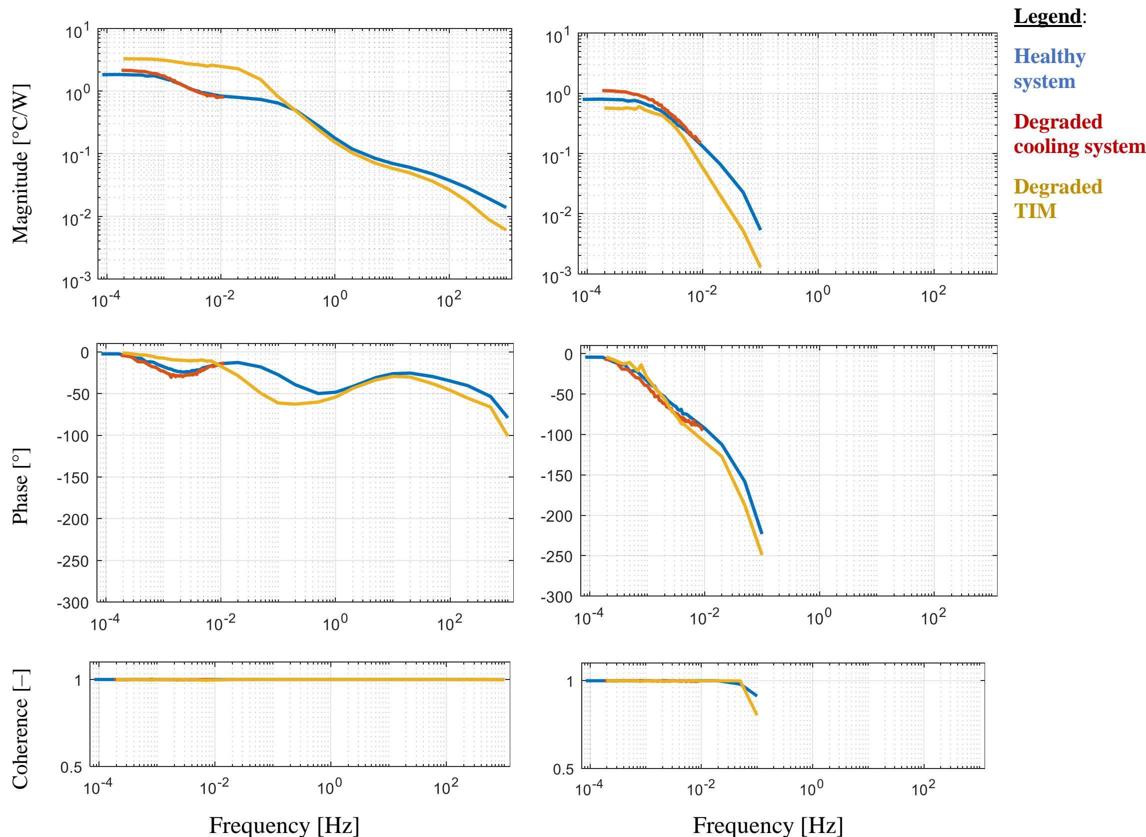

Fig. 4.3-1. Experimental FRFs as a function of cooling and TIM degradation

Based on the modeling results documented in this chapter, it was assumed that only low frequency heat transfer would be sensitive to cooling degradation. Therefore, only a single long duration system identification experiment was executed to characterize the impact of cooling degradation on FRF properties. As visible in Fig. 4.3-1, the FRF data corresponding to cooling degradation subsequently spans 100 μHz to 10 mHz.

Fig. 4.3-1 exhibits similar properties to those suggested by the models, documented earlier in this chapter. The impedance responses suggest cooling-sensitive properties exist at DC-to-low frequency. There, FRF magnitude increases, and the inception of phase delay is at a lower

frequency with less powerful cooling. This latter observation indicates that the time constant representing convection heat transfer increases.

Similarly, with TIM degradation, DC gain increases, also as predicted by a model. Further, one of the dominant phase response troughs in the driving point impedance plot begins at a lower frequency. Overall, the frequency range exhibiting the highest phase response sensitivity is 10 mHz to 1 Hz, also near to model predictions. However, unlike model predictions, the experimental responses are different throughout most of the 100 μHz to 1 kHz frequency range. This suggests that the method for simulating TIM degradation in the model does not replicate the result of bolted joint manipulation carried out in the lab.

4.3.1.2 Scalar sensitivity functions

Fig. 4.3-2 documents sensitivity functions formed by normalizing the degraded FRF data by that extracted from the system without degradation. Cooling sensitivity functions agree well with those from models, particularly the results in Fig. 4.2-9. The experimental results demonstrate how this type of degradation results in magnitude amplification and additional phase delay.

Fig. 4.3-2 illustrates more clearly how the TIM degradation implemented in the lab changed system frequency response properties. With TIM degradation, die-to-ambient had higher FRF amplitude response at the DC level, with a response peak at about 10 mHz. Further, the peak value of the die-to-ambient phase sensitivity occurred at around 100 mHz. The thermistor-to-ambient TIM sensitivity function also has properties predicted by model. For example, an amplitude roll-off starting about around 3 mHz is present.

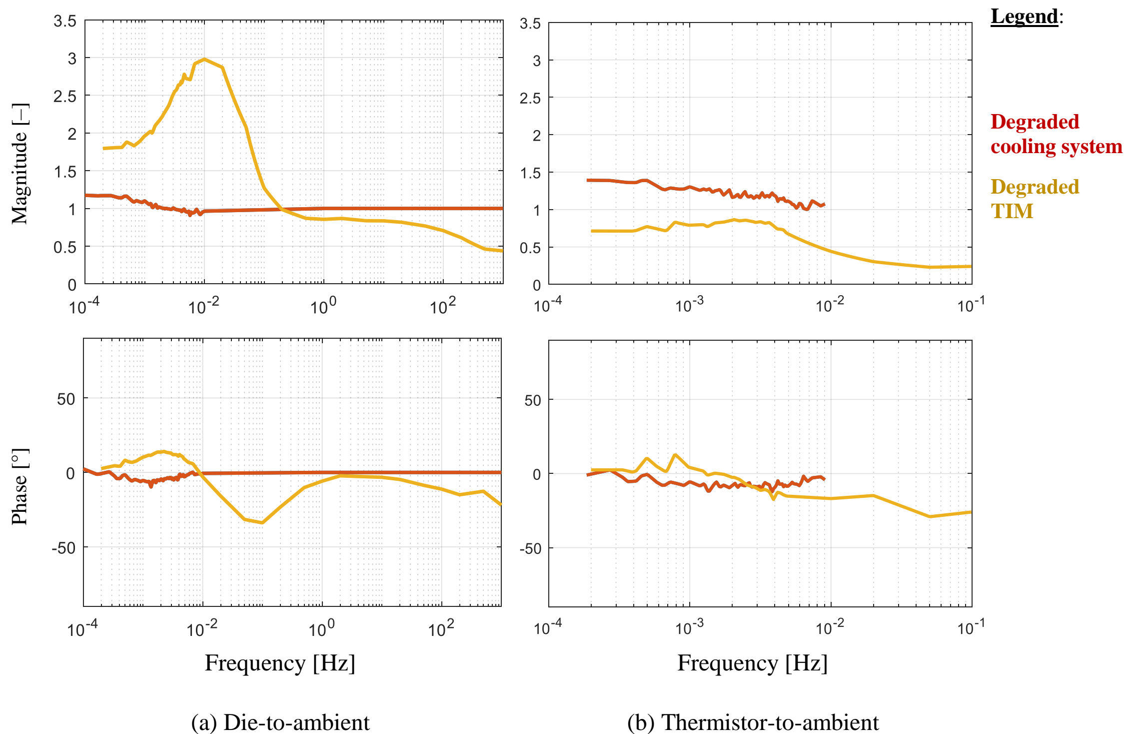

(a) Die-to-ambient

(b) Thermistor-to-ambient

Fig. 4.3-2. Experimental cooling and TIM degradation sensitivity functions

There inconsistencies between the TIM sensitivity functions measured in the lab and predicted by model. The model did not predict the high frequency roll-off property shown in Fig. 4.3-2(a). Furthermore, the model did not predict the DC gain attenuation property displayed in Fig. 4.3-2(b). The model also predicted that phase sensitivity rebounds to zero.

4.3.1.3 Complex impedance plots

Property shifts are visible in prior figures, but some can be more apparent in the Fig. 4.3-3 complex impedance plots, which utilize linear ordinate and abscissa scaling. For the (a) driving point impedance plot, the diameter of the second lobe increases. For the (b) distant impedance plot, the diameter of the only lobe increases. Lobe amplification indicates growth of thermal resistance quantities, which follows from the emulation of degradation, as expected. These trends were captured by models presented in subsection 4.1.

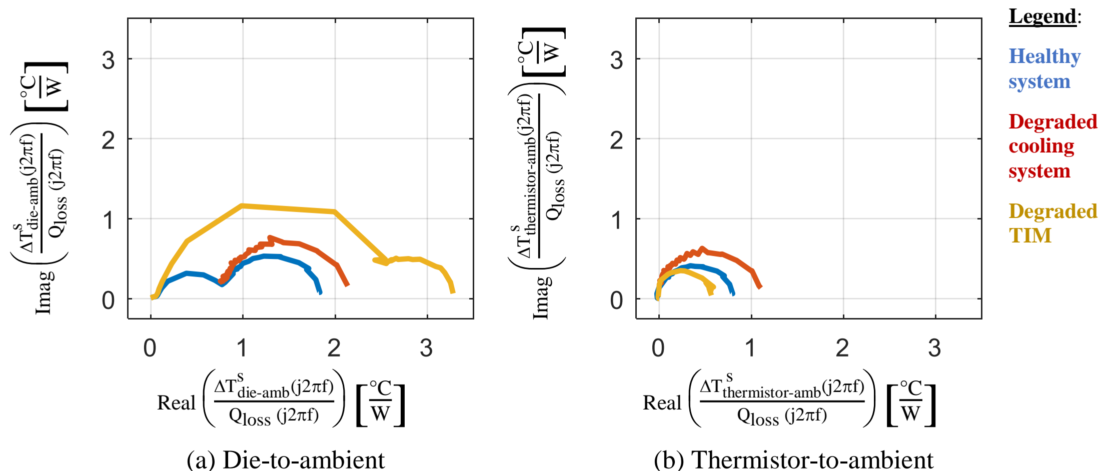

Fig. 4.3-3. Experimental die-to-ambient and thermistor-to-ambient complex ETI as a function of power electronic converter degradation

When viewed with complex impedance plots, the driving point FRF with TIM degradation is similar in form and scaling to that shown in Fig. 4.2-7. With TIM degradation, the distant point complex impedance has a smaller diameter than that of the healthy system. This result was not predicted by model.

4.3.2 IGBT converter characterization of TIM and die-attach sensitivity

4.3.2.1 Setup and methods

Device under test

Next, the test DC-DC converter's power MOSFET component was replaced with a decapsulated, discrete IGBT, shown in Fig. 4.3-4. The IGBT components were found in lab storage. Since the components were not identified, detailed, device-level specifications are not in possession. They were assumed to be rated for tens of amps and hundreds of volts. IGBT component operating characteristics did not limit application of system identification, which was again utilized for converter-integrated characterization of transient heat transfer.

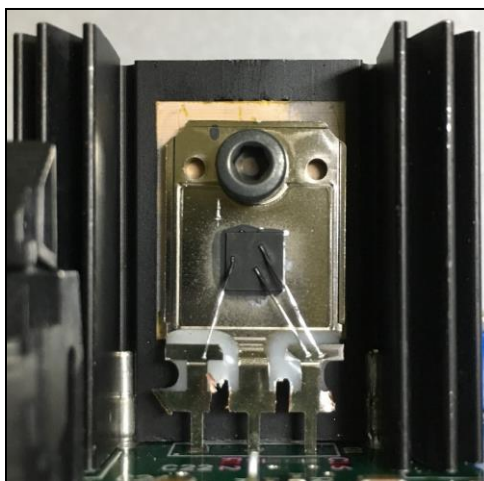

(a) IGBT sub-assembly before fabricating defects

(b) Heating of the IGBT to reflow the die-attach solder

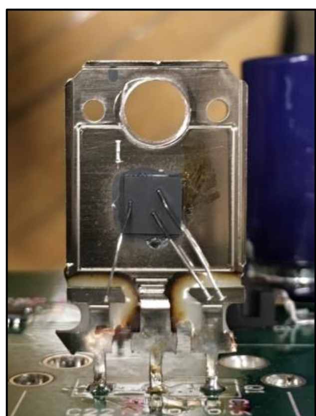

(c) IGBT after slight die-attach degradation

(d) Solder removed during slight die-attach degradation

Fig. 4.3-4. Images taken during a process to manually remove solder from an IGBT die-attach interface

Die temperature sensing

Once again, TSEPs of the actively switching semiconductor device were utilized to estimate die temperature in situ. Now, IGBT device current and forward voltage drop $V_{ce(on)}$ were sensed and correlated to die temperature. The dynamic TSEP calibration experiment was again executed to form an empirical model relating the variables. Fig. 4.3-5 shows data from a calibration experiment. Please note that the displayed effective on-state IGBT resistance variable, $R_{ce(on)}$, was computed by dividing on-state voltage by current.

Table 4.3-1. Calibrated parameters of the IGBT die temperature estimator (3.2-8)

	Lower bound	Upper bound	Units
A_1	29.9	31.5	°C/A
A_2	-220	-179	°C/Ω
A_3	-452	-435	°C/(A-Ω)
A_4	682	703	°C

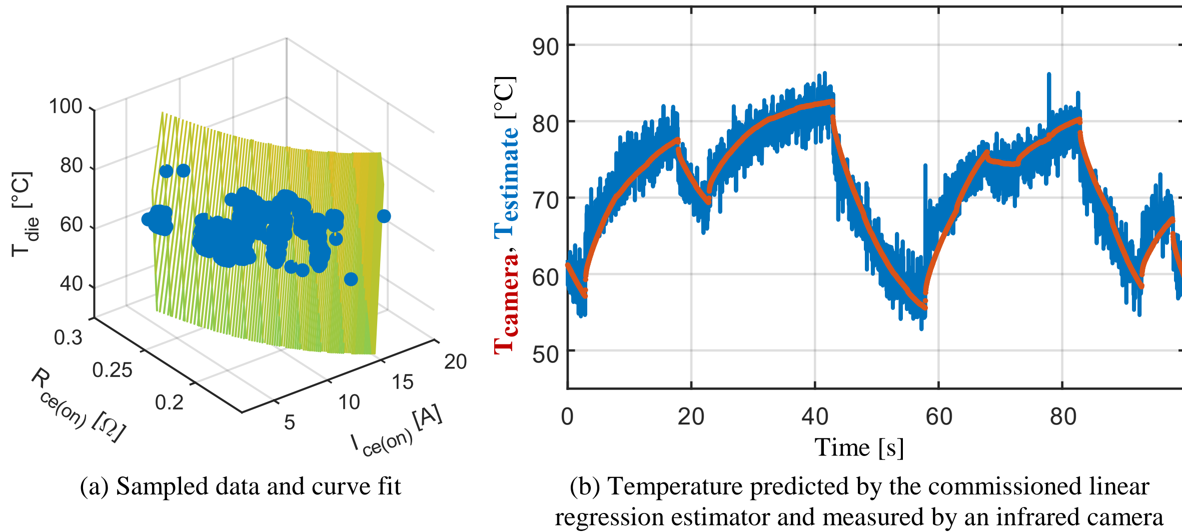

(a) Sampled data and curve fit

(b) Temperature predicted by the commissioned linear regression estimator and measured by an infrared camera

Fig. 4.3-5. Data used for calibrating an IGBT die temperature estimator

The fit of various linear regression models were studied in order to select an accurate real-time estimation model. The model (3.2-8) and other higher order variants were observed to all have coefficients of determination, R^2, around 88%. Therefore, (3.2-8) was selected as the model for the transient IGBT die temperature estimator.

$$\hat{T}_{die} = \hat{A}_1 I_{ce,on} + \hat{A}_2 R_{ce,on} + \hat{A}_3 I_{ce,on} R_{ce,on} + \hat{A}_4 \qquad (4.3\text{-}1)$$

Parameters corresponding to a 95% confidence interval for the linear regression estimator are displayed in Table 4.3-1. Please note that the best-fit parameter estimates, which were utilized to compute die temperature, are the average of the upper and lower bound values. For this model, 90% of the residuals fall within 95% confidence intervals to diagnose outliers.

The surface shown on top of the experimental data in Fig. 4.3-5(a) represents the multi-variable linear regression die temperature estimator. Fig. 4.3-5(b) displays the temperature data used to calibrate the model as a time series. Estimated die temperature, formed using current and voltage data which calibrate the model, is also shown in the figure. It has observable noise because of the temperature sensitivity of the IGBT device is relatively low, and less than the prior MOSFET test device. This necessitates the usage of relatively large gains to convert measured resistance to temperature, which amplifies $V_{ce(on)}$ measurement noise, for example.

Degradation emulation

TIM degradation was again emulated by loosening the bolted connection which pressed the IGBT component into the heat sink from its nominal 1.0 N-m torque level. Die-attach degradation was also emulated using manual fabrication steps. To intentionally induce damage in the die-attach solder interface, the system's heat sink, visible in Fig. 4.3-5(a), was removed. Then, as shown in Fig. 4.3-5(b), a heat gun was applied to the back side of the component to reflow the die-attach solder. The infrared image shows how the die reached over 325°C.

To induce a slight defect in the die-attach, the die was gently moved, and solder wick was utilized to extract solder. After solder extraction, the semiconductor die was then moved back to approximately its initial location. Fig. 4.3-5(c) shows the appearance of the component after die-attach defect fabrication. Fig. 4.3-5(d) shows the trace amounts of extracted solder on the copper solder wick material.

After characterization with this slight degradation to the die-attach, it was more severely damaged. To evaluate the response with under severe die-attach degradation, more solder was removed, and the die-attach solder could solidify such that approximately the right half of the

device was not bonded to the lead frame substrate. Before commencing with all system identification experiments, switching operation of the IGBT was verified.

4.3.2.2 Results

Severe cases of degradation

Since sensitivity to cooling properties was not of interest for this experimental work, sub-10 mHz response was not measured. Fig. 4.3-6 documents experimental results (a) as an overlay of dimensional FRFs and (b) sensitivity functions, in which FRFs for the three cases of degradation were normalized by a baseline FRF extracted at 1.0 N-m bolt fastening torque and no die-attach alterations. Fig. 4.3-6(b) includes a baseline sensitivity function ($= 0\angle 0°$ across all frequencies) as a trivial check of the sensitivity function division operation.

Upon initial glance, Fig. 4.3-6 shows that the baseline and slight die-attach degradation FRFs are similar, while severe die-attach and TIM degradation induced significant alterations in FRF. To start a discussion, it is remarked that the features of the TIM sensitivity function resemble those measured in Fig. 4.3-2. For instance, the sensitivity function's phase exhibits lag between 10 and 1 Hz, before returning to a steady value. TIM sensitivity function amplitude appears to peak at around 10 mHz, and cross below unity around 100 mHz. This property and the constant phase lag between 1 and 100 Hz are not predicted by evaluated models.

The DC gain of the FRF with TIM degradation increases from the baseline FRF, which is probably around 2°C/W. Response with die-attach degradation also has amplified DC gain. However, this response has unique properties not previously observed in lab and modeling work. First, the phase response exhibits significant roll-off in the 0.1-1 Hz range. At 1 Hz, the phase then relatively suddenly shifts toward response with increasingly less phase lag. Around this same

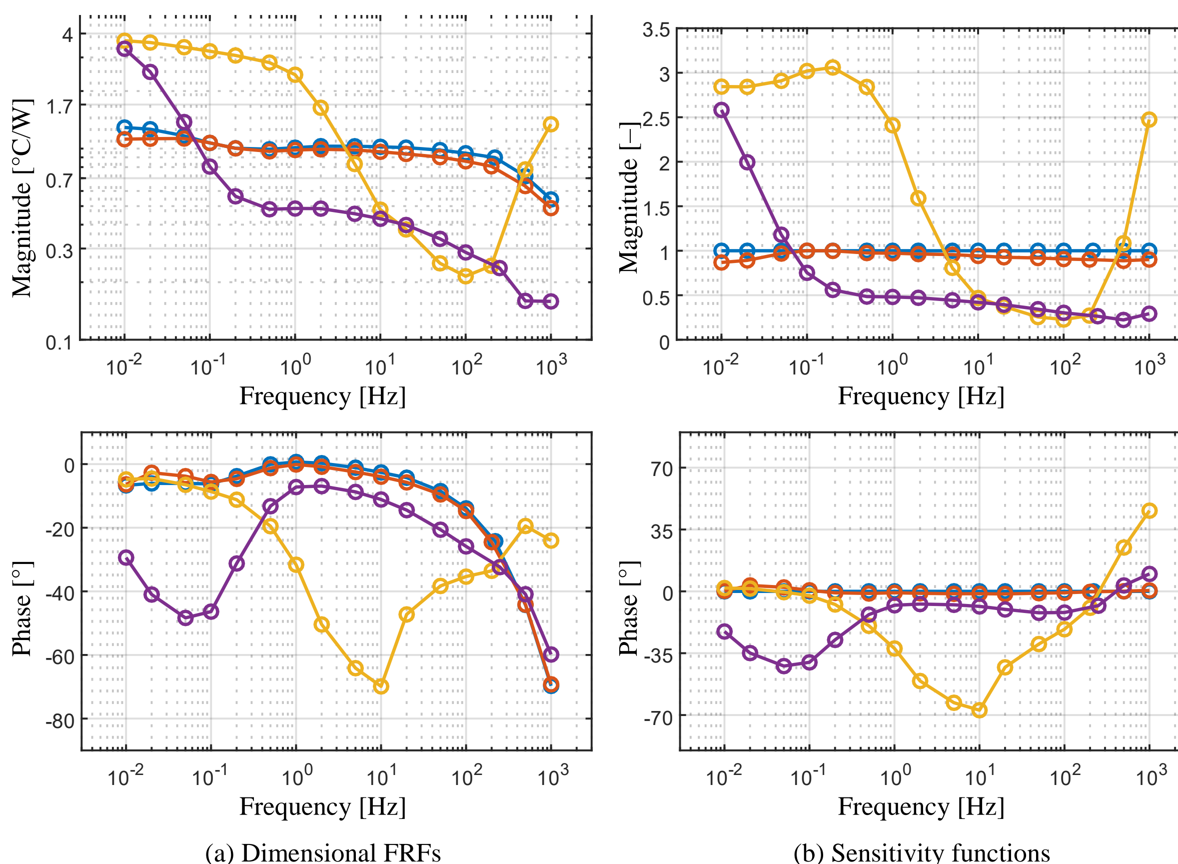

(a) Dimensional FRFs (b) Sensitivity functions

Legend: **Baseline** **Slight die-attach degradation** **Severe die-attach degradation** **TIM degradation**

Fig. 4.3-6. Impact of different sources of degradation on IGBT device driving point electrothermal impedance

harmonic frequency, the FRF amplitude grows. The final measured data point at 1 kHz has AC response amplitude within 20% of the DC gain value, and around 2.5 times larger than the DC gain of the baseline FRF.

The severe die-attach degradation defect is intended to be a limit case and perhaps not useful toward a goal of this research to integrate real-time degradation sensing in actively switching converters. However, it could have scientific significance. FRF amplitude attenuation followed by amplification is a traditional indicator of complex poles, and resonance phenomena, in open-loop system behavior. Resonant dynamics are not commonly associated with heat transfer, which, in one abstraction, is governed by a first-order state-space model. Further tests for verification are needed, however, these results suggest that resonant transient thermal response

behavior could be excited by extreme geometric constrictions in solids, and that such a constriction was induced during severe die-attach damage.

Slight die-attach degradation

Fig. 4.3-7 isolates the sensitivity function for slight die-attach degradation included in Fig. 4.3-6(b). It reveals that, at most, the magnitude and phase responses are about 12% and 4° sensitive to this defect. Next, recall that prior prediction of die-attach degradation by uniformly manipulating contact resistance parameters in a finite difference model, for example, suggested that die-attach degradation sensitivity appeared clearly above a frequency threshold. Fig. 4.3-7 does not exhibit this property in general.

For the cases of die-attach degradation, experimental control of the TIM was obtained by manually applying 1.0 N-m torque to the bolted joint pressing the IGBT against the heat sink. However, errors could have occurred during this process such that the die-attach and TIM were both altered after making the baseline FRF measurement. This could be a reason that the measured sensitivity function for slight die-attach degradation is relatively spread-spectrum, compared to Fig. 4.2-10(a), for example.

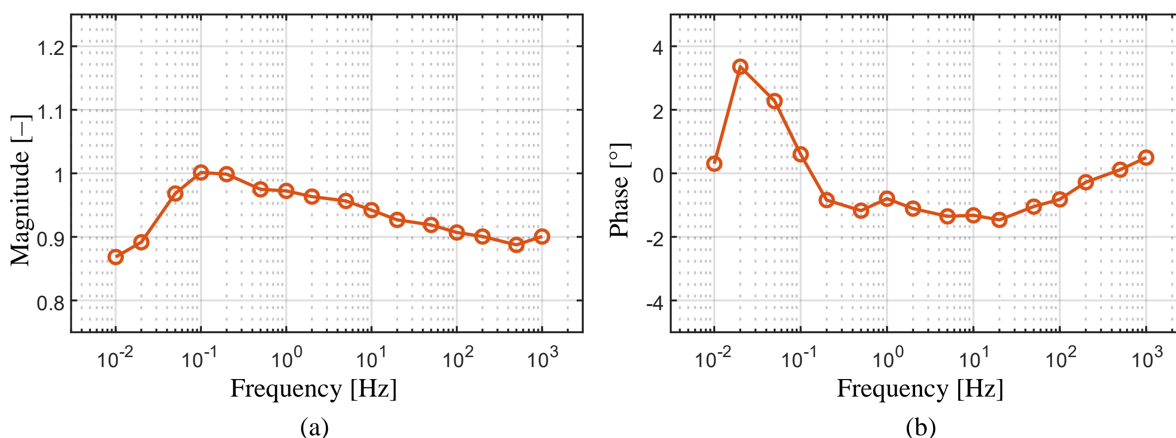

Fig. 4.3-7. Sensitivity function for slight die-attach degradation

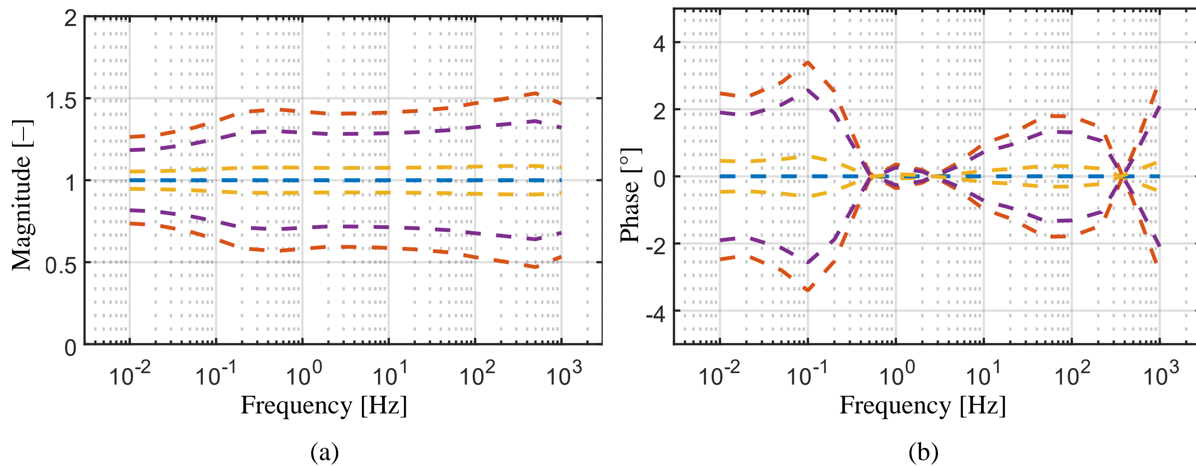

Legend: manipulation of A_1 A_2 A_3 A_4

Fig. 4.3-8. Sensitivity of the computed FRF estimate to parameters of the IGBT temperature estimator (3.2-8)

4.3.2.3 IGBT temperature sensing error quantification

Prior research suggests that AC loss modulation theoretically has magnitude-only parameter sensitivity for converters in PWM operation. So, FRFs formed based on electrical signal measurements can have magnitude error. This section will now quantify how errors can be incurred due to using a semiconductor device itself as a nonlinear chip temperature sensor, using the application of ETIS on the IGBT converter in this section as a case study.

Recall how a separate calibration experiment led to a characterization of the dependence of die temperature on switching device current and apparent resistance. The computed best-fit linear regression model (3.2-8) has four coefficients. Despite the optimal selection of these parameters by the regression optimizer, they do not perfectly estimate die temperature due to process and measurement noise. Their goodness-of-fit is further quantified by intervals of specified confidence. For example, 95% confidence interval limits are shown in Table 4.3-1.

The post-processing platform to transform time domain data into the frequency domain can evaluate arbitrary functions relating die temperature to instantaneous voltage and current, if these data are collected. So, for quantifying confidence bounds of IGBT temperature sensing, and subsequently FRF, accuracy, these parameters were individually evaluated at the limits of their 95% confidence intervals while all others were kept at their best-fit values. Resulting sensitivities of resulting FRF estimates are shown in Fig. 4.3-8. It shows how the sensitivity of the FRF calculation to regression model parameters is not constant in frequency.

The data displayed Fig. 4.3-8 can be interpreted error envelopes for the FRF amplitude and phase measurements made in this section. The FRF computation has zero sensitivity to the DC offset A_4, some to the on-state resistance gain A_2, and the most sensitivity to the current gain A_1. To gain insight about the origins of these variable sensitivity properties, (4.3-2) and (4.3-3) present partial derivatives of the governing regression model to the model inputs. As (4.3-4) and (4.3-5) show, variable sensitivities are treated as the reciprocal of these partial derivatives. Evaluation of sensitivity terms using data in Table 4.3-1 reveals that temperature sensitivity of $I_{ce(on)}$ is higher than to $R_{ce(on)}$. These results highlight, for the calibration data utilized, the relative insensitivity of $R_{ce(on)}$ to die temperature. Eq. (4.3-5) shows that about 300 μΩ resistance sensing resolution is needed for 1°C temperature sensing resolution.

$$\frac{\partial \hat{T}_{die}}{\partial I_{ce,on}} = \hat{A}_1 + \hat{A}_3\, R_{ce,on} \tag{4.3-2}$$

$$\frac{\partial \hat{T}_{die}}{\partial R_{ce,on}} = \hat{A}_2 + \hat{A}_3\, I_{ce,on} \tag{4.3-3}$$

$$\text{sens}(I_{ce,on}) \equiv \frac{\partial I_{ce,on}}{\partial \hat{T}_{die}} \qquad = \text{large} \tag{4.3-4}$$

$$\text{sens}(R_{ce,on}) \equiv \frac{\partial R_{ce,on}}{\partial \hat{T}_{die}} \qquad \approx -0.3\ \text{m}\Omega/^\circ\text{C} \tag{4.3-5}$$

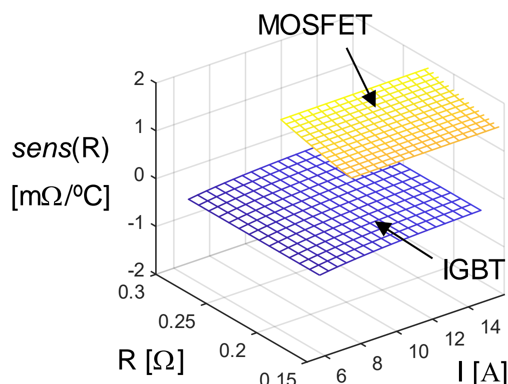

Fig. 4.3-9. Comparison of temperature sensitivities for the effective on-state resistance of the IGBT and MOSFET component characterized in Chapter 3

Fig. 4.3-9 displays the temperature sensitivity of the IGBT component's effective on-state voltage as a function of its operating point. It varies between around -0.35 and -0.15 mΩ/°C. The plot also shows how the on-state resistance component for the MOSFET, characterized in tests in the previous chapter, has about an order of magnitude larger sensitivity.

4.3.3 MOSFET component characterization of die-attach sensitivity

To investigate how the attachment between a power semiconductor device and its substrate influence transient heat transfer, an experiment was carried out. A power MOSFET die-attach was reflowed, using a heat gun, and the semiconductor die was displaced several mm from its nominal location, as shown in Fig. 4.3-11.

Then, the component was characterized experimentally to produce an FRF, the phase of which is shown in Fig. 4.3-10(a). The (b) plot shows the phase of the sensitivity function, which was computed using the FRF expressed in Fig. 3.2-11 as baseline. Please note that only phase results are displayed due to the conclusion of their accuracy made in the prior subsection.

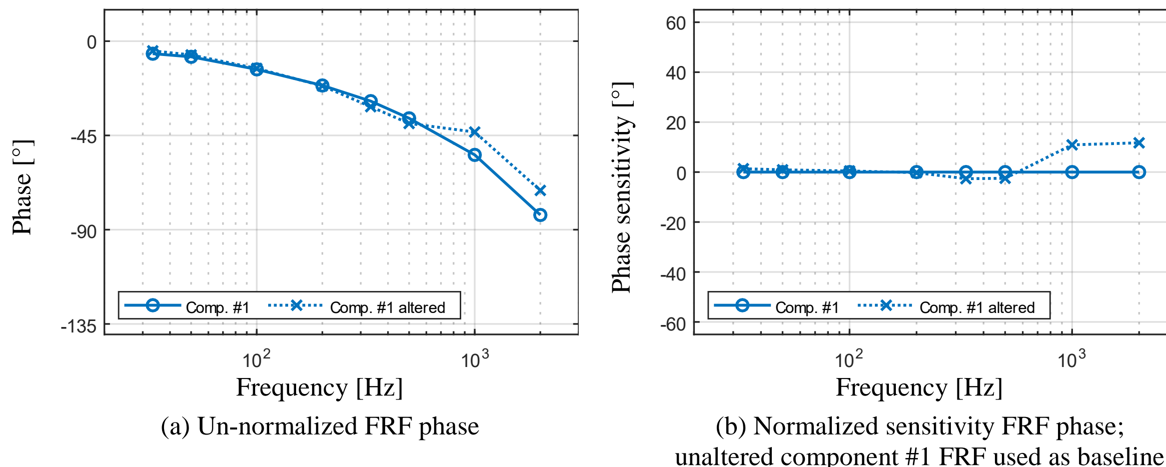

(a) Un-normalized FRF phase

(b) Normalized sensitivity FRF phase; unaltered component #1 FRF used as baseline

Fig. 4.3-10. Phase FRF with degradation to the die-attach interface of the DUT

A clear response deviation between 500 and 1000 Hz can be observed in Fig. 4.3-10. The phase delay with the die-attach alteration is about 15° less than without the alteration. This measurement matches what was predicted previously in this document by a 1D, transient heat transfer model including contact resistance.

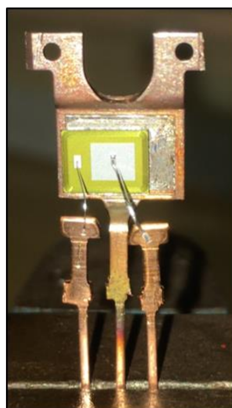

Fig. 4.3-11. DUT MOSFET after fabricated die-attach alteration

4.4 Chapter Summary

This chapter utilized models and experiments to characterize the impact of different sources of thermal-mechanical degradation on heat transfer FRF properties. Following scope definition, models built in Chapter 2 and Chapter 3 were augmented to reflect different sources of

degradation. Then, they were evaluated using different metrics to quantify FRF sensitivity to degradation. During this process, it was generally observed that degradation sensitivities appear at higher frequencies the closer the degradation source is to a source of losses. Response variations were viewed predominantly with FRF plots, but complex impedance plots are also revealing.

Experimental FRF data were extracted from an actively switching power electronic converter system and discrete components. The study spanned MOSFET and IGBT device types under healthy, limited cooling, altered TIM joint, and manipulated die-attach conditions. The model-based and measured properties under cooling degradation agree uniformly. TIM sensitivity functions between model and experiment exhibit some level of disagreement. One experiment to characterize the impact of slight die-attach degradation revealed a sensitivity region more spread in frequency that that predicted by uniform contact resistance manipulation in the model. Isolated characterization of a discrete MOSFET component revealed a distinct break frequency having sensitivity to its die-attach.

For further reading on the topic, reference [172] may be consulted.

Chapter 5 In-Situ Degradation Sensing based on Thermal Response Variation

0 illustrated how a power electronic system's spatiotemporal thermal response changes, in certain dynamic ranges, as a function of different sources of degradation that can occur in a converter's lifetime. This chapter begins the process of integrating aspects of heat transfer FRF characterization, introduced and utilized in past chapters, into power electronic systems serving specific mission profiles. First, methods for quantifying the usefulness of naturally occurring loss dissipation for in situ system identification are presented. Then, signal processing down-scaling is discussed. Finally, a concept for direct and automatic estimation of a degradation sensitive parameter is presented and experimentally evaluated. Elements of this chapter are also documented in publications [171], [173], [174].

5.1 Modeling Natural Loss Excitation Harmonics

This section develops models for characterizing semiconductor device loss harmonics as a function of converter application parameters.

5.1.1 Analytical modeling

Fig. 5.1-1 displays a circuit schematic of a half-bridge converter topology. The schematic includes controlled switching devices, the MOSFETs S_1 and S_2; passive switching devices D_1 and D_2; DC link capacitance C and voltage V_{DC}; pole inductance L; and a general load impedance Z. This schematic was used as the basis for developing an analytical model of loss harmonics near the fundamental frequency of the half-bridge.

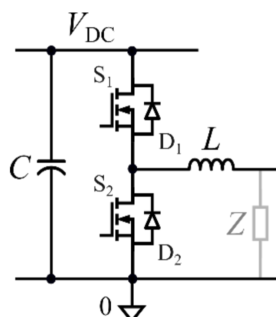

Fig. 5.1-1. Half-bridge circuit sourcing a load with impedance Z

To start, conduction losses were modeled. Eq. (5.1-1) presents an expression for high-side device conduction losses (in units of W) averaged over a switching period. In this model, d is the duty ratio of the switching device and I_{on} is the conducted on-state current. Resistive on-state behavior, quantified by an on-state resistance, R_{on}, is assumed for the MOSFETs.

$$Q_{cond} = d \cdot I_{on}^2 \cdot R_{on} \quad (5.1\text{-}1)$$

To relate the model to higher-level converter parameters, such as its fundamental operating frequency ($\omega = 2\pi f$) and the parameters in Fig. 5.1-1, a sine-triangle PWM scheme was assumed. For this chapter, (5.1-1) was eventually expressed in terms of three harmonics shown in (5.1-2)–(5.1-4). This simple model can be extended for other PWM algorithms, as done in [175], for example.

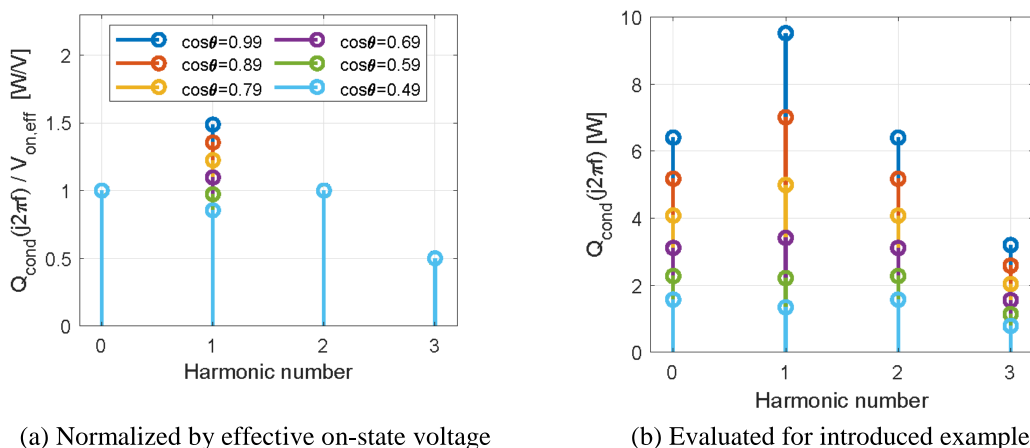

(a) Normalized by effective on-state voltage (b) Evaluated for introduced example

Fig. 5.1-2. Conduction loss amplitude by harmonic

1st harmonic: $2\cos(\omega t) + 2\cos(\omega t + 2\phi)$ (5.1-2)

2nd harmonic: $2\cos(2\omega t + 2\phi)$ (5.1-3)

3rd harmonic: $\cos(3\omega t + 2\phi)$ (5.1-4)

The relative amplitudes of the 2nd and 3rd harmonics are fixed, as shown in Fig. 5.1-2(a). The amplitude of the harmonics vary with the angle between the applied and resulting AC voltage and current, given by (5.1-5) for a resistive load.

$$\phi = \arctan(2\pi f \cdot L/R) \tag{5.1-5}$$

Ultimately, (2.3-1) compiles harmonic components and represents total device conduction losses. It is scaled by an effective device on-state voltage parameter, $V_{on,eff}$, given by (2.3-2) and, subsequently, a device's effective on-state current, $I_{on,eff}$, given by (3.2-8).

$$\frac{Q_{cond}}{1/4\, V_{on,eff}} = Q_{cond,1} + Q_{cond,2} + Q_{cond,3} \tag{5.1-6}$$

$$V_{on,eff} = I_{on,eff} \cdot R_{on} \tag{5.1-7}$$

$$I_{on,eff} = \frac{2 \cdot P_{real}}{V_{DC}} \tag{5.1-8}$$

Table 5.1-1. Parameter used for evaluation of the developed conduction loss harmonic model

Parameter	Value	Unit	Parameter	Value	Unit
V_{DC}	600	V	L	100	μH
V_o	280	V	$Z = R$	1	Ω
R_{on}	100	mΩ			

Examination of the $I_{on,eff}$ term reveals that conduction loss harmonic amplitudes are proportional to the real power delivered to a converter's load, P_{real}, and inversely proportional to V_{DC}. As suggested by (2.3-2) and (2.3-1), high current converters generate higher amplitude conduction losses.

The model was used to quantify conduction losses of the high-side MOSFET in a converter application. Parameters for the example are documented in Table 5.1-1, and Fig. 5.1-2(b) shows the resulting spectrum, again for a sweep of power factor. It shows that conduction loss harmonic amplitude scales with P_{real}, which varied between 9 and 40 kW for this example.

5.1.2 Numerical simulation

5.1.2.1 Three-phase traction inverter model

In this chapter, simulation was utilized to compute total conduction and switching losses for semiconductor devices in an electric vehicle drive. The simulation, based on [176], is centered around a two-level, voltage-source inverter in which the power switches were integrated in a single *HybridPACK2* power module. The traction inverter drove a 150-kW induction machine propelling a trolleybus.

The coupled dynamic model was implemented in *Simulink* to numerically simulate the behavior of a trolleybus following a driving cycle, shown in Fig. 5.1-3(a). Total semiconductor device losses, averaged over the fixed switching period of the converter, were extracted in the time domain. Inverter instantaneous fundamental frequency can be inferred from the output voltage and current waveforms. The losses of an IGBT device contain this content, as shown in Fig. 5.1-3(b).

5.1.2.2 Harmonic modeling

Fourier transform techniques quantify frequency content embedded in time-domain response signals. For this study 1000 s of extracted time domain simulation data were divided equally into ten segments and Fourier coefficients were computed for each segment. Fig. 5.1-4(a)

displays device loss harmonics for all ten segments. For clarity, Fig. 5.1-4(b) shows the spectrum of a single segment. It clarifies that the 10-50 Hz harmonics are most powerful.

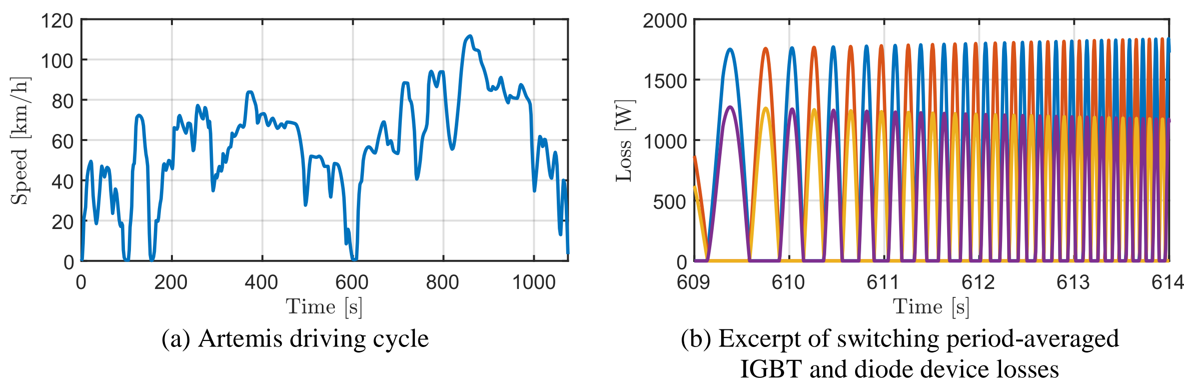

(a) Artemis driving cycle

(b) Excerpt of switching period-averaged IGBT and diode device losses

Fig. 5.1-3. Time domain data from simulation of an electrically driven trolley bus over a mission profile

Overall, the investigation of a traction drive traversing a standard electric vehicle load profile shows that loss harmonic content of AC converters is proportional to its fundamental modulation frequency. This naturally occurring harmonic excitation can be used to provide the actuation needed by degradation sensing. A process of designing a module for degradation sensing can therefore begin with a circuit schematic and quantification of its transient loss harmonics, which depend on load profile.

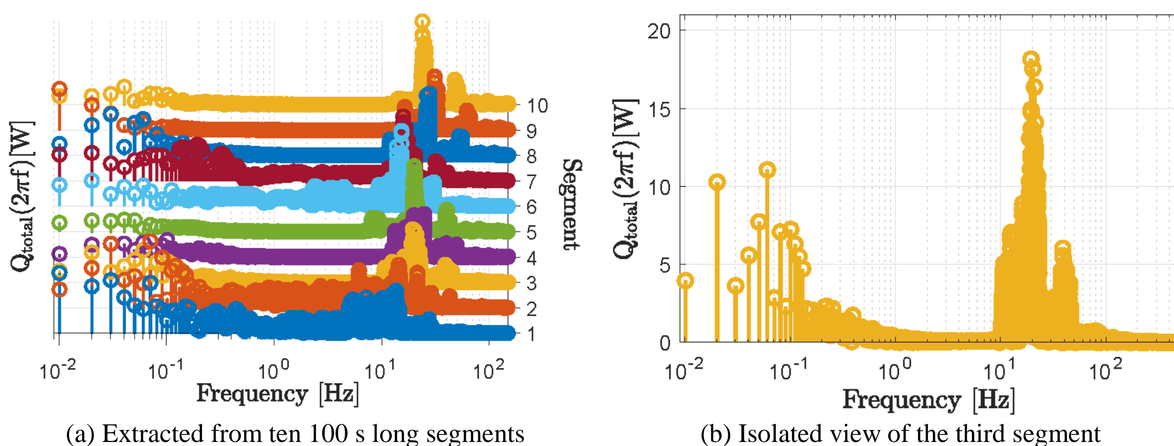

(a) Extracted from ten 100 s long segments

(b) Isolated view of the third segment

Fig. 5.1-4. Total loss spectrum of a single IGBT device of an inverter's power module

5.2 Extraction of Degradation Information

5.2.1 Tracking deviation from a baseline response

A recent paper demonstrated the capability of the sinusoidal correlation technique to function as a real-time FRF calculator [177]. This technique is suitable for implementation within a detection and diagnostics system. Fig. 5.2-1 diagrams high- and low-level components of the methodology to directly estimate FRF data and correlate them to state-of-health. Fig. 5.2-1(a) diagrams such a system, which utilizes an estimate of device conduction switching losses, sensed temperature information, and the sine correlation technique to estimate thermal impedances at discrete frequencies that are known or anticipated to have sensitivity to thermal-mechanical degradation sources. Fig. 5.2-1(b) provides a general block diagram of the orthogonal correlation technique, while Fig. 5.2-1(c) adopts it for real-time extraction of heat transfer FRF data.

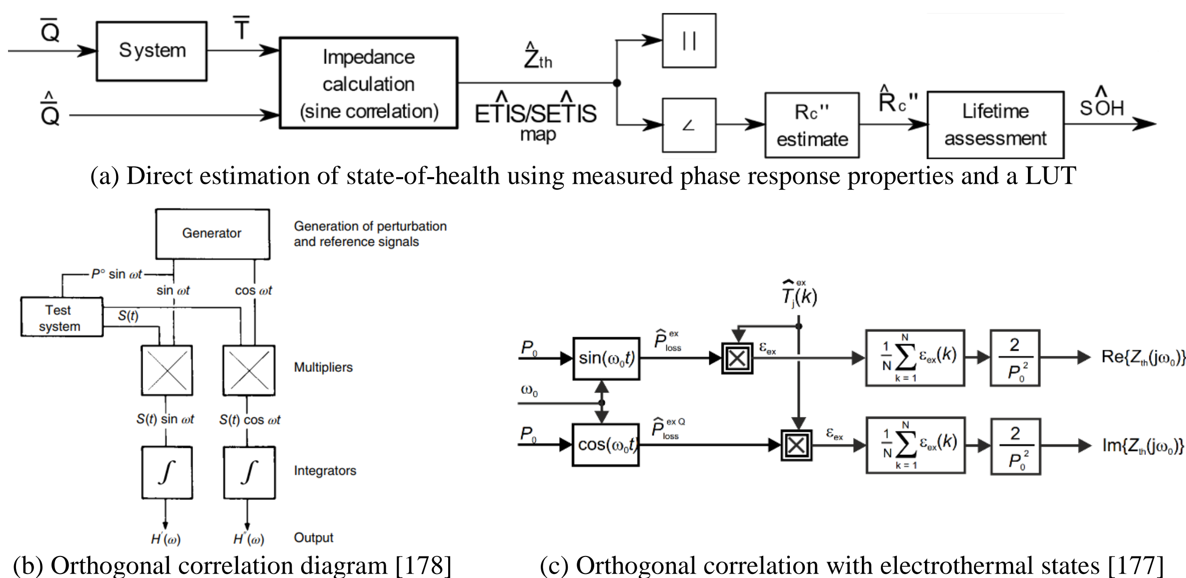

(a) Direct estimation of state-of-health using measured phase response properties and a LUT

(b) Orthogonal correlation diagram [178]

(c) Orthogonal correlation with electrothermal states [177]

Fig. 5.2-1. Block diagrams illustrating methods based on FRF data to assess state-of-health

The FRA-based methods for monitoring degradation are oriented toward quantifying structural degradation as close as possible to the die temperature measurement location as SNR

limits permit. To detect degradation of proximal features, algorithms should utilize the sensitive medium to high FRF frequencies. Additionally, parameter sensitivity is a desired feature of developed systems. Toward this objective, Fig. 5.2-1(b) intentionally relates an estimate of contact resistance to ETI phase, rather than magnitude, because the loss modulators employed in this research only have parameter sensitivity in the magnitude response.

5.2.2 Automatic, adaptive techniques

This subsection will document the design algorithms to automatically identify degradation-sensitive parameters of compact electrothermal models, like that derived in section 2.2. Fig. 5.2-2(a) and (b) diagram the general operating principle of such systems, which utilize principles of adaptive control theory.

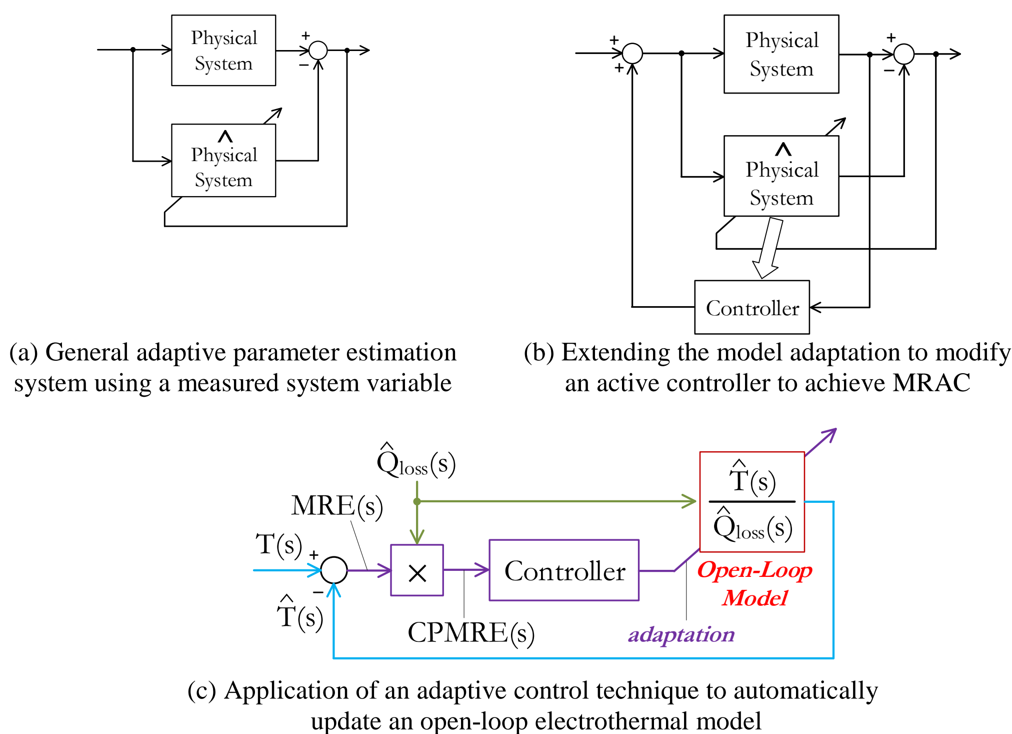

(a) General adaptive parameter estimation system using a measured system variable

(b) Extending the model adaptation to modify an active controller to achieve MRAC

(c) Application of an adaptive control technique to automatically update an open-loop electrothermal model

Fig. 5.2-2. Diagrams representing theoretical and applied adaptive parameter estimation and control techniques

The system shown in Fig. 5.2-2(c) uses an estimate of power device losses, $\hat{Q}_{loss}(s)$, and an open-loop electrothermal system model to dynamically estimate a physical temperature, $\hat{T}(s)$, along with a sensed temperature, T(s). The system correlates errors in estimated temperature to inaccuracies in the open-loop model. The system has a controller that attempts to null the model reference error (MRE) and coherent power of the MRE (CPMRE) by manipulating the model.

The adaptive system in Fig. 5.2-2 minimizes an error quantity by manipulating parameters of an open-loop model. Therefore, it is possible to interpret the observer as an optimal, closed-loop system. As will be shown in the presentation of the adaptive thermal capacitance observer, the optimization problem formalism can also yield in a system which minimizes additional quantities. The following subsections will provide more details about the operating principles embedded within these adaptive observer systems.

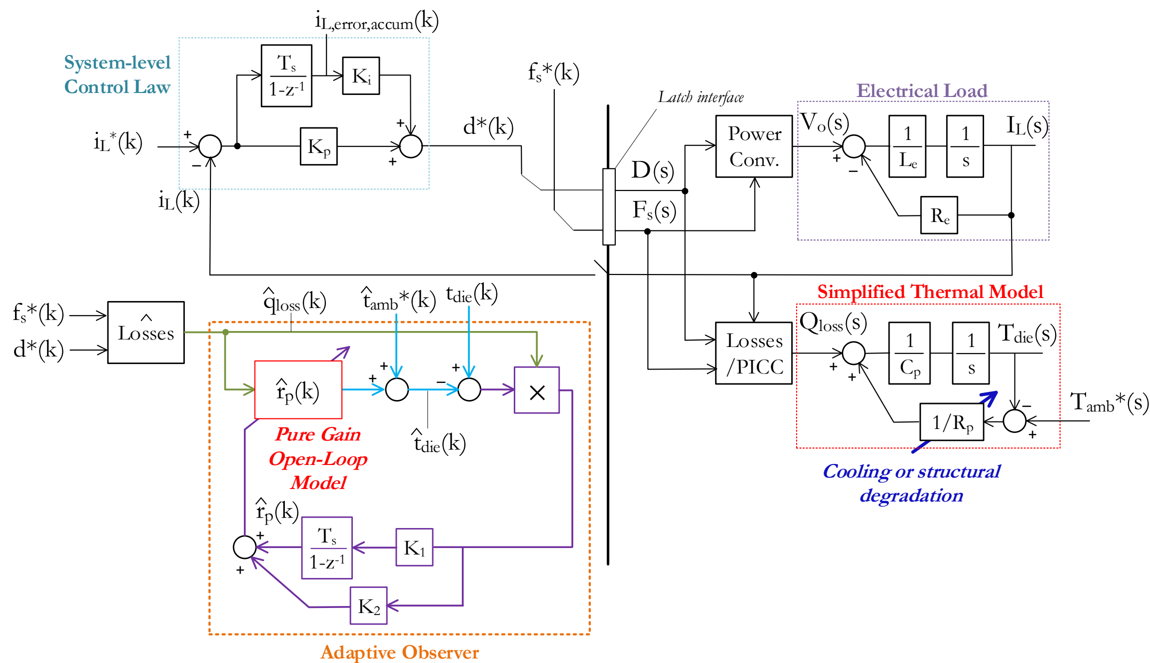

Fig. 5.2-3. Discrete-time implementation of the adaptive thermal resistance observer, having a compact pure thermal resistance gain open-loop model, shown adjacent to a closed-loop current regulated electrical system

5.2.2.1 Adaptive thermal resistance observer

An adaptive thermal resistance observer, building upon Fig. 5.2-2(c), is shown in Fig. 5.2-3 adjacent to a current controlled DC-DC converter system. Shown are manipulated inputs duty ratio [D(s)] and switching frequency [$F_s(s)$] exiting the latch interface and entering a power converter block. Output voltage, $V_o(s)$, is applied to a first-order electrical R-L load. Paralleled is the electrothermal process of device-generated conduction and switching losses being applied to a first-order thermal system having thermal resistance (R_p) and capacitance (C_p). Ambient temperature [$T^*_{amb}(s)$] is included as a non-zero virtual reference (NZVR), and die temperature is shown as the state variable of interest.

The adaptive electrothermal observer is included inside the digital portion of Fig. 5.2-2. The observer first estimates device losses using duty ratio, switching frequency, and a loss model, such as equations in subsection 3.1.2.1. The losses are delivered to an open-loop electrothermal model which sums with the NZVR to estimate die temperature.

The open-loop model topology can vary. For example, it can be a spatiotemporal lumped parameter model like (2.2-13), a high-fidelity state space model, or a pure (thermal resistance) gain. Experimental results documented later in this section utilize a maximally compact open-loop model, a pure $\hat{R}_p$ gain. No matter the model, it is adapted by the observer controller, with K_1 and K_2 gains, which minimizes the difference between estimated and sensed die temperatures.

$$\frac{d\Phi}{dt} = -\beta\, e(t)\, \frac{\partial e(t)}{\partial \Phi} \tag{5.2-1}$$

$$C_p \frac{dT(t)}{dt} = q_{loss}(t) - \frac{1}{R_p} T(t) \tag{5.2-2}$$

$$T(t) = q(t) \cdot R_p - C_p \frac{dT(t)}{dt} \Rightarrow \frac{\partial T(t)}{\partial R_p} = q(t) \tag{5.2-3}$$

$$\frac{d}{dt} \hat{R}_p = K_1 \left[T_{die}(t) - \hat{T}_{die}(t) \right] \hat{q}_{loss}(t) \tag{5.2-4}$$

Eq. (5.2-1)−(5.2-4) comprise a derivation of a parameter adaptation dynamic state equation for the case where the estimated electrothermal model is a pure gain, $\hat{R}_p$. Eq. (5.2-1) is the "MIT rule," where Φ represents an estimated parameter, and e(t) is estimation error [179]. The first-order thermal state equation is (5.2-2), and (5.2-3) executes algebraic manipulation to show how losses, temperature, and the thermal resistance parameter are intuitively correlated. Finally, utilization of (5.2-3) to follow (5.2-1) yields (5.2-4), which represents thermal resistance parameter adaptation dynamics having a K_1 process gain.

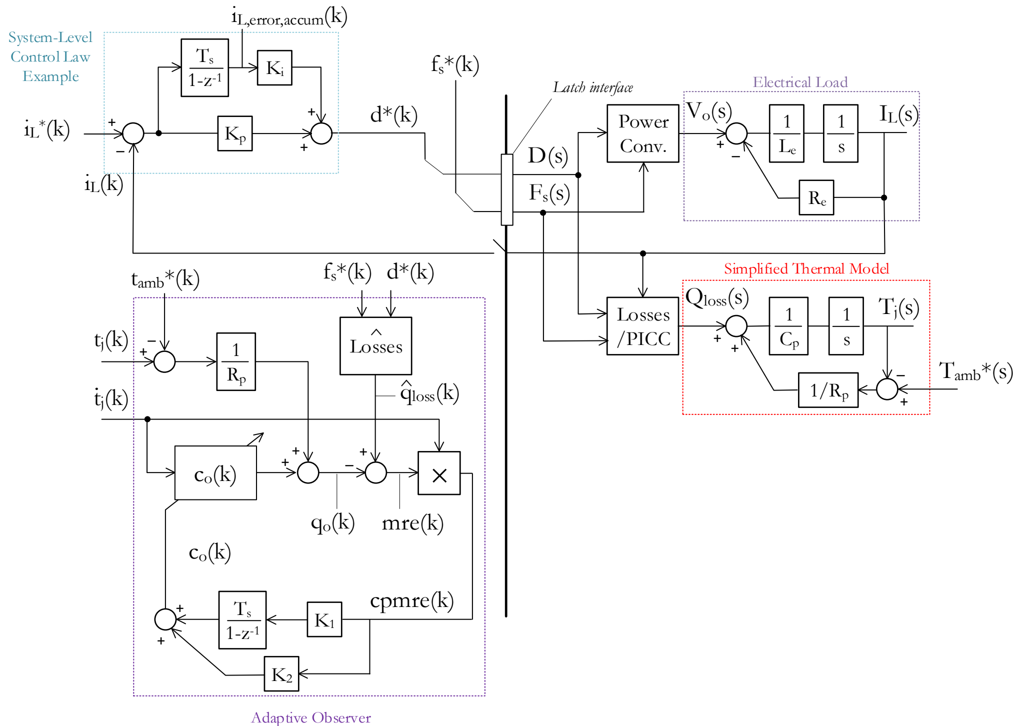

Fig. 5.2-4. State block diagram description of the adaptive thermal capacitance observer implemented in discrete-time

For thermal resistance estimation, the adaptive observer correlates the $\left[T_{die}(t) - \hat{T}_{die}(t)\right]$ error with losses to update $\hat{R}_p$ consistently with physical system degradation. Fig. 5.2-3 implements (5.2-1)−(5.2-4), with an observer controller having an optional K_2 proportional gain for adjusting fine-tuning convergence properties.

5.2.2.2 Adaptive thermal capacitance observer

Like systems designed to estimate lumped steady-state thermal parameters during real-time converter operation, it is possible to estimate transient thermal parameters. Eq. (5.2-5)−(5.2-7) starts with a first-order thermal system model to derive a system to adaptively manipulate the thermal capacitance parameter of an open-loop model following (5.2-1). Eq. (5.2-7) documents the adaptation dynamic state equation having a K_1 process gain. Fig. 5.2-4 implements (5.2-7) with a controller having a proportional gain term. Please note that this observer system requires an estimate of dT(t)/dt, which can be provided by another, cascaded observer system.

$$C_p \frac{dT(t)}{dt} = q(t) - \frac{1}{R_p} T(t) \qquad (5.2\text{-}5)$$

$$q(t) = C_p \frac{dT(t)}{dt} + \frac{1}{R_p} T(t) \Rightarrow \frac{\partial q(t)}{\partial C_p} = \frac{dT(t)}{dt} \qquad (5.2\text{-}6)$$

$$\frac{d}{dt} C_o = K_1 \left[q(t) - q_o(t)\right] \frac{dT(t)}{dt} \qquad (5.2\text{-}7)$$

5.3 Evaluation of Methods

5.3.1 Look-up table method

This subsection provides an example of a phase response-based R_c'' estimate using the 1D transient analytical model documented in subsection 4.2.1. Fig. 5.3-2(a) repeats the spatially-

varying phase response surface from the 1D transient model with zero-valued contact resistance and tags the data point at x→0 p.u. position (die temperature sensing assumed) and for a 1 Hz loss injection. Next, Fig. 5.3-2(b) provides the SETIS phase response map with R_c'' equal to the total healthy system die-to-ambient thermal resistance. The phase response at the same location is displayed, and it can be observed that the phase response value changes by approximately 60° due to the manifestation of contact resistance.

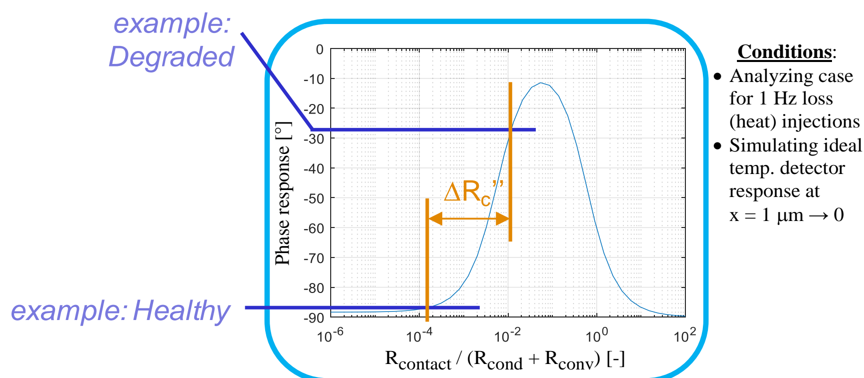

Fig. 5.3-1. Driving impedance phase response to 1 Hz fundamental frequency loss injections as a function of normalized contact resistance

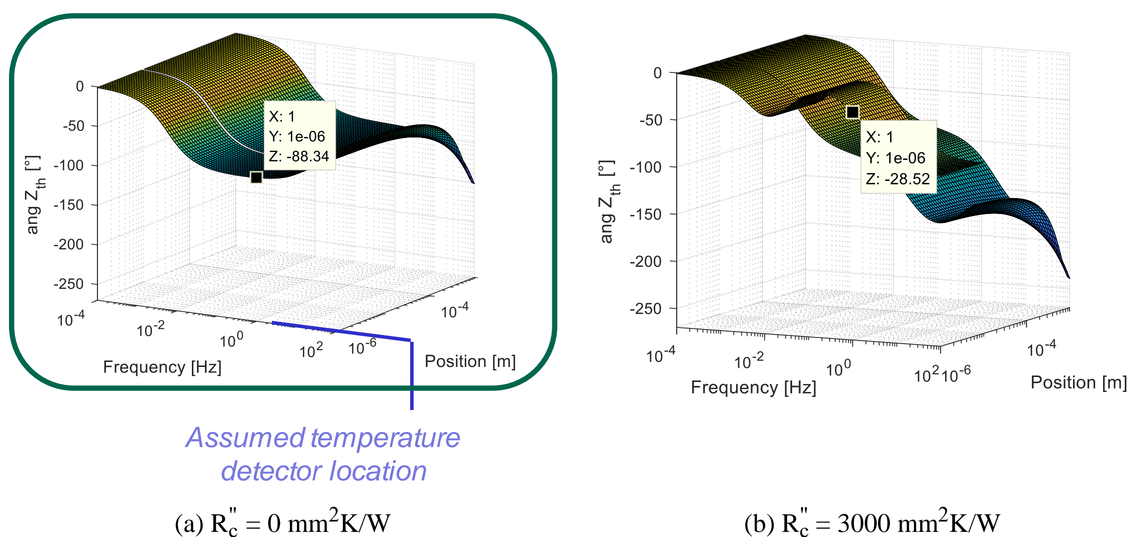

(a) $R_c'' = 0$ mm^{2}K/W (b) $R_c'' = 3000$ mm^{2}K/W

Fig. 5.3-2. Spatially-varying FRF phase extracted from a developed 1D transient analytical model

Fig. 5.3-1 generalizes the single result displayed by Fig. 5.3-2 by showing how the driving point impedance phase response changes as a function of R_c''. To implement in situ degradation sensing, this type of plot can be implemented and evaluated in the DSP of a power electronic system. The function is non-monotonic; however, it would be truncated before the second vertical bar, which corresponds to 100% degradation.

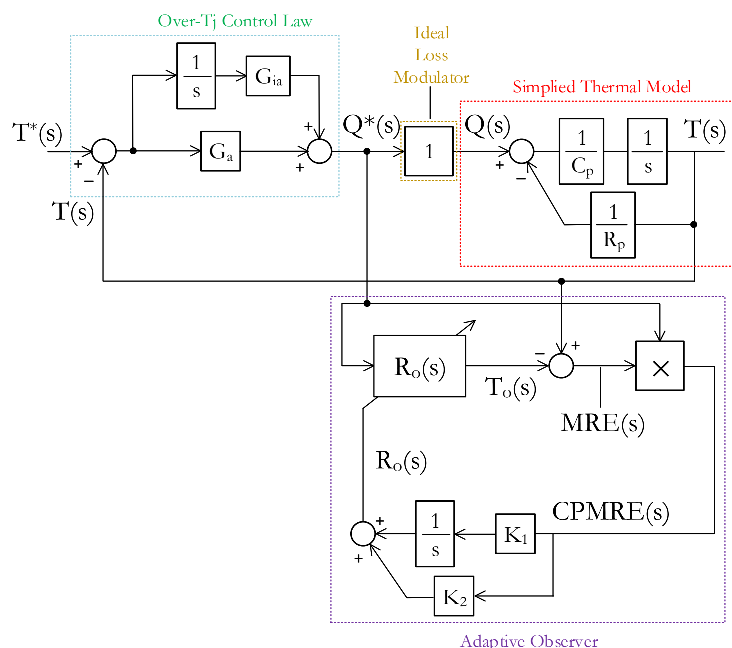

Fig. 5.3-3. Simulation model of an adaptive thermal resistance observer used with over-temperature system-level control

5.3.2 Adaptive observer

This subsection will document the simulative and experimental evaluations of the adaptive observer design topology, presented in subsection 5.2.2, populated with relatively compact zero-order or first-order open-loop electrothermal models. First, simulation results of the observer implemented as a standalone co-simulation system and as an integral component of a system-level controller will be provided. Then, experimental results, including a parameter sensitivity study, will be documented.

5.3.2.1 Simulation with Simulink

Baseline case

Fig. 5.3-3 diagrams a continuous time implementation of the adaptive observer with a pure gain thermal resistance open-loop model and a PI controller topology. Displayed in parallel is a simple, idealized conception of an active, over-temperature controller [163]. The observer system utilizes loss and temperature signals from the over-temperature control loop to estimate thermal resistance following a variant of (5.2-4).

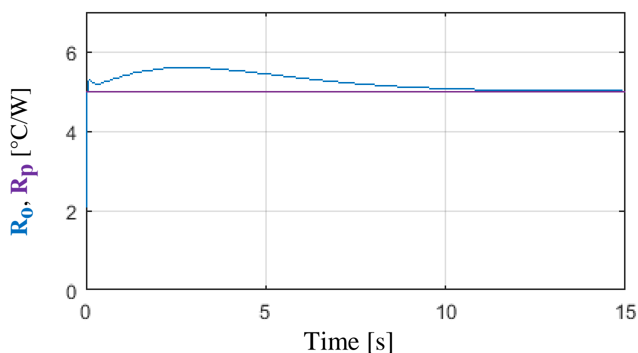

(a) Physical and observer-estimated thermal resistances

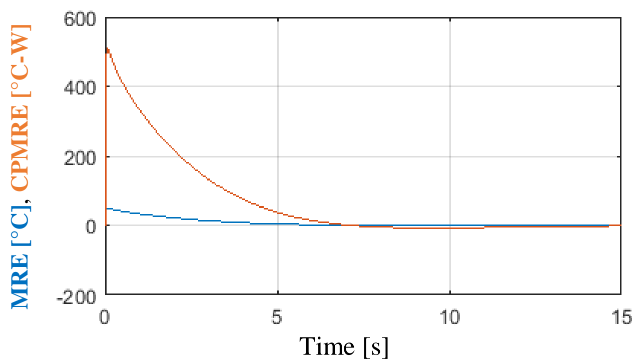

(b) Error quantities

Fig. 5.3-4. Results from Simulink simulation of Fig. 5.3-3

Fig. 5.3-4 present a simulation result of the system in Fig. 5.3-3. The simulation initialized the observer's thermal resistance at half of the physical system's thermal resistance and operated the over-temperature controller with a constant 50°C temperature reference. Fig. 5.3-4 displays

that the observer's estimate of thermal resistance converges to the physical system's value within 15 s, a time at which the observer's MRE and CPMRE converge to zero.

Standalone thermal resistance observer with a time-varying open-loop model

The thermal resistance observer system is intended to estimate parameters that quantify an open-loop electrothermal system response that vary in time due to degradation. The next simulation test was designed to evaluate this capability. The simulation diagram is identical to that shown in Fig. 5.3-3 except for two aspects:

1. the open-loop system model has thermal resistance that varies as shown in Fig. 5.3-5.
2. a first-order dynamic reference model, replicating the physical system's open-loop model, was evaluated in addition to the pure gain model

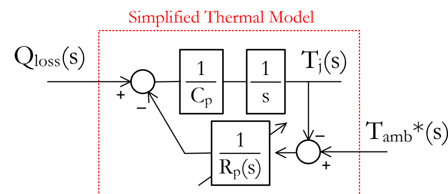

Fig. 5.3-5. First-order thermal model with variable thermal resistance used for adaptive observer simulations

Results from a simulation are documented in Fig. 5.3-6. The simulation design timed the physical system thermal resistance shifts such that the observer's convergence dynamic property is visible. The results demonstrate tracking of the time-varying thermal resistance. Also, the resistance estimate is smoother with a first-order, dynamic reference model.

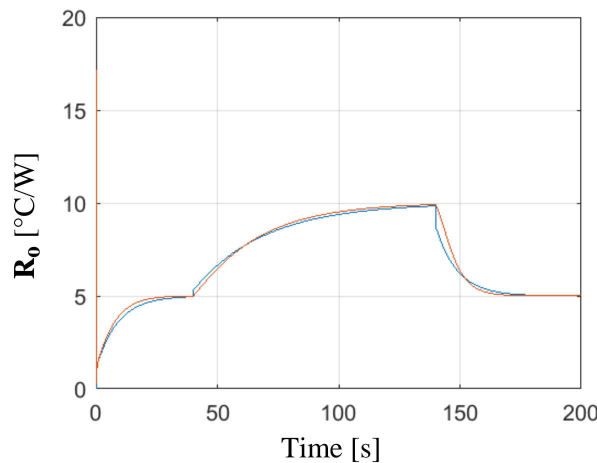

Thermal resistance variation:
- Start: 5 [°C/W]
- Step increase to 10 [°C/W] at 40 [s]
- Step decrease to 5 [°C/W] at 140 [s]

Observer properties:
- **Pure gain ref. model** **Dynamic ref. model**
- R_o is adapted
  $R_{o,o} = 2.0$ [°C/W]
- $K_1 = 0.005$ [W^{-2} s^{-1}]
  $K_2 = 0.01$ [W^{-2}]

Fig. 5.3-6. Simulation of the adaptive observer with the Fig. 5.3-5 physical system

Standalone adaptive thermal capacitance observer

Subsection 5.2.2.2 documented the design of an adaptive system to estimate a lumped thermal capacitance parameter, which is shown graphically in Fig. 5.2-4. A discrete-time simulation corresponding to Fig. 5.2-4, which included a cascaded, discrete-time electrothermal observer to estimate the temperature derivative state, was built. Fig. 5.3-7 documents a result from the simulation model in which the adaptive observer converges on an estimate of thermal capacitance within 15 s.

During simulation, it was observed that a converged estimate of thermal capacitance was unable to be produced if the converter did not operate with an AC trajectory that induced an AC temperature response. This is because the temperature derivative state is zero under non-AC converter operation, and this term drives the adaptive system, per (5.2-7).

5.3.2.2 Experimental evaluations

Automatic identification of thermal resistance with cooling system degradation

This sub-section will present experimental evaluation of the adaptive observer method for automatically identifying degradation-sensitive thermal parameters. Evaluations utilized a prototype MOSFET DC-DC converter having TSEP-based die temperature estimation like documented in subsection 3.1.2.1. During experiments, the converter operated under closed-loop current control with a constant 10 A reference. The observer was deployed having a pure $\hat{R}_p$ gain open-loop model, with $K_1 = 0.0005\ W^{-2}s^{-1}$, and $K_2 = 0.001\ W^{-2}$. Raw (non—filtered) estimated conduction loss, switching loss, and temperature signals were used by the algorithm.

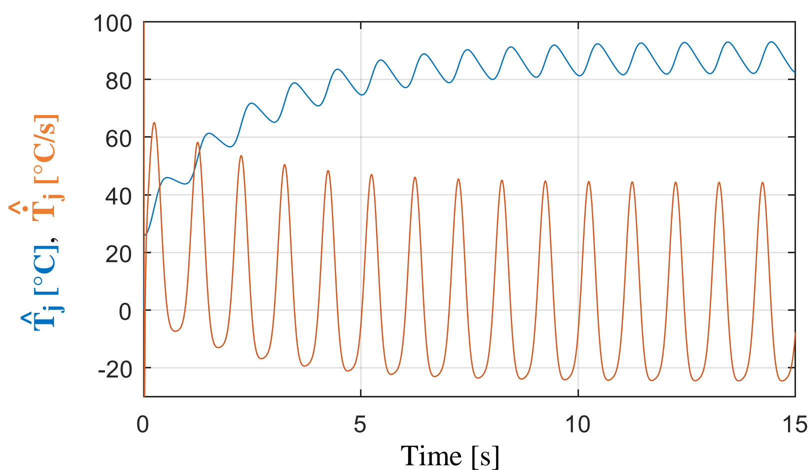

(a) Observer-estimated temperature and its derivative

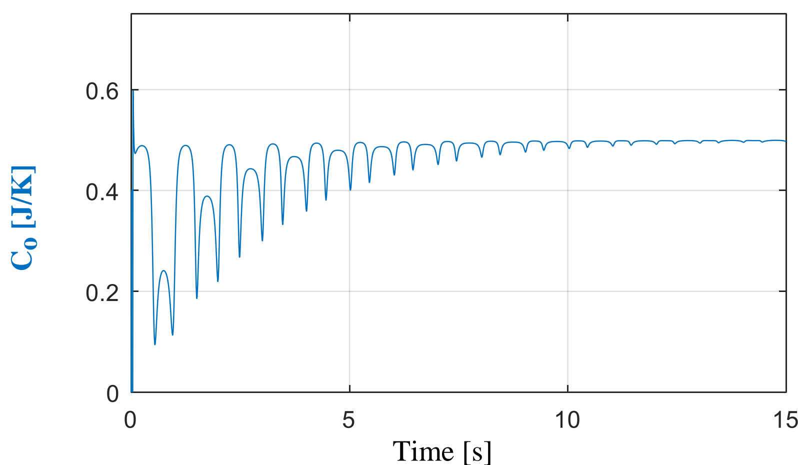

(b) Observer-estimated thermal capacitance

Current control properties:
- Closed-loop PI control on measured current:
- $I^* = 7.5 + 5\sin(2\pi t)$

Thermal system details:
- Ideal first order dynamics w/:
  $R_p = 5$ [°C/W]
  $C_p = 0.5$ [J/°C]

Observer properties:
- Dynamic ref. model
  C_o is adapted
  $C_{o,o} = 0.25$ [°C/W]
- CPRME =
  $(T - T_o) \times \dot{q}_{loss}$
- PI control:
  $K_1 = 0.005\ [W^{-2}\ s^{-1}]$
  $K_2 = 0.01\ [W^{-2}]$

Discrete, closed-loop T_j observer:
- Tuning:
  EVs at [100, 10] Hz
  $G_o = 334$ [W/°C]
  $G_{io} = 19100$ [W/°C-s]

Fig. 5.3-7. Simulation of the adaptive thermal capacitance observer in Fig. 5.2-4

To start, the system was brought to thermal equilibrium with fan cooling disabled. Fig. 5(a) illustrates the 3.7 °C/W thermal resistance estimated by the observer then. After 11 s, the fan was turned on, and the observer forced die temperature to track sensed die temperature by manipulating the open-loop model, $\hat{R}_p$. As shown at the 0 s point in Fig. 5(b), $\hat{R}_p$ converged to 2.3 °C/W with cooling enabled. Afterwards, cooling was again disabled, and the adaptive observer adapts $\hat{R}_p$, which converges to the 3.7 °C/W. Post-processing estimates an increase in the heat transfer coefficient, h, by over 50%, without forced air cooling.

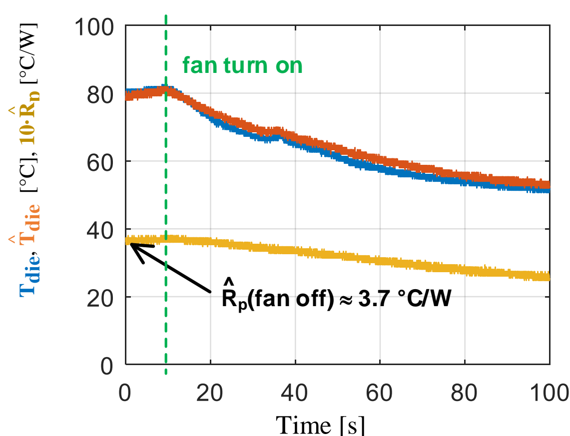

(a) Fan turn-on at 11 s

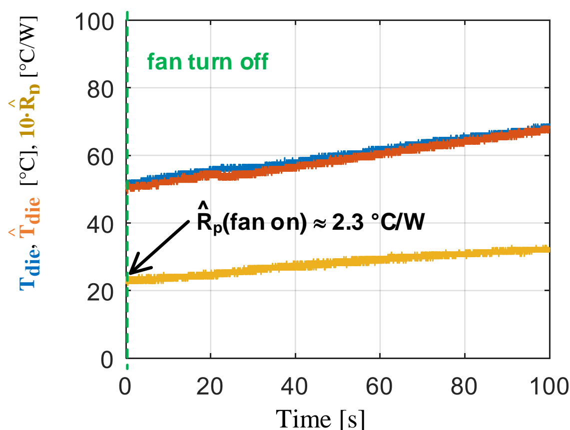

(b) Fan turn-off at 0 s

Thermal system properties:
- Force air cooling with A.O. Smith series 042106M motor
- At steady-state, without forced air cooling, $R_o = 3.4$ [°C/W]
- At steady-state, with forced air cooling, $R_o = 2.3$ [°C/W]

Current control properties:
- Closed-loop PI control on LEM measured current
- Constant i* = 10 [A]

Observer properties:
- Pure gain ref. model R_o is adapted
- CPRME = $(T - T_o) \times \dot{q}_{loss}$
- PI control topology: $K_1 = 0.0005$ [W^{-2} s^{-1}] $K_2 = 0.001$ [W^{-2}]
- T_{amb}* NZVR decoupling is included

Fig. 5.3-8. Experimental result showing the observer system in Fig. 5.2-3 tracking thermal resistance

Parameter sensitivity

Subsection 2.1.2 remarked that all thermal quantities are inherently relative and, even if ambient-referred, do require a quantity like an electrical ground. The state block diagram illustrations of adaptive observers in this section, like Fig. 5.2-3, all include the NZVR ambient temperature. This subsection experimentally evaluates the baseline performance of Fig. 5.2-3's adaptive thermal resistance observer with and without an ambient reference.

Fig. 5.3-9 shows an experimental result of the system's response without decoupling ambient temperature decoupling. The observer's adaptation mechanism properly causes the

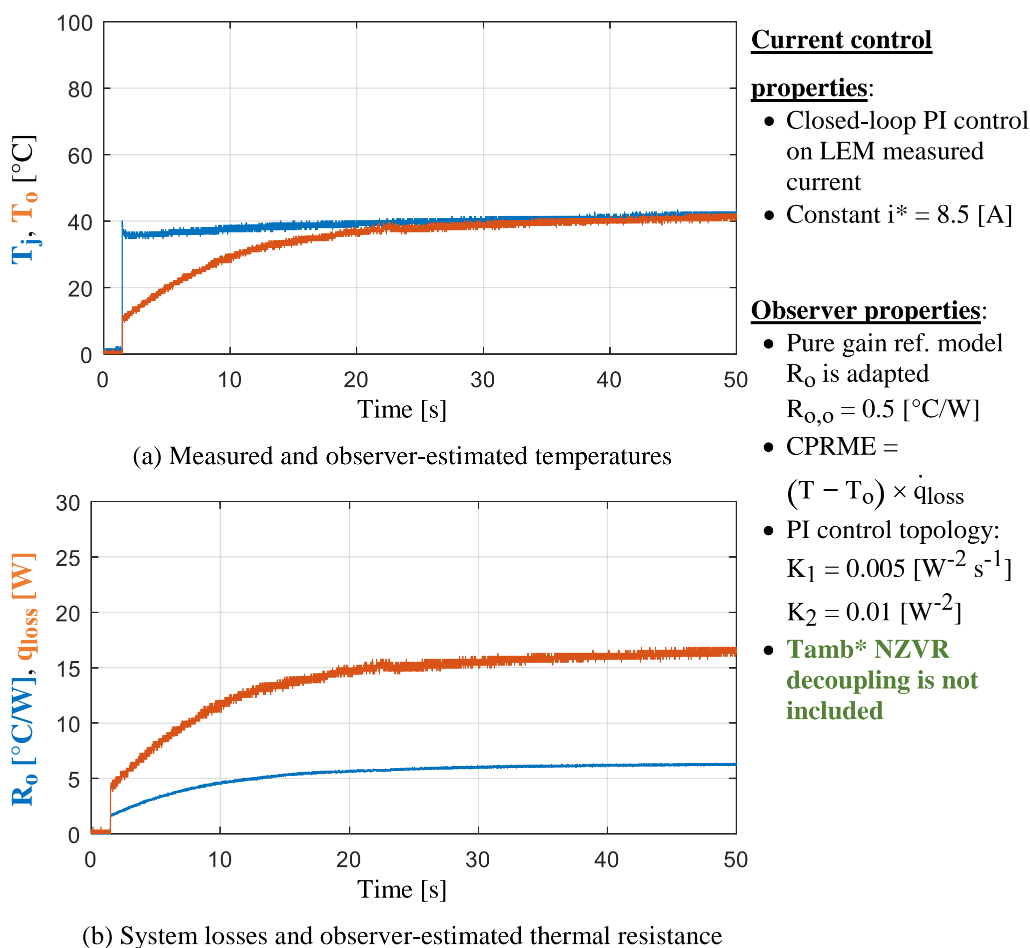

Fig. 5.3-9. Experimental result showing the observer system without the ambient temperature NZVR tracking an erroneous thermal resistance value

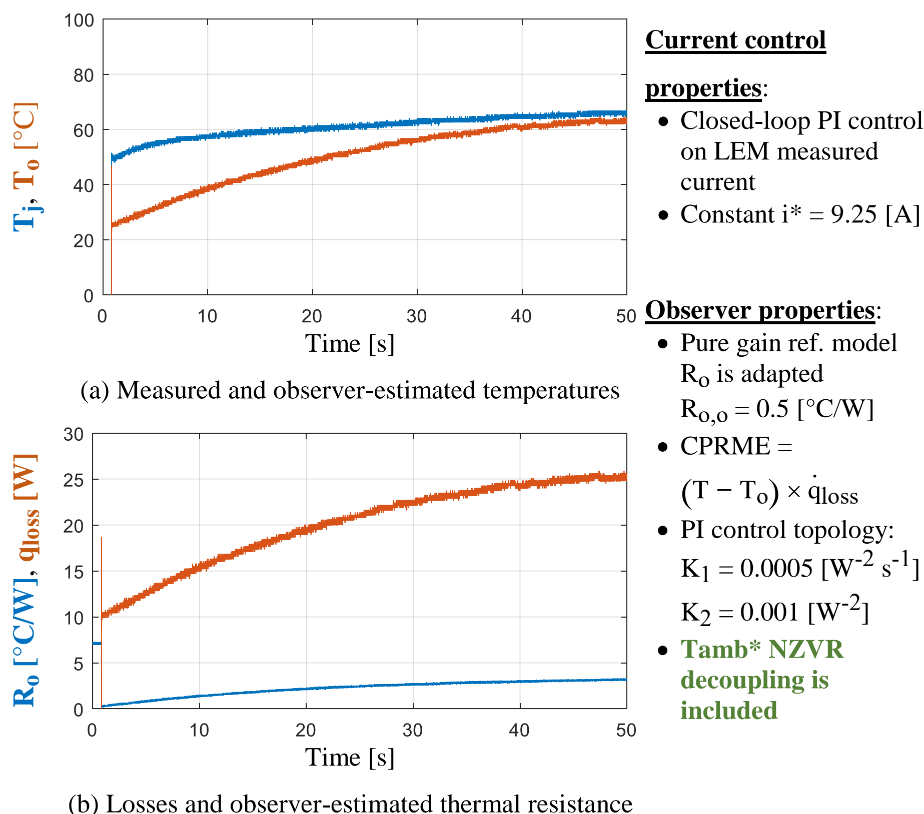

(a) Measured and observer-estimated temperatures

(b) Losses and observer-estimated thermal resistance

Fig. 5.3-10. Experimental result showing the observer system with the ambient temperature NZVR tracking the correct thermal resistance value

observer's estimate of temperature to converge to the value of the physical sensor signal. However, despite the global convergence that occurred, the estimated thermal resistance value is higher than what was known in advance.

The system was once again evaluated, but with NZVR decoupling included. Fig. 5.3-10 shows the experimental results in which the MRE is once again driven to zero and the system's resistance measurement is accurate. Overall, the results clearly reveal the need for accurate ambient temperature sensing/estimation for adaptive observer systems.

5.3.3 Industrial Application Requirements

5.3.3.1 Preferably high bandwidth, near-die temperature sensing

Methods in this section were evaluated using a signal provided by a die temperature estimator or sensor. Although all methods require some type of temperature estimation or sensing, some of methods can successfully achieve direct and accurate physical parameter estimation utilizing feedback from a less costly source, such as a thermistor. Table 5.3-1 generalizes temperature feedback properties in order to guide the future work.

Table 5.3-1. Road map of signal properties relevant to detection and diagnosis methods

Loss model possessed		**Proximal (die-level) temp. detector, e.g. a calibrated TSEP**	**Distal (substrate-level) temp. detector, e.g. thermistor**
Time-averaged	***High-freq. harmonic***		
Ideal		Ideal	
Incorrect from onset		Noisy	
Incorrect via aging		Finite bandwidth	
		(not available)	

Table 5.3-2. Road map of properties related a priori knowledge related to detection and diagnosis methods

***A priori* spatially-varying FRF data possessed**	
With degradation evolution projection	***W/o degradation evolution projection***
Complete map	
Incomplete map	
(not available)	

5.3.3.2 Transient semiconductor device loss models

The methods presented in this section rely on accurate modulation of losses. Table 5.3-1 also identifies loss model properties relevant to the implementation of degradation detection and

diagnosis algorithms, which include inaccuracies due to non-ideal parameter estimation and power module aging processes.

5.3.3.3 Libraries of heat transfer FRF data

Prior chapters extracted FRF data from the experimental power electronic system under degraded cooling and TIM conditions, and viewed and interpreted the data with FRF and complex impedance plots. A comprehensive application of a developed systems identification method was used in this effort, and effects of the two modes of degradation on ETI properties were directly measured.

Even after these results, FRF and complex impedance plots of healthy converter systems are still not well documented in the power electronics literature. Degraded system FRF data is even less common. Based on the current state of this research program, and limitation of available FRF data of power electronic systems, the author acknowledges that, long-term, the most robust way to design and evaluate methods for the assessment of an assembled converter system's state-of-health is for the research community to collective generate a library of experimental heat transfer FRF data. The data should be extracted to monitor the response at various stages of a converter's lifetime during its normal operation in an application and/or specified highly-accelerated lifetime testing (HALT).

5.4 Chapter Summary

This chapter examined steps necessary for integrating degradation sensing, based on measured variation in transient thermal response, into actively switching converter systems. First, a harmonic loss modeling method was developed. Two approaches were outlined: one approach

for deriving analytical relations of semiconductor device losses under assumed PWM schemes, the other utilizing numerical simulation and FFT post-processing. Next, to avoid potentially time-consuming, off-line calculation of FRF data, a signal processing technique, that can be integrated in converter embedded computer hardware, was identified.

A second developed method utilizes aspects of adaptive control theory. The proposed method minimizes the error between a sensed state and a state estimate. To minimize error, the system automatically updates an open-loop model, which physically changes with lifetime-varying processes like degradation, actively estimating parameters of the model. Low-order embodiments of the observer were exemplified. Simulation models suggest these systems can converge to time-varying thermal resistance and capacitance parameters. Experimental results demonstrated performance and parameter sensitivity.

When equipped with a pure gain open-loop model, the observer provides a compact, automatic method to identify low frequency degradation. However, changes to the system's open-loop model and methodical signal filtering allow identification of higher frequency transient parameters and degradation property shifts. The overall methodology provides a pathway for triggering converter maintenance if an estimated parameter or a parameter-insensitive phase response attribute deviates from baseline. Integrating look-up tables for more precise diagnosis of degradation is also enabled by developments in this chapter.

Chapter 6 Integrating Degradation Sensing into Multi-Chip Power Modules

This chapter analyzes challenges intrinsic to multi-chip power module components, e.g. the presence of multiple, closely packed heat sources, to identify boundaries toward integrating the presented degradation sensing concept. FRF and related sensitivity properties of a commercial wide-bandgap module are first identified using analysis. A method based on models for synthesizing constraints related to temperature sensing resolution is a result. The chapter then examines spatial degrees-of-freedom for placing additional degradation sensing temperature detectors. For that, spatially-varying electrothermal impedance sensitivity analysis is numerically and experimentally applied to a scaled-down module prototype. Following characterization of loss harmonics over mission profiles, presented in Chapter 5, this chapter strategically targets converter real-time applications for integration of degradation sensing, with expectation that other environments possess fewer constraints and boundaries to adoption. Elements of this chapter are also documented in a publication [173].

6.1 Tracking Chip Temperature Response Variation

This section develops a transient thermal model of a multi-chip power module to identify properties that guide the design of a real-time degradation sensing system.

6.1.1 Three-phase WBG module FEA setup and description

A 1.2 kV, 25 mΩ, three-phase SiC module from *Cree/Wolfspeed* was utilized as test vehicle for the investigation [180], [181]. It was analyzed with a finite element method having *ANSYS* as

a front-end user interface and custom frequency domain post-processing, from section 2.3. To initiate the method's usage, a solid model of the module without isolation gel was simplified by removing wire bond interconnects and pin-out terminals. The model was then subjected to meshing in which mesh density is inversely proportional to approximate component size, e.g. the semiconductor chips had a relatively fine mesh per volume. Table 6.1-1 documents mesh statistics by feature of the assembly.

Table 6.1-1. Power module finite element model details

Assembly description				**Mesh statistics**	
Category	**Component**	**Material**	**Instances**	**Nodes**	**Elements**
baseplate	substrate	copper	1	572	250
	DBC-attach	solder	1	378	160
direct bonded copper (DBC)	ceramic	AlN	3	308	130
	phase islands	copper	3	240	99
top copper sections	gate-source	copper	3	274	107
	middle	copper	3	562	245
	switch nodes	copper	3	628	263
diode	die-attach	solder	6	242	100
	chips	SiC	6	242	100
MOSFET	die-attach	solder	6	280	117
	chips	SiC	6	280	117
				13250	5546

Next, inputs and boundary conditions were specified. For test cases, which will be described later in this section, conduction and switching losses were modeled as volumetric generation (in units of W/mm^3) uniformly distributed throughout a semiconductor chip. For all test cases, the bottom of the module baseplate was exposed to a uniform convective heat transfer coefficient such that the baseplate-to-ambient thermal resistance was 1.0 K/W.

Although non-homogeneous chip temperature gradient measurements have been documented in the literature, for all comparative analysis in this paper individual mesh nodes located at the center of each semiconductor chip surface are treated as chip temperature. A related aspect of uncertainty quantification has been addressed in subsection 3.1.4.5.

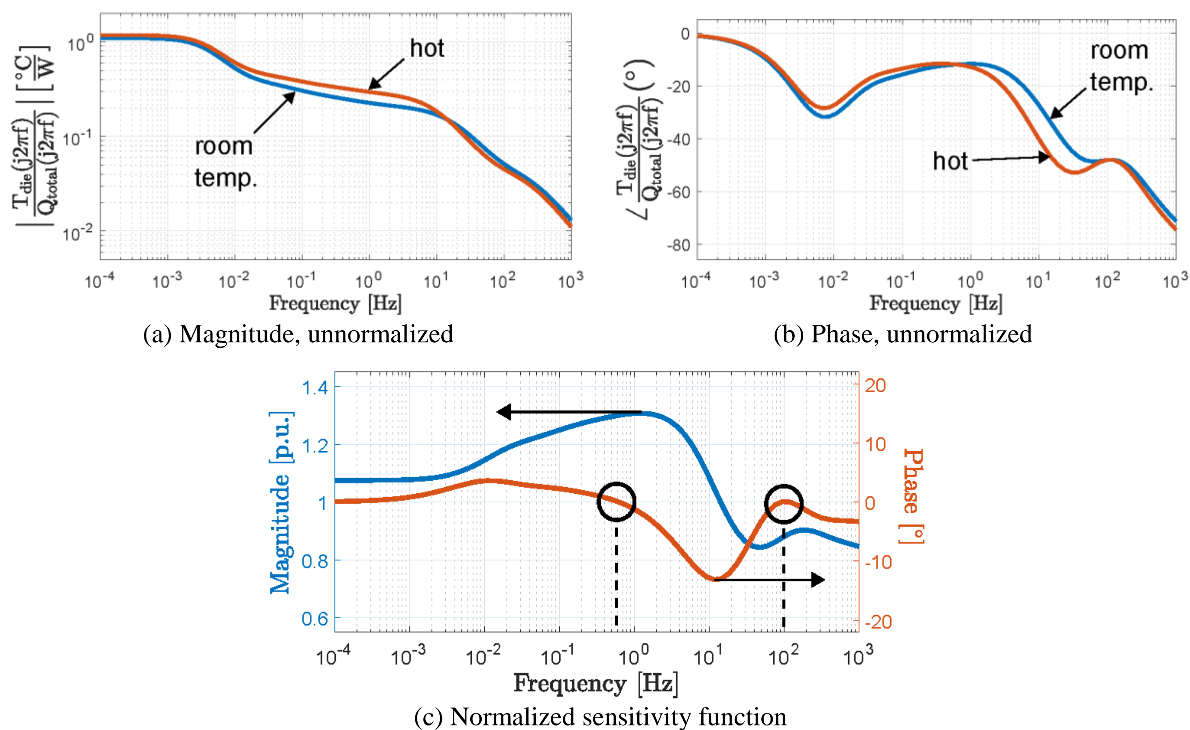

(a) Magnitude, unnormalized

(b) Phase, unnormalized

(c) Normalized sensitivity function

Fig. 6.1-1. Small signal thermal response of a SiC MOSFET in a module

6.1.2 Response nonlinearity constraints

Finite element as well as finite difference discretization of the heat conduction partial differential equation results in linear state-space models if thermal conductivity (k), specific heat capacity (c_p), and density (ρ) material properties are constant in temperature. However, per data accessed in the literature, the thermal conductivity of 4H-SiC is 2-4 times larger than that of silicon and its value at 150°C is approximately half of its room temperature value [182].

Table 6.1-2. Temperature-dependent material properties

Temperature	25°C			100-150°C		
Property	k^a	ρ^b	$c_p{}^c$	k^a	ρ^b	$c_p{}^c$
AlN	160	3300	740	90	3100	1200
copper	400	9000	390	390	8900	370
SiC	500	3200	710	250	3200	920
solder	68	7400	230	110	7300	240

units: $^a W/(m \cdot K)$ $^b kg/m^3$ $^c J/(kg \cdot K)$

This subsection presents heat transfer FRFs, extracted using material properties representing two different thermal operating points of the module, and treats them as small-signal quantities to efficiently quantify nonlinear heat conduction. To do so, the middle-phase, low side MOSFET device's electrothermal impedance, whose single-input, single-output frequency response function is defined according to (6.1-1) was inspected using the two different sets of material properties, shown in Table 6.1-2.

$$\mathrm{FRF}(j2\pi f) = \frac{T_{\mathrm{die}}(j2\pi f)}{Q_{\mathrm{total}}(j2\pi f)} \tag{6.1-1}$$

The properties span about 100°C to identify a worst-case envelope of nonlinearity distortion. Fig. 6.1-1 ultimately results after implementation of the different sets of material properties in otherwise identical models. The nonlinear effect is represented using overlay plots of the FRF in Fig. 6.1-1(a) and Fig. 6.1-1(b), and a sensitivity function plot in Fig. 6.1-1(c). To compute $\mathrm{FRF}_{\mathrm{sens}}(j2\pi f)$, the complex FRF for hot material properties is normalized by that for baseline, room temperature properties, following (6.1-2).

$$\mathrm{FRF}_{\mathrm{sens}}(j2\pi f) = \frac{\mathrm{FRF}_{\mathrm{comparison}}(j2\pi f)}{\mathrm{FRF}_{\mathrm{baseline}}(j2\pi f)} \tag{6.1-2}$$

The plots reveal that nonlinear effects are spread throughout the range of displayed frequencies. For the analyzed WBG module, the nonlinear distortion is generally largest between 1 and 10 Hz. However, insensitive unity and zero crossings of the sensitivity function magnitude (15 Hz) and phase (0.6 and 100 Hz), respectively, can be observed. The results generally suggest that the average module temperature must be known if state-of-health is to be accurately inferred from extracted thermal response harmonics. This can be accomplished using thermal observer structures. An alternative opportunity lies in utilizing the frequencies with nearly-zero nonlinearity

distortion, such as those circled in Fig. 6.1-1(c), as identification frequencies to avoid this complication.

6.1.3 Degradation sensitivity characterization

6.1.3.1 Emulation of die-attach degradation

Unlike modeling approaches in the recent past, all thermal contacts between components in the numerical model were specified as ideal because a more physical approach for simulating degradation was taken that is explained in the following. Fig. 6.1-2 shows the center half-bridge of the three-phase SiC power module after its meshing. The low-side MOSFET chip was not present in this photo to reveal the symmetrical, 1.5 mm fillets which cut the corners of the nominally rectangular solder layers. This geometric modification was utilized to approximate chip solder edge delamination observed in [183].

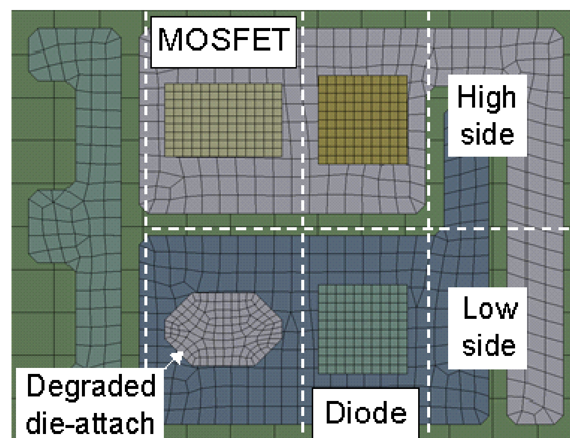

Fig. 6.1-2. Meshed view of the SiC module's center half-bridge sub-assembly, showing four semiconductor devices and how die-attach degradation was simulated

This method of geometric modification was used for all die-attach degradation simulations in this section. It reduced thermal contact areas between copper substrate and the MOSFET and diodes devices by 17% and 19%, respectively. Mesh controls were utilized to ensure that

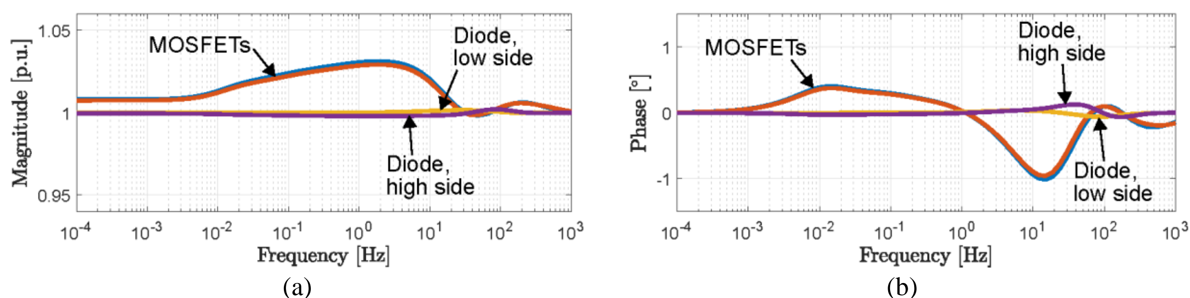

Fig. 6.1-3. For all middle-phase devices excited by self-heating, sensitivity to degradation of each device's die-attach interface

differences in solder layer discretization between healthy and degraded cases were minimized. In most cases mesh and element counts were within less than 1%. In the least matching case, for low-side diode die-attach degradation, the deviation was 11%.

6.1.3.2 Variation in individual driving point impedances

Die-attach delamination was modeled four times, for each of the semiconductor devices in the center, middle-phase half-bridge sub-assembly of the module. Four driving point electrothermal impedance FRFs were subsequently formed, in which response with nominal, rectangular solder layers is $FRF_{baseline}(j2\pi f)$, following (6.1-1).

Fig. 6.1-3 presents sensitivity functions. Compared to prior results which manipulated uniform thermal contact resistances to simulate die-attach degradation, these results suggest the impact of the source of degradation on transient heat transfer is more spread in its spectrum for devices in the WBG simulation model. For the MOSFETs, the maximum sensitivity is –1°, occurring at 15 Hz. This sensitivity maximum is less than shown in 0 where the die-attach degradation was distributed equally underneath die-center and edges.

The thickness of the MOSFET devices in the model was 180 μm. Meanwhile, the sensitivity of the 380 μm thick diodes to die-attach degradation is nearly zero. Since a power

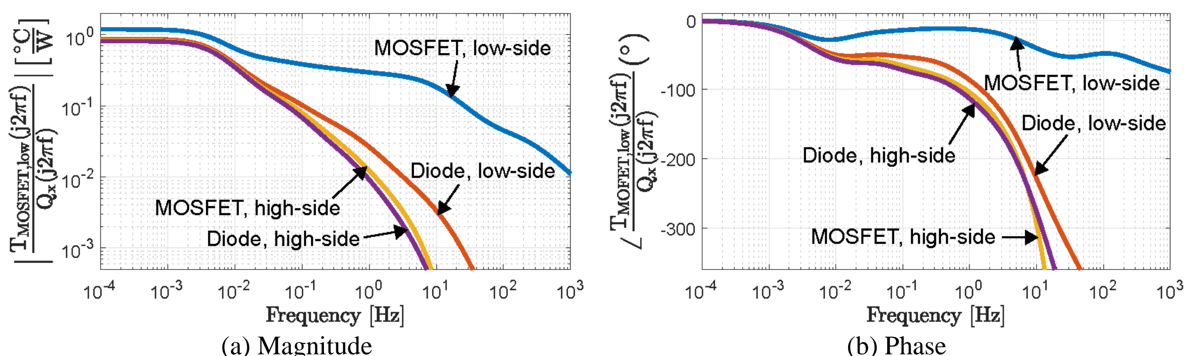

(a) Magnitude (b) Phase

Fig. 6.1-4. Cross-coupling FRFs where x = heat source, labeled on plot

module is often used in synchronous rectification, detecting diode die-attach degradation might not be a primary target for the method.

6.1.3.3 Variation in chip response to adjacent device heat dissipation

Prior work proposed a superposition framework to compute temperature responses at *m* discrete locations given *n* perturbation sources [161]. Subsection 6.1.3.2 effectively evaluated sensitivity of the diagonal terms of a proposed Z_{th} thermal impedance matrix. This subsection evaluates responses that can be considered the off-diagonal terms, which represent how a periodic heat dissipation perturbs response elsewhere.

Fig. 6.1-4 displays how the low-side MOSFET of the middle module phase responds to heat dissipation at all semiconductor devices, including itself. It shows that the DC offsets induced by the high-side MOSFET and diodes are significant - about 70% of that which is self-induced. However, above 300 mHz, the top, self-heating response trace is at least one or more orders of magnitude higher than those of the other devices. Relevant to compact modeling purposes, it is observed that responses above 10 mHz induced by neighboring devices resembles the spatiotemporal delay property identified in Chapter 2 and Chapter 3.

Following (6.1-2), the sensitivity of these impedances to die-attach degradation under the heat-sourcing chip was computed. Fig. 6.1-5 presents the FRF sensitivity. The low-side MOSFET sensitivity trace is the same data displayed in Fig. 6.1-3 and is included to provide scaling perspective. Fig. 6.1-5 reveals that the high-side MOSFET-induced response changes with its own die-attach degradation above 500 mHz. The plot further reveals that the diode-induced response does not change with its own die-attach degradation.

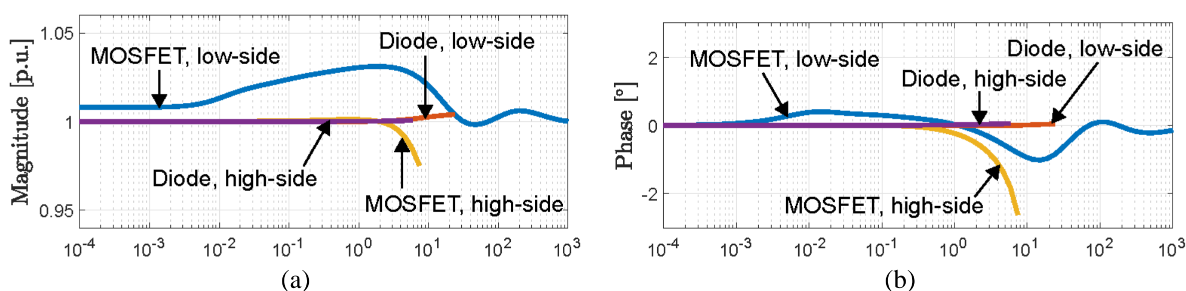

Fig. 6.1-5. Sensitivity to die-attach degradation located directly under each heat source labeled on the plot

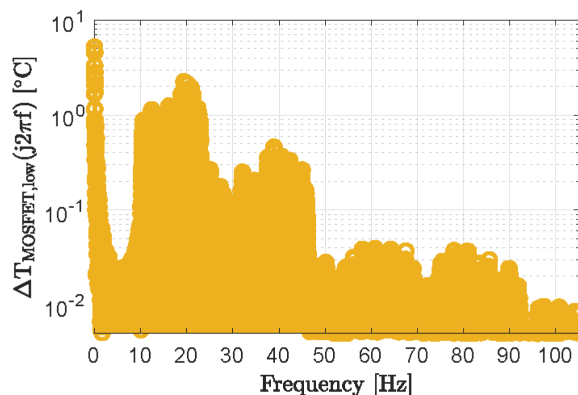

Fig. 6.1-6. AC ripple of the low-side, middle-phase MOSFET;
computed as a product of FRF amplitude and loss harmonic spectra

6.1.4 Differential usage of amplitude and phase properties

Whether based on intrinsic sensitivities of the semiconductor devices or dedicated detector hardware, transient temperature sensing is a challenge. Related limitations include amplitude and temporal resolution along with susceptibility to noise, such as electromagnetic interference.

Although prior analysis suggested the implementation of phase response tracking to minimize sensitivity to loss model parameters, magnitude information is still needed in the design process to interface with temperature sensing limitations. This subsection provides a method for including amplitude resolution limits in a degradation sensing design process.

Eq. (6.1-3) defines a spectral amplitude product. For its calculation, a harmonic spectrum of total semiconductor device losses is multiplied by heat transfer FRF amplitude.

$$\Delta T(j2\pi f) = Q(j2\pi f) * |FRF(j2\pi f)| \quad (6.1\text{-}3)$$

Thus, FRF amplitude figures already presented in this paper can be synthesized to predict resulting AC temperature ripple excited by device loss harmonics.

It was previously noted that the spectrum of Fig. 5.1-4(b) exhibits maxima between 10-50 Hz. Fig. 6.1-6 plots the temperature ripple using this spectrum and the driving point FRF of the middle-phase, low-side MOSFET in the analyzed WBG module. It can be seen that, since the amplitude FRF has about one order of magnitude attenuation in this range, the resulting spectral amplitude product is now largest at low frequencies, whose degradation sensitivity is less than the maximum for the WBG module, per Fig. 6.1-3. In terms of methodology, graphics like Fig. 6.1-6 guide selection of the harmonic(s) from which to infer degradation status from. In addition to traditional bandwidth limitations, they allow SNR constraints to be quantitatively addressed. If a temperature detector's amplitude resolution is 0.1°C, then only the 10-100 mHz and 10-45 Hz ranges provide resolution enough for real-time degradation sensing.

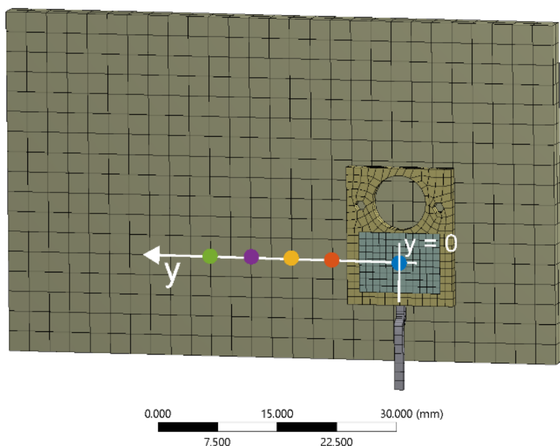

(a) Meshed view of a discrete MOSFET on a copper baseplate; vector and discrete nodes for sensitivity analysis are displayed

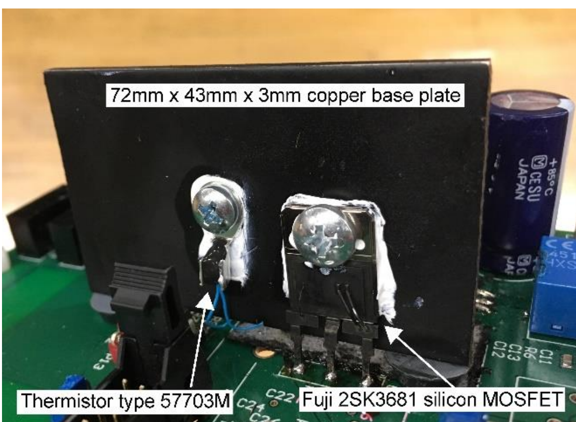

(b) MOSFET-baseplate sub-assembly hardware

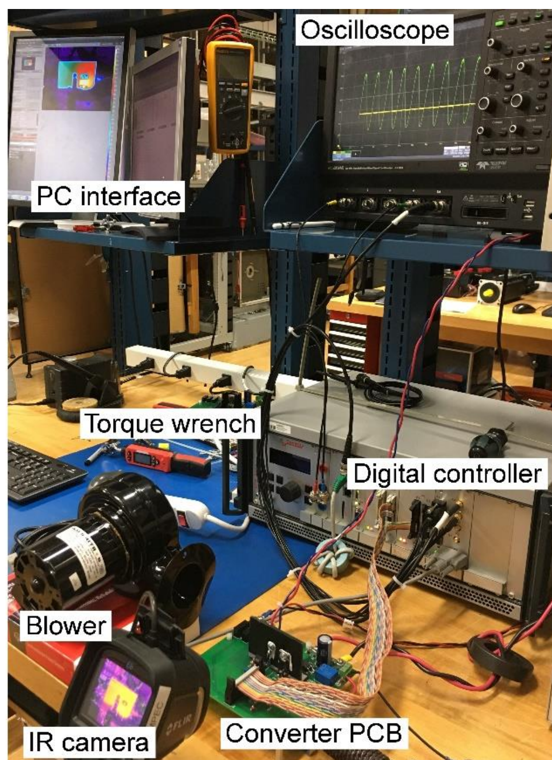

(c) Experimental setup

Fig. 6.2-1. Model and test setups for spatially-varying sensitivity analysis

6.2 Locating Substrate Temperature Detectors

This section examines a converter sub-assembly to quantify spatially-varying and degradation-sensitive heat transfer.

6.2.1 Baseplate-mounted test specimen

This research program has showed, with Fig. 6.1-1(a) and Fig. 6.1-4(a) in particular, that thermal FRF amplitude decreases monotonically with increasing excitation frequency. Fig. 6.1-4(a) also shows that locations further away from a heat source experience smaller amplitude

temperature excitation. The inverse relationship between response signal response amplitude and excitation frequency limits high frequency SNR ratio.

This section extracts a spatially-varying sensitivity function, previously defined along a vertical vector through die-center. In this case, response along a lateral vector across the top surface of a semiconductor device and baseplate is quantified. Fig. 6.2-1 shows a decapsulated, discrete MOSFET mounted to a baseplate, intended to be a scaled-down version of a power module for evaluating detailed sensitivity properties with simulation and experiments.

6.2.2 Spatially-varying electrothermal impedance analysis

The selected vector for a lateral analysis is indicated in Fig. 6.2-1(a). To extract a spatially-varying FRF, the finite element modeling workflow of the previous section was again utilized, i.e. losses were located within the volume of the semiconductor chip and convective boundaries were assigned. This time, responses along the indicated vector y were studied.

The analysis investigated thermal response sensitivity to degradation of the thermal interface between the MOSFET and baseplate. To evaluate a spatially-varying sensitivity function (6.2-1), two sets of FRF data were extracted: (a) for a baseline case, and (b) with a uniform increase of contact resistance at the MOSFET-baseplate interface by around 20%.

$$\mathrm{FRF_{sens}}(\mathrm{j}2\pi\mathrm{f},\mathrm{y}) = \frac{\mathrm{FRF_{comparison}}(\mathrm{j}2\pi\mathrm{f},\mathrm{y})}{\mathrm{FRF_{baseline}}(\mathrm{j}2\pi\mathrm{f},\mathrm{y})} \qquad (6.2\text{-}1)$$

Fig. 6.2-2 displays a spatially-varying FRF for thermal interface degradation. The plot shows how the driving point response at nodal position y = 0 increases, especially between 10 and 70 mHz. The baseplate responses, on the other hand, decrease, especially above 70 mHz. Most importantly, unlike their response amplitudes, the sensitivities of the four baseplate nodes do not

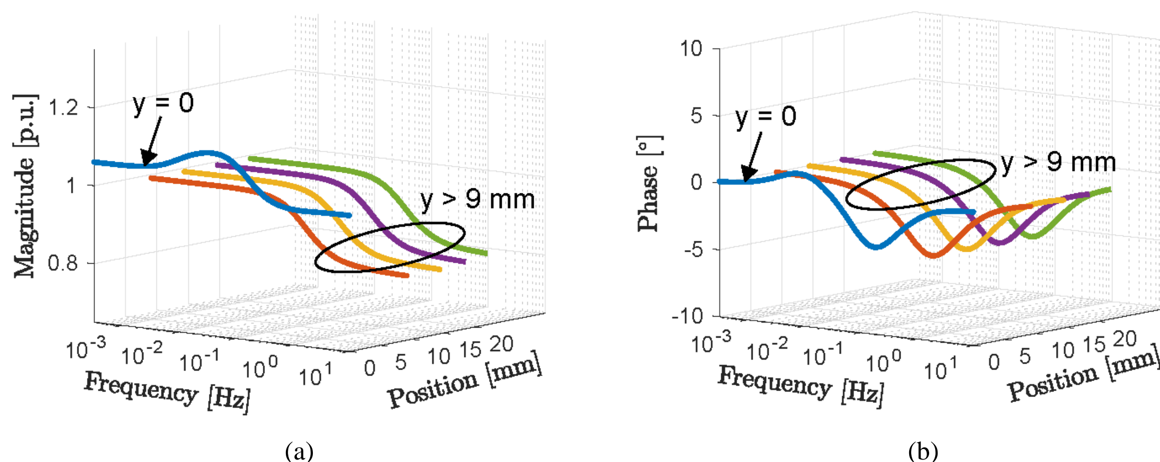

Fig. 6.2-2. Spatially-varying sensitivity function extracted from simulation; plot colors correspond to nodes highlighted in Fig. Fig. 6.2-1(a)

change in space. These and prior results show how chip transient thermal response can be used to infer die-attach and thermal interface degradation. To the current point, spatially-varying sensitivity analysis reveals geometric design freedom to place additional sensors for degradation sensing on baseplate or other module substrates.

6.2.3 Lab converter hardware and instrumentation

Again, a DC-DC converter having a single actively switched power MOSFET was used as a test platform to evaluate thermal interface degradation sensitivity. The Fig. 6.2-1(a) model replicates the experimental converter sub-assembly, Fig. 6.2-1(b). A thermistor, electrically embedded in an op-amp network, was mounted to the baseplate surface to measure the its AC temperature response while the converter operates.

The entire MOSFET-baseplate sub-assembly was painted black to facilitate more accurate infrared (IR) monitoring with a camera, shown with other components of the test bench, in Fig. 6.2-1(c). An *AixControl* digital control platform delivered PWM signals to the converter and sampled on-state forward voltage and current of the switching MOSFET. An oscilloscope was used for logging individual time domain records up 500 s in length.

6.2.4 Experimental characterization of thermal interface degradation

6.2.4.1 Measurements with an integrated temperature sensor

The MOSFET-baseplate thermal interface was manipulated in the lab using a bolt and nut fastening system, shown from the front side in Fig. 6.2-1(b). Using a torque wrench, the pressure of the joint was manipulated. Table 6.2-1 documents two utilized torque levels along with an estimate of the effective pressure at the joint between the MOSFET and baseplate.

Electrothermal impedance spectroscopy was then applied to extract FRFs for the two test cases in Table 6.2-1. The DC-DC converter was deployed in a conduction loss modulation mode to dissipate low-distortion loss harmonics in the MOSFET chip. Meanwhile, the transient response of the baseplate was monitored with the thermistor.

Table 6.2-1. Mechanical parameters of the TIM degradation experiment

	Test 1	**Test 2**	**Unit**
Bolt torque	1500	850	N-mm
Axial clamp force	390	220	mN
Joint area	200		mm^2
Joint pressure (P)	2	1.1	kPa
ΔP	40		%

Several single-sine tests were executed and FRF data was ultimately synthesized from time-domain data records offline using discrete Fourier transform techniques to verify near-unity data coherence. FRFs were truncated at 200 mHz because, despite the use of time-synchronous averaging to improve SNR of the sampled thermistor voltage, non-unity coherence above this frequency was not achieved.

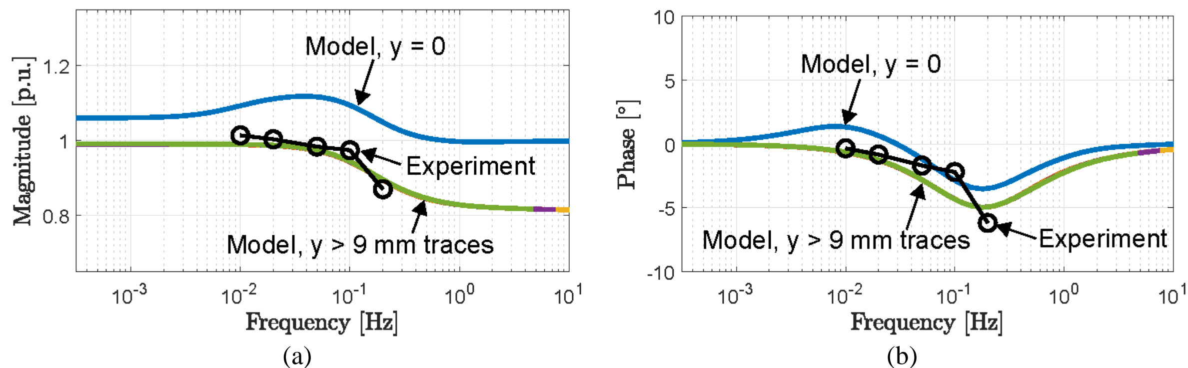

Fig. 6.2-3. 2D view of Fig. Fig. 6.2-2 results and a TIM degradation sensitivity function measured with a baseplate-mounted thermistor

Fig. 6.2-3 presents an experimentally extracted sensitivity function, along with the model results from Fig. 6.2-2. Referring to (6.2-1) and Table 6.2-1, the sensitivity function was formed treating test 1 and 2 as $FRF_{baseline}(j2\pi f)$ and $FRF_{comparison}(j2\pi f)$, respectively. Results reveal agreement between the lab measurement's trend and that embedded in the developed model, which had 20% uniformly distributed thermal interface degradation.

6.2.4.2 Measurements with infrared thermography

Quantification of spatial response attenuation

Relevant to the aspect of finite temperature sensing resolution introduced earlier in this section, infrared camera measurements acquired during single-sine FRF experiments (Fig. 6.2-4) measured how AC response amplitude diminishes the further from a heat source. As Fig. 6.2-5(a)

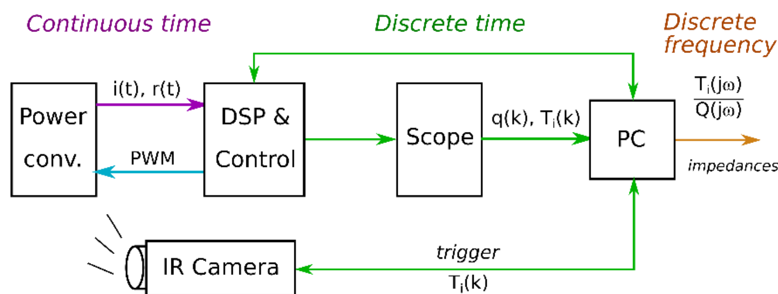

Fig. 6.2-4. Signal flow for characterization using an IR camera

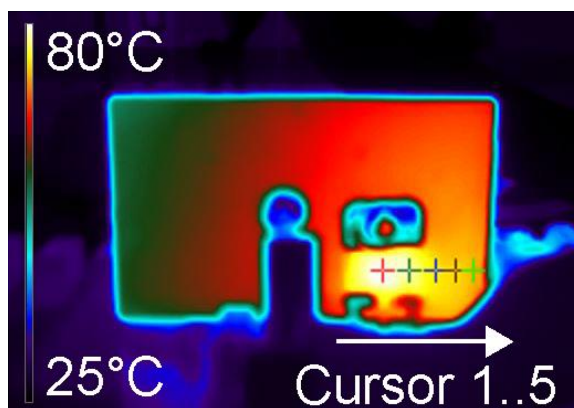

(a) FLIR ResearchIR screenshot showing cursors indicating measurement locations

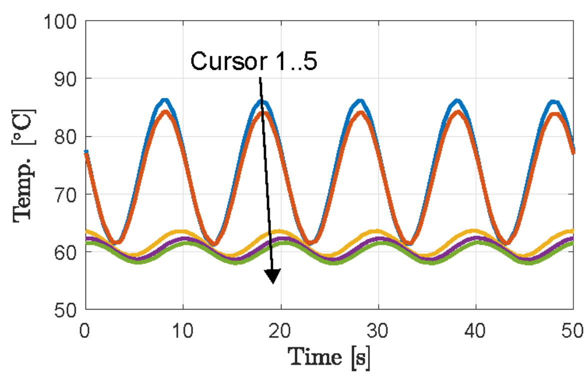

(b) Time-domain response with 0.1 Hz loss excitation

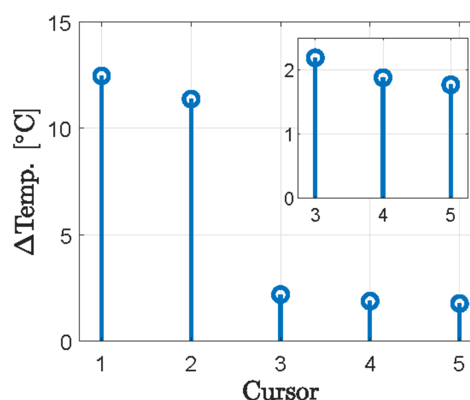

(c) AC amplitude of the traces in (b)

Fig. 6.2-5. Spatially-varying amplitude attenuation illustrated using infrared thermography

shows, approximately equally spaced cursors 1 and 2 were located on the MOSFET die and 3-5 on the baseplate. Fig. 6.2-5(b) summarizes periodic steady-state thermal response during 0.1 Hz converter loss modulation. It shows 50 s of measured data, and Fig. 6.2-5(c) summarizes response amplitudes. As expected, the amplitude of cursor 5 is lowest.

Fig. 6.2-2 suggests that, downstream from a physical site of degradation, degradation-induced changes to heat transfer do not appreciably change as a function of location on a monolithic component, like substrate sections in power modules. According to the analysis in this section, heat conduction in continuous solids, like pieces of power module assemblies, exhibit less spatial sensitivity to mechanical degradation than across component interfaces.

However, limits of physical temperature detectors and analog-to-digital conversion systems will limit degradation sensing performance if detectors are placed too far from a heat source. In terms of method, temperature detectors for monitoring degradation should be located considering converter loss harmonic amplitudes to ensure degradation sensitive temperature response signals are larger than minimum temperature sensing resolution. Metric (6.1-3) and Fig. 6.1-6 involve temperature SNR limitations in a design for degradation sensing process.

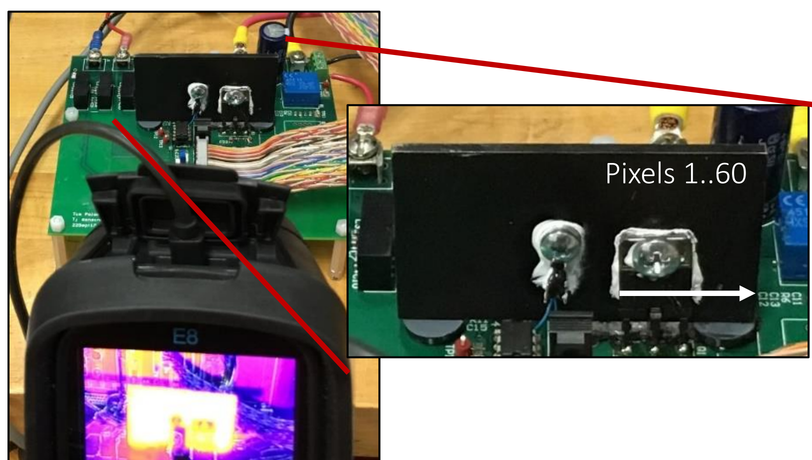

Fig. 6.2-6. Location of 60 sense pixels used for spatially-varying electrothermal impedance and sensitivity analysis

FFT analysis

To expand upon results shown in Fig. 6.2-5(c), which treated signal envelopes as AC true AC, harmonic response, formal Fourier transform analysis was applied to time domain waveforms extracted from infrared thermography. As shown in Fig. 6.2-6, response was quantified at 60 pixels along a vector starting at the left side of the MOSFET and extending to the right edge of the baseplate mount. For illustration, Fig. 6.2-7 shows 60 waveforms of a spatiotemporal temperature response. The variable amplitude and delay response property of the MOSFET-baseplate sub-assembly can be seen. Fig. 6.2-7 also shows the 50 mHz loss perturbation waveform.

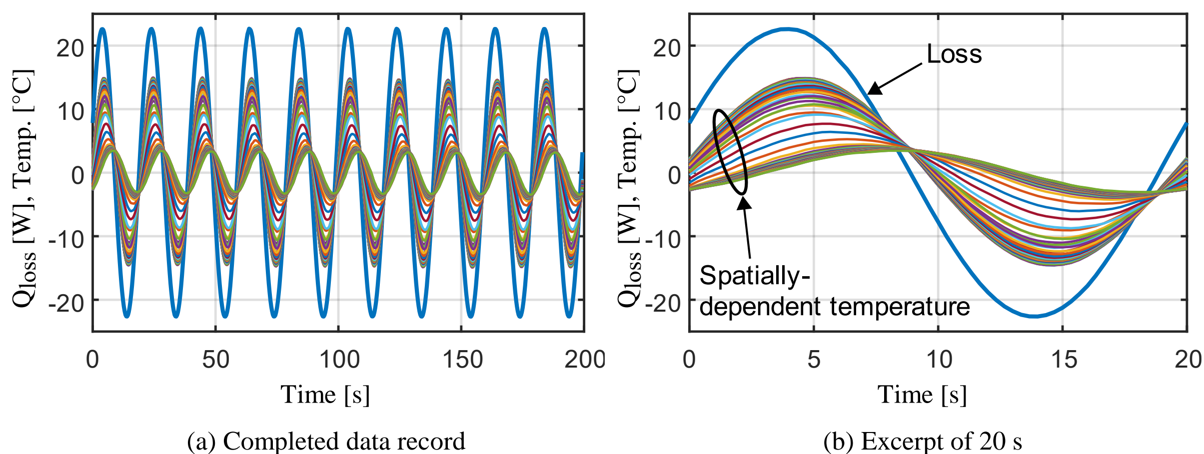

(a) Completed data record (b) Excerpt of 20 s

Fig. 6.2-7. AC power loss and spatially-varying temperature response, the latter of which was reconstructed from data extracted from an infrared camera; response to 0.05 Hz harmonic loss perturbation is shown

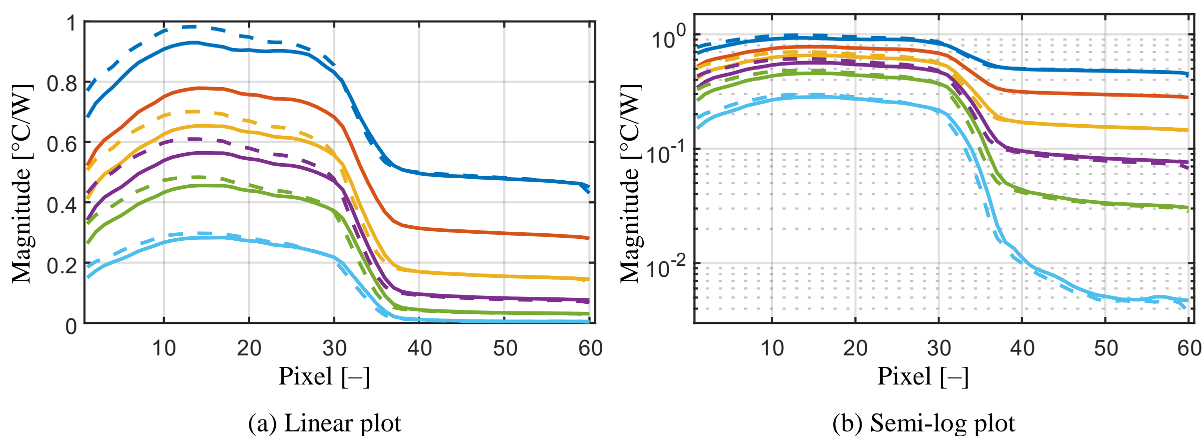

(a) Linear plot (b) Semi-log plot

Legend: ——*test 1* - - -*test 2* | f_{fund} = **0.01 Hz 0.02 Hz 0.05 Hz 0.1 Hz 0.2 Hz 0.5 Hz**

Fig. 6.2-8. Spatially-varying electrothermal impedance magnitudes, before and after altering bolt torque, estimated by dividing computed FFT spectra at the displayed fundamental excitation frequency, f_{fund}

FFT analysis was applied to all waveforms in Fig. 4.3-8, and all similar waveforms extracted at five other excitation frequencies in the 10-500 mHz range. A 2D view of spatially-varying FRF magnitude, the result of the post-processing, is displayed in Fig. 6.2-8. The semiconductor die is about covered by pixels 1-30. Fig. 6.2-8 therefore immediately shows the nonuniformity of the AC die temperature response, whose geometric center is approximately pixel 16. It shows a spatial temperature difference between the AC die temperature response and that of

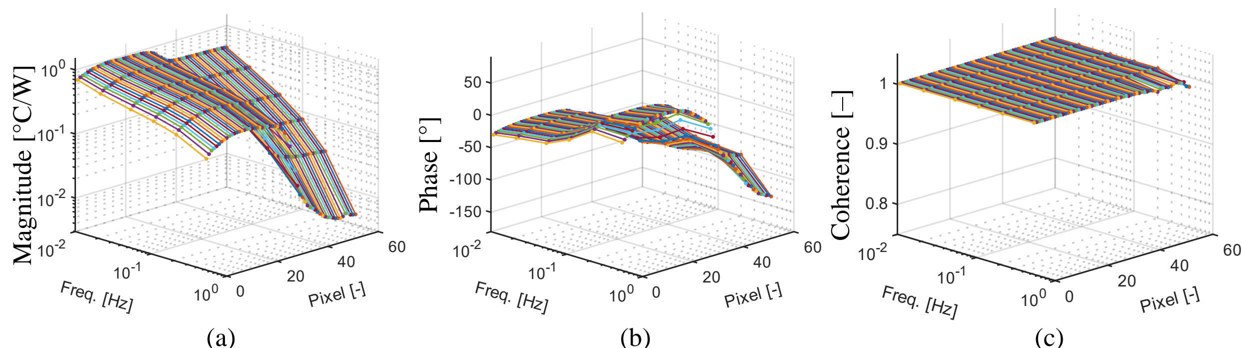

Fig. 6.2-9. Spatially-varying electrothermal impedance for test 1 computed using transfer function estimation

the adjacent baseplate material. This difference generally is larger at higher excitation frequencies. Fig. 6.2-8 also includes an overlay of data extracted before and after TIM manipulation, providing an initial sensitivity measurement.

Spatially-varying electrothermal impedance surface

Continuing, Fig. 6.2-9 presents a spatially-varying FRF, including magnitude, phase, and coherence obtained during post-processing. This figure shows the data represented by Fig. 6.2-8 in 3D space, so additional context for temporal response variation is provided. It helps identify, for example, that the distal response, at pixel ≈ 60, has magnitude attenuation that exponentially decreases with increasing harmonic frequency.

Unlike previous plots, this FRF surface data was computed using a complex transfer function estimation algorithm in *Matlab*, so a phase response property was included. The phase response has a wavy form in which distal response delay nearly increases monotonically, while the die surface temperature phase response exhibits less delay between 0.1 and 0.5 Hz than in the 0.01 to 0.01 Hz range. This phase response will be discussed further in a few subsections.

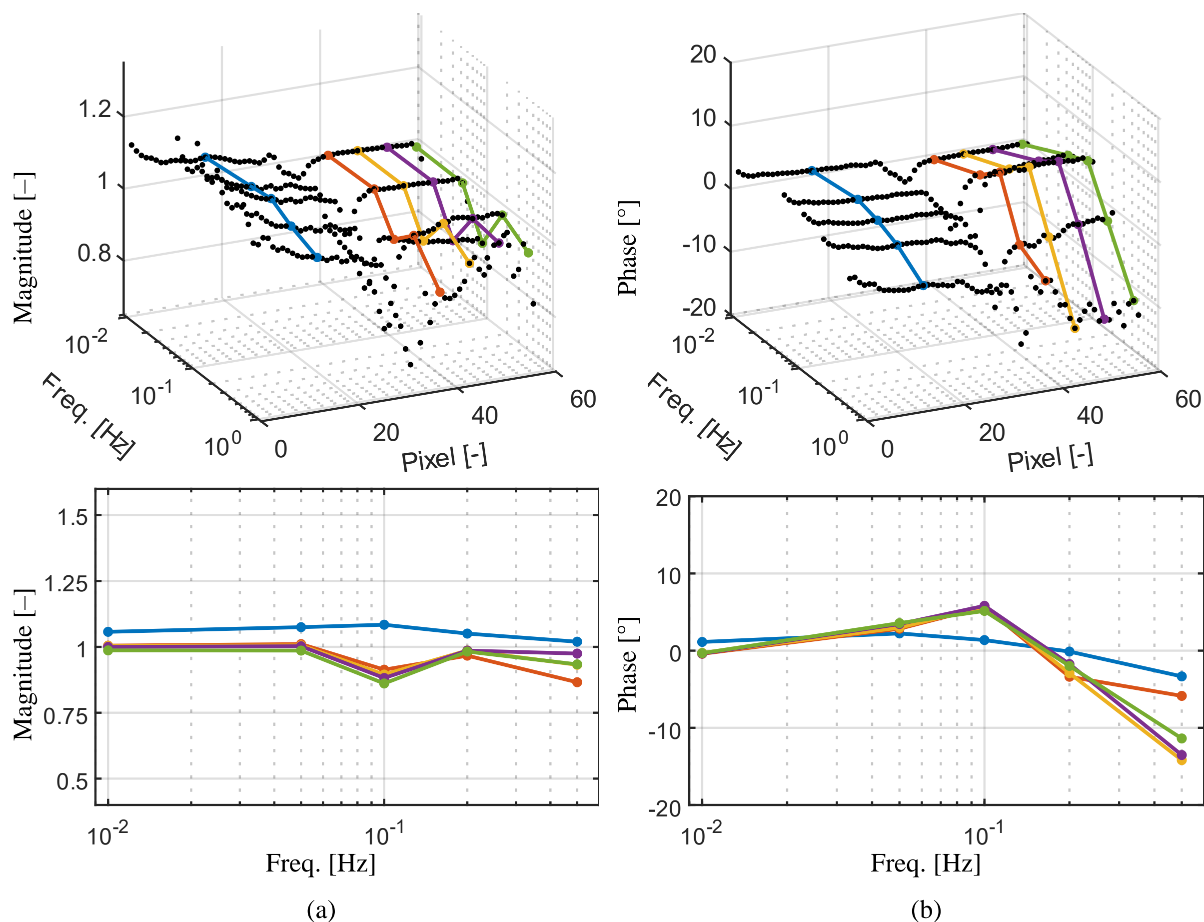

Fig. 6.2-10. Measured spatially-varying sensitivity function shown in 3D and 2D

Spatially-varying sensitivity function

Recalling Table 6.2-1, the transient thermal response of the MOSFET-baseplate sub-assembly was characterized twice under different amounts of pressure between the MOSFET and baseplate. Now, Fig. 3.2-12 presents experimental evaluation of (6.2-1) which characterizes resulting sensitivity of space-variant, conduction heat transfer.

The top two windows of Fig. 3.2-12 display, in terms of magnitude and phase, an entire sensitivity FRF surface. In the surfaces, there are regions with a relatively high amount of local variation. One especially noisy segment is the 0.5 Hz response vector, due to two reasons. First, response away from the die is naturally attenuated by thermal diffusion, so SNR was lowest at this

maximum frequency of the test plan. Second, fundamental-to-sampling frequency ratio, where data sampling with the infrared camera-PC system was 4 Hz at maximum, was smallest at this 0.5 Hz excitation frequency. Response near the pixel zero also appears relatively noisy. This pixel corresponds to the left side of the test MOSFET.

At pixel 30–35, transition between semiconductor device, its lead frame, and baseplate on the right side of the test MOSFET, sensitivity, marked by an amplitude attenuation and phase lag, is relatively large. This sensitivity increases with excitation frequency and has a different character than the sensitivity pattern beyond pixel 40, with maximal sensitivities of around 30% and 15°. Future work should expand the scope of modeling studies to examine response sensitivity very close to component interfaces in an assembly.

To simplify interpretation and mirror the scope of Fig. 6.2-3, five lines of response data were extracted from the response surfaces. The lines correspond to center of the semiconductor die, and three spots on the baseplate, away from the MOSFET-baseplate interface. They are displayed in the bottom windows of Fig. 3.2-12. Die-center response has apparent sensitivity on the order of 5% and a few degrees, for the fabricated TIM degradation. Measured baseplate sensitivity to the MOSFET-baseplate interface is slightly larger. It includes a few features not predicted during completed modeling work, such as the valley/peak in magnitude/phase at 100 mHz. It does have lagging sensitivity above this level, which was also measured by thermistor.

Extracted experimental results are not as clean as the modeling results shown in Fig. 6.2-2 and Fig. 6.2-3. However, this was expected due to limits of infrared equipment used to make measurements. Overall, this section has demonstrated an experimental methodology for ultimately locating temperature detectors degradation sensing in modules. The potential for the method to

provide sensitivity insight can be further realized with the use of more sophisticated imaging equipment. Final remark: please note that that sensitivity with 0.02 Hz loss excitation is not displayed in Fig. 3.2-12 and Fig. 6.2-8 because of an error that occurred during data acquisition for this experiment during test 2.

Measurement error

IR thermography usage in spatially-varying electrothermal impedance analysis relied on the *AixControl* digital control platform to trigger synchronous data records of device losses, estimated by the controller, and spatiotemporal transient temperature response, measured with an IR camera. Any time delays in the overall data acquisition system lead to errors in phase measurements.

Fig. 6.2-11 shows the phase response surface from Fig. 6.2-9(b) in a 2D view. It shows a leading phase response for pixels 0–30, the semiconductor component, above 100 mHz. The displayed FRFs quantify transient temperature response to die loss excitation harmonics. Since losses initiate dynamic thermal behavior, phase lead in this FRF is a physical impossibility.

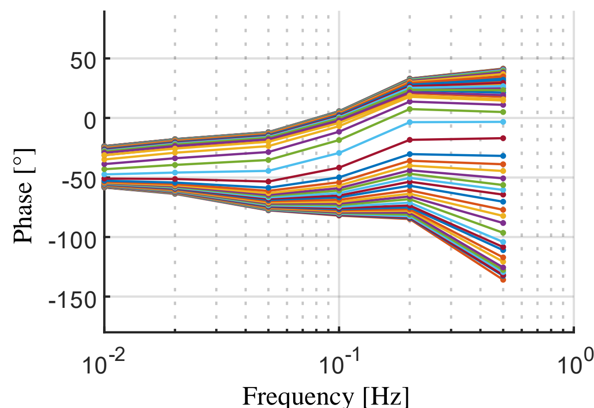

Fig. 6.2-11. Phase-frequency view of a measured spatially-varying electrothermal impedance

Fig. 6.2-11 therefore reveals that the employed data acquisition system, specifically the signal flow of loss information, has delay. Error on measured phase response induced by a time delay is quantified by (6.2-2). It shows how delay-induced phase errors are proportional to the fundamental test frequency and, of course, the delay time. This document overall has provided several concepts for essentially forming measurement error bars – this is another.

$$\varphi_{\text{delay}}\ [°] = 360°\ t_{delay}\ f_{fund} \qquad (6.2\text{-}2)$$

FRF phase in Fig. 6.2-11 and Fig. 6.2-9(b) is inaccurate. However, because test setups for test 1 and test 2 (Table 6.2-1) were, insomuch as possible, identical, uncompensated delays in signal flow are assumed to be present for all measurements. Relative metrics, like sensitivity function phase, thus retain accuracy since both elements of the calculation are equally delayed.

6.3 Design Methodology

The steps undergone in this chapter are compatible with a module/converter design workflow and can integrated as constraint analyses. Fig. 6.3-1 illustrates potential design steps and their sequencing.

A design for degradation sensing method starts shortly after converter conception, where converter input/output (IO) needs are identified and circuit topology and modulation schema are devised. This information is needed to begin conceptualizing a module-integrated degradation sensing system. To begin designing a degradation sensing system, conduction and switching losses can be estimated using analytical and simulation models, as shown in section 5.1. These properties are the excitation which drive in situ extraction of heat transfer FRF data.

Selection of feasible identification frequencies at which to gather thermal FRF properties is central to the design method. Limits in a converter concept's natural transient loss dissipation

disqualify many initial options. Analysis of heat transfer sensitivity to degradation identifies module thermal-mechanical and material properties which further reduce the scope of identification frequencies. Additional constraints due to nonlinear, temperature-dependent material properties and non-ideal temperature sensing are additional constraints for design.

Spatially-varying sensitivity analysis next quantifies design degrees-of-freedom and opportunity. It reveals the amount and accuracy of degradation information that can be inferred from fixed-position temperature sensors, such as the switching devices, or from a design space with sensing location degrees-of-freedom. Aside from synthesizing a spatial arrangement of additional detectors, a goal of the design method is to specify when, during a converter's load profile, information extraction will be fastest and most accurate.

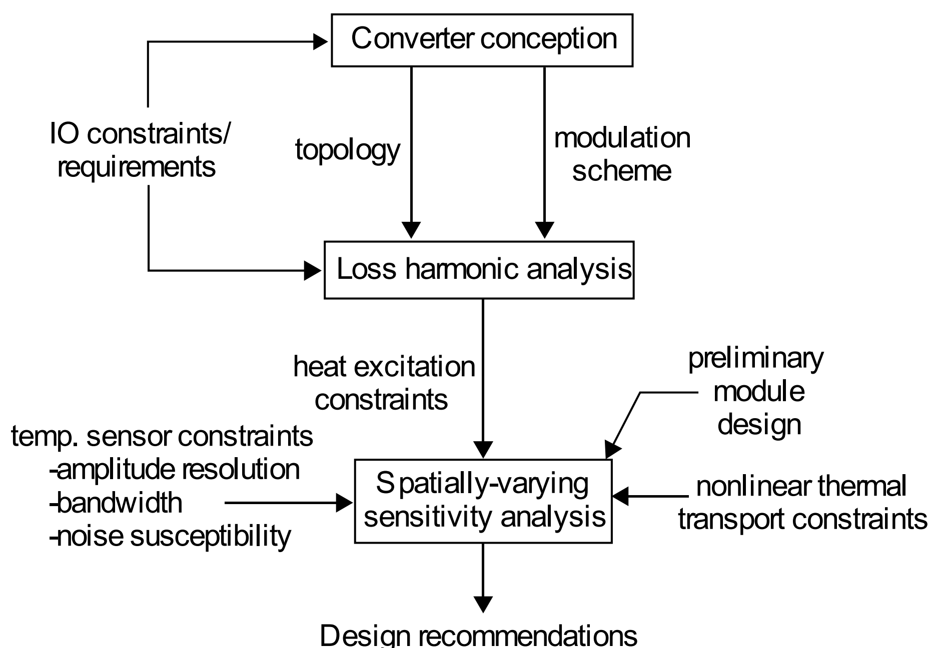

Fig. 6.3-1. Power module design for degradation sensing method

6.4 Chapter Summary

This chapter has developed a method, shown in Fig. 6.3-1, for sequencing analysis, simulation, and experimentation in order to implement degradation sensing into power modules. As 0 presented loss harmonic analysis, this chapter investigated sensitivity analysis, especially a spatially-varying version, focusing on constraints and opportunities that are unique to design in a multi-chip module environment.

First, a commercial, three-phase wide-bandgap power module was analyzed using the developed finite element method. After severe-case heat conduction nonlinearity constraints were identified, multiple FRFs quantifying heat transfer and its sensitivity to degradation of individual die-attach interfaces were presented. The main conclusions suggest that tracking AC response variation provides the advantage that neighbor-induced thermal response is small above around 100 mHz. Finally, loss harmonic analysis and diffusion-based attenuation of thermal response amplitude are linked to provide a figure which quantifies a tradeoff between temperature sensor resolution and possible extent of sensed degradation. The method thus enables designers to speak in terms of a degradation sensing bandwidth.

Finally, an investigation was made into factors influencing placement of a substrate temperature detector for degradation sensing. To do so, spatially-varying sensitivity analysis was applied to a scaled-down model of a power module. A modeling study of the scaled-down module suggested nearly-zero sensitivity gradient on the baseplate, and that substrate detectors should simply be located based on resolution limits. Experimental evaluation with a thermistor mounted on the module substrate and infrared thermography provided additional insight into FRF properties and sensitivity. Extracted spatially-varying electrothermal impedances clearly showed trends in

amplitude response attenuation. Insight provided by an estimated spatially-varying sensitivity function was less clear, however it highlights the opportunity for placing a temperature detector very close to a degrading interface for high sensitivity.

Chapter 7 Conclusions, Contributions, and Recommended Future Work

7.1 Research Conclusions

The following list summarizes key conclusions offered by this research.

Technology state-of-the-art

- During setup of a converter, there are generally three unknown electrothermal dynamic groups: losses, heat transfer, and calibration of temperature sensor(s).
- Temperature quantities are only defined relatively, with respect to references; every derived or measured thermal response is inherently spatial.
- Temporal ODE descriptions of thermal domains in power semiconductor assemblies are limited in accuracy; they are more completely modeled by PDEs.
- PDEs can be solved using numerical methods, e.g. finite difference/element modeling.
- Transient thermal impedance step response inputs are almost always assumed to be ideal, and are rarely examined.
- Thermal equivalent circuits are commonly formed by fitting step response curves, or by approximating thermal parameters from ODE heat transfer analysis.
- There is no meaningful difference between so-called Cauer thermal equivalent circuit models and coarsely gridded finite difference numerical models.
- Thermal modeling studies in the literature commonly compare outputs from a proposed approach with outputs from numerical models uncalibrated to real systems.
- Open-loop electrothermal domain observers are very commonly applied in the power electronics research literature, especially to obtain temperature feedback for control.
- Documented observers frequently embed ODE open-loop system models, but some examples embed numerical models or operating point-linear models.
- In the literature, evaluation of linear, electrothermal domain observer systems is most often performed using ad-hoc time domain evaluation.

- Signals from observers can drive parameter adaptation, including parameters embedded within the observer system itself.

- The literature contains relatively light signal processing techniques that can be used to compute magnitude and phase frequency response at discrete excitation frequencies.

Distributed parameter thermal system modeling

- Numerical models implicitly encode constant, non-diffuse high frequency response properties characterized by traditional, asymptotic high frequency response.

- The solution to an analytical, 1D transient model includes an exponential term which induces non-constant response attenuation and delay at high frequency/position.

- Numerical models effectively use many poles and zeros to represent the spatiotemporal delay property compactly present in an analytical, 1D transient model.

- The high frequency surface temperature phase response of the 1D transient model with a dynamic heat flux boundary is –45° with $R_c'' = 0$ and –90° with $R_c'' > 0$.

- A proposed hybrid, lumped-diffuse, dynamic model fits experimental FRF data well.

Heat transfer frequency response and its sensitivity

- Sensitivity of transient heat transfer to degradation can be viewed with scalar and vector FRFs and sensitivity functions and complex impedance plots.

- Even if heat transfer models are not closely correlated to measured FRFs, they have capability to identify degradation-sensitive dynamic response ranges and their space-variance.

- The closer a site of degradation is to heat-dissipating semiconductor chips influences, the higher the frequency range that is sensitive to it.

- Wire bonds can influence transient conduction at relatively high frequencies.

- Although slight differences remain, the form of spatial FRF data extracted from a converter is like the form of a simplified numerical model of the converter's MOSFET and heat sink.

- For an analyzed wide-bandgap module, transient conduction is sensitive to material properties having temperature sensitivity.

- Die-attach edge delamination influences transient conduction much less than degradation in the center and uniform contact resistance increases.

- Numerical model response predictions are sensitive to potentially uncertain properties, such as exact location of die temperature sensing.

Power semiconductor-based heat transfer characterization

Transient loss actuation

- Harmonic loss dissipation can be achieved in multiple ways, including the usage of established, passive power electronic circuit elements.
- The influence of duty ratios on both conduction and switching loss elements can be decoupled.
- A converter-integrated loss modulator's phase response accuracy is parameter insensitive since the converter samples and switches at assumed precisely regular intervals.
- AC converters naturally dissipate conduction losses having harmonic content proportional to its fundamental frequency.

Semiconductor device temperature sensing

- Semiconductor device usage at low current ensures dynamics embedded in its on-state resistance are induced due to device temperature fluctuations.
- When sensing temperature using forward voltage properties for FRF characterization, estimated phase response has negligible parameter sensitivity if device current-dependence is nullified.
- If current cannot be nullified, measured FRFs are sensitive to parameters of a die temperature self-sensing model.
- Errors in measured phase response are proportional to time delay between loss and temperature response time series data and perturbation fundamental frequency.

System identification experimental design

- System identification experiments are constrained by device under test upper temperature limits and duration and accuracy requirements.
- Subsequently, lower-level parameter such as cooling and allowable device voltages and currents are limited; these limits are influenced by the component or system selected as device under test.
- Multiple heat injection signals can yield nearly identical, coherent FRF data with repeatability.

- Single, low-distortion perturbation harmonics maximize high frequency data coherence.

Design of converter-integrated degradation sensing systems

- Degrees of freedom for degradation sensing system based on sensed heat transfer FRF variations include temperature sense location, magnitude or phase data usage, and identification frequency.

- As a conservative estimate, FRF phase estimation resolution less than 1° may be necessary to accurately estimate structural degradation incurred over years of degradation in converters.

- Module properties and converter mission profile disqualify potential identification frequencies.

- In the method under development, device temperature sensing is likely needed to detect device die-attach degradation in situ.

- High bandwidth, e.g. at least 100 Hz, die temperature sensing, ensures processing of its response can isolate die-attach degradation without corruption due to degradation at other interfaces.

- Above a threshold, such as 100 mHz for an analyzed module, neighbor-induced thermal response of a semiconductor chip is over an order of magnitude less than its response to self-heating.

- On a baseplate of a scaled-down module, the spatial gradient of its measured degradation sensitivity is small.

- An adaptive observer topology to automatically estimate a thermal resistance parameter can do so by correlation of temperature estimation error and losses.

- Adaptive observers can be implemented as standalone systems or within a model-reference control system, which uses an output from the observer as a feedback variable.

7.2 Research Contributions

The following list summarizes the key contributions made by this research.

Power electronics-integrated heat transfer system identification

- Developed a converter-integrated method to extract forced heat transfer response harmonics
- Developed a scaled-down, component-level method utilizing using circuit loss modulation
- Applied methods using MOSFET and IGBT semiconductor device temperature self-sensing
- Characterized parametric limits of temperature sense relationships on measurement accuracy

Spatially-varying electrothermal impedance analysis

- Identified and reconciled implicit, asymptotic limits of models in a single, low-order model
- Developed an industry-oriented finite element platform to enable detailed design studies
- Analyzed a wide-bandgap multi-chip power module to identify factors constraining selection of degradation-sensitive identification frequency(ies)
- Propagated uncertain model specifications, e.g. spatial distribution of losses and temperature sense locations, through models to quantify their impact on simulated response

Degradation sensitivity characterization

- Defined scalar and vector sensitivity function metrics
- Utilized analytical and numerical models to characterize a relationship between potential source of degradation, temperature sense location, and range of degradation sensitivity
- Experimentally characterized sensitivity to cooling and different amounts of TIM and die-attach manipulation using an assembled converter and discrete components
- Applied spatially-varying sensitivity analysis using infrared thermography

Loss modulator design and harmonic modeling

- Designed a transient loss modulation system based on manipulated input decoupling
- Identified the negligibility of phase response properties to loss model parameters
- Developed a method, based on loss harmonic analysis and temperature sensing amplitude resolution, to specify an effective degradation sensing bandwidth

Degradation-sensitive parameter estimation

- Interpreted FRF data using a developed low-order model to estimate response parameters
- Developed a converter-integrated method to automatically estimate a degradation-sensitive response parameter

7.3 Recommended Future Work

7.3.1 Basic research

7.3.1.1 Risk assessment

Develop demonstrators with increasingly application-realistic features and constraints

This research program experimentally extracted degradation sensitivity functions under various hardware configurations. It is recommended that future work extract additional FRFs from converters in situ, especially before, during, and after a more natural fatigue process. A goal should be to construct a detailed fatigue timeline quantifying how lifetime-varying properties of transient heat transfer, loss dissipation, and temperature sensing evolve. Phase response constancy identified in this work should also be further scrutinized.

Further investigate aspects of power semiconductor device electrothermal dynamics

One pathway to progress the research toward industrial application is to utilize a power semiconductor device as its own temperature sensor, as this work did with voltage drop. This property can itself, however, be degradation sensitive. It is recommended that future work search for temperature sensing options, especially to estimate die temperature, that are minimally sensitive to fatigue processes. For another topic, further characterization of device conduction and switching loss spatiotemporal dynamics, especially their spatial distribution, should be made. And, finally, limits and opportunities stemming from the ongoing adoption of wide-bandgap devices should be quantified.

7.3.1.2 Application growth

Spatial domain feature extraction

Inflections in FRFs can be quantified by the pole and zero temporal domain quantities. It is recommended that future work form spatial domain analogs to poles and zeros to describe inflections observable FRFs with location as the independent variable. Resulting shape factors should be a function of low-level geometric dimensions and could naturally complement or augment resource-intensive numerical approaches to solve conduction problems. A further use of analytical modeling to generally gain insight about degradation sensitivity is recommended.

Further develop automatic systems for parameter and state estimation

This dissertation provides groundwork needed for detailed development of cascaded and multi-rate observers adding estimation value to converters. It is recommended that future work utilize system identification characterization as a basis for forming dynamic open-loop models embedded in observer systems. The developed adaptive observer can be made to be compatible

with such a model. Another system could implement a multi-rate identification model and die temperature sensing to estimate disturbances, which can be correlated to location and extent of degradation. Furthermore, exploring opportunities to embed signal processing operations for fast extraction and fitting of coherent FRF data is recommended.

7.3.2 Commercialization

Identify target converter and converter product applications

Harmonic content of transient power semiconductor device losses depends on details of a power electronic converter. It is recommended that future work investigate this principle in more detail using categories for evaluation, such as circuit topology, mission profile, PWM method, and converter- and application-level control laws. Evaluation should attempt to quantify which converter applications present least costly barriers for integration of system identification. As a corollary, optimal system identification experimental design methods can also be developed to minimize cost- and time-related expenses associated with integrating and executing system identification in application-connected converters.

With other module and converter constraints, develop optimal hardware design methods

This work treated the topic of module design for degradation sensing using an assumed, hardware design. It is recommended that future work more comprehensively examine the topic, by, for example, including additional design constraint quantities, like loop inductances, in the formulation. Next, the developed computational heat transfer platform should be streamlined, for example by including sub-modeling features, to create a sensitivity computer. Optimization methods could then be employed to quantify multi-physics design space and tradeoffs.

References

[1] C. Nan, R. Ayyanar, and Y. Xi, "A 2.2 MHz Active-Clamp Buck Converter for Automotive Applications," *IEEE Trans. Power Electron.*, pp. 1–1, 2017.

[2] L. Wei, Y. Patel, and M. Csn, "Active front end rectifier design trade-off between PWM and direct power control method," in *2014 IEEE Energy Conversion Congress and Exposition (ECCE)*, 2014, pp. 1015–1021.

[3] D. Ludois and G. Venkataramanan, "An Examination of AC/HVDC Power Circuits for Interconnecting Bulk Wind Generation with the Electric Grid," *Energies*, vol. 3, no. 6, pp. 1263–1289, Jun. 2010.

[4] L. Wei, R. A. Lukaszewski, and T. A. Lipo, "Analysis of Power-Cycling Capability of IGBT Modules in a Conventional Matrix Converter," *IEEE Trans. Ind. Appl.*, vol. 45, no. 4, pp. 1443–1451, Jul. 2009.

[5] J. Lutz, U. Scheuermann, H. Schlangenotto, and R. De Doncker, "Power Semiconductor Devices—Key Components for Efficient Electrical Energy Conversion Systems," in *Semiconductor Power Devices*, Cham: Springer International Publishing, 2018, pp. 1–20.

[6] B. J. Baliga, "The IGBT Compendium: Applications and Social Impact," Raleigh, NC, 2011.

[7] H. Wang *et al.*, "Transitioning to Physics-of-Failure as a Reliability Driver in Power Electronics," Mar. 2014.

[8] Shaoyong Yang, A. Bryant, P. Mawby, Dawei Xiang, Li Ran, and P. Tavner, "An Industry-Based Survey of Reliability in Power Electronic Converters," *IEEE Trans. Ind. Appl.*, vol. 47, no. 3, pp. 1441–1451, May 2011.

[9] M. Held, P. Jacob, G. Nicoletti, P. Scacco, and M.-H. Poech, "Fast power cycling test of IGBT modules in traction application," in *Proceedings of Second International Conference on Power Electronics and Drive Systems*, 1997, vol. 1, pp. 425–430.

[10] M. Ciappa, "Selected failure mechanisms of modern power modules," *Microelectron. Reliab.*, vol. 42, no. 4–5, pp. 653–667, Apr. 2002.

[11] V. Smet *et al.*, "Ageing and Failure Modes of IGBT Modules in High-Temperature Power Cycling," *IEEE Trans. Ind. Electron.*, vol. 58, no. 10, pp. 4931–4941, Oct. 2011.

[12] L. Gopi Reddy, L. Tolbert, and B. Ozpineci, "Power Cycle Testing of Power Switches: A Literature Survey," *IEEE Trans. Power Electron.*, pp. 1–1, 2014.

[13] H. Oh, B. Han, P. McCluskey, C. Han, and B. D. Youn, "Physics-of-Failure, Condition Monitoring, and Prognostics of Insulated Gate Bipolar Transistor Modules: A Review," *IEEE Trans. Power Electron.*, vol. 30, no. 5, pp. 2413–2426, May 2015.

[14] C. Durand, M. Klingler, D. Coutellier, and H. Naceur, "Power Cycling Reliability of Power Module: A Survey," *IEEE Trans. Device Mater. Reliab.*, vol. 16, no. 1, pp. 80–97, Mar. 2016.

[15] K. Tikkanen, "Why do variable speed drives fail and how do we test them?" 2017.

[16] U.-M. Choi, F. Blaabjerg, and S. Jorgensen, "Power Cycling Test Methods for Reliability Assessment of Power Device Modules in respect to Temperature Stress," *IEEE Trans. Power Electron.*, pp. 1–1, 2017.

[17] H. S. Chung, H. Wang, F. Blaabjerg, and M. Pecht, *Reliability of Power Electronic Converter Systems*. The Institution of Engineering and Technology, 2015.

[18] H. Oh, B. Han, P. McCluskey, C. Han, and B. D. Youn, "Physics-of-Failure, Condition Monitoring, and Prognostics of Insulated Gate Bipolar Transistor Modules: A Review," *IEEE Trans. Power Electron.*, vol. 30, no. 5, pp. 2413–2426, May 2015.

[19] L. Gopi Reddy, L. Tolbert, and B. Ozpineci, "Power Cycle Testing of Power Switches: A Literature Survey," *IEEE Trans. Power Electron.*, vol. 30, no. 5, pp. 1–1, May 2014.

[20] D. C. Katsis and J. D. van Wyk, "Void-induced thermal impedance in power semiconductor modules: Some transient temperature effects," *IEEE Trans. Ind. Appl.*, vol. 39, no. 5, pp. 1239–1246, Sep. 2003.

[21] W. Lai *et al.*, "Study on the lifetime characteristics of power modules under power cycling conditions," *IET Power Electron.*, vol. 9, no. 5, pp. 1045–1052, Apr. 2016.

[22] W. Lai *et al.*, "Experimental Investigation on the Effects of Narrow Junction Temperature Cycles on Die-Attach Solder Layer in an IGBT Module," in *IEEE Transactions on Power Electronics*, 2017, vol. 32, no. 2, pp. 1431–1441.

[23] P. Lall, M. Pecht, and E. B. Hakim, *Influence of Temperature on Microelectronics and System Reliability: A Physics of Failure Approach*. CRC Press, 1997.

[24] M. G. Pecht, *Prognostics and Health Management of Electronics*. John Wiley & Sons, Inc., 2008.

[25] R. G. Budynas and K. J. Nisbett, *Shigley's Mechanical Engineering Design*. New York, NY: McGraw-Hill, 2014.

[26] K. C. Kapur and M. Pecht, Eds., *Reliability Engineering*. John Wiley & Sons, Inc., 2014.

[27] A. Feinberg, *Thermodynamic Degradation Science*. Chichester, UK: John Wiley & Sons, Ltd, 2016.

[28] M. Modarres, M. Amiri, and C. Jackson, *Probabilistic Physics of Failure Approach to Reliability*. Hoboken, NJ, USA: John Wiley & Sons, Inc., 2017.

[29] JEDEC, "JESD22-A122A: Power Cycling," Arlington, VA, 2007.

[30] K. Ma, U. M. Choi, and F. Blaabjerg, "Reliability metrics extraction for power electronics converter stressed by thermal cycles," in *2017 IEEE Energy Conversion Congress and Exposition, ECCE 2017*, 2017, vol. 2017-Janua, pp. 3838–3843.

[31] K. Tikkanen, "The embodiment of reliability for variable speed drives," 2017.

[32] D. A. Murdock, "Active Thermal Control of Power Electronics Modules," *M.S. Thesis*, 2002.

[33] M. Musallam and C. M. Johnson, "An Efficient Implementation of the Rainflow Counting Algorithm for Life Consumption Estimation," *IEEE Trans. Reliab.*, vol. 61, no. 4, pp. 978–986, Dec. 2012.

[34] U. Drofenik, I. Kovacevic, R. Schmidt, and J. W. Kolar, "Multi-domain simulation of transient junction temperatures and resulting stress-strain behavior of power switches for long-term mission profiles," in *2008 11th Workshop on Control and Modeling for Power Electronics*, 2008, pp. 1–7.

[35] I. F. Kovacevic, U. Drofenik, and J. W. Kolar, "New physical model for lifetime estimation of power modules," in *The 2010 International Power Electronics Conference - ECCE ASIA -*, 2010, pp. 2106–2114.

[36] A. A. Feinberg and A. Widom, "On thermodynamic reliability engineering," *IEEE Trans. Reliab.*,

vol. 49, no. 2, pp. 136–146, Jun. 2000.

[37] M. . Bryant, M. . Khonsari, and F. . Ling, "On the thermodynamics of degradation," *Proc. R. Soc. A Math. Phys. Eng. Sci.*, vol. 464, no. 2096, pp. 2001–2014, Aug. 2008.

[38] A. Imanian and M. Modarres, "Thermodynamics as a fundamental science of reliability," *Proc. Inst. Mech. Eng. Part O J. Risk Reliab.*, vol. 230, no. 6, pp. 598–608, Dec. 2016.

[39] H. Huang and P. A. Mawby, "A Lifetime Estimation Technique for Voltage Source Inverters," *IEEE Trans. Power Electron.*, vol. 28, no. 8, pp. 4113–4119, Aug. 2013.

[40] Y. Avenas, L. Dupont, N. Baker, H. Zara, and F. Barruel, "Condition Monitoring: A Decade of Proposed Techniques," *IEEE Ind. Electron. Mag.*, vol. 9, no. 4, pp. 22–36, Dec. 2015.

[41] S. Yang, D. Xiang, A. Bryant, P. Mawby, L. Ran, and P. Tavner, "Condition Monitoring for Device Reliability in Power Electronic Converters: A Review," *IEEE Trans. Power Electron.*, vol. 25, no. 11, pp. 2734–2752, Nov. 2010.

[42] D. Xiang, L. Ran, P. Tavner, S. Yang, A. Bryant, and P. Mawby, "Condition Monitoring Power Module Solder Fatigue Using Inverter Harmonic Identification," *IEEE Trans. Power Electron.*, vol. 27, no. 1, pp. 235–247, Jan. 2012.

[43] B. Ji, V. Pickert, W. Cao, and B. Zahawi, "In Situ Diagnostics and Prognostics of Wire Bonding Faults in IGBT Modules for Electric Vehicle Drives," *IEEE Trans. Power Electron.*, vol. 28, no. 12, pp. 5568–5577, Dec. 2013.

[44] S. Beczkowski, P. Ghimre, A. R. de Vega, S. Munk-Nielsen, B. Rannestad, and P. Thogersen, "Online Vce measurement method for wear-out monitoring of high power IGBT modules," in *2013 15th European Conference on Power Electronics and Applications (EPE)*, 2013, pp. 1–7.

[45] P. Ghimire, S. Beczkowski, S. Munk-Nielsen, B. Rannestad, and P. B. Thogersen, "A review on real time physical measurement techniques and their attempt to predict wear-out status of IGBT," in *2013 15th European Conference on Power Electronics and Applications (EPE)*, 2013, pp. 1–10.

[46] H. Chen, B. Ji, V. Pickert, and W. Cao, "Real-Time Temperature Estimation for Power MOSFETs Considering Thermal Aging Effects," *IEEE Trans. Device Mater. Reliab.*, vol. 14, no. 1, pp. 220–228, Mar. 2014.

[47] P. Ghimire, A. R. de Vega, S. Beczkowski, B. Rannestad, S. Munk-Nielsen, and P. Thogersen, "Improving Power Converter Reliability: Online Monitoring of High-Power IGBT Modules," *IEEE Ind. Electron. Mag.*, vol. 8, no. 3, pp. 40–50, Sep. 2014.

[48] J.-P. Sjoroos and K. Tikkanen, "Aging determination of power semiconductor device in electric drive system," 24-Jun-2016.

[49] Z. Wang, "Real-Time Internal Temperature Estimation and Health Monitoring for IGBT Modules," *Theses Diss. from Electr. Comput. Eng.*, 2017.

[50] U.-M. Choi, F. Blaabjerg, S. Jorgensen, S. Munk-Nielsen, and B. Rannestad, "Reliability Improvement of Power Converters by Means of Condition Monitoring of IGBT Modules," *IEEE Trans. Power Electron.*, vol. 32, no. 10, pp. 7990–7997, Oct. 2017.

[51] S. Zhou, L. Zhou, and P. Sun, "Monitoring Potential Defects in an IGBT Module Based on Dynamic Changes of the Gate Current," *IEEE Trans. Power Electron.*, vol. 28, no. 3, pp. 1479–1487, Mar. 2013.

[52] A. Hanif, S. Das, and F. Khan, "Active Power Cycling and Condition Monitoring of IGBT Power

Modules using Reflectometry," in *Applied Power Electronics Conf. and Expo (APEC) 2018*, 2018, pp. 2827–2833.

[53] X. Ye, C. Chen, Y. Wang, G. Zhai, and G. J. Vachtsevanos, "Online Condition Monitoring of Power MOSFET Gate Oxide Degradation Based on Miller Platform Voltage," *IEEE Trans. Power Electron.*, vol. 32, no. 6, pp. 4776–4784, Jun. 2017.

[54] A. Aliyu and A. Castellazzi, "Prognostic System for Power Modules in Converter Systems Using Structure Function," *IEEE Trans. Power Electron.*, pp. 1–1, 2017.

[55] V. Tiihonen and K. Tikkanen, "Method and apparatus for pre-emptive power semiconductor module fault indication," 19-Sep-2014.

[56] Bing Ji *et al.*, "<italic>In Situ</italic> Diagnostics and Prognostics of Solder Fatigue in IGBT Modules for Electric Vehicle Drives," *IEEE Trans. Power Electron.*, vol. 30, no. 3, pp. 1535–1543, Mar. 2015.

[57] Z. Hu, M. Du, and K. Wei, "Online Calculation of the Increase in Thermal Resistance Caused by Solder Fatigue for IGBT Modules," *IEEE Trans. Device Mater. Reliab.*, vol. 17, no. 4, pp. 785–794, Dec. 2017.

[58] M. Ciappa and A. Blascovich, "Reliability odometer for real-time and in situ lifetime measurement of power devices," *Microelectron. Reliab.*, vol. 55, no. 9, pp. 1351–1356, 2015.

[59] M. A. Eleffendi and C. M. Johnson, "In-Service Diagnostics for Wire-Bond Lift-off and Solder Fatigue of Power Semiconductor Packages," *IEEE Trans. Power Electron.*, vol. 32, no. 9, pp. 7187–7198, Sep. 2017.

[60] M. S. Haque, S. Choi, and J. Baek, "Auxiliary Particle Filtering-Based Estimation of Remaining Useful Life of IGBT," *IEEE Trans. Ind. Electron.*, vol. 65, no. 3, pp. 2693–2703, Mar. 2018.

[61] M. A. Eleffendi and C. M. Johnson, "Application of Kalman Filter to Estimate Junction Temperature in IGBT Power Modules," *IEEE Trans. Power Electron.*, vol. 31, no. 2, pp. 1576–1587, Feb. 2016.

[62] H. Dongming, Z. Dezhong, and G. Yuqin, "Experimental and numerical study on infrared thermal wave imaging," *Tsinghua Sci. Technol.*, vol. 2, no. 2, pp. 619–623, Jun. 1997.

[63] A. Rosencwaig, "Thermal-Wave Microscopy of Semiconductor Devices," in *Proc. Ultrasonics Symp*, 1981, pp. 828–831.

[64] A. Rosencwaig and J. Opsal, "Thermal Wave Imaging with Thermoacoustic Detection," *IEEE Trans. Ultrason. Ferroelectr. Freq. Control*, vol. 33, no. 5, pp. 516–528, Sep. 1986.

[65] A. Rosencwaig, "Thermal-Wave Imaging and Microscopy," in *Proc. Ultrasonics Symp*, 1980, pp. 600–607.

[66] E. R. Olson, "Design of integrated current and temperature sensors in power electronic modules using GMR point-field detectors," University of Wisconsin-Madison, 2006.

[67] F. Electric, "Power Semiconductors - IGBT 6-Pack." [Online]. Available: http://www.fujielectric.com/products/semiconductor/model/igbt/6pack.html.

[68] B. J. Baliga, *Fundamentals of power semiconductor devices*. Springer, 2008.

[69] Y. Avenas, L. Dupont, and Z. Khatir, "Temperature Measurement of Power Semiconductor Devices by Thermo-Sensitive Electrical Parameters—A Review," *IEEE Trans. Power Electron.*, vol. 27, no. 6, pp. 3081–3092, Jun. 2012.

[70] N. Baker, M. Liserre, L. Dupont, and Y. Avenas, "Improved reliability of power modules: A review of online junction temperature measurement methods," *IEEE Industrial Electronics Magazine*, vol. 8, no. 3. pp. 17–27, 2014.

[71] H. Niu and R. D. Lorenz, "Evaluating Different Implementations of Online Junction Temperature Sensing for Switching Power Semiconductors," *IEEE Trans. Ind. Appl.*, pp. 1–1, 2016.

[72] R. D. Lorenz, "Self-sensing as an integration focus for motor drives and power devices," in *Electrical Machines and Systems, 2007. ICEMS. International Conference on*, 2007.

[73] R. Schmidt and U. Scheuermann, "Using the chip as a temperature sensor - The influence of steep lateral temperature gradients on the Vce(T)-measurement," *Power Electron. Appl. 2009. EPE '09. 13th Eur. Conf.*, pp. 1–9, 2009.

[74] J. Lemmens, P. Vanassche, and J. Driesen, "Optimal Control of Traction Motor Drives Under Electrothermal Constraints," *IEEE J. Emerg. Sel. Top. Power Electron.*, vol. 2, no. 2, pp. 249–263, Jun. 2014.

[75] M. Denk and M. M. Bakran, "An IGBT driver concept with integrated real-time junction temperature measurement," *PCIM Eur. Conf. Proc.*, no. May, pp. 214–221, 2014.

[76] M. Denk and M. Bakran, "Junction Temperature Measurement during Inverter Operation using a T J -IGBT-Driver," *Proc. PCIM Eur. 2015; Int. Exhib. Conf. Power Electron. Intell. Motion, Renew. Energy Energy*, no. May, pp. 19–21, 2015.

[77] M. Denk, "IGBT Gate Driver with Accurate Measurement of Junction Temperature and Inverter Output Current," *PCIM Eur. 2017; Int. Exhib. Conf. Power Electron. Intell. Motion, Renew. Energy Energy Manag.*, no. May, pp. 16–18, 2017.

[78] N. Baker, S. Munk-Nielsen, F. Iannuzzo, and M. Liserre, "IGBT Junction Temperature Measurement via Peak Gate Current," *IEEE Trans. Power Electron.*, vol. 31, no. 5, pp. 3784–3793, May 2016.

[79] N. Baker, L. Dupont, S. Munk-Nielsen, F. Iannuzzo, and M. Liserre, "IR Camera Validation of IGBT Junction Temperature Measurement via Peak Gate Current," *IEEE Trans. Power Electron.*, vol. 32, no. 4, pp. 3099–3111, Apr. 2017.

[80] H. Niu and R. D. Lorenz, "Sensing Power MOSFET Junction Temperature Using Gate Drive Turn-On Current Transient Properties," *IEEE Trans. Ind. Appl.*, vol. 52, no. 2, pp. 1677–1687, Mar. 2016.

[81] H. Niu and R. D. Lorenz, "Sensing IGBT junction temperature using gate drive output transient properties," in *2015 IEEE Applied Power Electronics Conference and Exposition (APEC)*, 2015, pp. 2492–2499.

[82] H. Niu and R. Lorenz, "Real-time Junction Temperature Sensing for Silicon Carbide MOSFET with Different Gate Drive Topologies and Different Operating Conditions," *IEEE Trans. Power Electron.*, pp. 1–1, 2017.

[83] H. S. Carslaw and J. C. Jaegar, *Conduction of Heat in Solids*, 1st ed. Oxford University Press, 1948.

[84] G. F. Nellis and S. A. Klein, *Heat Transfer*. Cambridge University Press, 2009.

[85] A. G. Kokkas, "Thermal analysis of multiple-layer structures," *IEEE Trans. Electron Devices*, vol. 21, no. 11, pp. 674–681, Nov. 1974.

[86] J. J. Nelson, G. Venkataramanan, and A. M. El-Refaie, "Fast thermal profiling of power semiconductor devices using Fourier techniques," *IEEE Trans. Ind. Electron.*, vol. 53, no. 2, pp.

521–529, Apr. 2006.

[87] J. Reichl, J. M. Ortiz-Rodriguez, A. Hefner, and J.-S. Lai, “3-D Thermal Component Model for Electrothermal Analysis of Multichip Power Modules With Experimental Validation,” *IEEE Trans. Power Electron.*, vol. 30, no. 6, pp. 3300–3308, Jun. 2015.

[88] B. Du, J. L. Hudgins, E. Santi, A. T. Bryant, P. R. Palmer, and H. A. Mantooth, “Transient thermal analysis of power devices based on Fourier-series thermal model,” in *2008 IEEE Power Electronics Specialists Conference*, 2008, pp. 3129–3135.

[89] Bin Du, J. L. Hudgins, E. Santi, A. T. Bryant, P. R. Palmer, and H. A. Mantooth, “Transient Electrothermal Simulation of Power Semiconductor Devices,” *IEEE Trans. Power Electron.*, vol. 25, no. 1, pp. 237–248, Jan. 2010.

[90] I. R. Swan, A. T. Bryant, and P. A. Mawby, “Fast Thermal Models for Power Device Packaging,” in *2008 IEEE Industry Applications Society Annual Meeting*, 2008, pp. 1–8.

[91] E. J. Diebold and W. Luft, “Transient thermal impedance of semiconductor devices,” *Trans. Am. Inst. Electr. Eng. Part I Commun. Electron.*, vol. 79, no. 6, pp. 719–726, 1961.

[92] E. J. Diebold, “Temperature rise of solid junctions,” *Electr. Eng.*, vol. 77, no. 2, pp. 163–163, Feb. 1958.

[93] V. Székely and T. Van Bien, “Fine structure of heat flow path in semiconductor devices: A measurement and identification method,” *Solid. State. Electron.*, vol. 31, no. 9, pp. 1363–1368, Sep. 1988.

[94] P. E. Bagnoli, C. Casarosa, M. Ciampi, and E. Dallago, “Thermal resistance analysis by induced transient (TRAIT) method for power electronic devices thermal characterization. I. Fundamentals and theory,” *IEEE Trans. Power Electron.*, vol. 13, no. 6, pp. 1208–1219, 1998.

[95] P. E. Bagnoli, C. Casarosa, E. Dallago, and M. Nardoni, “Thermal resistance analysis by induced transient (TRAIT) method for power electronic devices thermal characterization. II. Practice and experiments,” *IEEE Trans. Power Electron.*, vol. 13, no. 6, pp. 1220–1228, 1998.

[96] T. Lopez and R. Elferich, “Thermal Impedance Extraction Technique for Power MOSFETs,” in *2007 IEEE Power Electronics Specialists Conference*, 2007, pp. 2140–2146.

[97] A. Volke and M. Hornkamp, *IGBT modules: Technologies, driver and application*, 3rd editio. Munich, Germany: Infineon Technologies AG, 2017.

[98] E. A. Guillemin, *Synthesis of Passive Networks*. New York, NY: John Wiley & Sons, 1957.

[99] M. Maerz and P. Nance, “Thermal Modeling of Power-electronic Systems,” *White Pap.*, 2000.

[100] Z. Wang and W. Qiao, “A Physics-Based Improved Cauer-Type Thermal Equivalent Circuit for IGBT Modules,” *IEEE Trans. Power Electron.*, vol. PP, no. 99, pp. 1–1, 2016.

[101] C. Yun, P. Malberti, M. Ciappa, and W. Fichtner, “Thermal component model for electrothermal analysis of IGBT module systems,” *IEEE Trans. Adv. Packag.*, vol. 24, no. 3, pp. 401–406, 2001.

[102] M. Ciappa, W. Fichtner, T. Kojima, Y. Yamada, and Y. Nishibe, “Extraction of Accurate Thermal Compact Models for Fast Electro-Thermal Simulation of IGBT Modules in Hybrid Electric Vehicles,” *Microelectron. Reliab.*, vol. 45, no. 9–11, pp. 1694–1699, Sep. 2005.

[103] A. S. Bahman, K. Ma, P. Ghimire, F. Iannuzzo, and F. Blaabjerg, “A 3-D-Lumped Thermal Network Model for Long-Term Load Profiles Analysis in High-Power IGBT Modules,” *IEEE J. Emerg. Sel.*

Top. Power Electron., vol. 4, no. 3, pp. 1050–1063, Sep. 2016.

[104] C. H. Van Der Broeck, R. D. Lorenz, and R. W. De Doncker, “Spatial Thermal Observers for Temperature Estimation in Power Electronic Modules,” in *Applied Power Electronics Conf. and Expo (APEC) 2018 (to appear)*, 2018.

[105] C. H. van der Broeck, L. A. Ruppert, A. Hinz, M. Conrad, and R. W. De Doncker, “Spatial Electro-Thermal Modeling and Simulation of Power Electronic Modules,” *IEEE Trans. Ind. Appl.*, vol. 54, no. 1, pp. 404–415, Jan. 2018.

[106] A. F. Emery and H. R. Mortazavi, “A comparison of the finite difference and finite element methods for heat transfer calculations,” Jan. 1982.

[107] F. T. Wenthen, “Computer-aided thermal analysis of power semiconductor devices,” *IEEE Trans. Electron Devices*, vol. 17, no. 9, pp. 765–770, Sep. 1970.

[108] G. E. Myers, *Analytical Methods in Conduction Heat Transfer*, 2nd editio. Madison, WI: AMCHT Publications, 1998.

[109] R. B. Hetnarski, *Encyclopedia of Thermal Stresses*. Dordrecht: Springer Netherlands, 2014.

[110] S. Karagol and M. Bikdash, “Generation of Equivalent-Circuit Models From Simulation Data of a Thermal System,” *IEEE Trans. Power Electron.*, vol. 25, no. 4, pp. 820–828, Apr. 2010.

[111] P. L. Evans, A. Castellazzi, and C. M. Johnson, “Automated Fast Extraction of Compact Thermal Models for Power Electronic Modules,” *IEEE Trans. Power Electron.*, vol. 28, no. 10, pp. 4791–4802, Oct. 2013.

[112] T. M. Mitchell, *Machine Learning*. McGraw-Hill, 1997.

[113] C. M. Bishop, *Pattern Recognition and Machine Learning*. Cambridge, U.K.: Springer, 2006.

[114] K. P. Murphy, *Machine Learning: a Probabilistic Perspective*, 4th editio. 2013: MIT Press, 2012.

[115] J. N. Davidson, D. A. Stone, and M. P. Foster, “Real-Time Prediction of Power Electronic Device Temperatures Using PRBS-Generated Frequency-Domain Thermal Cross Coupling Characteristics,” *IEEE Trans. Power Electron.*, vol. 30, no. 6, pp. 2950–2961, Jun. 2015.

[116] M. Cho, W. Song, S. Yalamanchili, and S. Mukhopadhyay, “Thermal system identification (TSI): A methodology for post-silicon characterization and prediction of the transient thermal field in multicore chips,” in *2012 28th Annual IEEE Semiconductor Thermal Measurement and Management Symposium (SEMI-THERM)*, 2012, pp. 118–124.

[117] J. Kung, M. Cho, S. Yalamanchili, and S. Mukhopadhyay, “On-line real-time temperature and power estimation of an IC using time-domain thermal filters,” in *2013 IEEE 22nd Conference on Electrical Performance of Electronic Packaging and Systems*, 2013, pp. 199–202.

[118] Jaeha Kung, Wen Yueh, S. Yalamanchili, and S. Mukhopadhyay, “Post-Silicon Estimation of Spatiotemporal Temperature Variations Using MIMO Thermal Filters,” *IEEE Trans. Components, Packag. Manuf. Technol.*, vol. 5, no. 5, pp. 650–660, May 2015.

[119] W. Yueh, Z. Wan, Y. Joshi, and S. Mukhopadhyay, “Design, Characterization, and Application of a Field-Programmable Thermal Emulation Platform,” *IEEE Trans. Components, Packag. Manuf. Technol.*, vol. 6, no. 9, pp. 1330–1339, Sep. 2016.

[120] M. S. Alshahed, Z. Yu, H. Richter, C. Harendt, and J. N. Burghartz, “Measurement-Based Compact Thermal Model Extraction Methodology for Packaged ICs,” *IEEE Trans. Components, Packag.*

Manuf. Technol., vol. 7, no. 11, pp. 1786–1794, Nov. 2017.

[121] D. G. Luenberger, “Observing the State of a Linear System,” *IEEE Trans. Mil. Electron.*, vol. 8, no. 2, pp. 74–80, 1964.

[122] D. Luenberger, “An introduction to observers,” *IEEE Trans. Automat. Contr.*, vol. 16, no. 6, pp. 596–602, Dec. 1971.

[123] R. D. Lorenz, “Course Notes: ME 746 - Dynamics of Controlled Systems.” University of Wisconsin-Madison, Madison, WI, 2014.

[124] R. D. Lorenz, “Observers and State Filters in Drives and Power Electronics,” in *Proc. of IEEE OPTIM Conference*, 2002, pp. XIX–XXVIII.

[125] B. Gopinath, “On the Control of Linear Multiple Input-Output Systems*,” *Bell Syst. Tech. J.*, vol. 50, no. 3, pp. 1063–1081, Mar. 1971.

[126] R. L. Williams and D. A. Lawrence, *Linear State-Space Control Systems*. Hoboken, NJ, USA: John Wiley & Sons, Inc., 2007.

[127] P. L. Jansen and R. D. Lorenz, “A physically insightful approach to the design and accuracy assessment of flux observers for field oriented induction machine drives,” *IEEE Trans. Ind. Appl.*, vol. 30, no. 1, pp. 101–110, 1994.

[128] P. L. Jansen, R. D. Lorenz, and S. Member, “Transducerless Position and Velocitv Estimation in Induction and Salient AC Machines,” vol. 31, no. 2, pp. 240–247, 1995.

[129] R. D. Lorenz and K. W. Van Patten, “High-resolution velocity estimation for all-digital, AC servo drives,” *IEEE Trans. Ind. Appl.*, vol. 27, no. 4, pp. 701–705, 1991.

[130] R. D. Lorenz, T. a. Lipo, and D. W. Novotny, “Motion control with induction motors,” *Proc. IEEE*, vol. 82, no. 8, 1994.

[131] G. Ellis and R. D. Lorenz, “Resonant load control methods for industrial servo drives,” *Conf. Rec. 2000 IEEE Ind. Appl. Conf. Thirty-Fifth IAS Annu. Meet. World Conf. Ind. Appl. Electr. Energy (Cat. No.00CH37129)*, vol. 3, pp. 1438–1445, 2000.

[132] M. J. Ryan, W. E. Brumsickle, R. D. Lorenz, and S. Member, “Control Topology Options for Single Phase UPS Inverter,” *Ieee Trans. Ind. Appl.*, vol. 33, no. 2, pp. 493–501, 1997.

[133] Xinmei Yuan, I. Brown, R. D. Lorenz, and Arui Qui, “Observer-based inverter disturbance compensation,” in *2009 IEEE Energy Conversion Congress and Exposition*, 2009, pp. 2520–2527.

[134] H.-Y. O. Yang and R. D. Lorenz, “Consistently achieving lowest losses with dual-loop finite-settling-step DC-to-DC converter control by using real-time parameter estimation,” in *2017 20th International Conference on Electrical Machines and Systems (ICEMS)*, 2017, pp. 1–6.

[135] R. I. Davis and R. D. Lorenz, “Engine torque ripple cancellation with an integrated starter alternator in a hybrid electric vehicle: implementation and control,” *IEEE Trans. Ind. Appl.*, vol. 39, no. 6, pp. 1765–1774, Nov. 2003.

[136] G. Ramirez, R. D. Lorenz, and M. A. Valenzuela, “Observer-Based Estimation of Modulus of Elasticity for Papermaking Process,” *IEEE Trans. Ind. Appl.*, vol. 50, no. 3, pp. 1678–1686, May 2014.

[137] K. K. Huh, R. D. Lorenz, and N. J. Nagel, “Gear Fault Diagnostics Integrated in the Motion Servo Drive for Electromechanical Actuators,” *IEEE Trans. Ind. Appl.*, vol. 48, no. 1, pp. 142–150, Jan.

2012.

[138] C. M. Wolf and R. D. Lorenz, “Using the Motor Drive as a Sensor to Extract Spatially Dependent Information for Motion Control Applications,” *IEEE Trans. Ind. Appl.*, vol. 47, no. 3, pp. 1344–1351, May 2011.

[139] C. W. Secrest, J. S. Pointer, M. R. Buehner, and R. D. Lorenz, “Improving Position Sensor Accuracy Through Spatial Harmonic Decoupling, and Sensor Scaling, Offset, and Orthogonality Correction Using Self-Commissioning MRAS Methods,” *IEEE Trans. Ind. Appl.*, vol. 51, no. 6, pp. 4492–4504, Nov. 2015.

[140] C. W. Secrest and R. D. Lorenz, “Adaptive Decoupling of Nonideal Machine and Sensor Properties for Extraction of Fine Details When Using the Motor Drive as a Diagnostic Sensor,” *IEEE Trans. Ind. Appl.*, vol. 53, no. 3, pp. 2925–2935, May 2017.

[141] C. J. Backi, J. Dimon Bendtsen, J. Leth, and J. T. Gravdahl, “Estimation of inner-domain temperatures for a freezing process,” in *2014 IEEE Conference on Control Applications (CCA)*, 2014, pp. 1759–1764.

[142] H. M. N. Achiri, V. Smidl, and Z. Peroutka, “Mitigation of electric drivetrain oscillation resulting from abrupt current derating at low coolant flow rate,” in *IECON 2015 - 41st Annual Conference of the IEEE Industrial Electronics Society*, 2015, pp. 003638–003642.

[143] M. Andresen, M. Schloh, G. Buticchi, and M. Liserre, “Computational light junction temperature estimator for active thermal control,” in *2016 IEEE Energy Conversion Congress and Exposition (ECCE)*, 2016, pp. 1–7.

[144] J. D. Holmes, M. P. Foster, and D. A. Stone, “System-wide temperature estimation for IMS based power electronics circuits,” in *2009 International Conference on Power Electronics and Drive Systems (PEDS)*, 2009, pp. 615–618.

[145] D. A. Murdock, J. E. R. Torres, J. J. Connors, and R. D. Lorenz, “Active thermal control of power electronic modules,” *IEEE Trans. Ind. Appl.*, vol. 42, no. 2, pp. 552–558, Mar. 2006.

[146] C. H. van der Broeck, R. D. Lorenz, and R. W. De Doncker, “Methods for Monitoring 3-D Temperature Distributions in Power Electronic Modules,” in *Applied Power Electronics Conf. and Expo (APEC) 2018*, 2018.

[147] Y. A. LIU and L. LAPLDUS, “Observer theory for distributed-parameter systems,” *Int. J. Syst. Sci.*, vol. 7, no. 7, pp. 731–742, Jul. 1976.

[148] T. Kobayashi, “Discrete-Time Observers and Parameter Determination for Distributed Parameter Systems with Discrete-Time Input–Output Data,” *SIAM J. Control Optim.*, vol. 21, no. 3, pp. 331–351, May 1983.

[149] A. EL JAI and M. AMOUROUX, “Sensors and observers in distributed parameter systems,” *Int. J. Control*, vol. 47, no. 1, pp. 333–347, Jan. 1988.

[150] T. Meurer, K. Graichen, and G. Ernst-Dieter, *Control and Observer Design for Nonlinear Finite and Infinite Dimensional Systems (Lecture Notes in Control and Information Sciences)*. Springer, 2005.

[151] T. Meurer, “On the Extended Luenberger-Type Observer for Semilinear Distributed-Parameter Systems,” *IEEE Trans. Automat. Contr.*, vol. 58, no. 7, pp. 1732–1743, Jul. 2013.

[152] N. N. Kamran and S. V. Drakunov, “Observer Design for Distributed Parameter Systems,” in *2015*

Proceedings of the Conference on Control and its Applications, Philadelphia, PA: Society for Industrial and Applied Mathematics, 2015, pp. 475–482.

[153] N. Kamran, "Sliding Mode Observers for Distributed Parameter Systems: Theory and Applications," *Ph.D. Thesis*, 2016.

[154] Z. Hidayat, R. Babuska, B. De Schutter, and A. Nunez, "Observers for linear distributed-parameter systems: A survey," in *2011 IEEE International Symposium on Robotic and Sensors Environments (ROSE)*, 2011, pp. 166–171.

[155] J.-W. Wang, Y.-Q. Liu, and C.-Y. Sun, "Luenberger observer design for state estimation of a linear parabolic distributed parameter system with discrete measurement sensors," in *2016 12th World Congress on Intelligent Control and Automation (WCICA)*, 2016, pp. 1123–1128.

[156] Hua Deng, Han-Xiong Li, and Guanrong Chen, "Spectral-approximation-based intelligent modeling for distributed thermal processes," *IEEE Trans. Control Syst. Technol.*, vol. 13, no. 5, pp. 686–700, Sep. 2005.

[157] T. A. Polom, M. Andresen, M. Liserre, and R. D. Lorenz, "Experimentally Extracting Multiple Spatial Thermal Models that Accurately Capture Slow and Fast Properties of Assembled Power Semiconductor Converter Systems," in *2018 IEEE Energy Conversion Congress and Exposition (ECCE)*, 2018, pp. 7391–7398.

[158] T. A. Polom, M. Andresen, M. Liserre, and R. D. Lorenz, "Frequency Domain Electrothermal Impedance Spectroscopy of an Actively Switching Power Semiconductor Converter," *IEEE Trans. Ind. Appl.*, pp. 1–11, 2019.

[159] J. A. Free, T. A. Polom, and R. D. Lorenz, "Computational Heat Transfer Platform for Frequency Domain Reliability Design," in *2019 20th Workshop on Control and Modeling for Power Electronics (COMPEL)*, 2019, pp. 1–7.

[160] T. A. Polom, C. H. van der Broeck, R. W. De Doncker, and R. D. Lorenz, "Spatially-Varying Electrothermal Impedance Analysis for Designing Power Semiconductor Converter Systems," in *2019 18th IEEE Intersociety Conference on Thermal and Thermomechanical Phenomena in Electronic Systems (ITherm)*, 2019, pp. 117–126.

[161] J. N. Davidson, D. A. Stone, M. P. Foster, and D. T. Gladwin, "Measurement and Characterization Technique for Real-Time Die Temperature Prediction of MOSFET-Based Power Electronics," *IEEE Trans. Power Electron.*, vol. 31, no. 6, pp. 4378–4388, Jun. 2016.

[162] K. Ma, N. He, M. Liserre, and F. Blaabjerg, "Frequency-Domain Thermal Modeling and Characterization of Power Semiconductor Devices," *IEEE Trans. Power Electron.*, vol. 31, no. 10, pp. 7183–7193, Oct. 2016.

[163] T. A. Polom, "ΔTj Control of Switching Power Devices At Thermal Boundaries Via Physics-Based Loss Manipulation," *M.S. Thesis*, 2016.

[164] T. A. Polom, B. Wang, and R. D. Lorenz, "Control of Junction Temperature and Its Rate of Change at Thermal Boundaries via Precise Loss Manipulation," *IEEE Trans. Ind. Appl.*, vol. 53, no. 5, pp. 4796–4806, Sep. 2017.

[165] R. D. Lorenz, "Course notes: ME/ECE 577 - Automatic Controls Laboratory." Madison, WI, 2018.

[166] P. Welch, "The use of fast Fourier transform for the estimation of power spectra: A method based on time averaging over short, modified periodograms," *IEEE Trans. Audio Electroacoust.*, vol. 15, no. 2, pp. 70–73, Jun. 1967.

[167] H. Niu and R. D. Lorenz, “Evaluating Different Implementations of Online Junction Temperature Sensing for Switching Power Semiconductors,” *IEEE Trans. Ind. Appl.*, vol. 53, no. 1, pp. 391–401, Jan. 2017.

[168] F. Stella, G. Pellegrino, E. Armando, and D. Dapra, “Online Junction Temperature Estimation of SiC Power mosfets Through On-State Voltage Mapping,” *IEEE Trans. Ind. Appl.*, vol. 54, no. 4, pp. 3453–3462, Jul. 2018.

[169] N. Kumar, C. Joishi, Z. Xia, S. Rajan, and S. Kumar, “Electro-Thermal Simulation of Delta-Doped β-Ga2O3 Field Effect Transistors,” in *2019 18th IEEE Intersociety Conference on Thermal and Thermomechanical Phenomena in Electronic Systems (ITherm)*, 2019, pp. 370–375.

[170] Cree, “Silicon Carbide Power MOSFET C3M.” pp. 1–11, 2016.

[171] T. A. Polom, C. van der Broeck, R. W. De Doncker, and R. D. Lorenz, “Real-Time, In Situ Degradation Monitoring in Power Semiconductor Converters,” in *2019 IEEE Applied Power Electronics Conference and Exposition (APEC)*, 2019, pp. 2720–2727.

[172] C. H. van der Broeck, S. Kalker, T. A. Polom, R. D. Lorenz, and R. W. De Doncker, “In-situ Thermal Impedance Spectroscopy of Power Electronic Modules for Localized Degradation Identification,” in *Proc. of the 2019 International Exhibition and Conference for Power Electronics, Intelligent Motion, Renewable Energy and Energy Management*, 2019, pp. 1097–1104.

[173] T. A. Polom, C. H. van der Broeck, R. W. De Doncker, and R. D. Lorenz, “Designing Power Modules for Degradation Sensing,” in *Proc. of the 2019 IEEE Energy Conversion Congress and Exposition (ECCE)*, 2019, pp. 1–8.

[174] C. H. van der Broeck, T. Polom, R. D. Lorenz, and R. W. De Doncker, “Thermal Monitoring of Power Electronic Modules Using Device Self-Sensing,” in *2018 IEEE Energy Conversion Congress and Exposition (ECCE)*, 2018, pp. 4699–4706.

[175] M. H. Bierhoff and F. W. Fuchs, “Semiconductor losses in voltage source and current source IGBT converters based on analytical derivation,” in *Proc. IEEE 35th Annual Power Electronics Specialists Conf. (IEEE Cat. No.04CH37551)*, 2004, vol. 4, pp. 2836--2842 Vol.4.

[176] C. H. van der Broeck, L. A. Ruppert, A. Hinz, M. Conrad, and R. W. De Doncker, “Spatial Electro-Thermal Modeling and Simulation of Power Electronic Modules,” *IEEE Trans. Ind. Appl.*, vol. 54, no. 1, pp. 404–415, Jan. 2018.

[177] C. van der Broeck, T. A. Polom, R. D. Lorenz, and R. W. De Doncker, “Thermal Monitoring of Power Electronic Modules using Device Self-Sensing,” in *Proc. of the 2018 IEEE Energy Conversion Congress and Exposition (ECCE)*, 2018.

[178] E. Barsoukov and J. R. Macdonald, Eds., *Impedance Spectroscopy*. John Wiley & Sons, Inc., 2005.

[179] Y. Wang, N. Niimura, and R. D. Lorenz, “Real-Time Parameter Identification and Integration on Deadbeat-Direct Torque and Flux Control (DB-DTFC) Without Inducing Additional Torque Ripple,” *IEEE Trans. Ind. Appl.*, vol. 52, no. 4, pp. 3104–3114, Jul. 2016.

[180] Cree, “1.2kV, 25mOhm All-Silicon Carbide Six-Pack Module.” 2013.

[181] A. J. Morgan, Y. Xu, D. C. Hopkins, I. Husain, and W. Yu, “Decomposition and electro-physical model creation of the CREE 1200V, 50A 3-Ph SiC module,” in *Proc. IEEE Applied Power Electronics Conf. and Exposition (APEC)*, 2016, pp. 2141–2146.

[182] B. J. Baliga, Ed., *Wide Bandgap Semiconductor Power Devices*. Elsevier Science & Technology,

2018.

[183] O. Schilling, M. Schäfer, K. Mainka, M. Thoben, and F. Sauerland, “Power cycling testing and FE modelling focussed on Al wire bond fatigue in high power IGBT modules,” *Microelectron. Reliab.*, vol. 52, no. 9–10, pp. 2347–2352, Sep. 2012.